Silicon vacancy color centers in chemical vapor deposition diamond: New insights into promising solid state single photon sources

Dissertation
zur Erlangung des Grades Doktor der Naturwissenschaften
der Naturwissenschaftlich-Technischen Fakultät II
- Physik und Mechatronik -
der Universität des Saarlandes

von

Elke Katja Neu

Saarbrücken

2012

Tag des Kolloquiums:	08.06.2012
Dekan:	Univ.-Prof. Dr. rer. nat. Helmut Seidel
Mitglieder des Prüfungsausschusses:	Univ.-Prof. Dr.-Ing Michael Möller
	Univ.-Prof. Dr. rer. nat. Christoph Becher
	Univ.-Prof. Dr. rer. nat. Gregor Jung
	Univ.-Prof. Dr. Fedor Jelezko
	Dr. rer. nat. Frank Müller

Abstract

This work extensively investigates single silicon vacancy (SiV) color centers in diamond which are promising candidates for solid state single photon sources. The SiV centers are hosted by synthetic chemical vapor deposition diamonds in which they are created during the growth due to the incorporation of silicon impurities. The SiV centers display outstanding spectral properties including bright zero-phonon-lines (ZPLs, wavelengths mostly between 736 nm and 746 nm) with linewidths as narrow as 0.7 nm together with a distinct concentration of the fluorescence (approx. 70%) in the ZPL. With single photon count rates up to 6.2 Mcps under continuous excitation, SiV centers are the brightest single color centers at present. Intensity auto-correlation measurements reveal three level population dynamics including a shelving state from which the SiV center can be reactivated by the excitation laser. Besides the ZPL, we identify previously unobserved electronic transitions in the spectral range between 820 nm and 840 nm. Using polarization spectroscopy, we investigate for the first time the transition dipole(s) for a single SiV center and find a single $\langle 110 \rangle$-oriented dipole enabling fully linearly polarized single photon emission. Spectroscopy at cryogenic temperature for the first time reveals the ZPL fine structure of a single SiV center as well as mostly temperature independent population dynamics.

Kurzzusammenfassung

In dieser Arbeit werden einzelne Silizium-Fehlstellen (SiV) Farbzentren in Diamant untersucht. Diese sind vielversprechende Kandidaten für festkörperbasierte Einzelphotonenquellen. Die SiV Zentren entstehen während des Wachstums in synthetischen, durch Gasphasenabscheidung hergestellten Diamanten aus Silizium-Verunreinigungen. SiV Zentren zeigen herausragende spektrale Eigenschaften darunter eine intensive Null-Phononen (NP) Linie (Wellenlänge meist zwischen 736 nm und 746 nm) mit einer Breite von minimal nur 0.7 nm zusammen mit einer ausgeprägten Konzentration der Fluoreszenz (ca. 70%) in der NP Linie. SiV Zentren sind mit Einzelphotonenraten bis zu 6.2 Mcps bei kontinuierlicher Anregung die hellsten einzelnen Farbzentren zum jetzigen Zeitpunkt. Intensitäts-Autokorrelationsmessungen zeigen eine Drei-Niveau Besetzungsdynamik mit einem Shelving Zustand, aus dem das SiV Zentrum durch den Anregungslaser reaktiviert werden kann. Neben der NP Linie werden erstmals elektronische Übergänge zwischen 820 nm und 840 nm identifiziert. Mit Hilfe von Polarisationsspektroskopie wird die Dipolausrichtung einzelner SiV Zentren untersucht und ein einzelner Dipol in $\langle 110 \rangle$ Kristallrichtung identifiziert. Tieftemperaturspektroskopie liefert erstmals die Feinstruktur der NP Linie eines einzelnen SiV Zentrums und zeigt eine weitgehend temperaturunabhängige Besetzungsdynamik.

Zusammenfassung

Einzelphotonenquellen sind eine grundlegende Vorraussetzung für die sog. Quanteninformationsverarbeitung, die Gesetze der Quantenmechanik z.B. zur abhörsicheren Übertragung von Informationen nutzt. In den vergangenen Jahren wurden einzelne Farbzentren in Diamant als vielversprechende Kandidaten für praktikable, festkörperbasierte Einzelphotonenquellen identifiziert. Farbzentren sind optisch aktive Komplexe bestehend aus Fremdatomen und/oder intrinsischen Defekten z.B. Gitterfehlstellen im Diamantgitter. Farbzentren in Diamant bieten als Einzelphotonenquellen mehrere Vorteile. Zum einen kann die Fluoreszenz von Farbzentren unter Normalbedingungen (Raumtemperatur, Atmosphärendruck) zur Einzelphotonenemission genutzt werden, was den technischen Aufwand minimiert. Farbzentren können optisch angeregt werden und zeigen eine hohe Photostabilität, was die zeitlich unbegrenzte Nutzung ermöglicht. Die optische Selektion einzelner Zentren wird in dieser Arbeit mit einem konfokalen Lasermikroskop erreicht, bei dem sowohl durch eine scharfe Fokussierung des Laserlichts als auch durch eine Raumfilterung der Fluoreszenz der untersuchte Raumbereich minimiert wird.

Der Großteil der bisher durchgeführten Arbeiten zur Einzelphotonenerzeugung mit Farbzentren verwendet das intensiv erforschte Stickstoff-Fehlstellen Farbzentrum (engl. nitrogen vacancy, NV). Mit einer Emissionsbandbreite von ca. 100 nm im sichtbaren Spektralbereich ermöglicht das NV Zentrum jedoch keine schmalbandige Einzelphotonenemission, die eine effiziente spektrale Filterung zur Trennung von Einzelphotonen und Untergrundlicht ermöglicht. Im Rahmen dieser Arbeit wird das weniger intensiv erforschte Silizium-Fehlstellen Farbzentrum (engl. silicon vacancy, SiV) als vielversprechende Alternative identifiziert und ausführlich auf seine Eignung als Einzelphotonenquelle untersucht. Zur Nutzung als Einzelphotonenquelle müssen SiV Zentren mit geringer Dichte hergestellt werden, um eine optische Anregung einzelner Zentren zu ermöglichen. Im Rahmen dieser Arbeit wurden in Kooperationen synthetische Diamanten mit Hilfe der sog. Gasphasenabscheidung hergestellt. In diesen wurden im Wachstumsprozess durch Silizium-Verunreinigungen SiV Zentren gebildet. Als besonders geeignetes Substratsystem für das Wachstum von Diamanten mit einzelnen SiV Zentren wurde ein Mehrlagensystem aus Silizium, einer Pufferschicht und einem epitaktischen Iridium Film als oberste Schicht identifiziert. Je nach Nukleationsprozess wurden auf diesen Substraten zufällig orientierte Nanodiamanten, sowie orientierte Nanodiamanten (Nanoinseln) oder Diamantfilme gewachsen.

Die untersuchten SiV Zentren zeigen herausragende spektrale Eigenschaften: ihre Fluoreszenz ist hauptsächlich (ca. 70%) in einer schmalen Linie der sog. Null-Phononen (NP) Linie konzentriert. Dieser rein elektronische Übergang liegt für die meisten der beobachteten einzelnen SiV Zentren zwischen 736 nm und 746 nm. Die Streuung der Wellenlängen ist bedingt durch lokale Verspannungen im Kristallgitter. Die beobachteten NP Linien sind mit Raumtemperatur-Linienbreiten von minimal 0.7 nm die schmalsten bisher nachgewiesenen Emissionslinien von Farbzentren. Neben der NP Linie untersuchen wir ausführlich die vibronischen Seitenbanden des SiV

Zentrums, d.h. Übergänge mit Phononenbeteiligung. Auch hier zeigt sich eine starke Beeinflussung der Zentren durch die kristalline Umgebung: Seitenbandintensitäten und Energien variieren signifikant.

Messungen der Intensitäts-Autokorrelationsfunktion $g^{(2)}$ der Fluoreszenz einzelner SiV Zentren weisen eindeutig den Einzelphotonencharakter nach und geben die Besetzungsdynamik der Farbzentren wieder. Alle untersuchten Farbzentren zeigen eine Dynamik, die neben den beiden Niveaus des NP Übergangs ein drittes langlebigeres Niveau, einen sog. Shelving Zustand, aufweist. Zur Beschreibung der Intensitätsabhängigkeit der Besetzungsdynamik wurde ein erweitertes Drei-Niveau-Modell entwickelt, das eine anregungsintensitätsabhängige Reaktivierung des Farbzentrum aus dem Shelving Zustand mit einschließt. Einzelne SiV Zentren zeigen Sättigungszählraten von bis zu 6.2×10^6 cps unter kontinuierlicher Laseranregung und sind damit die hellsten bisher beobachteten einzelnen Farbzentren in Diamant. Diese Beobachtung steht im Gegensatz zu vorhergehenden Arbeiten an einzelnen SiV Zentren, die durch Ionenimplantation erzeugt wurden und die mit ca. 1000 cps eine sehr niedrige Einzelphotonenemissionsrate zeigten. Neben der NP Linie bei ca. 740 nm werden erstmals weitere elektronische Übergänge des SiV Zentrums im Wellenlängenbereich von ca. 820 nm bis 840 nm mit Linienbreiten vergleichbar zur NP Linie nachgewiesen. $g^{(2)}$ Messungen zeigen, dass diese Übergänge einem zusätzlichen Relaxationspfad zuzuordnen sind und nicht mit dem oben beschriebenen Shelving Zustand zusammenhängen.

Die Fluoreszenz von Farbzentren lässt sich als die Abstrahlung eines oder mehrerer Dipole beschreiben. Die Ausrichtung dieser Übergangsdipole im Diamantgitter ist entscheidend für die Kopplung von Farbzentren an photonische Strukturen wie z.B. photonische Kristalle in Diamant. Zur Dipolausrichtung einzelner SiV Zentren lagen bisher keine Ergebnisse vor. Polarisationsmessungen an SiV Zentren in orientierten Diamant Nanoinseln identifizieren einen einzelnen Dipol in $\langle 110 \rangle$ Kristallrichtung des Diamantgitters für das SiV Zentrum. Diese Beobachtung stimmt mit vorhergehenden Beobachtungen an SiV-Ensembles überein, steht jedoch im Widerspruch zu den in der Literatur vorgestellten theoretischen Modellen des SiV Zentrums.

Bei tiefen Temperaturen ist die Verbreiterung der NP Linie durch Phononen signifikant reduziert, somit kann eine bei Raumtemperatur ausgewaschene Feinstruktur (FS) der NP Linie sichtbar gemacht werden. Für SiV-Ensembles wird in der Literatur eine FS mit 4 Linienkomponenten berichtet. In dieser Arbeit konnte zum ersten Mal die FS der NP Linie an einzelnen SiV Zentren beobachtet werden. Die 4 FS-Komponenten zeigen eine gemeinsame lineare Polarisationsrichtung; Aufspaltung und rel. Intensitäten variieren für individuelle Zentren auf Grund von lokalen Verspannungen. Zeitliche Sprünge der Resonanzfrequenz (spektrale Diffusion) limitieren die minimale Linienbreite bei 5 K auf ca. 50-100 GHz für die meisten Emitter. Es werden jedoch auch SiV Zentren mit geringerem Einfluss der spektralen Diffusion beobachtet (Spektrometerauflösung begrenzt Linienbreite). Die homogene Linienverbreiterung variiert mit der dritten Potenz der absoluten Temperatur. Neben einer Linienverschmälerung bewirkt die Kühlung auf ca. 5 K eine Blauverschiebung der NP Linie um ca. 1.2 nm. Temperaturabhängige $g^{(2)}$ Messungen zeigen eine praktisch temperaturunabhängige Besetzungsdynamik des SiV Zentrums.

Contents

Introduction

The availability of single photons is one of the fundamental prerequisites for *quantum information processing*, i.e., the processing of information harnessing quantum mechanical phenomena (for a review see, e.g., Ref. [1]). In this context, photons serve as fast carriers of quantum information, offering the possibility of being transmitted through optical fibers for long distance communication. This property is especially exploited in *quantum cryptography*, where a secret key is encoded and transmitted using single photons (*quantum key distribution*). If a suitable protocol is chosen this secret key, in principle, offers absolutely secure exchange of information. Several protocols, using different degrees of freedom of the photon to encode the information, have been described in the literature using, e.g., polarization states of single photons [2] or the phase of a single photon. For a review on quantum cryptography see, e.g., Ref. [3]. In addition to secure transport of information, single photons can be used as *quantum bits* in *quantum computers* or *quantum networks*. In contrast to a classical bit, a quantum bit can exist in any superposition state of its two internal states. Quantum computers potentially offer to solve several important tasks faster than classical computers (for a review see, e.g., Ref. [4]). Photons can serve as the main building block of a quantum computer in so called all-optical schemes. However, to be useful in an optical quantum computer rigorous requirements for the spectral properties of the photons have to be fulfilled: The photons have to be indistinguishable to enable interference. The most prominent scheme is the Knill-Laflamme-Milburn scheme that proposes all optical quantum computing using beamsplitters, phase shifters, single photon sources and photo-detectors [5]. However, no information can be stored in this system. In contrast, in a quantum network single photons act as flying qubits that exchange quantum information between distant qubits (see, e.g., Ref. [6]). The advantage of such hybrid approaches is that long lived matter qubits store the quantum information, while photons provide the interaction of the qubits [7]. In another approach, the so called measurement based quantum computing scheme, an entangled state is created probabilistically via measurement of the emitted photons and then used for a quantum algorithm (for a review focussed on spins in solids see Ref. [8]).

Different approaches to the creation of single photons have been reviewed, e.g., in Refs. [9–11]. Quasi single photon sources have been realized using faint laser pulses with average photon numbers far below one and photon pairs created via nonlinear optical processes (parametric downconversion). However, these approaches always include a small probability of producing two photons at the same time. In the pres-

ence of lossy communication channels, these multi-photon events, especially for faint laser pulses, can significantly lower the security in quantum cryptography via the so called *photon number splitting attack* [12–14]: Assume that a potential eavesdropper can establish a lossless transmission channel. Furthermore, the eavesdropper is able to deterministically extract single photons from pulses with multiple photons and can also store these photons. The eavesdropper extracts a single photon from all pulses containing multiple photons and sends the rest of the corresponding pulse to the original receiver of the transfer via a lossless channel. All single photon pulses are blocked by the eavesdropper. If the probability for a multi-photon event is equal to the transmission probability of a photon through the lossy channel the receiver does not detect the presence of the eavesdropper: The photon rate he receives matches the expected rate. Simultaneously, the eavesdropper holds a photon from each pulse that was measured by the receiver. The security of quantum cryptography relies on the fact that the presence of an eavesdropper introduces errors in the transmission [12]. However, in the above described case, the eavesdropper can obtain the transferred information without introducing errors. To enhance the security, more sophisticated protocols can be used see, e.g., Ref. [14]. However, an ideal single photon source with the same rate of non-empty pulses as the quasi-single photon source, in general, allows for higher secure transfer rates than any protocol involving faint laser pulses [11]. Moreover, security considerations always have to include the possibility that the devices used for quantum cryptography have been manipulated by a third party to allow for eavesdropping [15,16]. In Refs. [15,16], the authors discuss the possibility to realize so called *device independent quantum key distribution*: Using single photon sources, entanglement can be distributed between sender and receiver over a long distance. By analyzing the entangled state, sender and receiver can make sure that they can get a secure key from the entangled state independent of the loss in the system or manipulations of measurement devices.

To realize a true single photon source, a single quantum system is necessary: The light emitted from a single quantum system inherently consists of a stream of single photons as the excitation-emission cycle of a single quantum system never takes place twice simultaneously. Thus, under continuous excitation, a stream of single photons with stochastic emission times is created: One never finds two photons at the same time, adjacent photons always retain a time distance. This characteristic is termed *photon antibunching* and can be verified by measurements of the *intensity auto-correlation function* $g^{(2)}$. For applications, e.g, in quantum key distribution, it is favorable to create single photons following a trigger event at as defined as possible points in time: In this case, encoding of information and detection of photons can be synchronized to the emission times of the photons. The trigger event is often realized by a short laser pulse exciting the single photon source [17,18]. The uncertainty in the emission time of the photon is determined by the lifetime of the excited state as the photon is generated by spontaneous emission. Such a triggered single photon emission is often termed *photons on demand* in the literature [17,18].

First observations of single photons have been made using atomic beams with less than one excited atom on average [19]. Later, single atomic systems have been used, e.g., a trapped Mg ion [20]. Single dye molecules in a matrix material have

demonstrated the ability of single photon emission in 1999 [21]. The first solid state single photon sources have been demonstrated in 2000 using semiconductor quantum dots. Due to their nanoscale dimensions, these semiconductor structures represent quantum mechanical potential wells, confining excitons with quantized energy. InAs quantum dots have been employed as first single photon sources [22]. In the same year, the first observation of single photon emission from a single color center in diamond has been reported by two groups [23, 24]. A color center in diamond is an optically active complex involving impurity atoms and/or intrinsic defects (self interstitial, vacancy) in diamond. More than 500 color centers in diamond have been reported [25]. The first demonstrations of single photon emission have been performed using the well investigated negatively charged nitrogen vacancy (NV^-) center in diamond. The NV^- center enables emission in the visible spectral range, the room temperature spectrum spans a wavelength range from approx. 650 nm to 750 nm due to phonon-assisted transitions (sidebands). The purely electronic transition, termed zero-phonon-line (ZPL), is located at 637 nm. Since then, several other color centers in diamond have proven the ability to emit single photons, spanning a large range of wavelengths: In Ref. [26], single photon emission at 470 nm is demonstrated using the TR12 center, a carbon self interstitial. In the near-infrared spectral region around 800 nm, single photon emission has been reported due to nickel-related color centers [27–32]. In the wavelength range from 740 nm to 750 nm, single photon emission from chromium-related centers [33–36] and silicon vacancy (SiV) centers [37, 38] has been observed.

Beyond the demonstration of single photon emission, the question of the practicability of the single photon source has to be raised. For practical single photon sources, the experimental effort should be kept low. Thus, realizations that require sophisticated vacuum systems or extensive cooling are unfavorable. Here, single atoms or ions in traps require larger experimental effort than solid state systems and molecules that can be operated without the need for ultra high vacuum. Additionally, color centers in diamond as well as single molecules allow for a *room temperature operation*, whereas single quantum dots mostly have to be cooled. These advantages of color centers in diamond have led to the development of the first commercially available true single photon source which is based on an NV center in diamond.[1] When operating at room temperature, the single photon source should, nevertheless, enable *narrow bandwidth single photon emission*, thus allowing for efficient spectral filtering. Spectral filtering is inevitable, especially if the single photon source is intended for the implementation of free space and, in particular, daylight quantum key distribution where background counts lead to significantly enhanced error rates. In Ref. [39], short distance free space quantum key distribution has been demonstrated using a spectral window of 6 nm (Rep. Rate 5 MHz, 5 ns gate time). In this regard, color centers in diamond, especially nickel-related centers, have demonstrated narrow room temperature linewidths down to approx. 1.2 nm. To keep the experimental effort low, the excitation of the fluorescence has to be realized in a practical way. For most systems, *optical excitation* is employed. A further reduction of the experimental effort is possible using direct *electrical excitation*.

[1] For detailed information see http://qcvictoria.com

This has been demonstrated for quantum dots (e.g., Ref. [40]) and very recently for single dye molecules [41]. Color center ensembles in diamond, including nitrogen- and xenon-based centers as well as SiV centers, also have demonstrated the ability of electrical excitation [42, 43]. Very recently, single photon emission from electrically excited, neutral NV^0 centers in a diamond p-i-n diode was observed [44].

Furthermore, a practical single photon source should feature a high efficiency, i.e., the probability to gain a single photon after an excitation pulse should be as close to unity as possible. Therefore, the *collection efficiency* for the single photons has to be high. Additionally, integration with common fiber optic components is desirable. In practice, solid state single photon sources often suffer from a small collection or photon extraction efficiency. First, due to *total internal reflection* a large fraction of the light emitted by solid state single photon sources is lost in the high refractive index host material. Second, the *radiation pattern* of the source, that can be often approximated as a single radiating dipole, often hinders a high collection efficiency as a large fraction of the light is emitted into the host material or at large angles that cannot be collected with standard optics. It should be emphasized that the collection efficiency also critically depends on the orientation of the radiating dipole (see, e.g., Ref. [45]). Typical values for the collection efficiency of single photons from solid state materials are small. 8% collection efficiency has been estimated for a single NV center in diamond (NA 1.3 oil-immersion objective, [23]). For semiconductor quantum dots embedded in bulk material, the collection efficiency is in the order of 1% [46, 47] or lower: Ref. [18], e.g., gives 0.15% for their experiments. However, especially for solid state based single photon sources, a lot of promising approaches to enhance the collection efficiency have been pursued in recent years (for a review see Ref. [46]): For quantum dots, e.g., the incorporation into cylindrical *micropillar cavities* has been demonstrated to enable high efficiency single photon creation with a collection efficiency of up to 70% [46] (for a review see Ref. [47]). For color centers in single crystal diamond, cylindrical structures termed *nanowires* have been shown to enhance the collection efficiency by an order of magnitude compared to bulk diamond [48]. Furthermore, for color centers in diamond, a photon extraction efficiency enhancement can be obtained using color centers in *nanodiamonds* instead of bulk diamond [49–51]. Ref. [51] finds a collection efficiency of up to 20% for nanodiamonds on a sapphire substrate. Hemispherical *solid immersion lenses* (SILs) are interesting to geometrically avoid any refraction at the diamond-air interface. SILs can be directly fabricated in bulk diamond containing single color centers [52–55] or color centers in nanodiamonds can be deposited onto a SIL made out of a high refractive index material, e.g., ZrO_2 [56]. For SILs in diamond, a collection efficiency of 30% for a NA of 0.9 has been calculated for NV centers [52]. Single molecules have been incorporated into a dielectric layer system termed *dielectric antenna* that enables collection efficiencies up to 96% [57]. The scheme is applicable also to other types of emitters, e.g., color centers in nanodiamonds [58].

Apart from enhancing the collection efficiency, recently developed techniques allow for the controlled nano-positioning of nanometer sized diamonds on various photonic structures [59,60]. Using these techniques, enhanced single photon emission from color centers in nanodiamonds as a result of lifetime shortening via the coupling

to *metallic nanoparticles* has been demonstrated [61]. Also coupling to non-diamond *photonic crystals* [62] or microsphere resonators [63] and direct placement on *fiber facets* has been shown [64, 65].

For most proposals in quantum information, the spectral and polarization properties of the photons are significant: Often *indistinguishable photons* are required. Experimentally, the indistinguishability of photons is tested via *two-photon interference* experiments: If two indistinguishable photons simultaneously impinge on a beamsplitter they always exit the beamsplitter at the same output port [66]. For solid state systems, in contrast to atomic systems, the creation of indistinguishable photons mostly requires the tuning of resonances due to the inhomogeneous spread of resonance frequencies of individual emitters. Color centers in diamond have demonstrated the ability for a high tuning range using electric fields [35, 55, 67]. Very recently, distant NV centers have been tuned into resonance using Stark shifting and the indistinguishability of single photons from these NV centers has been shown [55]: Polarization filtered (linearly polarized) photons from one spin selective transition within the ZPL of two NV centers at 9 K are employed in a two photon interference experiment. Note that as the broad phonon-assisted transitions of the NV center have to be filtered out, less than 4% of the photons emitted by the NV center can be used, rendering a high collection efficiency especially important.

To realize a quantum network as introduced above, an interface between single photons and matter qubits/single photon sources has to be available. Several proposals suggest to integrate the single photon source into a cavity with high Q-factor (corresponding to a long photon storage time) and a small modal volume. In diamond, first approaches toward such coupling have been demonstrated using diamond ring resonators [68] and photonic crystals [69].

The discussion above illustrates that color centers in diamond are promising candidates for solid state single photon sources. Most experiments mentioned above have been performed using NV centers. However, NV centers exhibit some detrimental properties, e.g., for applications in quantum key distribution or cavity coupling, in particular due to the broad emission spanning approx. 100 nm at room temperature. The aim of this work is to thoroughly investigate an alternative color center with promising spectral properties: SiV centers display an emission wavelength of approx. 738 nm with a significantly reduced emission bandwidth of only 5 nm (single SiV center at room temperature) [37]. Furthermore, SiV centers can be excited using red laser light (e.g., 685 nm from a diode laser [37]). We emphasize that the narrow emission bandwidth together with the feasibility of excitation with red laser light, render SiV centers in nanodiamonds not only interesting as single photon sources but also as *fluorescent labels for in-vivo imaging*. Several experiments have successfully employed nanodiamonds containing NV centers as fluorescent labels for in-vivo imaging (see, e.g. Refs. [70–72]). Here, nanodiamonds stand out owing to photostable fluorescence [70], biocompatibility [71], and feasible surface functionalization [72]. However, the need for excitation with typically green laser light (532 nm) and the broad emission bandwidth in the visible spectral range of the NV center are unfavorable compared to SiV centers: First, excitation with red laser light can minimize tissue autofluorescence in imaging applications [70, 73]. Furthermore, the

absorption of a red excitation laser in biological tissue is about 20 times smaller than for a green excitation laser [73] and thus enables the imaging of deep tissue. Second, the emission wavelength of the SiV centers is situated in the near-infrared spectral window of biological tissue featuring small absorption together with a low autofluorescence level. Third, the narrow emission bandwidth of the SiV centers enables spectral filtering to additionally discriminate label luminescence from background signals.

Despite the promising spectral properties of SiV centers, previous reports investigating single SiV centers as single photon sources [37, 74] found a lack of brightness for single SiV centers created by ion implantation. We here pursue the approach to create single optically addressable SiV centers as well as ensembles of SiV centers during the chemical vapor deposition (CVD) synthesis of diamond (*in situ*). We exploit advanced material systems including CVD nanodiamonds, bound to substrates or in a colloidal solution, as well as oriented CVD diamond nanocrystals and films. The feasible production of fluorescent nanodiamonds in a colloidal solution is especially interesting in the context of fluorescent labels for in-vivo imaging applications. Using these advanced material systems enables, for the first time, the detailed spectroscopy of single bright SiV centers. The measurements partially approve findings from previously reported ensemble investigations but also supply surprising new results, e.g., considering the linewidths of single centers and additional electronic transitions. Within the scope of this thesis, we extensively investigate single SiV centers with regard to their suitability as single photon sources. These investigations include a detailed study of the brightness of single centers as well as the population dynamics of the centers, studied via intensity auto-correlation ($g^{(2)}$) measurements.

The work is structured as follows. Chapter 1 introduces diamond as a host material for single color centers and summarizes the state of knowledge concerning SiV centers in the literature. Chapter 2 describes concepts from group theory that aid in deducing properties of physical systems, here color centers, from their symmetry properties. Chapter 3 gives an overview of the experimental setup employed to locate and investigate single color centers. Chapter 4 specifies the employed samples and the fabrication methods. Chapter 5 presents room temperature spectroscopy of single SiV centers, exploits the internal population dynamics using photon-correlation measurements and demonstrates room temperature single photon emission. In Chapter 6, we perform polarization spectroscopy on single SiV centers in nanodiamonds with defined orientation to obtain information about the orientation of the emission and absorption dipole of single SiV centers. Chapter 7 deals with the low temperature properties of single SiV centers. In particular, we measure the spectral properties of the SiV center ZPL fine structure components which allow to explore the mechanisms of line broadening. Finally, Chapter 8, for the first time, investigates the near-infrared photoluminescence of single SiV centers in the spectral region from approx. 820 nm to 840 nm.

Chapter 1

Silicon vacancy (SiV) centers in diamond

This chapter introduces the relevant properties of diamond as a host material for single color centers. Subsequently, the properties of the silicon vacancy (SiV) center reported in the literature are introduced, focussing on the properties significant for the application of single SiV centers as single photon sources. In particular, the atomic composition and possible approaches to create SiV centers are summarized. Furthermore, the excitation methods as well as the spectral characteristics of the luminescence are introduced. The discussion includes the properties of the purely electronic transition, the so called zero-phonon-line (ZPL), as well as the influence of the electron-phonon coupling leading to additional vibration assisted transitions, the so called vibronic sidebands.

1.1 Diamond as host material for single color centers

Diamond is, besides graphite, one of the crystalline forms of carbon. At room temperature and normal pressure, graphite is the thermodynamically stable form of carbon; however, diamonds are metastable. Natural diamonds are created at depths around 200 km below the earth's surface involving simultaneously pressures of $70 - 80$ kbar and temperatures of $1400 - 1600\,^{\circ}\mathrm{C}$ [75]. The synthesis of diamond by the high-pressure-high-temperature (HPHT) method mimics this process. First demonstrated in 1955 [76], HPHT synthesis has been the most important industrial way to manufacture diamonds for the past decades [75]. To allow for a manageable process, so called solvent metals are added (Fe, Ni, Co). These metals are to some extent incorporated into the diamond together with a mostly high (up to 100 ppm) concentration of nitrogen [75]. Similar to that approach, detonation synthesis of diamond uses the high pressure and high temperature condition created during an explosion to synthesize diamond nanoparticles [77]. In contrast to this, the synthesis of diamond from the gas phase using chemical vapor deposition (CVD) does not rely on reaching the condition of thermodynamical stability of diamond but on reaction kinetics. In a plasma containing atomic hydrogen and carbon-containing

molecules/molecule-fragments, the formation of diamond is favored over the formation of graphite. This is due to the fact that the atomic hydrogen preferentially etches sp^2 bonded carbon, i.e., graphite. To dissociate hydrogen molecules, they have to be heated to temperatures above 2000 K. The different CVD methods use different energy sources to obtain that dissociation including arcs (arc-jet, DC arc), heated metal wires ('hot filaments') and microwave plasmas [75, 78, 79]. Generally, CVD enables the synthesis of high purity diamonds. Thus, the samples investigated in this work are all synthesized by a CVD method. The two CVD methods employed to synthesize the samples studied in this work are introduced in more detail in Sec. 4.1.

A perfect single crystal of diamond resembles a cubic, cubo-octahedral or octahedral shape depending on the crystal faces that develop. Figure 1.1(a) displays an octahedral crystal shape in comparison to the cubic shape. Figures 1.1(b)+(c) display examples of cubo-octahedral shapes. For a crystal displaying {111} faces, an octahedron is found, {100} faces form a cubic crystal. A cubo-octahedral crystal displays {100} as well as {111} faces (dark blue and light blue faces in Figs. 1.1(b)+(c), respectively). Depending on the relative size of the {111} and {100} faces the cubo-octahedral crystal shape changes, e.g., for small {111} faces and large {100} faces the crystal shape is close to cubic resembling a 'cube with cut off corners'. In a CVD process, the growth parameters can determine the crystal shape. More detailed drawings of these crystal shapes can be found, e.g., in Refs. [78, 80–82]. For a discussion of the lattice symmetry of diamond, see Chapter 2.

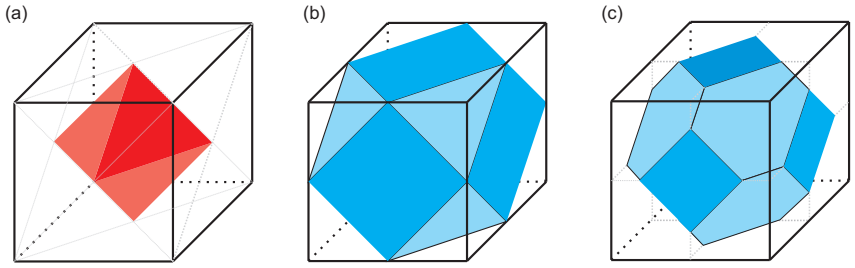

Figure 1.1: Shapes of diamond single crystals: (a) cubic shape, indicated by black lines and octahedral shape, indicated by filled red faces. The faces of the cube are {100} faces of the diamond lattice, the faces of the octahedron are {111} faces. (b)+(c) examples of cubo-octahedral crystals with {100} faces (dark blue) and {111} faces (light blue).

Historically, natural diamonds have been classified as type I or II. Thereby, diamonds of type II lack specific infrared absorption bands [83] later identified being due to nitrogen impurities [75]. Class I is further divided into subclass Ib representing diamonds with isolated nitrogen atoms incorporated on a substitutional lattice site as dominant impurity. For subclass Ia, aggregated nitrogen dominates. Subclass IIb represent p-type semiconducting diamonds. IIa represents diamonds that are 'pure' in the sense of a lack of infrared defect absorption [84]. Today, most CVD diamonds belong to class IIa, while HPHT diamonds often belong to type Ib. However, for modern high purity CVD diamonds the IIa classification is insufficient: It does not allow to specify the purity of current synthetic diamonds adequately.

Instead, the concentrations of the most common impurities, substitutional nitrogen $[N]^S$ and boron [B], are given explicitly. To date, commercially available CVD diamonds[1] reach purities of $[N]^S < 1\,\text{ppm}$, [B]$< 0.05\,\text{ppm}$ (standard single crystal) down to $[N]^S < 5\,\text{ppb}$, [B]$< 1\,\text{ppb}$ ('electronic grade diamond'). Recently, even purer 'quantum grade' diamonds have been synthesized revealing less than 1 ppb $[N]^S$ [85]. Simultaneously, in these diamonds the fraction of C^{13} isotopes is reduced from the natural abundance of 1.1% to 0.3% or even less [85,86]. Thus, these diamonds allow for a reduced density of paramagnetic defects due to nitrogen impurities and C^{13} atoms. (The application of these diamonds is discussed at the end of this section.) The feasibility of producing high purity synthetic diamonds, not only as single crystal diamond but also as nanodiamonds, forms the prerequisite for the application of diamond as host for single photon emitters and also in photonic applications. In the following, we summarize the properties of diamond relevant to the mentioned applications.

Pure, single crystalline diamonds are transparent in the visible and even up to the ultraviolet spectral range for wavelengths longer than 230 nm [87] as a consequence of the large bandgap energy of diamond. However, for imperfect diamonds or diamonds containing high impurity concentrations, especially for polycrystalline and nanocrystalline diamond films, the onset of the absorption is shifted to lower energies due to broad defect induced states in the bandgap (see e.g., Ref. [88–90]). Diamond has an indirect band gap of 5.5 eV, the direct band gap energy even amounts to 7.3 eV corresponding to a wavelength of 170 nm. The electronic band structure has been calculated, e.g., in Ref. [91]. Due to this large bandgap, a large energy range is accessible for the formation of discrete, impurity induced energy levels in the bandgap. The absorption of optically active impurities or impurity complexes gives rise to the color of natural diamonds, thus these impurities are commonly termed color centers. Nearly 500 color centers in diamond have been reported [25]. Due to the small size of the carbon atom and the tight bonds of the diamond lattice, large impurities do not fit into the lattice without inducing significant stress and thus defect concentrations of heavy impurities are generally low [84]. However, even very heavy impurities like rare earth metals have been shown to occupy lattice sites after ion implantations [92,93].

Apart from the available energy range for electronic states, color centers are also influenced by coupling of electronic transitions to phonons. Here, diamond stands out owing to the fact that its lattice supports comparably high energy phonons with energies of 70 meV up to 168 meV (Debye frequency corresponding to 150 meV) [25]. The phonon density of states, in particular its low energy contributions, significantly influences the linewidth of electronic transitions in a solid [94,95]. Therefore, the comparably high phonon energies in diamond can be advantageous. For a detailed discussion on electron-phonon coupling, see Sec. 1.3.3.

The refractive index n of diamond amounts to 2.4 in the spectral region around 740 nm [96]. Thus, compared to other materials transparent in the visible range, e.g., glass ($n = 1.4 - 1.9$ [97]), SiN ($n = 2.02$ [98]) it is comparably high. However, there are materials, e.g., GaP ($n = 3.3$ [99]) that exhibit a superior refractive index.

[1] See e.g., http://www.e6cvd.com

The large refractive index allows for the implementation of photonic microstructures in diamond, e.g., nanowires [48], microring resonators [68] and photonic crystals [69, 100] which generally rely on a high refractive index material. These photonic elements potentially offer enhanced single photon sources and, depending on the structure size and type, strong light matter interaction.

For the application of single color centers to create single photons without using photonic structures, however, the high refractive index of diamond is detrimental as illustrated in Fig. 1.2: The critical angle for total internal reflection at a diamond-air interface amounts only to 24.6 °. Thus, depending on the radiation pattern, a large portion of the color center's fluorescence is not extracted from the diamond. Even for light impinging perpendicularly to the surface, a fraction of 17% is reflected back into the diamond material (Fresnel reflection). Fortunately, the efficiency of fluorescence extraction can be enhanced by using nanodiamonds smaller than the wavelength of the color center fluorescence. This has been demonstrated, e.g., for nitrogen vacancy (NV) color centers in Ref. [49]. The enhanced fluorescence extraction is explained in Ref. [49] in terms of an efficient suppression of total internal reflection. However, individual NV centers in nanodiamonds often exhibit a broad distribution of lifetime and brightness, whereas lifetime and brightness are not correlated. The spread of lifetime and brightness may arise from the local electric fields inside the nanodiamonds that influence the centers as discussed in Ref. [50] for spherical nanodiamonds: For nanodiamonds significantly smaller than the wavelength of the fluorescence light, a low, uniformly distributed electric field amplitude develops inside the nanoparticle. This effect is termed dielectric shielding, here, the field mostly localizes outside the nanoparticle. Thus, these findings explain the experimental observation of a prolonged lifetime of color centers in nanodiamonds [49, 50] and may also correspond to the picture of suppressed total internal reflection. For larger particles, Mie-resonances corresponding to spatial modes of the electric field inside the nanoparticles occur. These modes can significantly alter the radiative properties of a color center dipole: The dipole emission couples to these modes, therefore leading to altered radiative rates as well as an altered radiation pattern for the fluorescence mediated by the particle modes. This, e.g., leads to a more directional emission.

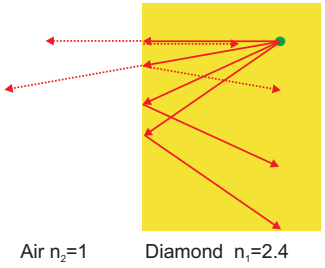

Figure 1.2: Illustration of collection efficiency reduction due to total internal reflection at diamond air interface.

Due to the cubic lattice symmetry, diamond does not exhibit birefringence. However, due to stress induced in the proximity of crystal defects (e.g., dislocations) birefringence is commonly observed. High quality diamonds with low birefringence have recently been produced [101] and can now be used, e.g., as intracavity heat

spreaders for lasers (diamond has the highest thermal conductivity of all materials at room temperature) [75] or as active material in diamond Raman lasers [87]. For the latter application, the high Raman gain of diamond [87] is significant. Visible Raman lasers [87] as well as broadband Raman sideband generation have been demonstrated [102].

Another outstanding property of diamond is connected to the fact that the most abundant carbon isotope C^{12} does not exhibit a nuclear spin. Recently, high purity diamonds with controlled isotopic purity of C^{12} have been produced (see above and Ref. [85, 86]). In these isotopically pure diamonds, single electron spins of nitrogen vacancy centers show room temperature dephasing times of up to 1.8 ms, as the interaction with the spin-bath of C^{13} nuclear spins is significantly reduced [86]. Thus, the mostly spin free lattice renders diamond a very interesting host for spin qubits realized using color centers.

1.2 Atomic structure and creation of SiV centers

To decide whether a color center might be successfully applied as a single photon source, first, feasible fabrication approaches including the required impurity atom(s) have to be identified. The SiV center is often referred to as the 1.68 eV center due to the energy of its very pronounced zero-phonon-line (ZPL). It is probably the most common defect center introduced during growth (*in situ*) in synthetic CVD diamonds. The first observation of SiV luminescence was reported in 1980 by Vavilov et al. [103]. It has since then been detected in diamonds grown by hot filament CVD (e.g., [104–107]) and microwave plasma-assisted CVD (e.g., [105, 108–112]) as well as other CVD techniques. The main source of the incorporated silicon (Si) is often a Si substrate used for the growth which is etched by the deposition plasma [109, 113, 114]. The etched Si is subsequently transferred to the plasma and incorporated into the diamond as illustrated in Fig. 1.3. Doping of single crystal CVD diamond with up to $3 \times 10^{19}\,\mathrm{cm}^{-3}$ Si atoms has been demonstrated by placing a piece of Si beside the growing diamond [105]. Residual Si contamination might always be present if a similar etching process applies to reactor walls often made of quartz. Clark and Dickerson [110] find that if the deposition plasma is in direct contact with the quartz reactor walls this process might even become the main Si source. Additionally, in hot filament CVD, Si might originate from filament impurities [107]. Furthermore, the center can also be created *in situ* in high-pressure-high-temperature (HPHT) diamonds grown from Si doped carbon-metal melts [115]. Recently, the SiV center has been observed for the first time in natural diamonds [116]. These reports in the literature suggest that the *in situ* formation of SiV centers especially in CVD diamond is highly efficient. For the application as a single photon source, low densities of SiV centers are required. Thus, one goal of this work is to identify strategies to obtain CVD diamond samples with a sufficiently low SiV center density. The investigated approaches are discussed in detail in Chapter 4.

The occurrence of the 1.68 eV center in CVD diamond grown 'in contact' with Si as described above, supplies strong evidence but is not an unambiguous prove that Si participates in the formation of the center. Still other impurities or the influence

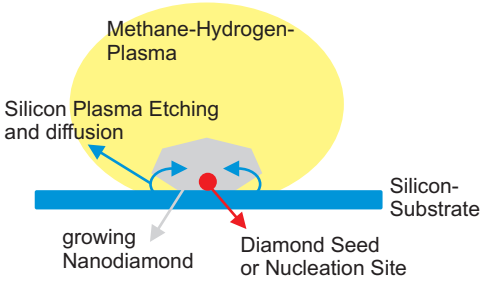

Figure 1.3: Illustration of *in situ* incorporation of Si from substrate material into CVD diamond.

of the Si on the growth could be involved. Furthermore, due to the very strong covalent bonds in diamond, the electronic structure, i.e., the energy levels of impurities incorporated into the lattice, is strongly modified compared to free atoms or ions. The crystal field in diamond is so strong that even noble gases are forced to form covalent bonds [25]. Therefore, using the observed electronic transition energies to deduce the constituting impurities by comparing them to transition energies of free atoms or ions is not feasible [25]. The unambiguous prove that Si is involved in the formation of the 1.68 eV center was attained by creating it via ion implantation of Si into various diamond materials [37, 74, 110, 117]. Using ion implantation, the incorporated dose can be controlled and any influence of the growth process can be ruled out if the diamonds are investigated before and after implantation. However, ion implantation always has to include annealing processes to remove damage introduced by the stopping of the ions. This process may also create additional luminescent centers, e.g., nitrogen vacancy centers by trapping of vacancies at nitrogen impurities. Previous studies on 1.68 eV centers created by μm deep ion implantation in bulk diamond in Refs. [37, 74] suggest that these centers show inferior luminescence properties, i.e., low single photon emission rates. We thus here pursue the approach to create SiV centers *in situ*.

In addition to establishing the impurity responsible for the color center formation, the corresponding impurity complex has to be identified by additional measurements. For the 1.68 eV center, different models were suggested. Clark and Dickerson [110] first introduced the now widely accepted model of the center consisting of a Si atom and a lattice vacancy. The model is motivated by the following observation [110,118]: Lattice vacancies were created via electron irradiation in polycrystalline CVD diamond films.[2] In diamond, lattice vacancies are associated with a fluorescent color center the so called GR1 center. Here, GR is the abbreviation for 'general radiation' as this center is observed in all diamonds after irradiation [84]. The fluorescence signal of the GR1 center anneals out at 700 °C indicating that lattice vacancies become mobile and recombine with carbon atoms at this temperature. Simultaneously, the same annealing leads to a significant increase of the 1.68 eV luminescence [110] and absorption [118], respectively, thus evidencing that the trapping of vacancies is involved in the formation of the 1.68 eV center.

In contrast to the formation of SiV centers via ion implantation, the *in situ* formation is more challenging to understand. As discussed in Ref. [119], inclusion

[2] In Ref. [110], samples grown on Si were used after removing the Si substrate. In Ref. [118], commercial free standing films are used, the substrate originally used is not specified.

of lattice vacancies near the growth surface might stabilize diamond during CVD growth. However, mostly no direct evidence for residual vacancies in CVD diamond is found. An indirect evidence, however, is given by the existence of vacancy-related color centers like nitrogen vacancy and SiV centers in as-grown CVD diamond. It should be pointed out that CVD diamonds are typically grown at temperatures close to the temperature at which lattice vacancies in diamond become mobile [120]. Thus, for the formation of vacancy-related complexes, in principle, two explanations are possible. First, vacancies may be preferentially formed next to sites where impurity atoms are located, thus directly forming the vacancy-related impurity complexes. Second, vacancies might occur at random positions at the growing surface and migrate to be trapped at impurity atoms incorporated into the diamond lattice. Allers and Mainwood find evidence for the second model by observation of vacancies (GR1 luminescence) close to the growth surface and SiV defects only deeper in the CVD diamond films, evidencing migration and trapping of vacancies. Additionally, modeling of the vacancy migration yields spatial concentration profiles of SiV and GR1 centers similar to the observed profiles [120]. In contrast, more recently, evidence for the direct formation of the SiV complex has been found in Ref. [121]. Here, the orientation of SiV color centers with emission at 946 nm, identified as an additional charge state of the 1.68 eV center, have been investigated using electron spin resonance techniques (discussion of charge states see below). The authors assume that the connecting line between Si atom and lattice vacancy is a $\langle 111 \rangle$ direction in the crystal. If a diamond grows in $\langle 110 \rangle$ direction (the growth plane is a $\{110\}$ plane) two out of the four equivalent $\langle 111 \rangle$ directions lie in the growth plane, while the other two point out of the growth plane. Ref. [121] reports a preferential alignment of the *in situ* formed SiV color centers in the directions pointing out of the growth plane. This is interpreted as follows: A Si atom is incorporated in the growing $\{110\}$ diamond layer, substituting a carbon atom. In the next layer, the formation of a lattice vacancy in the nearest neighbor site is favored due to the presence of the Si atom in the underlying layer. Subsequent layers overgrow the complex and thus stabilize it. Ref. [121] also finds that only a small fraction of Si atoms forms SiV centers during CVD growth. This is also supported by Refs. [110, 118] showing significant enhancements of SiV luminescence after vacancy formation in Si containing diamonds. Taking into account the two models of the formation of the SiV complex, the growth parameters of the CVD process together with the Si impurity level present can significantly influence the probability to form SiV centers.

In addition to the identification of the impurity complex, the spatial structure of the complex in the diamond lattice is of importance. Here, the question has to be answered where the Si atom is located with respect to the carbon lattice sites. For nitrogen vacancy centers, it is known that the nitrogen atom resides on a carbon lattice site neighboring a lattice vacancy [122]. However, simulations of the SiV center yield, that the Si atom is unstable on a lattice site and relaxes to the so called *split-vacancy configuration* by moving toward the neighboring vacancy [122]. Also other spatial positioning of the Si atom has been discussed, e.g., in Ref. [123]. The actual spatial structure thus is still subject to discussion, the different models will be discussed in detail in Sec. 2.3. The different spatial configurations lead to different

symmetry properties of the center and accordingly to different possible electronic states. The implications of different color center symmetries will be discussed in detail in Chapter 2.

Moreover, one has to determine the charge state of the color center. It is well investigated that color centers in diamond can exist in multiple charge states. E.g., for the nitrogen vacancy (NV) center, a negatively charged and a neutral form have been observed often in the same diamond sample [124]. Also single NV centers have been shown to continuously switch their charge state and therefore also their luminescence properties: The negatively charged state has a ZPL at 637 nm, while the neutral charge state emits at 575 nm [125]. This charge state conversion under illumination is called photochromism. It should be noted here, that the charge state of a color center in diamond is strongly depending on the local environment, thus often varying in the same sample or between individual centers. This topic is discussed in detail in Ref. [124]: In diamond, most donor and acceptor impurities feature high ionization energies. Thus, these impurities are not mandatorily thermally ionized. As a consequence, instead of being determined by a global Fermi level in the crystal, the color center charge state is more probably determined by close proximity to a donor or acceptor impurity that transfers an electron to the color center or removes an electron from the color center. Additionally, proximity to a crystal surface might change the charge state: Santori et al. [126] find a charge depletion layer below the surface of implanted CVD diamond, here NV^- centers are converted to neutral NV^0. Close to the surface, the probability to find NV^0 centers is about four times higher than in the bulk diamond, within about 200 nm it decreases to the value in the bulk diamond.

For the SiV center, the charge state associated with the dominant 1.68 eV luminescence is still subject to discussion. Using simulations, Ref. [123] associates the neutral charge state (SiV^0) to the 1.68 eV luminescence, while Ref. [122] associates it to the negatively charged state (SiV^-). In experimental work, Ref. [127] identifies the 1.68 eV luminescence with SiV^-. However, the quenching measurements with additional illumination used therein only allow to associate SiV^{x-1} to the luminescent and SiV^x to a non-luminescent state of the center. In a more recent publication (Ref. [128]), the same authors identify the 1.68 eV luminescence with SiV^0 due to similarities with the neutral vacancy in diamond. Refs. [127,128] both claim that the charge state SiV^x with one electron charge less than the charge state corresponding to 1.68 eV luminescence does not lead to luminescence. Recent studies, however, identify the 1.68 eV luminescence with SiV^- but find a luminescence line due to SiV^0 centers at 1.31 eV (946 nm) [121, 129]. The oscillator strength corresponding to the 1.31 eV line is 23 times weaker than for the 1.68 eV line. The charge state inter-conversion between SiV^- and SiV^0 has been shown for ensembles of centers using heating (conversion to SiV^-) and ultraviolet photoexcitation with photon energies larger than the bandgap energy of diamond (conversion to SiV^0) (discussion Ref. [121], original measurements [129]). The authors interpret the formation of SiV^- centers after heating as the capture of thermally excited electrons, e.g., from nitrogen donors [121], at SiV^0 centers. The formation of SiV^0 centers under ultraviolet photoexcitation is attributed to electron-hole-pair (exciton) creation followed

by trapping of holes at SiV^- centers to form SiV^0 centers, while the electrons are trapped by other defects. However, the charge state inter-conversion using a single center has so far not been shown for the SiV center.

1.2.1 Interaction of SiV centers with other impurities/defects

Due to the possible charge state changes discussed above, SiV centers might be influenced by other impurities or defects in the surrounding diamond that might act as electron donors or acceptors, as already indicated above. This interaction might be crucial for the use of SiV centers as single photon sources as decreased luminescence (quenching) or enhanced luminescence can occur. This in turn would influence the brightness of single centers. Considering the interaction with other impurities, only results on the 1.68 eV luminescence have been published. Unfortunately, these results are contradictory, similar to the charge state identification.

The first question is how sensitive the 1.68 eV luminescence of the SiV centers reacts on the quality of the surrounding crystalline environment. In this context, 'quality' is related to the content of non-sp^3 phases and the density of lattice defects. There is no consistent picture of the influence of crystal quality on SiV luminescence in the literature: Refs. [130] and [113] report that the SiV luminescence is most intense in regions of low crystalline quality in polycrystalline diamond (PCD) films. Low crystalline quality is indicated by graphite-related Raman signals in Ref. [130].[3] In Ref. [113], low crystalline quality is attributed to a high vacancy density at the initial stages of PCD growth. In contrast to that, Refs. [127,131] report full quenching of the SiV luminescence in films containing graphite. The quenching is attributed to a change of the Fermi level in diamond close to grain boundaries and graphite and subsequent ionization of color centers [127]. However, again contradictory, bright SiV luminescence has been observed in ultra-nanocrystalline films with only 5 nm grain size despite significant graphite content of the films [132].

The influence of other impurities on the SiV luminescence is also controversially discussed in the literature. Refs. [103,133,134] report the quenching of SiV luminescence upon incorporation of boron or oxygen. The influence of nitrogen impurities does not lead to clear results: The results of Sittas et al. [115] indicate a luminescence quenching of SiV centers due to the presence of nitrogen. This is explained in terms of nitrogen impurities competing more successfully in trapping vacancies. In contrast, Collins et al. [117] observe enhanced luminescence in diamonds with high nitrogen content after Si implantation. This finding motivated the use of nitrogen-coimplantation to enhance the luminescence rates of single SiV color centers in Ref. [74]. Nevertheless, no unambiguous enhancement of the luminescence has been observed. This might be associated to the fact that the enhancement observed in Ref. [117] has only been verified for as-implanted, not annealed samples.

For *in situ* produced centers, it might also be crucial whether they only form if the diamond grows in certain crystal directions. Ref. [115] reports no growth sector dependence of SiV formation in HPHT diamonds. The same is reported for CVD

[3] For further discussion on the investigation of crystalline quality via Raman scattering, see page 37.

diamonds in Ref. [103]. We thus assume that SiV centers can be created in different growth directions.

As the reports in the literature concerning other impurities are highly contradictory, our approach will include no co-doping of the diamonds used. Instead, we will pursue the approach of growing high purity, high quality diamonds, to ensure a preferably defined crystalline environment.

1.3 Luminescence properties of SiV centers

1.3.1 Excitation of the luminescence

For the application of color centers in diamond as single photon sources, an excitation method is necessary that allows for the efficient excitation of the single color center without simultaneously introducing significant background luminescence, i.e., luminescence from other types of color centers or broadband luminescence from the diamond host (for a discussion on the origin of broadband fluorescence see page 73).

SiV center luminescence is observed under excitation with an electron beam with a typical electron energy in the keV range (cathodoluminescence) [103, 117]. However, this excitation method is not suitable for single photon generation as the high energy electron beam potentially excites a lot of other defects in diamond. Another excitation possibility is direct electric excitation in a p-n-junction (electroluminescence). Recently evidence for direct electrical excitation of SiV centers has been found [42, 135]. However, no single electrically excited SiV centers have been observed so far and the use of electroluminescence requires the fabrications of p-n-junctions in diamond. The implementation of this excitation technique for single photon generation is currently under investigation for NV centers [44].

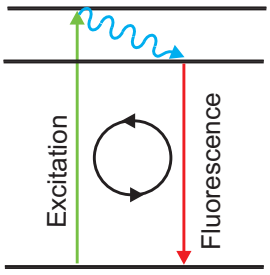

Figure 1.4: Illustration of non-resonant excitation of a color center.

To excite color centers in diamond as single photon sources, optical excitation is employed here. To separate the excitation laser light and the single photon fluorescence, an excitation wavelength shorter than the fluorescence wavelength of the color center is employed (see illustration in Fig. 1.4). Therefore, for this above resonance excitation scheme a relaxation dissipating excess energy in the excited state has to take place.

To test whether a defect in diamond can be optically excited, one may first investigate the absorption due to the defect. At high SiV center concentration, the transitions of the SiV center can be observed in absorption [117, 118]. Instead of direct detection of the absorption, i.e., extinction of light, one may also excite

the color center with a varying wavelength and detect the fluorescence intensity of the color center depending on the excitation wavelength. Assuming that no saturation occurs, the fluorescence intensity is then proportional to the absorbed light intensity. This method is termed photoluminescence excitation spectroscopy (PLE). Employing this method, it has been found that SiV centers can be excited, although not with constant efficiency, in a broad spectral range between 1.75 eV and 2.55 eV [131]. Resonance features in the excitation efficiency are reported in Ref. [136], where an absorption enhancement at 1.98 eV is reported and assigned to a second excited state 0.3 eV above the first excited state.

In addition to the efficiency of the excitation, for single centers, one also has to consider the possibility of ionization of the center: E.g., for nitrogen vacancy centers, a charge state conversion using 2.33 eV (532 nm) laser light has been shown [125]. As the single photons have to be detected at a defined wavelength, a charge state conversion reduces the effective fluorescence rate due to a change in the emission wavelength. Charge state conversion might also be the reason for longer times of fluorescence intermittence (blinking) observed for color centers in diamond [35, 137]. For SiV centers, also quenching of the SiV ensemble luminescence, especially for illumination with wavelengths shorter than 450 nm, was observed [127]. Thus, it might be advantageous to choose an excitation energy as low as possible and not capable of photo-ionizing the color center. According to Refs. [128, 131, 138], the ground state of the SiV center charge state responsible for 1.68 eV (738 nm) luminescence can be found 2.05 eV (605 nm) below the conduction band edge. In this work, we will employ excitation wavelengths of 671 nm (1.85 eV) as well as 685 nm (1.81 eV) up to 715 nm (1.73 eV) for the presented measurements on single centers. For ensembles, also excitation at 532 nm (2.33 eV) will be employed. Several tests using 532 nm excitation for single SiV centers yielded an enhanced probability for photobleaching of the centers with this excitation wavelength. Figure 1.5 illustrates the excitation schemes and the position of the energy levels in the bandgap.

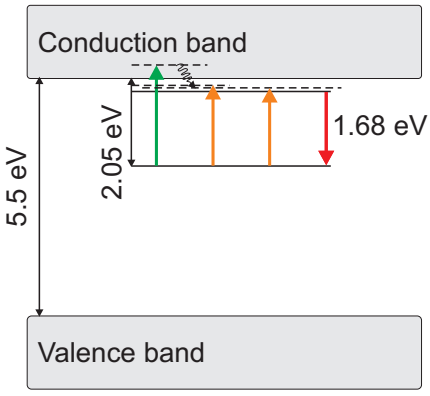

Figure 1.5: Illustration of the position of the SiV center's electronic states in the diamond bandgap and the excitation wavelengths used. Excitation paths from left to right: green arrow: 532 nm, orange arrows: 671 nm and 695 nm. All energies drawn to scale.

1.3.2 Spectral properties of the ZPL

Generally, the purely electronic transition of a color center, the zero-phonon-line (ZPL), is the spectrally narrowest transition of the color center. In contrast, vibra-

tion assisted electronic transitions (vibronic sidebands) are much broader. Thus, to enable low bandwidth single photon emission, a color center's fluorescence should concentrate into a narrow ZPL. The SiV center is a promising candidate for such a low bandwidth emitter as discussed in the following sections.

Previous reports in the literature often reflect the luminescence properties of (large) ensembles of SiV centers. Feng et al. [139] report a linewidth of 15 meV (6.5 nm) for an ensemble of SiV centers in polycrystalline diamond (PCD). Gorokhovsky et al. [112] specify 13.6 meV (6 nm) in the same material system. More recently, Vlasov et al. [132] find a width of 7 nm for SiV centers in PCD and 8 nm for ultrananocrystalline diamond. In highly stressed low quality PCD, the ZPL of the SiV center might be split and broadened to span the wavelength range of $733 - 745$ nm [96]. Thus, several reports indicate that the ZPL of the SiV centers may be sufficiently narrow to enable low bandwidth single photon emission. The spread of linewidths observed in these reports indicates that the linewidth of SiV ensembles is influenced by inhomogeneous broadening. The significant influence of inhomogeneous broadening becomes especially visible in low temperature spectra, where the homogenous broadening due to phonons that dominates at room temperature is strongly reduced and only the linewidth due to inhomogeneous broadening remains. A detailed discussion of the line broadening mechanisms for the ZPL is presented in Sec. 7.2.1. Feng et al. [139] measure a linewidth of 10 meV (4.4 nm) at 10 K. Clark et al. [140] find a width of 16.8 meV (7.4 nm) at 77 K, with a reduction to 8.4 meV (3.7 nm) after an HPHT annealing step. The major source for the inhomogeneous broadening is mechanical stress in the diamond [96]. A detailed discussion of the sources of stress in the samples employed in this work can be found in Sec. 5.2.1.

Only two reports of the linewidth of single centers exist: Wang et al. report a ZPL linewidth of 5 nm [37] and 6 ± 1 nm [74] at room temperature. We point out that in the work of Wang [74] also centers with significantly lower linewidth have been observed: A center with an emission wavelength of 736.8 nm and 1.3 nm ZPL width is not identified as an SiV center due to the short emission wavelength. Nevertheless, this blue shift of the ZPL might be due to the crystalline environment in the vicinity of the center: As mentioned above, reports in the literature clearly indicate inhomogeneous broadening of the ZPLs of ensembles of SiV centers in the nm range. Thus, one expects line positions spread over the inhomogeneous linewidth when observing single emitters and a ZPL observed at 736.8 nm might be due to an SiV center.

At low temperature, in diamond with a low inhomogeneous broadening of the ZPL, a four line fine structure of the ZPL transition has been observed [111, 140]. This specific line pattern might be considered as the 'spectral fingerprint' of the SiV center and might be used to prove the identification of single color centers as SiV centers. A detailed discussion of the pattern as well as the associated level scheme is performed in Sec. 7.1. Together with a narrowing of the line upon cooling and the occurrence of the four line pattern, the SiV ZPL blue shifts 1.2-1.4 nm upon cooling [112, 139].

1.3.3 Electron-phonon coupling of the SiV center

In a solid, in general, electronic transitions of color centers are coupled to vibrations of the surrounding host. This can be visualized like follows: If a color center is excited, electrons bound to that color center undergo transitions to a higher lying orbital with a different spatial wave function. This changes the charge distribution in the vicinity of the color center, consequently changing the equilibrium positions of the neighboring nuclei. The electron-phonon coupling thus couples the motion of the lattice and electronic transitions of a color center [94]. Starting the line of argument from the lattice vibrations, the electron-phonon coupling is induced because the movement of the lattice atoms and the atoms of the defect changes interatomic distances, thus directly influencing the electrons or the electronic wave functions respectively [25]. Mathematically, the coupling can be expressed as follows: If one assumes a single vibrational mode, the energy of the bare, uncoupled system is the sum of the electronic energy and the vibrational energy. Here, the excited state energy V_e is given by

$$V_e = E_e + \frac{1}{2} m\omega^2 Q^2, \tag{1.1}$$

where E_e is the electronic energy corresponding to the excited state. ω is the frequency of the vibrational mode, while m is the effective mass associated with the mode. Q is the displacement of the nuclei from the equilibrium positions. If electron-phonon coupling occurs Eq. (1.1) has to be amended to read [94]

$$V_e = E_e + \frac{1}{2} m\omega^2 Q^2 + aQ + bQ^2 \tag{1.2}$$

Here, aQ denotes linear electron-phonon coupling, while bQ^2 describes quadratic electron-phonon coupling. The linear term accounts for the fact that the vibration does not occur around the same equilibrium point in excited and ground state. A large linear electron-phonon coupling strength reveals a strong shifting of the vibrational parabolas in the excited and ground state without changing the spacing of the vibrational energy levels. For low linear electron-phonon coupling, the vibrations occur about the same equilibrium point [141]. On the other hand, the quadratic term accounts for a change of vibrational frequency in the excited state due to the changed bonding strength. In general, several vibrational modes have to be considered. Equation (1.2) is extended to read [94]

$$V_e = E_e + \frac{1}{2} \sum_i m_i \omega_i^2 Q_i^2 + \sum_i a_i Q_i + \sum_{i,j} b_{ij} Q_i Q_j \tag{1.3}$$

Here, the summation takes into account the different modes. For the quadratic interaction, the diagonal parameters b_{ii} change the frequency of the ith mode analogous to the single mode model. Furthermore, the off-diagonal terms b_{ij} mix different vibrational modes [94]. Due to the linear interaction, vibration assisted electronic transitions, so called vibronic sidebands, emerge in the luminescence and absorption spectra of color centers. The quadratic electron-phonon coupling is responsible for the fact that absorption and emission spectra can lack mirror symmetry about the

ZPL [94]. Additionally, the quadratic interaction term is responsible for temperature dependent shifting and broadening of the ZPL, especially the off-diagonal terms b_{ij} are crucial [95]. The electron-phonon coupling of a color center cannot be directly measured, it has to be deduced from (temperature dependent) luminescence or absorption spectra. Thus, it is desirable to relate the line broadening due to quadratic electron-phonon coupling to a measurable quantity. The line broadening due to quadratic electron-phonon coupling can be expressed in terms of the one-phonon absorption spectrum. However, the assumption of a quadratic relation between the linear coupling coefficients a_i and the quadratic coupling coefficients b_{ij}, i.e,

$$b_{ij} \propto a_i a_j, \tag{1.4}$$

has to be made. This assumption is justified only in the limit of long-wavelength vibrations which are not significantly affected by the presence of the color center as the spatial extent of the color center is small compared to their wavelength [94,95].[4]

The linear electron-phonon coupling of the SiV center will be discussed in the following, while further discussion of quadratic electron-phonon coupling is shifted to section 7.2.2, where it is used to interpret temperature dependent spectra of single SiV centers.

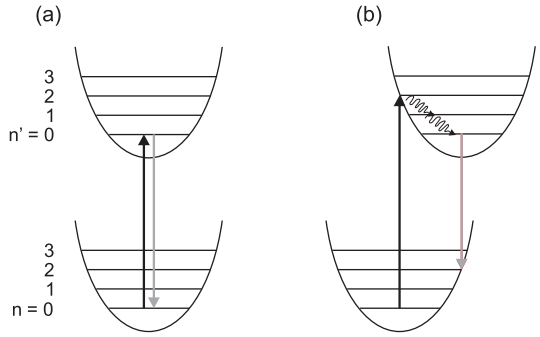

Figure 1.6: Most probable transitions in absorption and emission for (a) a Huang-Rhys factor S of close to zero and (b) for $S = 2$

Vibronic sidebands in emission mostly occur as transitions from the vibrational ground state ($n' = 0$) of the excited electronic state to higher vibrational states ($n > 0$) of the electronic ground state (for the level scheme see Fig. 1.6). Consequently, these lines are red shifted compared to the ZPL in luminescence. The red shift gives the phonon energy of the corresponding phonon mode if $n = 1$ (one-phonon sideband). For higher order sidebands ($n > 1$), the energy is a multiple of the phonon energy. In absorption, sidebands are blue shifted compared to the ZPL. Here, absorption mostly takes places from the vibrational ground state ($n = 0$, highest population) in the electronic ground state to higher vibrational states ($n' > 1$) in the excited electronic state. The sideband spectrum together with the ZPL is characteristic for a specific color center [25], assisting to identify the emitting centers. The vibronic sidebands of the SiV center are weak compared to the ZPL even at room temperature. This indicates a weak linear electron-phonon coupling and renders

[4] For another approach to link sideband spectra and quadratic electron-phonon coupling, see e.g., Ref. [142]; however, restrictive approximations for the vibrations are used too.

SiV centers especially suitable as low bandwidth emitters. The linear electron-phonon coupling is measured either by the Debye-Waller factor (DW) or the Huang-Rhys factor (S). The Debye-Waller factor is defined as the integrated luminescence intensity of the ZPL I_{zpl} divided by the integrated luminescence intensity of the color center I_{tot} [27]. The Huang-Rhys factor S is defined by $\frac{I_{zpl}}{I_{tot}} = \exp(-S)$ [84]. The Huang-Rhys factor can be interpreted as an indication of the most probable (vibration assisted) transition (discussion following Ref. [84]). Figure 1.6 indicates the situation for a Huang-Rhys factor S close to zero and for $S = 2$. For a very low Huang-Rhys factor, the most probable transition is the ZPL, it dominates the luminescence spectrum. For a Huang-Rhys factor of $S = 2$, the most probable absorption transition brings the color center to the vibrational state with $n' = S = 2$ phonons in the excited electronic state. This transitions marks the maximum of the absorption band. Subsequently, the color center relaxes the excess energy of $n' = S$ phonons in the excited state. The most probable luminescence transition then brings the color center to the vibrational state with $n = S$ phonons in the ground state. This transition marks the maximum of the emission band. The intensity $|M_{0n}|^2$ of the vibronic sideband involving n phonons is given by [94]

$$|M_{0n}|^2 = S^n \frac{e^{-S}}{n!}. \tag{1.5}$$

In the literature, measurements on SiV center ensembles have been used to determine the Huang-Rhys factor S: Rossi et al. [136] report $S = 0.1$ deduced from luminescence measurements at room temperature using 457 nm excitation. Gorokhovsky et al. [112] report $S = 0.08$ also deduced from luminescence measurements at 9 K using 515 nm excitation. Collins et al. [118] report $S = 0.24 \pm 0.02$ in absorption at room temperature. These experiments have been performed using polycrystalline CVD diamond grown on Si substrates. We point out that different spectral ranges have been investigated in the publications mentioned above: Ref. [136] discusses spectra ranging down to 1.4 eV, while Ref. [112] gives spectra only down to 1.59 eV for 515 nm excitation. In Ref. [118], absorption spectra with energies up to 1.78 eV are used. Due to the restricted spectral ranges investigated, the question whether all possible sidebands have been taken into account might be raised (for a discussion of sideband energies of the SiV center see below). Additionally, in Ref. [136] a background substraction is performed before S is calculated from the luminescence spectrum, while this is not discussed in Refs. [112] and [118]. Furthermore, the authors of Refs. [112, 118, 136] do not discuss whether the employed data has been corrected for a varying detection efficiency of the experimental setup throughout the investigated spectral range. Considering these experimental issues, it is not clear which of the values most closely describes the linear electron-phonon coupling of the SiV center and how the values compare to each other.

Assuming a Huang-Rhys factor of $S = 0.24$, the relative intensities compared to the ZPL are 24% for the one-phonon sidebands and only 2.8% for the two-phonon sideband. Thus, the ZPL dominates the spectrum. Additionally, one would not expect to observe sidebands related to two-phonon processes for SiV centers. These findings are in accordance with reports in the literature that in general color centers

involving heavier impurities tend to exhibit low linear electron-phonon coupling [25]. In contrast, for nitrogen vacancy centers a Huang-Rhys factor of $S = 3.73$ [94] leads to nearly undetectable ZPL emission at room temperature and very strong sideband emission.

Figure 1.6 displays an extremely simplified picture of electron-phonon coupling assuming that only one vibrational mode couples to the color center. Additionally, the nature of the mode responsible for the sideband transitions has not been discussed yet. In a solid state host, different types of vibrational modes can lead to sideband emission:

- Lattice modes: These modes correspond to lattice vibrations of the undisturbed diamond lattice.
- Local and quasi-local modes: These modes are specific of the defect. They represent vibrations involving the defect and its neighboring carbon atoms.

Coupling to lattice modes is governed by the phonon density of states of the diamond lattice. The density of states has been calculated and measured in the literature, e.g., in Refs. [25, 143–145]. Here, electronic transitions predominantly couple to phonons with wave vectors at the high symmetry points of the Brillouin zone, the so called critical points [25, 139]. This has two reasons: First, these phonons have the shortest wavelengths. Thus, they can induce the strongest changes in interatomic distances, as their wavelengths are comparable to the spatial dimension of the color centers. This enables efficient coupling [25]. Second, the phonon density of states peaks at these points [25, 139], as the phonon dispersion relations displays a vanishing slope [144, 146]. A list of the phonon energies corresponding to these critical points is summarized in Ref. [147] and is displayed in Tab. 1.1. Electronic transitions predominantly couple to optical phonons as the anti-phase movement of the lattice atoms in these modes evidently induces strong interatomic distance changes. For acoustic modes, only short wave acoustic modes induce significant interatomic distance changes and thus couple efficiently. The phonon density of states in diamond has a sharp high energy cut off at around 165 meV and diminishes strongly below approx. 70 meV [25, 143–145]. Therefore, all sideband features shifted less than 70 meV or more than 165 meV cannot be induced by modes of the diamond lattice: Features with high energy shift may arise from multi-phonon processes. However, for SiV centers, multi-phonon processes are very improbable and the features most probably arise from local modes of the color center. In contrast, the features with a low energy shift are fully attributed to local modes of the color center.

Quasi-local and local modes arise solely due to the presence of the impurity. If the energy of these modes lies within the energy range of the lattice phonon density of states, the modes are referred to as quasi-local. If the energy is > 165 meV or < 70 meV they are termed local modes. The vibrational frequencies of these modes are determined by the masses of the impurities as well as the interatomic bonding forces that act as springs for the vibration [25]. Brout and Vischer introduced a simplified model to determine the quasi-local mode frequencies ω_{QL} and their resonance width $\Delta\omega_{QL}$ for heavy impurities assuming that these impurities do not

change the interatomic forces significantly [25, 148].

$$\omega_{QL} = \omega_D \sqrt{\frac{M_C}{3(nM_I - M_C)}} \qquad \Delta\omega_{QL} = \frac{\pi}{6}\omega_D \frac{M_C}{3(nM_I - M_C)} \tag{1.6}$$

Here, M_C and M_I are the masses of the carbon atom and the impurity respectively. n denotes the number of impurity atoms participating in the vibration. ω_D is the Debye frequency in diamond, which corresponds to 150 meV. For an impurity incorporating one Si atom, one would thus expect a quasi-local mode at 75 meV. Indeed, sidebands with a comparable energy shift at approx. 80 meV have been observed (see Tab. 1.1). More advanced calculations using estimated force constants for lattice and defect were performed in Ref. [143]. The results for a Si atom sitting in a 'split-vacancy' site are summarized in Tab. 1.1, indicating the existence of several high energy local modes.

Vibronic sidebands of SiV centers have been examined in several publications. The results are summarized in Tab. 1.1. Sittas et al. [115] examined the sideband structure in Si-doped HPHT diamonds. In low temperature experiments, they find a significant spectral narrowing of the three highest energy features corresponding to emission at 776 nm, 797 nm and 812 nm. Thus, they attribute these lines to purely electronic rather than vibronic transitions. This indicates that discrimination of vibronic sidebands and electronic transitions is not always clear as for defects involving heavy impurities the linewidths of sideband features due to local modes can be comparable to the ZPL linewidth [25].

There are several indications in the literature that vibronic sidebands and, therefore, the linear electron-phonon coupling for SiV centers significantly depends on the local environment. Sternschulte et al. find a sideband feature shifted by 166 meV only in some positions on a homoepitaxial CVD diamond [111]. Gorokhovsky et al. report that in polycrystalline diamond vibronic sideband features could not be resolved under non-resonant 514 nm laser excitation [112]. However, upon resonant excitation with 737 nm, a distinct sideband structure evolves. The authors explain that observation in terms of the excitation of only a sub-ensemble featuring a ZPL at the excitation laser wavelength. This sub-ensemble within the inhomogeneously broadened ensemble displays defined vibronic sidebands. These sidebands are spectrally washed-out if all inhomogeneously broadened SiV centers are excited and the differing sideband spectra add up. This observation supports the assumption of strongly environment dependent electron-phonon coupling. Thus consequently, for single emitters, one would also expect to observe varying vibronic sidebands for individual emitters.

Additionally, the authors of Ref. [112] report that if the excitation wavelength is tuned to longer wavelengths, thus selecting another sub-ensemble, the vibronic sideband structure changes: The most prominent vibronic sideband now displays a smaller energy shift with respect to the ZPL. Thus, the energy of the corresponding phonon mode has to be reduced for the sub-ensemble selected with longer wavelength laser excitation. In contrast, the shifting behavior for a higher energy sideband shows no clear trend. Thus, different vibronic sidebands show a deviant behavior under

environmental changes that shift the ZPL. Furthermore, simultaneously the width of the phonon sidebands changes [112].

As displayed in Tab. 1.1, vibronic sidebands identified as local modes as well as sidebands due to lattice phonons [147] have been reported for SiV centers. The reports in the literature display a spread in the observed positions and also in the number of features observed, again indicating a dependence on the environment. If the diamond lattice is stressed, lattice phonon energies change. Additionally, energetically degenerate phonon modes split up [149]. Shifting rates for the optical zone center phonon ($165.2\,\mathrm{meV} = 1332.4\,\mathrm{cm}^{-1}$) amount to [149]

$$\Delta_{hydro} = 0.40 \pm 0.02 \frac{meV}{GPa} \qquad \Delta_{[111]} = 0.27 \pm 0.02 \frac{meV}{GPa} \qquad \Delta_{[100]} = 0.09 \pm 0.01 \frac{meV}{GPa}$$

for hydrostatic pressure and compressive uniaxial stress along [111] or [100] direction. The optical zone center phonon is the only phonon were a direct observation of the shift due to stress is possible as it can be detected via Raman scattering of light. For local modes, however, no similar direct measurements of the phonon energies is possible. Thus, it is challenging to discriminate between changes in the electron-phonon coupling of a color center or changes in the mode frequencies.

Ref.	Method									
[110]	PL 515 nm		63			123		154		
[136]	PL 457 nm		60			120				
[118]	Absorption	33								
[115]	PL 488\514 nm	36	64	*83*		*125*		*155*		
[111]	PL 488 nm	42	65	85		126		153	166	
[112]	PL 737 nm	42	64			125	148	155	163	
[139]	PL 515 nm	43	67		104	129		155		
[143]	Simulation		56	80	107				168	184
	local modes			81					168	187
[147]	critical points		70		100	122	138	150		
	diamond lattice					133	147	155		

Table 1.1: Sideband shifts of the SiV center reported in the literature. All values are given in meV. The values obtained from Ref. [143] are calculated values of local modes. Ref. [147] identifies the critical points with high phonon density, see original manuscript for identification of phonon types. Values written in italic are tentatively attributed to electronic transitions by the authors of Ref. [115].

Chapter 2

Symmetry considerations of color centers

This chapter introduces basic concepts that aid in deriving physical properties from symmetry properties of a system. Symmetry considerations are fundamental to the investigation of physical problems as symmetries, e.g., enable to determine conservation laws for certain parameters. Additionally, symmetry often directly indicates the degeneracy of eigenstates of the system as well as selection rules. The following chapter introduces the use of group theory to derive physical properties of a given system, here a color center in diamond, from its symmetry properties. The discussion mainly follows Ref. [150]. At the end of the chapter, different models for the SiV center including the respective symmetry discussed in the literature are summarized.

2.1 Group theory approach

2.1.1 Basic concepts

The symmetry properties of a system can be described by symmetry operations, e.g., rotations, inversions, reflections. These operations, mathematically speaking, form a group. Thus, it is possible to use conclusions from group theory to deduce the properties of the physical problem. The symmetry operations $A, B, C \ldots$ form a group if the following four conditions hold:

1. The product of any two elements of the group is again an element of the group. Thus, relations of the type $AB = C$ are valid for all group elements. This holds for symmetry operations, as performing several concatenated symmetry operations again forms a symmetry operation of the problem.

2. The associative law is valid: $(AB)C = A(BC)$.

3. A unit element E, also called identity element, exists such that $AE = EA = A$.

4. An inverse element A^{-1} exists for each group element A with $AA^{-1} = E$.

The *multiplication table* of a group lists all possible products AB of group elements and thus fully defines the group. Each group element can be associated with a square matrix $M(A)$, $M(B)$, $M(C)$. This identification of symmetry operations with square matrices fulfilling the multiplication table of the group is the general concept of a *representation* of a group. Using a representation of the group, geometrical symmetry operations can be reduced to matrix operations which can be easily computed.

The matrix representation of a symmetry group is not unique: The matrices $M(A)$, $M(B)$, $M(C)$ can always be transformed by an equivalence transformation $UM(A)U^{-1}$ using a unitary matrix U to form another representation of the group. An equivalence transformation of a physical problem might, e.g., be a rotation of the coordinate system. Additionally, one might think of using matrices with unnecessarily high dimensionality, i.e., the number of rows and columns of the matrices. To overcome this arbitrariness, the concept of *irreducible representations* is introduced. To check whether a representation is irreducible can be complicated and has to be done by performing equivalence transformations [150]. The most important feature of an irreducible representation is that it cannot be expressed by representations of lower dimensionality, i.e., by representations using matrices with lower dimensionality.

The main reason for the application of group theory to physical problems is that group theory aids in making simplifications without knowing the detailed Hamiltonian $\hat{\mathcal{H}}$ of the physical system. The symmetry operators $\hat{\mathcal{P}}_R$ of the system commute with $\hat{\mathcal{H}}$, as they leave the physical system unchanged. Assume that ψ_n is an eigenfunction and E_n is an eigenvalue (energy) of the problem, with $\hat{\mathcal{H}}\psi_n = E_n\psi_n$. Then we can also write:

$$\hat{\mathcal{P}}_R\hat{\mathcal{H}}\psi_n = \hat{\mathcal{P}}_R E_n\psi_n = \hat{\mathcal{H}}(\hat{\mathcal{P}}_R\psi_n) = E_n(\hat{\mathcal{P}}_R\psi_n).$$

Thus, $\hat{\mathcal{P}}_R\psi_n$ again is an eigenfunction and corresponds to the same eigenvalue E_n. Using the symmetry properties, one can generate all eigenfunctions of a degenerate set starting from one eigenfunction using the symmetry properties. Furthermore, introducing the concept of irreducible representations of the symmetry group, each irreducible representation describes the transformation properties of a set of eigenfunctions and thus corresponds to a distinct energy eigenvalue. Thus, it is possible to deduce symmetries (transformation properties) and degeneracies of energy levels directly from the symmetry of the problem. However, it has to be emphasized that this approach does not suffice to derive the ordering of energy levels or the absolute energies. This ordering of the energy levels is crucial to deduce the occupation numbers of the different states and to derive the multi-electron term of the system. Thus, further considerations are necessary to deduce the electronic states from the group theoretical considerations (for the nitrogen vacancy center see, e.g., Ref. [151]). However, no such rigorous group theoretical treatment for the SiV center exists.

For many applications, it is not necessary to consider the explicit matrix notation of the irreducible representations. Instead the so called *character* of the matrices is considered. The character, which is the trace of a matrix (sum over the diagonal el-

ements), remains invariant under any equivalence transformation and thus is unique for each irreducible representation.

An important concept to classify symmetry operations within a group is the concept of *classes*. The symmetry operations of a group may be divided into different kinds of operations, e.g., one might think of rotations of $\frac{2\pi}{3}$ about equivalent threefold axes as a class of symmetry operations. In mathematical terms, a class is the totality of elements which can be obtained from a certain element A by conjugation. The conjugate element B is defined by $B = XAX^{-1}$ where X is an arbitrary element of the group. For an irreducible representation, the character for each element in a class is the same. Additionally, the number of irreducible representations of a given symmetry group is equal to the number of classes in the group. This information on classes and characters of a group is summarized in the so called *character table*, which can be found in standard textbooks for most symmetry groups (e.g., Ref. [150]).

2.2 Point groups and nomenclature

At this point, the nomenclature of symmetry groups according to Schoenflies is introduced. This nomenclature has been developed to label so called point groups. Point groups involve only symmetry operations for a fixed spatial point. In contrast, space groups additionally involve translational symmetry. Point groups are significant for the description of the symmetry of point defects and the surrounding lattice as the presence of a point defect (color center) breaks the translational symmetry. A point defect is always described by a reduced set of symmetry operations out of the symmetry operations of the lattice. It cannot introduce new symmetry operations as these would be no symmetry operations of the surrounding lattice and thus do not describe the combined system of a point defect and the surrounding lattice. Mathematically speaking, the symmetry group of a defect can only be a subgroup of the point group of the lattice [151, 152]. The diamond lattice is characterized by two face centered cubic sublattices (distance of atoms at the cube corners a). The sublattices are shifted along the space diagonal by $\frac{\sqrt{3}a}{4}$ [153]. The cubic point group describing the point symmetry of a carbon lattice site in diamond is labeled T_d. The symmetry group of the diamond lattice is O_h. Subgroups of defects have to be subgroups of O_h [84].

There are 32 different point groups. They can be labeled in the so called Schoenflies symmetry notation. We introduce only the symmetry operations necessary to denote the point groups suggested for the SiV center symmetry:

- C_n denotes a rotation through $\frac{2\pi}{n}$ and thus a so called n-fold rotation axis in the problem.
- σ_ν denotes a reflection in the vertical plane.
- i is an inversion.
- iC_n is a compound rotation–inversion. It consists of a rotation followed by an inversion.

Classes denoted C_n only display a n-fold rotation axis (and the identity operation E that belongs to all groups). In Ref. [154], a C_2 symmetry (monoclinic) is suggested for SiV centers, deduced from experimental results. Table 2.1 gives the character table for point group C_2 including the classes (E, C_2) and the irreducible representations (A, B). Note that the number of irreducible representations is equal to the number of classes. The character of the unit element E in each irreducible representation is equal to the dimensionality of the irreducible representation. Thus, class C_2 has only one dimensional irreducible representations. As discussed above, each irreducible representation corresponds to an eigenstate of the system. As the dimension of the irreducible representation corresponds to an orbital degeneracy, for this group only non-degenerate energy levels are expected [84].

	E	C_2
A	1	1
B	1	-1

Table 2.1: Character table for the symmetry group C_2 according to Ref. [150]. The first column of the table lists the irreducible representations, while the first row lists the classes. The dimensionality of the irreducible representation is equal to the character of the identity operation E.

Classes denoted D have non-equivalent symmetry axes in perpendicular planes. To denote non-equivalent axes, a superscript is induced (here x, y, z). Ref. [154] finds point group D_2 (rhombic) as a second alternative for the symmetry group of the SiV center. Point group D_2 is associated with only one dimensional irreducible representations too as listed in Tab. 2.2.

	E	C_2^z	C_2^y	C_2^x
A_1	1	1	1	1
B_1	1	1	-1	-1
B_2	1	-1	1	-1
B_3	1	-1	-1	1

Table 2.2: Character table for the symmetry group D_2 according to Ref. [150].

Theoretical studies imply a higher symmetry for the SiV center: Ref. [123] suggests a $C_{3\nu}$ (trigonal) symmetry for the SiV center. Table 2.3 gives the character table for the symmetry group $C_{3\nu}$. The group has three classes: the class of the identity element E, the class of three-fold rotations C_3 as well as a class involving vertical reflections σ_ν. Consequently, for point group $C_{3\nu}$, three irreducible representations exist labeled A_1, A_2 and E. $A_{1,2}$ denote the one dimensional representations, while E denotes a two dimensional representation.[1] As the dimension of the irreducible representation corresponds to an orbital degeneracy, for this group non-degenerate as well as degenerate energy levels are expected [84].

	E	$2C_3$	$3\sigma_\nu$
A_1	1	1	1
A_2	1	1	-1
E	2	-1	0

Table 2.3: Character table for the symmetry group $C_{3\nu}$.

[1] Note that E denotes a two dimensional irreducible representation as well as the unit element E of the group.

Other theoretical work [122], in contrast, indicates a D_{3d} (trigonal) symmetry. This point group is also characterized by two and one dimensional irreducible representations. It has 6 classes: the class of the unit element E, two and three fold rotation axes C_2, C_3 and a reflection in a vertical plane σ_ν that have been discussed before. Additionally, an inversion i and a compound rotation inversion iC_3 are included. As the group involves an inversion symmetry i, irreducible representations that are symmetric under the inversion, labeled with a subscript g and irreducible representations anti-symmetric under the inversion, labeled with a subscript u, have to be considered. Table 2.4 gives the character table for the symmetry group D_{3d}.

	E	$2C_3$	$3C_2$	i	$2iC_3$	$3\sigma_\nu$
A_{1g}	1	1	1	1	1	1
A_{2g}	1	1	-1	1	1	-1
E_g	2	-1	0	2	-1	0
A_{1u}	1	1	1	-1	-1	-1
A_{2u}	1	1	-1	-1	-1	1
E_u	2	-1	0	-2	1	0

Table 2.4: Character table for the symmetry group D_{3d}.

The electronic states of a system of known symmetry, as discussed above, are connected to its symmetry properties (point group) as each irreducible representation of the point group corresponds to an electronic eigenstate (orbital) of the system. These considerations hold for a single electron; however, they can be extended to multi-electron states (e.g., Ref. [155]). Note that other degrees of freedoms as, e.g., the electron spin, have to be considered in addition to the orbital eigenstates determined by the irreducible representations.

2.3 Application of symmetry considerations to SiV centers

The symmetry of a color center is crucial as it determines the fundamental characteristics of the luminescence of the color center including, e.g, line splitting under stress or external fields as well as the polarization of the emitted light and the selection rules for luminescence. The axis of highest symmetry of a color center in diamond may only be oriented along $\langle 100 \rangle$, $\langle 110 \rangle$ or $\langle 111 \rangle$ crystal axes [152]. As summarized in Ref. [84], e.g., for a trigonal defect, the highest symmetry axis is oriented along the $\langle 111 \rangle$ symmetry axis of the diamond lattice, whereas a monoclinic defect is oriented along $\langle 110 \rangle$ direction. Due to further symmetry considerations, the transition dipoles of the color center can be either parallel to the high symmetry axis (z-dipole) or perpendicular (x,y-dipoles) [154].

If a color center has orbitally degenerate states, a so called Jahn-Teller effect might occur: Any symmetric point defect with degenerate electronic states will distort its spatial configuration, thereby lowering the symmetry and lifting the degeneracy of its eigenstates, if the final states have a smaller energy than the initial state with higher symmetry [84]. As a consequence, degenerate energy levels are often split up. This effect either occurs as a static Jahn-Teller effect or as a dynamic

Jahn-Teller effect. For the dynamic case, a reorientation between different distortions takes place and the original symmetry can be effectively restored [84]. Several examples for the static Jahn-Teller effect have been found, e.g., a single substitutional nitrogen atom should, like a carbon atom in diamond, exhibit a tetrahedral T_d symmetry. However, the observed symmetry is trigonal and thus lower [84]. In contrast, other defects retain the higher symmetry, e.g., the GR1 center (neutral vacancy) exhibits the T_d symmetry of the lattice site [84].

The symmetry of a defect can, in principle, be measured by several methods: e.g., by employing the Stark effect (e.g., Ref. [156]) or the Zeeman effect (e.g., Ref. [84]). Additionally, polarization measurements can reveal the dipole orientation and thus indicate the symmetry [157]. However, the most common method is to apply defined stress along a defined crystal axis (uniaxial stress) and measure the splitting and shifting of the zero-phonon-line (ZPL) [84, 152, 158]. Often polarization and stress measurements are combined (e.g., [159, 160]). For color centers observed in absorption, also so called magnetic circular dichroism (MCD) measurements can be performed probing the differential absorption of left and right circularly polarized light with a magnetic field applied in the light propagation direction (see e.g., [161]).

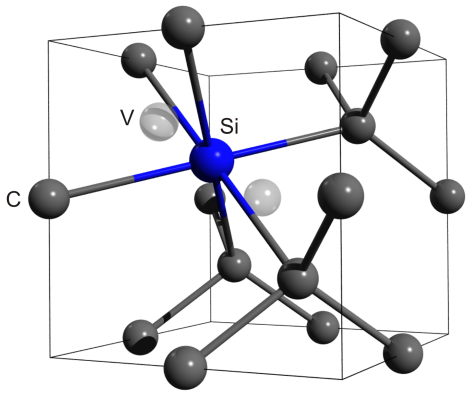

Figure 2.1: Illustration of the spatial structure of the SiV complex in the diamond lattice assuming D_{3d} symmetry according to Refs. [122,155]. Dark gray spheres indicate the position of carbon atoms, labeled C. The blue sphere indicates the position of the silicon atom, labeled Si. The light gray spheres indicate lattice sites at which carbon atoms are missing, labeled V. Note that the connection lines between the spheres are guidelines to the eye. Especially for the SiV complex, they should not be straightforwardly interpreted as bonds in the crystal. Illustration by Janine Riedrich-Möller (Quantum Optics Group, Saarland University), reproduced with permission.

The four symmetries which are under discussion for the SiV center correspond to the point groups $C_{3\nu}$ [123], D_{3d} [122] and C_2 or D_2 [154] as introduced above. In addition to the symmetry, the charge state of the center is under discussion as summarized on page 8. Goss et al. [122, 155] model the SiV center as a negatively charged color center with D_{3d} symmetry. This symmetry arises, as the Si atom is unstable on a carbon lattice site (substitutional site) and moves toward the neighboring

vacancy. Such a configuration results from searching states of minimum energy in simulations using density functional theory. Thus, the silicon atom now is located at the center of the connection line of vacancy and Si atom in the *split-vacancy configuration* as illustrated in Fig. 2.1. It should be noted, that in Ref. [155] it is also pointed out that a displacement of the Si atom along a $[1\bar{1}0]$ direction would lead to a C_2 symmetry, as experimentally observed. However, the simulations performed in Ref. [155] do not find a stable structure for such a displacement. The calculations in Refs. [122,155] identify a ${}^2E_g \rightarrow {}^2E_u$ transition as the 1.68 eV ZPL. The superscript identifies the spin-multiplicity of the states, E_g and E_u identify the corresponding irreducible representations in D_{3d} symmetry (see Tab. 2.4). As reported in the literature and summarized on page 12, the ZPL of the SiV center splits into four line components at low temperature. This splitting is attributed to a Jahn-Teller effect of degenerate E terms in the model proposed in Refs. [122, 155].

An alternative model introduced by Moliver in Ref. [123], on the other hand, assumes the center being in the neutral charge state (SiV^0). The silicon atom is shifted off center along the [111] direction, out of the above discussed split vacancy configuration, resulting in a reduced $C_{3\nu}$ symmetry. In Ref. [123], the 1.68 eV ZPL is associated with a ${}^3A_2, {}^3E \rightarrow {}^3A_2$ transition in $C_{3\nu}$ symmetry. The ZPL splitting is explained in terms of a tunneling of the Si atom between equivalent sites of the $C_{3\nu}$ configuration. A similar *inversion splitting* is also known for the ammonia (NH_3) molecule, where the carbon atom tunnels between equivalent sites. This situation corresponds to a double-well potential and thus leads to the splitting of the energy levels [153]. As a result of the splitting in the excited and ground state, four transitions can be observed thus explaining the fine structure of the ZPL experimentally observed for SiV centers. It should be noted, that the transitions between such split levels are possible and have e.g., been used as the active transition in the first microwave laser [153]. Direct transitions between the split states might influence the relative intensities of the fine structure components as they might enable population transfer (thermalization) between these states.

In contrast to the theoretical proposals, experimental investigations mostly indicate a lower symmetry for the SiV center: In Ref. [154], polarized emission studies on SiV ensembles yield C_2 (monoclinic) or D_2 (rhombic) symmetry. Other measurements indirectly indicate a $\langle 111 \rangle$ orientation of the SiV center: Ref. [112] suggests an orientation of the SiV center along $\langle 111 \rangle$ direction due to the strong interaction with L-point phonons as deduced from luminesce spectra. Ref. [162] employs Zeeman measurements, however, the measurements give rather inconclusive results yielding a possibly tetragonal symmetry which includes 4-fold rotational axes. However, also a perturbation toward monoclinic symmetry is suggested in Ref. [162] and later the same data is interpreted in terms of monoclinic or rhombic symmetry [163]. Uniaxial stress measurements in Ref. [111] have only been performed for one crystal direction and are not discussed with respect to symmetry properties. No measurements of the Stark effect of the SiV center are reported in the literature.

Summarizing, the symmetry properties of the SiV center are not clear to date. Therefore, also the nature of the ZPL transition and the origin of the fine structure has not been identified. Theoretical models and experimental findings are contra-

dictory. No symmetry investigations on single centers have been performed so far. The symmetry properties of the SiV center will be discussed again in the context of polarization measurements on single centers that aim at deducing the transition dipole orientation of the SiV center in Sec. 6.4.

Chapter 3

Experimental Setup

The following chapter briefly introduces the experimental setup used to locate and characterize single SiV centers during this work. The setup has been described in detail in Chapter 4 of Ref. [164]. It comprises of a confocal laser microscope and a Hanbury Brown and Twiss (HBT) interferometer to measure the intensity autocorrelation ($g^{(2)}$) function of the emitted light as well as a grating spectrometer to analyze its spectral properties. To investigate the crystalline quality of the diamond samples, especially the content of non-diamond phases, we additionally employ a Raman spectrometer briefly introduced in the last part of this chapter.

3.1 The confocal microscope

Principles, sample positioning and cooling

Figure 3.1 schematically shows the employed setup that has been assembled during this work. To locate single SiV centers, a confocal laser microscope is employed (see Ref. [165] for a review on confocal microscopy). It is based on the excitation of a limited volume of the sample by tightly focussing the excitation light. Simultaneously, only the fluorescence originating from a small sample volume is mapped into the detection optics by using a pinhole in the detection path. In the setup employed here, the focussing of the excitation light and the collection/imaging of the fluorescence is done using the same microscope objective (Olympus LMPLFLN100x, numerical aperture NA 0.8). The pinhole is realized by coupling the fluorescence light into a multimode fiber, where the aperture of the multimode fiber (core diameter 62.5 μm) serves as the pinhole. The light is focussed onto this pinhole using a 50 mm focal distance achromatic lens doublet. The achromatic lens doublet is designed to minimize chromatic abberation between 700 nm and 1000 nm, thus enabling the efficient coupling of broad fluorescence spectra. We point out that using, e.g., a single mode fiber as pinhole, together with a shorter focal length focussing lens, a tighter filtering and thus an enhanced resolution can be obtained (for a detailed discussion see Ref. [164]). However, this configuration would be more susceptible to misalignments and the enhanced resolution is not necessary for the experiments performed throughout this work. The setup employed here enables a resolution in the sample plane

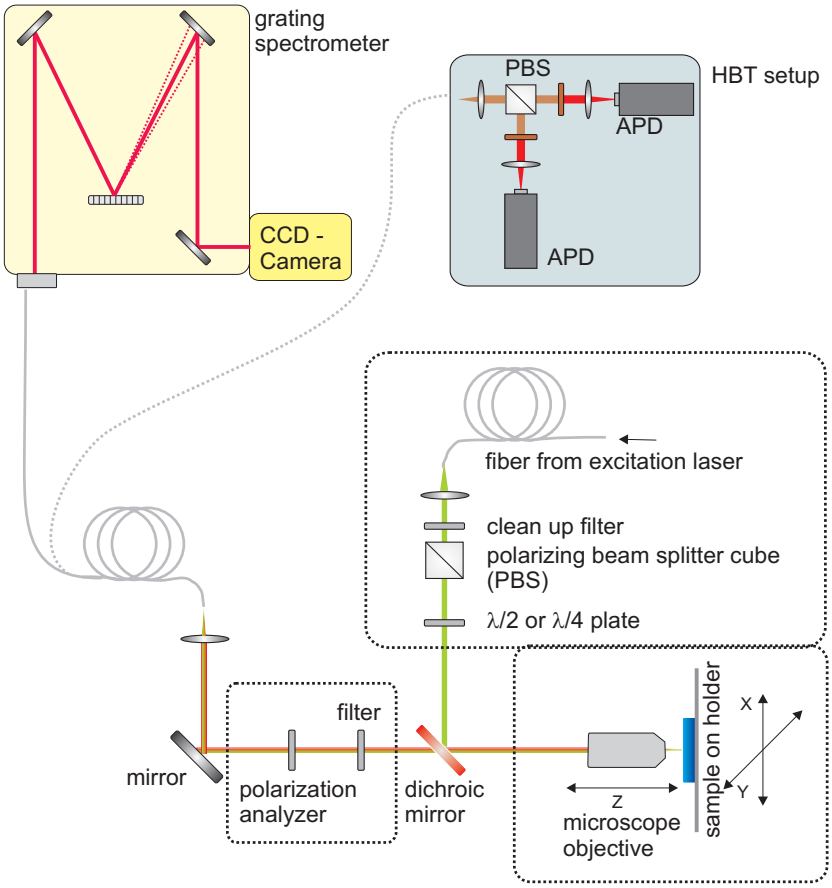

Figure 3.1: Schematic drawing of the experimental setup including the confocal microscope setup. The setup is employed to locate single SiV centers. A grating spectrometer and a HBT setup serve to analyze the fluorescence light. The light is guided to the HBT setup and the spectrometer via a multimode fiber. Several laser sources can be coupled into the confocal setup. For simplicity, most steering optics are omitted.

(x and y direction), i.e., the plane perpendicular to the laser propagation direction, of approx. 0.6 μm. In the direction of the laser propagation, an axial resolution of only 2.2 μm is obtained. To obtain single photon emission, only a single color center should be present in this imaged volume. For the samples investigated during this work, the axial resolution is not a limiting factor as only very thin (< 200 nm) films or nanodiamonds will be used (description of samples see Chapter 4). Also the lateral resolution is not very critical here as in the analyzed samples single SiV centers are spatially separated by more than 0.6 μm due to optimized manufacturing parameters. Thus, the setup designed here enables a suitable resolution for the experiments to be performed.

To locate single SiV centers, the sample is scanned in x and y direction through the laser focus. To perform the scans, the sample is mounted on two perpendicularly installed translation stages (Newport, M-UMR8.25) driven by stepper motors (Newport, LTA-HL). The axial position of the laser focus is set by controlling the

distance between the sample and the microscope objective. For this purpose, the microscope objective is mounted on a translation stage equipped with a stepper motor identical to the x-y-positioning equipment. The stepper motors allow a minimal step size of 50 nm. During the scans, the fluorescence light intensity is recorded using the avalanche photo-diodes (APDs) in the HBT setup discussed below. Dielectric bandpass filters positioned in front of the APDs allow for the selection of spectral windows of > 10 nm. Therefore, the confocal scans allow to locate single color centers with preselected wavelengths for further investigation. For a detailed discussion and an example of the procedure to locate single SiV centers, see Sec. 5.1. The detection efficiency of the setup is discussed on page 90.

Generally, for emitters in a solid state host line broadening at elevated temperatures occurs. Thus, specific spectroscopic investigations require cooling of the investigated samples. To enable low temperature investigations of the color centers, a liquid helium flow cryostat (Janis Research, ST-500LN) can be attached to the x-y-positioning system described above. In this cryostat, the sample is mounted in an isolation vacuum in thermal contact to a sample mount made of copper. This sample mount is cooled from the backside by a flow of liquid helium. Using controlled electrical heating, temperatures between approx. 4.7 K and room temperature can be established. To enable optical access to the sample in the isolation vacuum, an optically transparent window is necessary (here sapphire window, thickness 0.4 mm). As the microscope objective is not optimized for the imaging through a window, the performance of the confocal setup deteriorates when the cryostat is used. Appendix B, Sec. B.4 gives an experimental estimate of the performance degradation. It includes less efficient excitation of the color centers as well as a loss in collection efficiency for the fluorescence light. This experimental issue has to be taken into account when comparing measurements at room temperature and at cryogenic temperature as, e.g., in Secs. 7.4.1 and 7.4.2.

Excitation light sources

In this work, several lasers operating in continuous wave mode will be used as excitation light sources. To enable exchange of the laser source without readjusting the setup and to ensure a suitable spatial mode profile, the laser light is coupled into the confocal setup using fibers with FC-APC connectors. Standard single mode fibers are employed; however, these fibers do not conserve the linear polarization of the laser light: Due to (partially stress induced) birefringence of the fiber core, an elliptical polarization is generated. For measurements of the polarized absorption of the color centers, a defined polarization of the excitation laser light is necessary. Therefore, we first control the polarization change of the light by controlled bending of the fiber. Second, we insert a polarizing beamsplitter cube after the single mode fiber directly in front of the dichroic mirror (discussion see below) to enable a defined polarization without distortions due to steering optics (see Fig. 3.1). Additionally, a half-wave or quarter-wave retarder plate enables either to rotate the linear polarization or to set up a circular polarization.

The employed lasers deliver wavelengths/photon energies of 532 nm/2.33 eV,

671 nm/1.85 eV and 685 nm/1.81 eV to 715 nm/1.73 eV.[1] The first two wavelengths are created using diode-pumped solid state lasers (Newport Spectra, Millenia Pro and Shanghai Dream lasers, SDL-671-LN-050T). Laser light with wavelengths longer than 685 nm is created using a tunable titanium-sapphire laser (Sirah, Matisse) pumped by the 532 nm laser described above. For each laser, spectral filtering (bandwidth approx. 10 nm) is employed to remove residual light, e.g., light from the pump diodes or amplified spontaneous emission from the titanium doped sapphire crystal but also light created in the fiber core due to fluorescence and Raman scattering. This is necessary as very low light levels coinciding with the emission wavelength of the color centers significantly affect the measurements. All lasers deliver at least 2 mW of laser power, measured in front of the microscope objective, to the confocal setup. This laser power allows to fully saturate the observed color centers (see Sec. 5.3.1). We point out that the setup can also be operated using a pulsed laser source (titanium-sapphire laser, Newport Spectra, Tsunami) to perform pulsed single photon generation as well as lifetime measurements, for a detailed description see Refs. [164, 166].

Separating fluorescence and excitation light: dichroic mirrors

The excitation laser light is reflected of a dichroic mirror before being focussed onto the sample as illustrated in Fig. 3.1. A dichroic mirror here is a longpass filter designed to operate under an angle of 45°. As introduced in Sec. 1.3.1, to excite the luminescence a wavelength shorter than the emission wavelength of the SiV center is employed. The dichroic mirror therefore fulfills two purposes: First, it provides a high reflectivity (approx. 90%) for the excitation laser light. Thus, a low excitation light power can be used as it is efficiently transported to the sample. This reduces background fluorescence created within the setup. Second, it offers a high transmission for the fluorescence light. Thus, it separates fluorescence light and excitation laser light reflected from the sample surface. However, the dichroic mirror also imposes experimental restrictions. First, it might limit the observable wavelength range for the color center fluorescence. Depending on the design of the dielectric coating used for the dichroic mirror, often a second spectral region with high reflectivity occurs. The transmission measurements for the two dichroic mirrors used for the observation of single color centers are given in Appendix B, Sec. B.1.1. For one of the dichroic mirrors, this region of 'unintended' high reflectivity starts already at 900 nm, thus limiting the observable spectral region for color center fluorescence (see also discussion in Sec. 5.2). Second, the dichroic mirror changes the polarization of the reflected as well as transmitted light. On the one hand, this influences the polarization state of the laser light impinging onto the sample. On the other hand, it changes the polarization state of the fluorescence light upon transmission through the dichroic mirror. Measurements quantifying the change of linear polarization are summarized in Appendix B, Secs. B.1.2 and B.1.3. The influence of this experimental issue on the polarization dependent measurements is discussed in Chapter 6.

[1] Longer wavelengths are possible but are not employed here.

The separation of reflected excitation laser light and fluorescence by the dichroic mirror is not efficient enough due to the different power levels of excitation light and fluorescence. To illustrate the issue: $10\,\mu$W at a wavelength of 671 nm correspond to 10^{13} photons/second. Fluorescence from single color centers starts at 10^3 photons/second. Thus, to enable efficient single photon detection, at least 10-12 orders of magnitude of laser light suppression are necessary. Therefore, one or two additional longpass filters are added in the detection path (see Fig. 3.1). The employed filters (Omega optical, third millenium, longpass 710, 720 or 730 nm) supply a suppression of 6 orders of magnitude each according to the manufacturer. This suppression suffices to measure the spectra of single centers without detrimental influence of the residual laser light. For the measurement of the intensity auto-correlation discussed below, additional bandpass filters (Omega optical, third millenium BP730-750) are inserted supplying additional 6 orders of magnitude (on average) suppression.

3.2 Analysis of the fluorescence light

The fluorescence light can be analyzed with regard to three different properties:

- Linear polarization degree
- Spectral properties
- Intensity auto-correlation function $g^{(2)}$

To analyze the degree of linear polarization of the emitted fluorescence, a linear polarization analyzer (Edmund Optics, TechSpec laminated linear polarizer film for visible light) is inserted into the detection beam path if needed. This polarization analysis is performed before the light passes any steering optics. However, the dichroic mirror induces polarization modifications as already introduced above. We therefore thoroughly characterize the employed dichroic mirrors with respect to polarization changes. The experimental data is summarized in Appendix B, Sec. B.1.3. The influence on the measurements is discussed in Sec. 6.2.

Spectral characterization

To measure the spectral properties of the fluorescence light, a grating spectrometer is employed (Horiba Jobin Yvon, iHr 550). This spectrometer uses three selectable gratings equipped with 600, 1200 and 1800 grooves/mm. The spectrometer operates as imaging spectrometer: The entrance slit is imaged into the detector plane. The employed detector is a liquid nitrogen cooled high sensitivity, low noise CCD camera (Horiba Jobin Yvon, Symphony BIDD) with 1024×256 pixels. This detector features a quantum efficiency of approx. 90% at 740 nm according to manufacturer specifications. The CCD camera enables detection of light with wavelengths up to 1000 nm, however, with reduced quantum efficiency down to 20%. The fluorescence light is coupled into the spectrometer using a fiber adapter equipped with a

metal coated focussing mirror to avoid chromatic abberations. Thus, the fluorescence light can be directed either to the spectrometer or to the HBT setup using the multimode fiber as depicted in Fig. 3.1. The spectral resolution of an imaging spectrometer critically depends on the positioning of the detector in the image plane of the spectrometer. We thus experimentally determine the maximum resolution of the employed spectrometer using the 1800 grooves/mm grating. The resolution measurement is done by imaging a narrow spectral line at 546.07 nm from a gas discharge. The experimental results are summarized in Appendix B, Sec. B.2. We estimate a maximum resolution (here: width of the instrument response function) of 0.04 nm. This maximum resolution is crucial for low temperature measurements discussed in Sec. 7.2. For room temperature measurements, the 600 grooves/mm grating is employed to enable simultaneous observation of a larger wavelength range with a reduced resolution of approx. 0.2 nm according to the manufacturer. The results of spectroscopy at room temperature are discussed in Chapter 5.

Measurements of the intensity auto-correlation function

To measure the intensity auto-correlation function $g^{(2)}(\tau)$, defined by

$$g^{(2)}(\tau) = \frac{\langle I(t)I(t+\tau)\rangle}{\langle I(t)\rangle^2}, \tag{3.1}$$

we employ a Hanbury Brown and Twiss setup. Here, $\langle\rangle$ denotes temporal averaging. $I(t)$ is the intensity at time t, while $I(t+\tau)$ is the intensity at time $t+\tau$. This type of intensity interferometer has been experimentally demonstrated in 1956 by Robert Hanbury Brown and Richard Twiss to measure correlations between photons emerging from stars [167]. As a preceding test experiment, they also demonstrated the measurement of the correlations of photons in coherent beams [168]. We here employ the $g^{(2)}$ function to prove single photon emission in our experiments and to investigate the population dynamics of single color centers in Sec. 5.3.2 and Sec. 7.4.2.

The light is coupled into the HBT setup using an aspherical lens as collimator at the exit of the multimode fiber. The experimental setup consists of a non-polarizing (nominal) 50:50 beamsplitter cube (B. Halle Nachfl. GmbH, TWK1) that splits up the incoming light onto two avalanche photo-diodes (APDs) (Perkin Elmer, SPCM-AQRH-14) as depicted in Fig. 3.1. According to the manufacturer, the splitting ratio amounts to 45:45% (±5%) for unpolarized light.[2] The loss in the beamsplitter is induced by the metallic (silver) layer used to establish the splitting. After passing through the multimode fiber, the linear polarization of the fluorescence light has been measured to be mostly lost, we thus assume that the splitting ratio for unpolarized light is a reasonable approximation. To enable efficient detection, the light is focussed onto the APD's active area (diameter 175 μm) using a 50 mm focal distance lens. Additionally, an iris diaphragm assists in filtering out background signal. The APDs typically feature a quantum efficiency of 65% at 740 nm according to manufacturer specifications. Spectral filtering is obtained using dielectric bandpass filters.

[2] However, the splitting layer has a slightly polarization dependent splitting ratio: The transmission of the p-polarized component is about 5 to 15% higher than that of the s-component.

Using suitable filter combinations, we can thus measure the auto-correlation function of the light but also the cross-correlation of light emitted at different wavelengths (see Sec. 8.3).

The $g^{(2)}$ function introduced above should, in principle, also be observable using a single detector. However, the employed detectors suffer from a dead time of typically 50 ns after each detection event. Thus, time delays τ shorter than this time period would not be accessible using a single detector. For the setup described above, two photons separated by less than 50 ns can be dispensed onto the two detectors and can thus be detected. The $g^{(2)}$ function can be obtained from a normalized histogram of the delay times between detection events on the two detectors [169]. Additionally, using two detectors raises the maximum photon count rate at which measurements can be performed as a single detector saturates at typically 10 Mcps (10^7 counts per second). We here record the arrival times of the photons ('time tags') using a counting electronics (Pico Quant, Pico Harp 300) with a maximum uncertainty of 12 ps. From these lists of arrival times, we calculate the $g^{(2)}$ function using a suitable time bin width and overall delay range τ (see [164]). This method offers the advantage that the raw data enables calculation of $g^{(2)}$ functions with different bin widths and overall ranges to observe the full dynamics of the investigated color centers. Apart from the high resolution of the counting electronics, the APDs introduce an uncertainty of the time tagging due to an intrinsic time uncertainty of the photon detection process (timing jitter). This jitter has been measured to amount to 354 ps, for more details on the measurement see Sec. 5.3.2 and Ref. [164]. The influence of the timing jitter on the $g^{(2)}$ function will be discussed together with the experimental results in Sec. 5.3.2.

3.3 Raman Spectrometer

The confocal microscope setup described above offers high sensitivity and allows for the detection and investigation of single color centers. However, only laser light with wavelengths exceeding 532 nm can be used and as the setup uses a monochromator with only one grating, fluorescence measurements require the suppression of reflected laser light via dielectric filters. The crystalline quality of diamond samples can be measured via inelastic light scattering so called Raman scattering. For a detailed discussion, see Sec. 4.2.1. To perform Raman spectroscopy on diamond, shorter laser wavelengths down to the ultraviolet spectral range can be favorable. Furthermore, it is desired to allow for a spectral filtering without the use of dielectric filters: The Raman scattered light from diamond is shifted by 1332.5 cm^{-1} or 165 meV, corresponding to a shift of approx. 40 nm in the visible spectral range. For some non-diamond phases, the shift is even lower, down to 1150 cm^{-1} [170], thus Raman spectroscopy requires filters with a steep transition from the blocking range to the transmission range. These steep edge dielectric filters, however, can influence the measured spectrum, e.g., add oscillations.

Raman spectroscopy is thus performed using a commercial Raman microscope (Horiba Jobin Yvon, T64000). For a detailed description, see Ref. [171]. Light from a krypton/argon mixed gas ion laser (Coherent, Innova spectrum 70C) is focussed

on the sample using a selectable microscope objective with magnification 5x, 20x or 50x (NA 0.13, 0.4, 0.55). The laser allows to select (among others) the wavelengths 647.1 nm, 568.2 nm, 514.5 nm, 488 nm and 457.9 nm. The scattered light is collimated by the same microscope objective, focussed onto a pinhole (confocal filtering) and coupled into the Raman spectrometer. This spectrometer uses three gratings, each equipped with 1800 grooves/mm. The first two gratings together act as a tunable filter: The first grating disperses the light. The light then passes an intermediate slit, the desired wavelength range is selected by adjusting the slit width. Choosing a suitable position of the first grating and a suitable slit width, reflected laser light is rejected, thus superseding the use of dielectric filters. The second grating inverses the dispersion of the first grating. Now, the transmitted light can be focussed onto the entrance slit of the actual spectrometer. The spectrometer uses a third grating to disperse the light onto a CCD camera (Horiba Jobin Yvon, Symphony, 1024x256 pixel, front illuminated open electrode). The CCD camera is cooled to 140 K and features an average quantum efficiency of 40%. Due to the use of three gratings, the sensitivity of the setup is not as high as for the confocal setup described above; however, it allows to measure the Raman spectrum of diamond samples using different laser wavelengths with a maximum resolution of 0.038 nm (corresponding to 1.5 cm^{-1} at 500 nm).[3]

[3]The resolution has been calculated using manufacturer specifications: grating dispersion 0.7 nm/mm at 500 nm, resolution better than 2 CCD-pixels with 27 μm size.

Chapter 4

Fabrication strategies for single SiV centers

The fabrication of SiV centers has been demonstrated by *in situ* doping synthetic diamond during the growth (e.g., [105, 108–112, 115]) or by ion implantation (e.g., [37,74,110,117]). The center has been created in various diamond materials including natural diamonds [37,74], HPHT diamonds [115] and CVD diamonds [111,112]. For CVD and HPHT diamond, *in situ* doping as well as ion implantation is feasible, whereas for natural diamonds ion implantation is required. Additionally, natural diamonds contain an uncontrolled amount of different impurities, while synthetic diamonds can be manufactured with defined impurity content [75]. Thus, synthetic diamonds offer the opportunity to create SiV centers in a diamond material with defined purity.

During this work, various ion implantations involving silicon (Si) ions have been carried out using Ib HPHT diamonds as well as CVD diamonds with several impurity contents (see, e.g., [164,172]). A large range of implantation energies (30 keV–1.76 MeV) as well as ion doses ($1 \times 10^8\,\mathrm{cm}^{-2}$–$1 \times 10^{14}\,\mathrm{cm}^{-2}$) was investigated. SiV centers were successfully created at elevated doses and for several implantation energies, but no bright, single centers could be isolated. This observation is in accordance with the findings of Ref. [74], indicating that SiV centers created by ion implantation deep in natural bulk diamond do not exhibit bright single photon emission (count rate only approx. 1000 cps). As a consequence, this work focusses on the fabrication of (single) SiV centers *in situ* during the CVD process. Starting the chapter, we briefly introduce the two CVD methods used to grow the diamond samples. The chapter then concentrates on the discussion of the types of samples used throughout the thesis, their respective morphology and, if applicable, post growth treatment.

4.1 Microwave and hot-filament CVD process

As discussed in Sec. 1.1, synthesis of diamond via the CVD method is performed in an atmosphere of atomic hydrogen, which preferably etches sp^2 bonded carbon and leads to an overall formation of diamond from carbon containing precursor

gases (here methane CH_4). For a detailed discussion of the reaction kinetics, see, e.g., Ref. [78]. Different CVD methods mainly differ in the activation method for the precursor gases. In the hot filament (HF)CVD process, a metal filament made of a high-melting metal (typically tungsten, tantalum or rhenium [173]) is heated to temperatures above 2000 K, thus thermally dissociating hydrogen and precursor molecules [75,78,174]. In contrast to this, in a microwave plasma assisted (MW)CVD process a microwave driven plasma serves as the source of activation energy [175]. From the point of view of color center spectroscopy, both methods are suitable, as high quality diamonds can be synthesized (see, e.g., [107] and [176]). HFCVD might lead to unwanted incorporation of filament material (see discussion below), while MWCVD might lead to enhanced substrate etching due to a higher concentration of atomic hydrogen and thus a more aggressive plasma. Samples produced by a modified HFCVD process have been supplied by the company Komet rho-Best, Innsbruck. Not all growth parameters are given for these samples as the details of the production process are confidential. Samples synthesized by microwave plasma assisted (MW)CVD were supplied by the CVD diamond group at the University of Augsburg headed by Dr. Matthias Schreck. The MWCVD samples were grown using a commercial CVD reactor manufactured by IPLAS using a CYRANNUS plasma source. The growth parameters of all samples are summarized in Appendix A.

Generally, CVD diamond samples can be subdivided into epitaxial and non-epitaxial diamond films. Epitaxial diamond films have a defined orientation that is given by the substrate orientation. If a diamond (mostly HPHT diamond) is used as a substrate, the process is called homoepitaxy. If a non-diamond substrate is used the process is termed heteroepitaxy. To implement heteroepitaxial growth, a process has to be identified that induces an epitaxial, i.e., oriented, nucleation of diamond. Furthermore, it can be favorable if the lattice constants of diamond and the non-diamond substrate match closely; however, it is not mandatory to achieve heteroepitaxy. For a review see, e.g., Ref. [79]. Non-epitaxial films nucleate at randomly oriented nanodiamond seeds or surface features, thus the diamond grains are also randomly oriented. These films are termed polycrystalline films, which can be further specified as nano- and microcrystalline dependent on the grain size.

4.2 Sample types

4.2.1 Homoepitaxial thin films

Our first approach to create single SiV centers is the growth of thin CVD diamond films on a single crystal Ib (001) HPHT diamond substrate using a HFCVD process. This approach enables the investigation of SiV centers in a crystalline environment of high quality [111]. As HPHT diamonds do not contain SiV centers, unless intentionally doped, the observed centers definitely reside in the high quality CVD grown layer. Moreover, they are created in a crystalline environment of defined orientation (here (001) orientation), as a single crystal diamond substrate enables diamond growth with defined orientation (homoepitaxial diamond growth). Diamond deposition is usually performed at temperatures above 500°C. Thus, if diamond is grown

on a non-diamond substrate, stress arises due to thermal expansion mismatch of substrate and diamond layer. The use of a diamond substrate erases this source of stress and enables growth of films with a low stress level. Nevertheless, the quality of a homoepitaxial diamond film depends critically on the quality of the diamond substrate as extended defects intersecting the growth surface of the HPHT substrate can propagate through the CVD diamond film: Defects such as dislocations may be introduced due to, e.g., polishing imperfections of the substrate [79, 101]. Additionally, control of the growth parameters is crucial to obtain highly oriented defect free films, as pointed out in Refs. [107] and [176]. Similar to Ref. [176], the optimized growth conditions for the homoepitaxial thin film (sample HaStP070) employ a low methane fraction (0.26%) and a slow growth rate (approx. 10 nm/h). For photoluminescence (PL) experiments on thin films, one also has to consider that background PL from the underlying diamond substrate superimposes and possibly prevails over the fluorescence of the CVD grown diamond film.

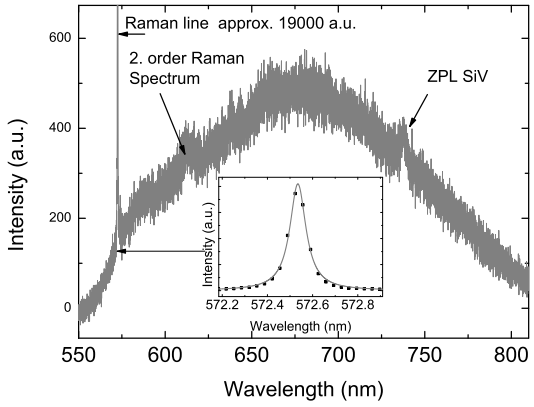

Figure 4.1: Photoluminescence spectrum of thin, homoepitaxial CVD diamond film (sample HaStP070) at room temperature excited with 6.7 mW at 532 nm. Inset: Raman line including Lorentzian fit. Explanation of a Lorentzian lineshape and broadening of the Raman line can be found, e.g., in Refs. [177–179].

Crystalline quality

Figure 4.1 displays a luminescence spectrum of the homoepitaxial thin film. The spectrum reveals a broadband luminescence. For a general discussion of the origin of broad luminescence bands in diamond, see page 73. This broadband luminescence is partially attributed to the underlying HPHT substrate (luminescence due to nitrogen vacancy centers in the substrate or other broadband luminescence). Furthermore, first and second order Raman scattered light from the diamond is observed. This light is due to inelastic scattering of the excitation laser light in diamond: A fraction of the photon energy of the laser light is transferred to a phonon in the diamond crystal, thus the resulting light is shifted to longer wavelengths (Stokes Raman effect, first discovered for molecules see, e.g., Ref. [180]).

For high crystalline quality diamond, the first order Raman spectrum consists of a single line shifted by $1332.5\,\mathrm{cm}^{-1}$. It is induced by an optical phonon with wavevector in the center of the Brillouin zone [96]. In general, due to momentum conservation in the scattering process, Raman spectroscopy only reveals phonon modes displaying a vanishing phonon momentum [181]. For high quality natural diamonds, this diamond Raman line is as narrow as $1.9 - 2.2\,\mathrm{cm}^{-1}$ [179] and for

high quality homoepitaxial films linewidths of 1.8 cm^{-1} have been found [96]. In contrast, the inclusion of sp^2 bonded or disordered carbon leads to additional often broad Raman bands. The best known are the G-band attributed to sp^2 bonded phases (1520-1610 cm^{-1}) and the D-band attributed to disordered phases (1310-1450 cm^{-1}) [96]. Thus, the Raman spectrum of a diamond sample can be used, first, to confirm its sp^2/sp^3 carbon ratio (where different Raman scattering cross sections for sp^2 and sp^3 bonded phases have to be taken into account) [177]. Second, the first order diamond Raman linewidth can serve as a measure of crystalline quality [96] if the linewidth of the laser employed to perform the Raman spectroscopy is narrow enough and the resolution of the spectrometer is high enough [179]. Different defect induced contributions broaden the first order Raman line and thus indicate a lowering of the crystalline quality: First, in a defect rich crystal, the lifetime of phonons is reduced due to scattering by lattice defects. This leads to a Lorentzian (lifetime) broadening of the Raman line [177–179]. As already introduced in Sec. 1.3.3, phonon energies are influenced by stress in the diamond lattice. Thus, also stress influences the Raman line and the distribution of the stress in the material leads to a Gaussian broadening [179]. For nanometer sized diamonds, another effect has to be taken into account: If phonons are confined to a small spatial volume, due to the uncertainty principle, phonons with different phonon momentums can participate in the Raman process [181]. This also induces a broadened and possibly shifted line [177].

The first order Raman linewidth[1] of 2.6 cm^{-1} observed here is close to linewidths observed for high quality diamonds and thus confirms high crystalline quality for substrate and epitaxial film. Additionally, no Raman bands due to sp^2 or disordered carbon are detected which would be visible on the linearly rising background emission.

SiV center concentration

Optical addressing of single SiV centers is not feasible using this sample: A homogeneous distribution of SiV ensemble luminescence in the film is observed in confocal scans. Despite the high density of SiV centers, luminescence from the SiV centers is weak and background fluorescence prevails (Fig. 4.1). We attribute the incorporation of SiV centers to residual Si contamination of the CVD reactor. We exclude Si stemming from the filaments used in the growth process as described, e.g., in Ref. [107] as the tantalum filament used here does not contain Si according to supplier information. At cryogenic temperatures, the SiV PL is more pronounced and the sample can be used to perform spectroscopy of SiV ensembles in high quality single crystalline diamond. These measurements are described in detail in Sec. 7.1.1.

4.2.2 Polycrystalline CVD films

Polycrystalline (microcrystalline or nanocrystalline) films can be grown on large areas of non-diamond substrates if a suitable substrate material is chosen. First, the

[1] FWHM of Lorentzian fit, not corrected for spectrometer resolution.

substrate material has to withstand the temperature of the CVD process exceeding 500 °C. Second, an adequate chemical resistance to the growth plasma is required. Growth of poly- and nanocrystalline diamond has been demonstrated on various substrates including Si, SiC, SiO_2 (quartz) and several metal substrates [79]. Si is a highly suitable substrate especially for the growth of thin films as high nucleation densities can be obtained (see discussion below).

The growth of diamond on a non-diamond substrate requires nucleation sites to start the diamond growth. Nucleation sites can be formed by surface features, e.g., scratches in a substrate [182]. For the polycrystalline film investigated here, the nucleation is started by seeding a Si substrate with nanocrystalline diamond powder (see, e.g., Ref. [183]). To spread the diamond seeds on the substrate, it is ultrasonically treated in a nanodiamond (ND) solution (see, e.g., Ref. [184]). This method enables high seed densities in excess of $10^{11}\,\mathrm{cm}^{-2}$ [184]. Figure 4.2(a) displays a cross section scanning electron microscope (SEM) image of a polycrystalline diamond (PCD) film on Si (sample SlGh45) grown via HFCVD. Due to the random orientation of the seed diamonds, the grains in the film are randomly oriented as well. As visible in the image, the grain size varies with the film thickness: As grains from individual seeds become larger, other grains disappear. During film growth, grains coalesce leading to mechanical stress between the crystallites [96]. A typical value for the grain size of a PCD film is approx. 10% of the film thickness [75]. The film thickness determined from Fig. 4.2(a) is approx. 2 μm. Figure 4.2(b) reveals grains of approx. 0.5 μm, slightly larger than the expected value.

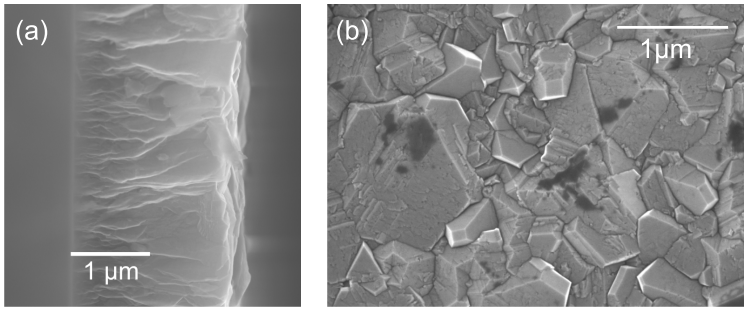

Figure 4.2: SEM images of CVD grown polycrystalline diamond (PCD) film SlGh45: (a) cross section SEM image of PCD film, the growth direction is from left to right in this image (b) surface image of PCD film.

Raman spectra of the PCD film displayed in Fig. 4.3(b) show a distinct diamond Raman line at $1330.03\,\mathrm{cm}^{-1}$ featuring a width of $5.9\,\mathrm{cm}^{-1}$ indicating a moderate stress in the PCD film [96]. The additional broader feature at approx. $1500\,\mathrm{cm}^{-1}$ indicates non-diamond phases (see, e.g., Ref. [96, 109]). We assume that these non-diamond phases mostly reside between the grains of the PCD film. Recent studies find that in the grain boundaries of PCD films amorphous carbon is present and to a lesser extent graphitic inclusions [185]. Extended studies on the crystalline quality (including multicolor Raman spectroscopy) and impurities in PCD films have been performed in Ref. [186] and more recently in Ref. [171] supporting a high crystalline quality of the PCD films together with the identification of non-diamond phases as

discussed above.

The black curve in Fig. 4.3(a) displays the PL spectrum of sample SlGh45 under 532 nm laser excitation. In addition to a broad fluorescence background, several distinct fluorescence lines are observed: At approx. 738 nm, the ZPL of the SiV center emerges. Between 680 nm and 705 nm, a line triplet is located. In the literature, these PL lines have been attributed to the incorporation of tantalum (Ta) from the filaments of the HFCVD process [187]. Observation of filament metal-related PL seems reasonable as the incorporation of various filament metals into diamond grown via the HFCVD method has been reported in the literature: Depending on growth parameters, filament metal concentrations in the diamond range from several tens of ppm to several 10000 ppm [173, 188]. Considering an application as single photon source, however, Ta color centers seem unfavorable as their fluorescence is weak and their emission wavelength coincides with the maximum of the broad fluorescence background of the film. In the discussed PCD film, as well as in much thinner films (sample HaSt027, thickness 0.17 μm) optical addressing of single SiV centers was not possible. We here attribute the incorporation of Si to chemical etching of the Si substrate and subsequent incorporation of Si into the diamond. This process has been shown to be a very efficient source of Si incorporation into CVD diamond [105,189]. Therefore, it seems not feasible to reduce the concentration of SiV centers in PCD films on Si to a level that permits optical addressing of single SiV centers. The fluorescence from these PCD films will be used to investigate the broadening of the SiV ZPL at low temperature in Sec. 7.1.1. Furthermore, PCD films are the starting material for nanodiamond (ND) production as discussed in the following.

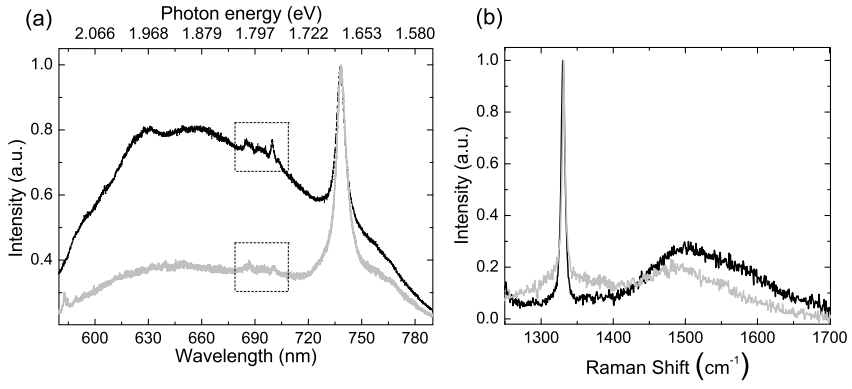

Figure 4.3: (a) PL spectra of sample SlGh45 (black curve) and of BASD NDs (gray curve) produced from sample SlGh45, (b) Raman spectra of polycrystalline film (black curve) and BASD NDs (gray curve). PL measurements performed under 532 nm excitation. Raman measurements have been performed using 488 nm excitation in the Raman microscope described in Sec. 3.3.

4.2.3 BASD NDs from PCD films

As discussed above, optical addressing of single SiV centers in PCD films grown on Si was not feasible. Additionally, for spectroscopy of single centers and applications as single photon sources, nanodiamonds (NDs) are more favorable due to an enhanced fluorescence collection efficiency (for a detailed discussion on collection efficiency see Sec. 5.3.4). In cooperation with the research group of Prof. Dr. Anke Krüger (organic chemistry department, University of Würzburg) the *bead assisted sonic disintegration* (BASD) method is employed to produce NDs from PCD films. The method described in Refs. [190,191] was originally developed to de-agglomerate nanoparticles. It uses 50 μm sized milling beads made of ZrO_2. Shock waves induced by ultrasonic cavitation, i.e., the occurrence of violently collapsing bubbles in a liquid sonicated with high intensity, propel the beads in a solution containing the nanoparticles, thus breaking the agglomerates. Here, we employ the BASD technique, first, to separate the grains of the PCD film. Second, the grains of the PCD film are crushed to form smaller NDs. Results of ND production via the BASD method have been published in Ref. [192] and are briefly summarized here. After the BASD process and several purification steps to remove contamination from the milling process, we obtain a colloidal suspension of NDs in deionized water. Dynamic light scattering[2] reveals a size distribution maximum of $70 - 80$ nm, more than 80% of the NDs are smaller than 100 nm. Thus, apart from the application discussed here, these NDs in solution are also highly suitable as fluorescence markers for *in vivo* fluorescence imaging applications [71]. To enable the observation of single NDs via confocal laser microscopy, we perform a low density spin coating, e.g., onto Si substrates. Figure 4.4(b) shows NDs spin coated onto a Si substrate without agglomeration of the NDs. Detailed SEM images [Fig. 4.4(a)] reveal facetted shapes for individual NDs, indicating a crushing of the diamond grains along lattice planes.

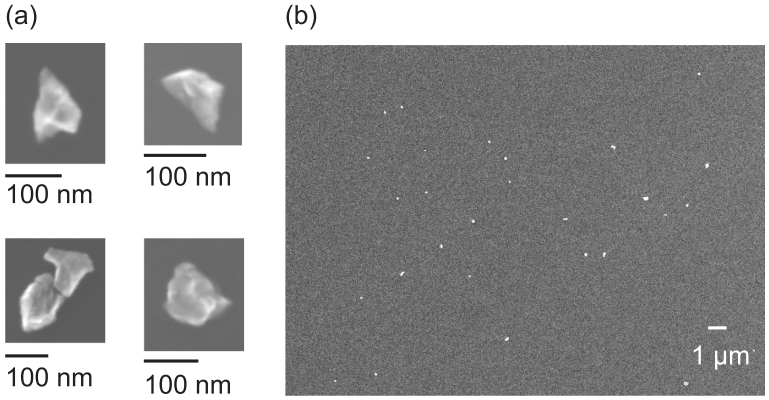

Figure 4.4: SEM images of BASD NDs produced from a polycrystalline CVD film: (a) detailed images of individual NDs (b) NDs spread on Si substrate via spin coating. As visible from the image, the NDs are mostly distributed as single NDs, not showing agglomeration.

[2]Measurements performed by the group of Prof. Dr. Krüger, University of Würzburg

A crucial topic concerning the ND production is the conservation of crystalline quality throughout the BASD process. Figure 4.3(b) displays the Raman spectrum of an ensemble of BASD NDs. A distinct diamond Raman line ($1331.2\,\mathrm{cm}^{-1}$) featuring a width of $5.1\,\mathrm{cm}^{-1}$ is observed, thus we conclude that the crystalline quality is conserved upon ND formation. The Raman signal due to non-diamond carbon is even slightly reduced. The fluorescence spectrum of an ensemble of BASD NDs [Fig. 4.3(a)] reveals the conservation of narrow PL lines of tantalum-related color centers and SiV centers. In comparison to the starting material, broadband background luminescence is reduced. Single NDs reveal SiV ensembles, as well as single SiV centers [192]. Luminescence investigations of single BASD NDs at cryogenic temperature are discussed in Sec. 7.1.2.

4.2.4 CVD nanodiamonds on Ir

An alternative approach to produce optically addressable single NDs is direct growth in a CVD process (see also Ref. [193]). The samples described in the following were prepared using a MWCVD process. Here, we employ an advanced substrate system: The substrate consists of an epitaxial (001) Ir film (150 nm thickness) on a 40 nm buffer layer of (001) yttria-stabilized-zirconia (YSZ) on a (001) Si substrate. This multilayer system was developed at the University of Augsburg as a substrate for heteroepitaxial diamond growth [194–196]. This substrate system offers four major advantages for the growth of single optically addressable NDs containing single SiV centers:

- Due to the high corrosion resistance of Ir, it enables the growth of high purity diamond as the substrate is only very weakly etched in the harsh CVD environment and Ir is not efficiently incorporated into the diamond. This statement is supported by two observations: First, no substrate-related color center luminescence has been detected in diamond grown on Ir during this work or during previous works in the CVD diamond group at the University of Augsburg. Second, Rutherford backscattering measurements, which are very sensitive detecting Ir in diamond, did not detect any Ir incorporation [197]. Rutherford backscattering spectrometry uses the analysis of the energy spectrum of highly energetic (MeV), light ions (often He) backscattered from a target. From this energy spectrum, the atomic masses of the elements present in the target can be obtained. Due to an enhanced Rutherford scattering cross section for heavier elements (proportional to the square of the atomic number), the technique has an enhanced sensitivity for heavy elements (for a review see, e.g., Ref. [198]).

- Etching of the uncovered edges of the Si substrate is a low concentration source of Si impurities.

- The Ir substrate has been found to exhibit a very low fluorescence background if excitation wavelengths typical for SiV centers ($> 660\,\mathrm{nm}$) are used.

- The metal substrate strongly alters the radiation pattern of the SiV centers as well as the lifetime of centers close to the metal surface. While close proximity

to the metal surface might lead to fluorescence quenching, the change in the radiation pattern due to the presence of the metal can also lead to an enhanced collection efficiency. This latter effect might enhance the effective brightness of single color centers (for detailed discussion see Sec. 5.3.4).

To control the density of NDs growing on the Ir surface, we use a low density seeding process. Fully de-agglomerated synthetic NDs (Microdiamant Liquid Diamond MSY) are spin coated from an aqueous solution. Figure 4.7(a) displays a size distribution of the seed diamonds as measured by the manufacturer. We use concentrations of 0.0031 ct/kg (sample MFDIA865) and 0.0016 ct/kg (sample MFDIA957). Spin coating with 2000 rpm on cleaned substrates (acid clean with permonosulfuric acid, rinsing in purified distilled water) leads to seed densities of 2.5 seeds per μm^{-2} for a concentration of 0.0031 ct/kg. Spontaneous nucleation is not possible in the employed CVD process, thus CVD crystal densities equal or lower than the seed density are expected. The seeded substrates are subjected to a MWCVD process with the following parameters:

- Sample MFDIA865: 25 min, 1% CH_4 in H_2, microwave power 2000 W, pressure 30 mbar
- Sample MFDIA957: 55 min, 0.4% CH_4 in H_2, microwave power 2000 W, pressure 30 mbar

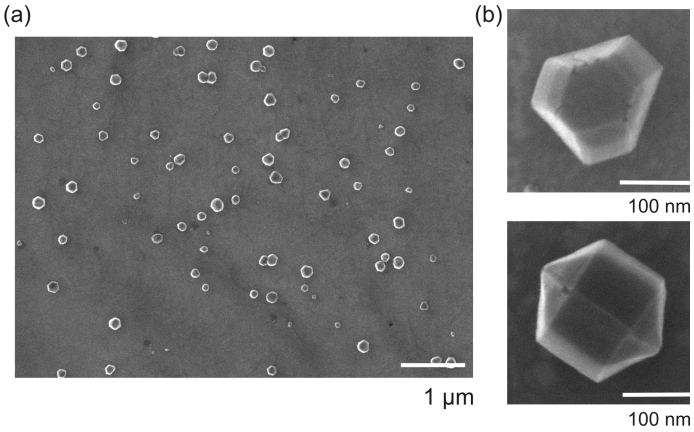

Figure 4.5: SEM images of CVD grown NDs on sample MFDia865B: (a) overview image displaying spatially isolated NDs (b) detailed images of well faceted NDs.

SEM images of the resulting NDs are shown in Figs. 4.5 and 4.6. Figures 4.5(a) and 4.6(a) show the distribution of the NDs on the Ir substrate. Both samples exhibit spatially separated NDs. We find densities of 1.7-2.2 NDs per μm^2 on sample MFDIA865, while for sample MDFIA957 a reduced density of 1 ND per μm^2 is observed. Thus, on sample MFDIA957 optical addressing of single NDs is feasible, while on sample MFDIA865 on average more than one ND is present in the laser focus.

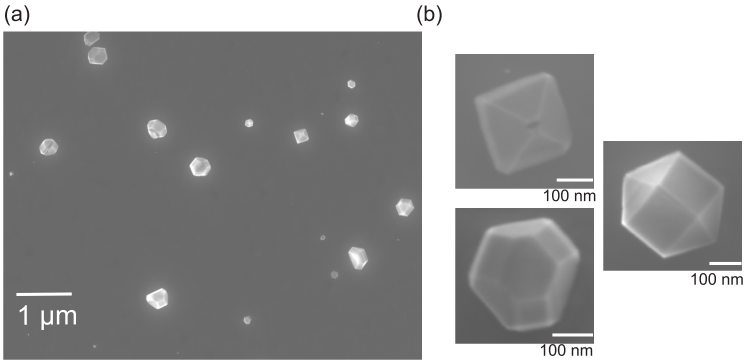

Figure 4.6: SEM images of CVD grown NDs on sample MFDia957: (a) overview image displaying spatially isolated NDs (b) detailed images of well faceted NDs.

Detailed SEM images of the NDs [Figs. 4.5(b) and 4.6(b)] reveal well facetted NDs. The NDs on sample MFDIA957 grown with a lower methane fraction are found to exhibit even cleaner surfaces without cracks and distortions. These well facetted NDs, in contrast to NDs with a polycrystalline 'cauliflower morphology', indicate a high crystalline quality [193] and low graphite content due to the absence of high grain boundary concentrations. This is crucial for the observation of SiV centers as they might be quenched in the presence of graphite [131]. Perfect diamond crystals reveal a so called cubo-octahedral shape (see Sec. 1.1, Fig. 1.1). Depending on the growth parameters, the shape is closer to the cubic shape or closer to the octahedral shape [81, 193]. Several crystals show a close to cubo-octahedral shape: the upper image in Fig. 4.5(b) and the lower left crystal in Fig. 4.6(b). Also crystals close to octahedral shape have been found (upper image 4.6(b)). Thus, in principle, these crystals might be considered as small single crystals, while others have to contain at least a twin (grain boundary), e.g., the lower image in Fig. 4.5(b). From the SEM images, we also estimate the size distribution of the NDs shown in Fig. 4.7(b). For sample MFDIA865, we find a size of 130 nm with a standard deviation of 40 nm. For sample MFDIA957, we find 216 nm with a standard deviation of 81 nm. Moreover, the size distribution of NDs for sample MFDIA957 shows an asymmetric tail toward larger NDs. A certain spread in the NDs sizes arises from the spread of sizes of the seed crystals used [see Fig. 4.7(a)]. The difference in the form of the size distributions, however, remains unclear. Additionally, we point out that a random orientation of the seed crystals on the substrate leads to a random orientation of the grown NDs.

The samples described above enable detection of single SiV centers. First results on the characterization of single centers have been published in Ref. [38]. The yield of SiV centers is approx. one single, bright center per 50x50 μm^2 sample area (sample MFDIA865). The properties of single centers are described in detail in Chapter 5. Detailed cryogenic temperature characterization of the NDs is discussed in Sec. 7.1.2. It should be noted, that these CVD NDs are optimized for a high purity, not only with respect to the incorporation of impurities from the substrate, but also

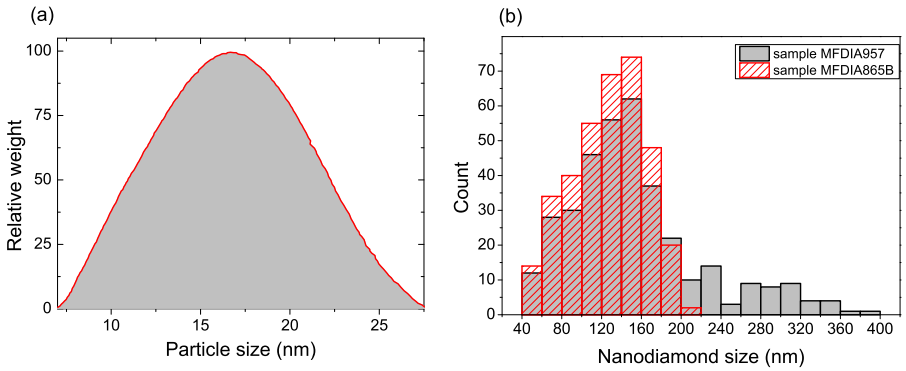

Figure 4.7: (a) size distribution of the seed NDs used for samples MFDIA865 and 957 as measured by the manufacturer (b) size distribution of the CVD NDs on samples MFDIA865 and 957. SEM images covering an area of 240 μm^2 for sample MFDIA865 and an area of 103 μm^2 for sample MFDIA957 have been used to determine the size distribution.

with respect to impurities from the gas phase: For the growth, gas purifiers are used to reduce the amount of nitrogen impurities in the hydrogen feed gas. Thus, the concentration of nitrogen in the gas phase is only about 1 ppm. In the literature, it has been found that the incorporated nitrogen/carbon (N/C) fraction is about four orders of magnitude lower than the N/C fraction in the gas phase of the reactor [199]. Thus, high purity diamond growth can be established by the growth technique discussed here: Only 40 ppb substitutional nitrogen have been detected by electron spin resonance techniques in previously investigated homoepitaxial samples [197].

4.2.5 Oriented heteroepitaxial nanoislands

The CVD ND samples discussed above all feature randomly oriented diamonds, thus for an individual ND observed in the confocal microscope, the crystal orientation is unknown. From the polarization properties of the light emitted by single color centers as well as the polarized absorption, one can deduce the orientation of the transition dipole moment(s) of the color center (see Chapter 6). If in addition the crystal orientation is known, also the dipole orientation with respect to the diamond lattice can be determined. Based on the dipole orientation, information on symmetry and possible models of a color center's spatial structure can be deduced. This option, together with the superior fluorescence extraction properties of NDs, makes the use of oriented NDs for polarization spectroscopy on single SiV centers extremely favorable. Oriented NDs, which we will term *nanoislands* in the following, are obtained via heteroepitaxial growth on a single crystal (001) Ir surface. The Ir multilayer substrate system used has been introduced above. In contrast to the flat Ir films used for the spin coating, we now use nanostructured Ir surfaces: The deposition process has been modified to yield isolated, flat (001) regions (facets) terminated by steep side walls. The isolated facets are visible in SEM images, e.g., in the marked areas in Fig. 4.8. On these facets, nucleation areas are formed via a *bias enhanced nucleation* (BEN) process: The substrates are subjected to a microwave

plasma (power 2000 W, 40 mbar, 3% CH_4 in H_2) but, in contrast to the growth process, a negative bias voltage of −300 V is applied. This induces an intensive ion bombardment of the substrate held at 800 °C. The procedure introduces epitaxial diamond nuclei, which in contrast to seeding with NDs, lead to oriented diamond growth [200].

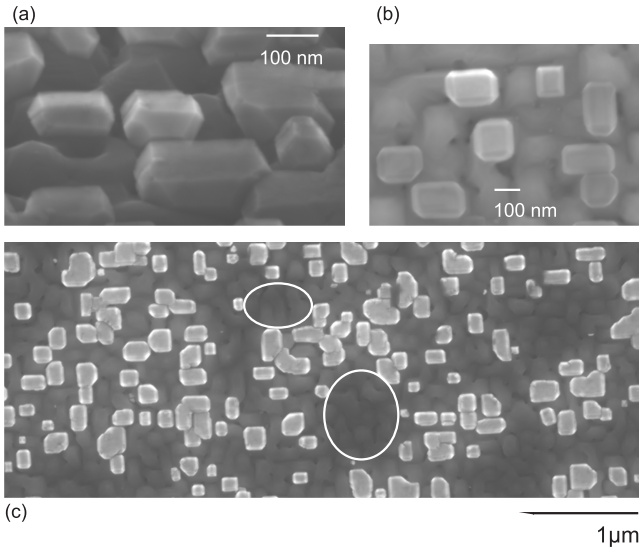

Figure 4.8: SEM images of the diamond nanoislands (a) side view of the nanoislands, sample tilted by 60°, scale bar corrected for tilt angle, (b) detailed top view of nanoislands, (c) overview top view of nanoisland sample. All pictures taken from sample MFDIA945. In the marked areas in picture (c), the nanostructured Ir surface is clearly visible due to a low diamond nanoisland density.

Following the BEN process, the bias voltage is switched off and CVD growth using 0.5% CH_4 in H_2 is performed for 20 min. Figure 4.8 displays several SEM images of the sample revealing epitaxial diamond nanoislands. From images of the tilted sample [see Fig. 4.8(a)], the cubo-octahedral shape of the diamond nanoislands with {001} and {111} faces can be identified [201]. We infer a mean lateral size of 160 nm (standard deviation of 60 nm). Furthermore, we estimate a thickness of 75 nm (standard deviation of 12 nm). Therefore, the nanoislands feature subwavelength sizes to enable efficient fluorescence extraction with negligible total internal reflection. Single optically addressable SiV centers are created *in situ* due to plasma etching of the Si substrates and incorporation of Si into the growing diamond analogous to the growth of randomly oriented NDs. Polarization measurements on SiV centers in nanoislands are discussed in detail in Chapter 6. The properties of single SiV centers in nanoislands with respect to their application as single photon sources, including spectral properties and population dynamics, are addressed in Chapter 5.

4.2.6 Heteroepitaxial diamond films

As outlined above, NDs offer superior fluorescence collection efficiency. However, recently developed techniques allow for the production of tailored photonic structures in single crystalline diamond or single crystal diamond thin films. These structures including, e.g., nanowires [48] and photonic crystals [69] (see also introduction) allow for a more deterministic enhancement of the collection efficiency and also for enhanced coupling of light to color centers contained in these structures. Thus, investigations of SiV centers in diamond films, here in thin heteroepitaxial diamond films, are also of great interest. For this approach, two samples have been produced, a 90 nm thick (001) oriented film (MF4DIA562_1) and a 45 nm thick (111) oriented film (MFDIA455). Figure 4.9 displays a SEM image of the (111) oriented film. Visible in the image are the epitaxial diamond grains coalescing to form the diamond film. In both types of films, single SiV centers were observed. However, due to the reduced fluorescence collection efficiency as well as the larger diamond volume in the laser focus, the observed SiV centers suffer from larger background fluorescence contributions. The results on the polarization properties of SiV centers in the (001) film will be addressed in Chapter 6, whereas the spectral properties will be discussed in Sec. 5.2.

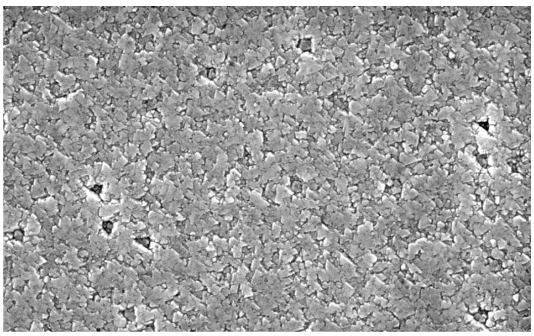

Figure 4.9: SEM image of heteroepitaxial (111) oriented diamond film

Chapter 5

Room temperature single photon emission from SiV centers

This chapter discusses in detail the properties of single SiV centers relevant for the application as a room temperature single photon source. First, we illustrate the method used to locate single SiV centers in the diamond samples. Second, we investigate the spectral properties of single SiV centers, including the zero-phonon-line (ZPL) as well as the vibronic sidebands. Third, we address the brightness of single SiV centers via saturation measurements under continuous excitation. Extensive, intensity dependent $g^{(2)}$ measurements allow for a detailed investigation of the single photon nature of the emitted light as well as the population dynamics of the color center. We interpret these measurements in the framework of a newly developed extended three level model. The third part of the chapter addresses quantum and collection efficiency of SiV centers in nanodiamonds (NDs) on Ir, forming crucial parameters for single photon sources.

5.1 Locating single SiV centers in nanodiamond samples and diamond films

In Chapter 4, different approaches to create single, optically addressable SiV centers *in situ* during a CVD process have been summarized. Due to a high concentration of SiV centers, addressing of single centers was not possible in thin homoepitaxial CVD diamond films as well as thin polycrystalline diamond films grown on Si (using HFCVD). Not until the polycrystalline diamond films were disassembled to form nanodiamonds (NDs) single SiV centers could be detected, however, with underlying ensemble emission (for a discussion see Sec. 7.1.2). Single SiV centers without underlying ensemble emission were created using MWCVD growth on Ir. Samples with different morphologies have been obtained: As discussed in Secs. 4.2.4, 4.2.5 and 4.2.6, samples with randomly oriented nanodiamonds (NDs), oriented nanoislands (NI) and diamond films have been produced. The following section introduces

the procedure to locate individual SiV centers in these samples.

In the ND samples, due to the low density of NDs, on average only one or a few NDs are located in the laser focus. We emphasize that an individual ND with 130 nm size is significantly smaller than the laser focus exceeding 500 nm. In contrast, for the NI samples due to the higher density of the NIs, the excited diamond area is closer to the area of the laser focus. For the continuous films, it is equal to the area of the laser focus. For all samples investigated here, the thickness of the diamond layer is far below the axial resolution of the confocal microscope setup (see Chapter 3), thus SiV centers in different depths of the samples are excited simultaneously. In all sample types, single optically addressable SiV centers are found with a density of typically several centers within a 50×50 μm^2 area. An efficient routine to identify these centers in fluorescence maps, i.e., scans over the sample while recording the fluorescence using the confocal setup, is desirable. Bright emission in such fluorescence maps can originate both from single SiV centers or from comparably bright, broadband emission observed from some NDs or NIs, thus complicating the identification of single SiV centers in fluorescence maps. This broadband fluorescence is most probably due to NDs/NIs with low crystal quality. Furthermore, in the diamond films, the fluorescence of single SiV centers might be superimposed on a broadband luminescence background, enhanced in comparison to the NDs, due to the larger volume of diamond material excited. For a discussion of the origin of broadband luminescence, see page 73.

To facilitate the fast identification of single SiV centers from fluorescence maps, we take advantage of the narrow bandwidth of the SiV center luminescence. The zero-phonon-line (ZPL) of the SiV centers has a wavelength of approx. 738 nm with a width of less than 10 nm. (For a discussion of SiV center linewidths observed in the literature, see Sec. 1.3.2.) We thus employ a dielectric bandpass filter transmitting light in the wavelength range of 730 nm to 750 nm in front of one photo-detector (APD) in the HBT setup to detect the fluorescence from the SiV ZPL. To discriminate between spots with broadband luminescence and single SiV centers, a filter in front of the second APD selects a wavelength range of 755 nm to 765 nm. In this wavelength range, a single SiV center shows only weak emission due to vibronic sidebands. In contrast, for broadband luminescence, the integrated count rates in the two spectral windows differ little. (For a very broadband fluorescence, a reduction by a factor of approx. two is expected due to the different widths of the filter windows.) We thus identify single SiV centers via the ratio of the intensities in the 730 nm to 750 nm and the 755 nm to 765 nm windows: For bright single SiV centers with low broadband background contribution, ratios of at least 10:1 are observed.

Figure 5.1 gives an example of a fluorescence map from a ND sample recorded in the two disjunct spectral windows introduced above. As apparent from Fig. 5.1, a region on the sample with inhomogeneous ND density is observed. Such density gradients arise due to a nonuniform distribution of the seeds in the spin coating process. Figure 5.1(a) displays the fluorescence from the SiV ZPL, Fig. 5.1(b) shows the fluorescence in the longer wavelength control window. At the position indicated by the solid, red arrow, a single SiV center (emitter ND1, see below) is located. The dashed, red arrow indicates an additional bright spot in

the scan. Furthermore, a lot of 'empty' NDs are observed that show neither SiV luminescence nor bright broadband luminescence, revealing the density of NDs on the sample. Comparing both maps allows to identify the SiV center: For the SiV center, a count rate of 229 kcps is observed between 730 nm and 750 nm, while only 7 kcps are observed in the spectral range 755 nm to 765 nm, corresponding to a ratio of 32:1. For the additional bright spot, 165 kcps are recorded in the shorter wavelength window and 42 kcps in the control window, leading to an intensity ratio of only 4:1. The fluorescence maps in Fig. 5.1 illustrate how the comparison of the scans using two spectral windows allows for the fast identification of the narrow fluorescence of single SiV centers in the presence of bright, broadband luminescent spots.

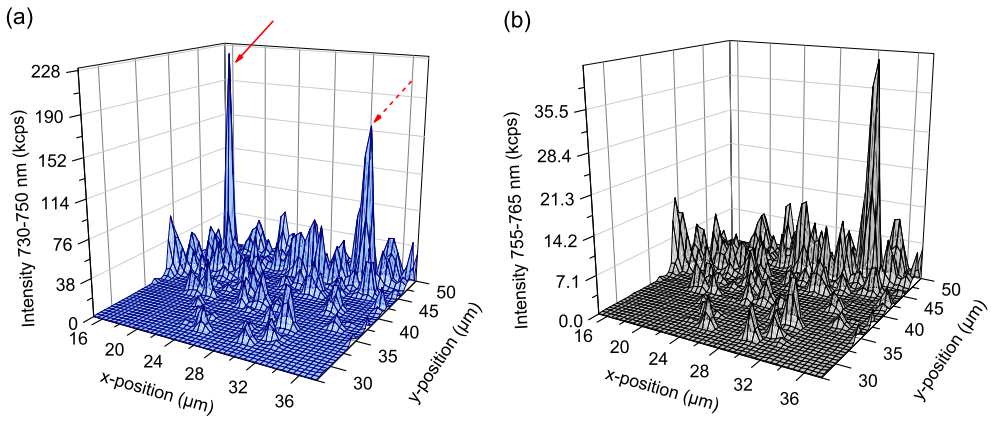

Figure 5.1: Fluorescence maps taken from sample MFDIA865a. Laser excitation at 671 nm with 85 μW was employed. The laser light was circularly polarized. The step size of the scan is 0.5 μm and the integration time for each point was chosen to be 100 ms. To obtain these fluorescence maps, the stepper motors were moved over one line of the scan (x-direction) in a defined time while the fluorescence counts were continuously recorded. From these data, the fluorescence counts for each pixel of the scan are calculated. Subsequently, a defined step, here 0.5 μm, is performed to reach the next line. (a) Fluorescence recorded in the spectral window 730 nm to 750 nm (b) Fluorescence recorded in the spectral window 755 nm to 765 nm. The solid, red arrow marks the position of an SiV center (emitter ND1, see below), while the dashed, red arrow marks a spot with broadband fluorescence.

5.2 Spectral properties of SiV centers in as grown CVD diamond

This section compiles photoluminescence spectra of individual SiV centers located in the diamond samples introduced above. The spectra have been selected to illustrate all kinds of observed properties of single SiV centers as completely as possible. Figures 5.2, 5.3 and 5.4 present photoluminescence spectra of single SiV centers recorded using the setup described in Chapter 3. The excitation wavelength for each measurement setting is given in the figure caption. In Fig. 5.2, spectra of four

emitters hosted by randomly oriented CVD NDs on Ir are displayed (sample description see Sec. 4.2.4). Further emitters investigated in this sample are discussed in Ref. [38]. Figure 5.3 features five emitters located in (001) oriented nanoislands (NIs) (sample description see Sec. 4.2.5). Further spectra are shown in Ref. [202]. Finally, Fig. 5.4 represents the spectra of four emitters identified in a (001) heteroepitaxial diamond film on Ir (sample description see Sec. 4.2.6). Intensity auto-correlation measurements ($g^{(2)}$ measurements) identify all emitters as single color centers. The $g^{(2)}$ measurements will be discussed in detail in Sec. 5.3.2.

It is clearly observable in the individual spectra that all emitters show an intense, narrow ZPL with weak sideband emission. As also discernible from the spectra, low background emission is observed especially for NDs and NIs. The ZPLs show a spread in peak wavelength and width: For the emitters displayed here, we observe wavelengths ranging from 735.3 nm to 746.2 nm. The ZPLs feature widths between 0.7 nm and 1.3 nm (full width at half maximum (FWHM) of Lorentzian fit). The combination of a narrow ZPL with low contribution of (spectrally broad) sideband emission renders these SiV centers highly suitable as narrowband, room temperature single photon sources. The ZPL linewidths observed here are superior to the linewidths of other narrow emission color centers like chromium-related centers ($4 - 10$ nm, [36]) and nickel nitrogen centers (NE8, $1.2 - 2$ nm [27–29, 31, 203]). The scatter of the peak wavelength and width of the ZPL as well as the correlation of these properties are investigated in detail in Sec. 5.2.1.

The sideband spectra of individual SiV centers noticeably differ: E.g., in Fig. 5.3 the sideband spectrum of emitter NI2 is dominated by an intense narrow line, while for emitter NI1 additional broader sidebands at shorter wavelength and multiple narrow lines are identified. Other emitters show no intense narrow lines in the sideband region (see, e.g., Fig. 5.4, emitter EF4). Furthermore, the varying sideband spectrum is not clearly connected to the ZPL position: When comparing emitter NI2 and NI3, similar properties of the ZPL are found but the sideband spectra strongly vary. A striking feature observed in many sideband spectra is the occurrence of lines as narrow as the ZPL especially in the spectral region 820 nm to 845 nm.[1] As pointed out in Ref. [25], color centers involving heavy impurities might exhibit narrow sideband features due to local vibrational modes. On the other hand, narrow lines might be attributed to additional purely electronic transitions. In this context, it is also appropriate to suspect that these lines originate from additional color centers. The properties of the sideband spectra are analyzed in detail in Sec. 5.2.2. Additional investigations on the 820 nm to 845 nm infrared luminescence are presented in Chapter 8. The results indicate that these lines originate from additional electronic transitions of the individual SiV centers.

A common feature of all sideband spectra is that the fluorescence signal strongly diminishes at wavelengths exceeding 850 nm. This is mostly due to a low detection efficiency of the experimental setup in the infrared spectral region: Due to decreasing performance of the spectrometer (grating efficiency, CCD camera sensitivity) as well as a decreasing reflectivity of the steering optics, the detection efficiency at 950 nm

[1] For the randomly oriented NDs, spectra were recorded in a range up to 770 nm only, thus it is not clear weather narrow lines in the region beyond 800 nm could be observed in principle.

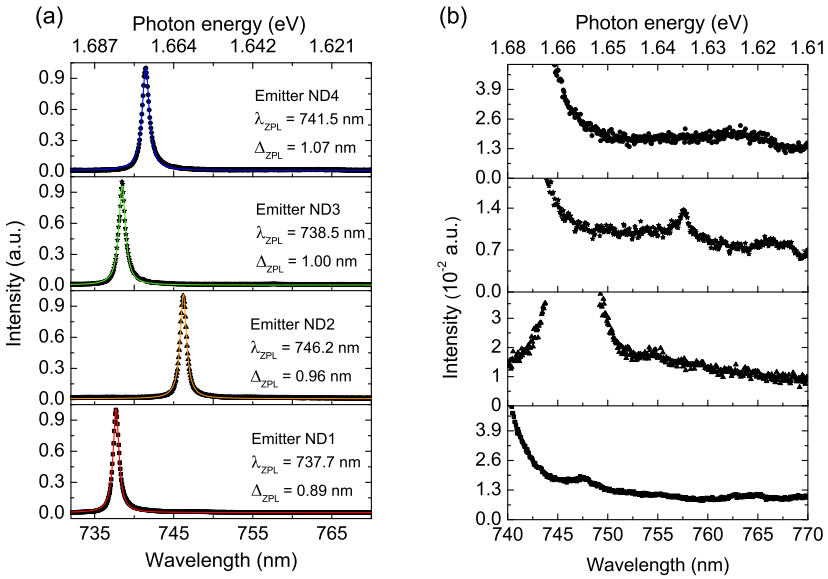

Figure 5.2: Fluorescence spectra of single SiV centers in randomly oriented NDs (samples MFDIA865 and MFDIA943). Emitter ND1-ND3 excited at 671 nm, ND4 at 695 nm. (a) spectra of the ZPL of single SiV centers, λ_{ZPL} gives the peak wavelength of the ZPL, Δ_{ZPL} its FWHM obtained from fitting a Lorentzian line shape. Fit curves are given as solid lines. (b) sideband spectra of the same individual emitters, note the reduced y-scale.

is only approx. 11% of the efficiency at 738 nm. Additionally, the dichroic beamsplitters exhibit reduced transmission in that wavelength region (see Appendix B, Sec. B.1.1 for transmission measurements). The dichroic mirror used for excitation with 695 nm laser light, e.g., is highly reflecting above 890 nm, thus the detection efficiency at 900 nm (950 nm) amounts only to 0.56% (0.25%) of the efficiency at 738 nm. This detection efficiency issue might hinder the detection of the recently reported 946 nm fluorescence of the neutral SiV center [121]. Nevertheless, detecting almost the full SiV center sideband range reported in the literature, up to 830 nm (Energy ZPL − 185 meV), should be possible (compare Tab. 1.1).

5.2.1 Properties of the ZPL

For the application of single SiV centers as single photon source, besides the bandwidth, one has to consider the inhomogeneous spread of line positions observed for single emitters: It ultimately limits the production of indistinguishable photons from different emitters. Figure 5.5(a) displays a histogram of the measured ZPL peak wavelengths in different diamond hosts. The observed wavelengths spread over 20 nm. However, Fig. 5.5(a) reveals a concentration of emitters between 736 nm and 746 nm. For (001) oriented NIs, we find a mean wavelength of 742.6 ± 5.1 nm (error reflects standard deviation). For randomly oriented NDs grown with 1% methane in the growth plasma, we find 739.7 ± 4.1 nm. For NDs grown with a reduced methane fraction (0.4%), the mean ZPL wavelength amounts to 741.2 ± 4.8 nm. Accounting

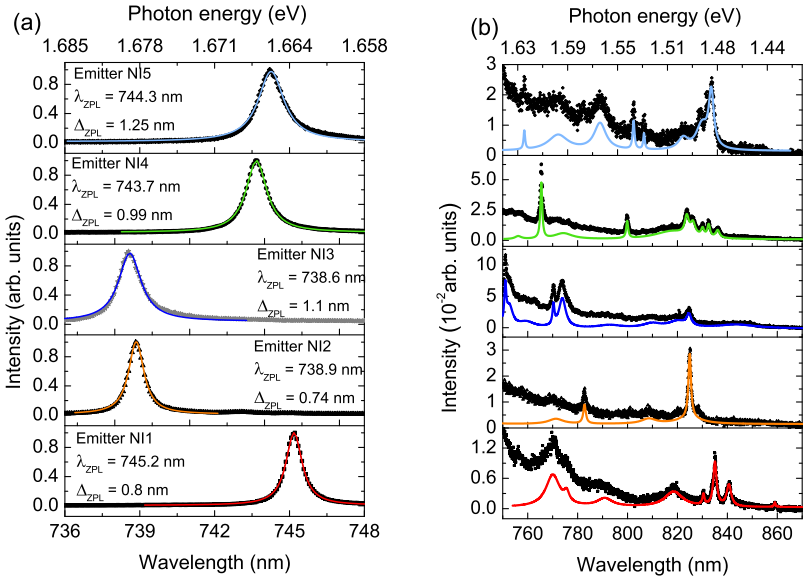

Figure 5.3: Fluorescence spectra of single SiV centers in (001) oriented NIs (sample MF-DIA946), excited at $695 - 696\,\text{nm}$. (a) spectra of the ZPL of single SiV centers, λ_{ZPL} gives the peak wavelength of the ZPL, Δ_{ZPL} its FWHM obtained from fitting a Lorentzian line shape. Fit curves are given as solid lines. (b) sideband spectra of the same individual emitters, note the reduced y-scale. Solid lines are multi peak Lorentzian fits to the baseline corrected data (see text for details).

for these very similar characteristics, Fig. 5.5(a) summarizes emitters from both types of ND samples. For emitters in the heteroepitaxial (001) film, the mean wavelength is $736.7 \pm 2.1\,\text{nm}$, estimated from 9 emitters.

The scatter of peak wavelengths observed is due to environment dependent lineshifts. For ensembles of SiV centers in high quality, low stress homoepitaxial diamond films, we find a room temperature linewidth of 4.5 nm (see Sec. 7.1.1). However, for stressed polycrystalline material, increased ensemble linewidths are reported in the literature (detailed discussion see Sec. 1.3.2). These linewidths reflect the inhomogeneous broadening due to environment dependent lineshifts of the ZPL in the ensemble. Considering single emitters experiencing similar stress, the inhomogeneous broadening of the ensemble ZPL should indicate the distribution of the emission wavelengths of individual emitters. Summarizing the findings in the literature, room temperature ZPL widths up to 15 nm (35 meV) have been reported in PCD films [96]. Often the broadening is accompanied by an asymmetric tail toward longer wavelengths, indicating a preferential red shift [140]. Cryogenic temperature (10 K) linewidths for SiV ensembles in PCD still amount to approx. 4.4 nm (10 meV) [139]. The scatter of line positions and the preferential red shift observed for single centers here is thus comparable to the inhomogeneous broadening of the ZPL of ensembles in PCD. In general, the ZPL position is shifted by stress as demonstrated in Refs. [111, 162] by applying external stress in ⟨100⟩ direction. Additionally, external magnetic (Zeeman effect) or electric fields (Stark effect) might

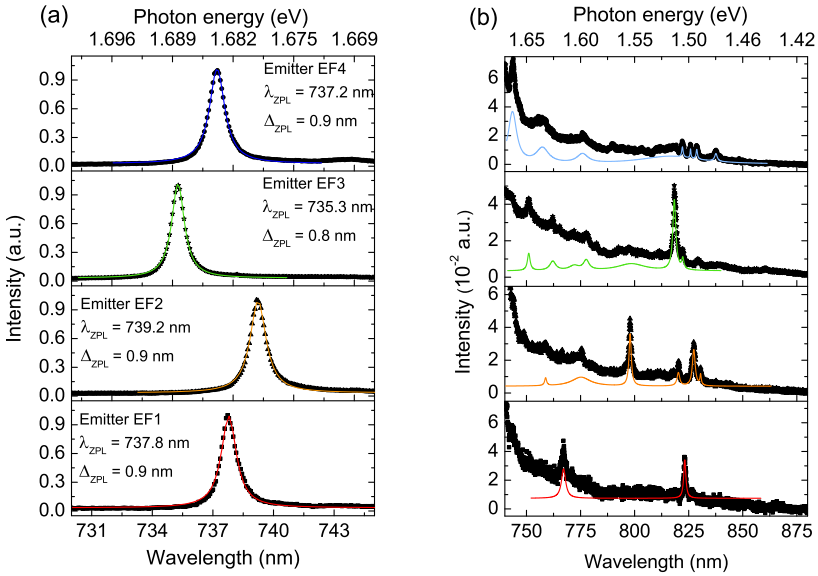

Figure 5.4: Fluorescence spectra of single SiV centers in a (001) oriented epitaxial diamond film (sample MFDIA562_1), excited at 671 nm. Fit curves are given as solid lines. (a) spectra of the ZPL of single SiV centers, λ_{ZPL} gives the peak wavelength of the ZPL, Δ_{ZPL} its FWHM obtained from fitting a Lorentzian line shape. (b) sideband spectra of the emitters individual emitters, note the reduced y-scale. Solid lines are multi peak Lorentzian fits to the baseline corrected data (see text for details).

shift the ZPL. No data on the Stark effect for SiV centers is available in the literature and the Zeeman effect is very weak: In Ref. [162], clear changes in the spectrum are only observed for magnetic fields exceeding 2 T. Thus, residual mechanical stress in the diamond material is most likely the major source for the observed ZPL lineshifts, as also pointed out in the literature [96].

For CVD diamond grown on a non-diamond substrate, several different sources of stress are relevant: First, stress builds up due to the mismatch in the coefficients of thermal expansion of substrate and diamond. For the samples utilized here, the 0.5 mm or 3 mm thick Si substrate is the main source of expansion mismatch, as the other layers in the substrate system (Ir, YSZ) are much thinner (for details on the substrates see Sec. 4.2.4). The substrate induces a biaxial compressive stress[2] of -0.68 GPa in heteroepitaxially grown diamond when the sample is cooled down from deposition temperature to room temperature at the end of the growth process [194]. For the NDs grown on spin coated nanodiamond seeds, it is not clear to which extend the stress due to thermal expansion mismatch affects the NDs: In contrast to the diamond grown heteroepitaxially after bias enhanced nucleation, NDs grown on seeds have a comparably weak adhesion to the Ir substrate. The weak adhesion is evident, as they can be removed from the substrate, e.g., by wiping with a tissue.

[2]Note that throughout this work, compressive stress is denoted with a negative sign, while tensile stress is denoted with a positive sign.

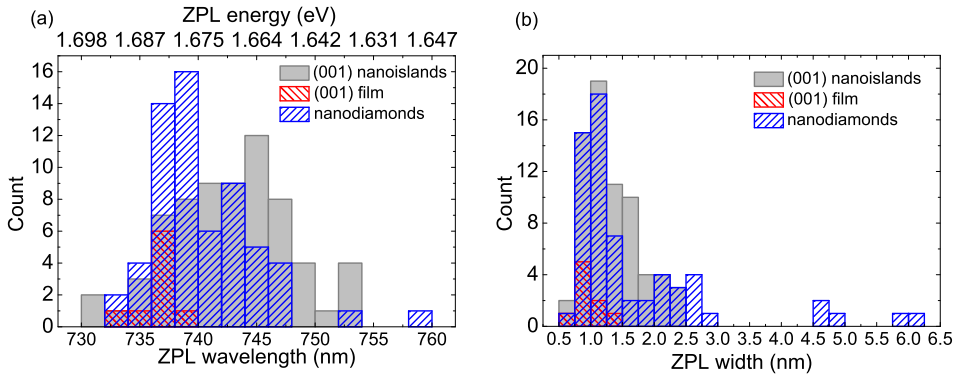

Figure 5.5: (a) Histogram of observed ZPL peak wavelengths of SiV centers in heteroepitaxial (001) oriented NIs, (001) thin film and randomly oriented NDs. (b) Histograms of observed ZPL linewidths. Histograms obtained from NIs takes into account 68 emitters, (001) film 9 emitters, NDs 62 emitters.

Thus, one might conclude that depending on the adhesion of the individual ND, a different stress state arises with complete or partial relaxation of the thermal mismatch stress at the interface. Moreover, for isolated diamond nanostructures (NDs and NIs), in contrast to closed films, a fraction of the imposed stress can relax elastically [204, 205]: For diamond NIs modeled as (truncated) pyramids, where the stressed base of the pyramid is connected to the substrate, simulations find an almost complete relaxation of stress for the tip of the pyramid [204, 205]. Thus, this effect leads to locally varying stress within the crystallites. Furthermore, the stress relaxation depends on the geometry and size of the diamond nanostructures [204, 205], thus also a variation between NIs/NDs with different size and shape is expected. We point out that we do not observed an enhanced stress shift in the closed epitaxial film, which might be expected due to the absence of elastic stress relaxation in the closed film. Nevertheless, this might be misleading due to the low number of emitters investigated in the film in comparison to the NIs/NDs [see Fig. 5.5(a)].

A second contribution specifically important in heteroepitaxial material systems is coherency stress. With the substrate system employed for heteroepitaxy only an imperfect lattice constant matching is obtained: The lattice constant of Ir exceeds the lattice constant of diamond by 7.6%. The model that the growing diamond film adopts the lattice constant of the underlying Ir layer at the interfacial plane (pseudomorphic growth, [204]) is unrealistic: This situation would yield an implausibly high in-plane stress of +89 GPa. As a result, misfit dislocations are introduced already in the initial stage of film growth, thus relaxing misfit stress. The film thickness at which the introduction of dislocations is energetically favored is of the order of 0.5 nm [204]. In Ref. [205], stress analysis of a 0.6 μm thick diamond layer on Ir/$SrTiO_3$(001) yielded a residual coherency stress of +0.9 GPa. Various measurements on 0.5-1 μm thick diamond films on Ir/YSZ/Si(001) indicate even a complete stress relaxation of the diamond films [206].

Growth stress is a third source of stress especially for heteroepitaxial diamond. It results from the interaction of initially isolated epitaxial grains when they merge during lateral growth. For NDs grown on seeds, similarly, crystals growing on different seeds might merge. However, care is taken to avoid this by using fully deagglomerated seeds as well as a low seed density. In PCD films, nearly exclusively tensile growth stress has been reported. It is attributed to attractive forces typically explained in the framework of the grain boundary relaxation model [207]. In Ref. [205], a growth stress of +0.3 GPa was reported. Very recent work identifies growth stress in heteroepitaxial as well as homoepitaxial diamond as highly deposition temperature dependent and related to the progression of dislocations in the diamond film [208]. The partially high values of growth stress found in heteroepitaxial diamond films are correlated to the dislocation density in these films that amounts to $10^8\,\mathrm{cm}^{-2}$ [208].

The previous discussion mainly focussed on *macroscopic stress* in a diamond sample. This macroscopic stress in the sample can be measured, e.g., via x-ray diffraction (XRD) [205] or Raman spectroscopy (shift of the diamond Raman line, e.g., Ref. [149]). However, as already indicated in the discussion of elastic stress relaxation, all these processes also lead to locally varying *micro stress fields*. These micro stress fields lead to line broadening in XRD measurements [205] and Raman measurements (see discussion on page 37 or, e.g, Ref. [179]). Thus, these techniques typically used to measure stress in diamond reveal the spread of the micro stress fields in the probed sample volume, they cannot measure the micro stress at a specific lattice site. However, for individual color centers, the local stress field at the color center site is relevant for the level scheme and the optical transitions of the color centers (for a discussion on NV centers see, e.g, Refs. [209, 210]). In this context, individual color centers are probes for the local stress field. As described in Refs. [211] and [212], during the coalescence of slightly misoriented grains (misorientation $< 2°$, [211]), small angle grain boundaries can be substituted by disclinations, i.e., an assembly of line defects in the crystal [212]. This process takes places when it is energetically favored and partially transforms the misorientation into an elastic deformation of the lattice [212]. Thus, with ongoing growth, the initially individual crystals can continue to grow as one single crystal. The coalescence process involves strong local bending of the crystal lattice yielding high amplitudes of micro stress: In Ref. [212], stress of about 1 GPa is calculated in proximity (distance about 1 μm and smaller) to a disclination. Thus, these microscopic stress fields that arise during the coalescence of epitaxial grains can be comparable to or even higher than the macroscopic stress discussed above. Furthermore, this stress has to be described as a three dimensional stress state [212] with unknown orientation. Besides disclinations, also other extended defects such as dislocations lead to associated micro stress fields [75]. Therefore, also dislocations, e.g., introduced due to the lattice misfit of substrate and diamond can influence color centers.

Former studies [213] revealed a density of $2\times10^{11}\ \mathrm{cm}^{-2}$ epitaxial diamond grains on Ir after bias enhanced nucleation and 10 s growth. According to these observations, we estimate that about 10 grains have merged to form the heteroepitaxial (001) NIs. Due to the high activation energy for the gliding of dislocations in dia-

mond (3.3 eV, [214]), we assume that most of the dislocations/disclinations are still present in the NIs. The same considerations hold for the coalescence of grains in epitaxial thin films. These stress fields are locally experienced by the SiV centers and induce the observed distribution of ZPL positions (see preceding discussion). Similar considerations hold for diamonds grown on seeds: In homoepitaxial CVD diamond growth, dislocations might be introduced due to defects of the diamond substrate (polishing faults, stacking faults, dislocations) [101]. Also for the growth of NDs, it has been found that extended defects from the seed (twinning faults), are transferred onto the growing NDs [193]. Thus, we also expect micro stress fields due to dislocations and other extended defects to be present in the randomly oriented NDs.

For SiV centers, as mentioned before, only one measurement of stress shift rates is reported in the literature: In Refs. [111, 162], stress shifting and quenching of the SiV fine structure at low temperature have been investigated under compressive stress applied in $\langle 100 \rangle$ direction. Shift coefficients ranging from -9 to $8.6\,\mathrm{meV\,GPa^{-1}}$ have been determined for different fine structure components. However, there are neither measurements of shift coefficients at room temperature nor investigations of lineshifts for stress applied in other directions. Thus, we can conclude that the observed spread in ZPL positions is due to varying micro stress fields acting on individual SiV centers in the different diamond host materials discussed above. But as both lineshift coefficients and stress orientations are unknown, we cannot determine the stress field magnitude and thus comparison with measured values of (macro) stress is not feasible.

Figure 5.5(b) displays a histogram of the observed ZPL linewidths. For the NIs, we find $1.3 \pm 0.5\,\mathrm{nm}$, while for the NDs, we find $1.7 \pm 1.2\,\mathrm{nm}$. For the (001) oriented epitaxial film, we find $1.0 \pm 0.2\,\mathrm{nm}$, where again the small number of emitters characterized in the epitaxial film has to be emphasized. The large standard deviation of the linewidth for the NDs is mostly induced by a small number of emitters found with linewidths exceeding 4.5 nm. As not all emitters used in these histograms have been proven to be single emitters, these significantly higher linewidths might occur for NDs with several SiV centers leading to a broadened line. Notably, linewidths of about 5 nm have been reported in the literature for single SiV centers at room temperature [37, 74]. Thus, the linewidths observed here for the majority of SiV centers are significantly lower than the linewidths reported in the literature.

A possible explanation for the observation of a varying linewidth directly relates to the broadening mechanism for the ZPL: According to Refs. [94, 95], quadratic electron-phonon coupling leads to a broadening of the ZPL. As introduced in Sec. 1.3.3, it is commonly assumed that linear and quadratic electron-phonon coupling coefficients are linked by a quadratic relation [see Eqs. (1.3) and (1.4) and associated discussion]. Using this assumption, the linewidth of the ZPL can be expressed in terms of the directly measurable one-phonon-assisted absorption spectrum of the color center, which arises due to linear electron-phonon coupling [see Eq. (7.7)]. However, we did not perform measurements of the absorption of single SiV centers but luminescence measurements. In the absence of quadratic electron-phonon coupling, emission and absorption spectra reveal a mirror symmetry around the ZPL.

In the presence of quadratic electron-phonon coupling, this statement is no longer valid [94]. We thus cannot derive the absorption spectrum from the measured emission spectrum. Nevertheless, it can be reasonably assumed that significant changes in the emission spectrum will also influence the absorption spectrum: In Ref. [142], the author points out that the integrated intensity of emission and absorption sideband spectrum is equal even if mirror symmetry is lacking. We find strongly varying sideband spectra for different emitters (see next section) indicating a locally varying electron-phonon coupling and/or changes in the phonon density of states. For the broadening of the ZPL, the phonon density of states and the thermal occupation probability of the phonon modes have to be taken into account [see Eq. (7.5)], thus low energy phonon modes stronger contribute to ZPL broadening as high energy phonon modes. As discernible from Figs. 5.2-5.4, also the low energy sideband spectrum (close to the ZPL) is subject to significant variations for individual emitters. However, Eq. (7.7) is derived using the assumption that no local modes have to be taken into account. As the low energy modes of the SiV center are assigned to be local modes, it is questionable if Eq. (7.7) can be used to fully describe the system. However, no exact expression linking linewidths and measured sideband spectra has been derived in the literature. Ref. [215] successfully applies Eq. (7.7) to describe the temperature dependent linewidth of several color centers (e.g., NV centers) even if low energy local modes are obviously responsible for the broadening. Thus, we conclude that the changes in the sideband spectrum indicate a change in quadratic electron-phonon coupling and can be at least qualitatively linked to the varying linewidth. From the preceding discussion, we derive that the ZPL linewidth of the SiV centers depends on the local environment. A more quantitative analysis of the sideband spectra, including a discussion of the correlation of ZPL linewidth and sideband spectra, is included in the next section.

Taking into account the findings discussed above, we tentatively attribute the reduced linewidths found in our experiments, compared to previous experiments, to an altered electron-phonon coupling or changes in the phonon density of states: Previous investigations on single SiV centers were carried out using SiV centers created via deep, high energy (MeV) ion implantations into natural diamonds [37,74]. Ion implantation induces damage in the diamond lattice (e.g. vacancies, carbon interstitials). Annealing steps serve to reduce this damage. However, as investigated in Ref. [181] via Raman spectroscopy, some implantation induced defects and their respective phonon modes are particularly temperature stable: E.g., a di-vacancy-related defect anneals out only at temperatures above 1200 K. Even annealing at 1473 K does not suffice to restore the diamond Raman linewidth of the un-implanted diamond. This indicates the presence of residual defects that broaden the Raman line [181] (discussion of Raman line broadening see page 37). Raman spectroscopy only reveals phonon modes with vanishing momentum; however, changes in the Raman spectrum might also indicate further changes in the phonon density of states. Thus, the resulting phonon density of states effectively coupled to individual SiV centers might be different in ion implanted diamond and in CVD diamond with *in situ* formed centers. However, we point out that also in Ref. [74], centers with significantly reduced linewidth emitting in the spectral range of SiV centers were

observed (e.g., peak 736.8 nm, width 1.3 nm) but not identified as SiV centers. This might also indicate a varying electron-phonon coupling. As discussed in Chapter 7, we here unambiguously identify low linewidth single centers as SiV centers by low temperature spectroscopy.

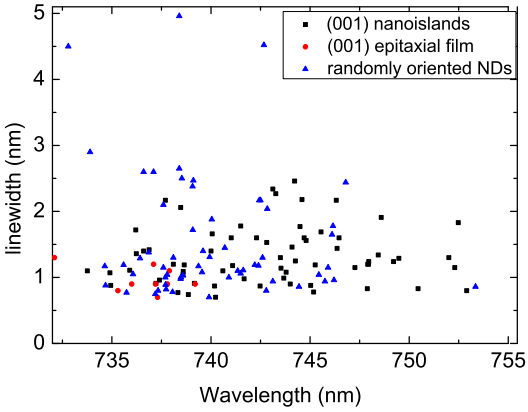

Figure 5.6: Plot of ZPL width versus ZPL peak wavelength for emitters observed in an (001) epitaxial film, as well as (001) NIs and randomly oriented NDs, data also shown in Fig. 5.5

In the preceding discussion, the spread of linewidths and peak wavelengths as well as the mechanisms leading to these inhomogeneous effects have been discussed. The question arises, whether these mechanisms are coupled, i.e., if the peak wavelength of the ZPL influences its linewidth. Figure 5.6 shows the ZPL linewidths versus their peak wavelengths. From Fig. 5.6, no correlation between linewidth and peak wavelength is obvious. Thus, the mechanisms shifting the ZPL and broadening it, seem to be independent.

Summarizing this section, we find that single SiV centers in NDs, NIs and thin heteroepitaxial diamond films reveal intense, narrow ZPLs. The spread of ZPL peak wavelengths amounts to approx. 20 nm and is therefore comparable to inhomogeneous linewidths observed for SiV ensembles in PCD films. We attribute the observed distribution of wavelengths to local stress fields at the sites of the SiV centers and identify stress sources, especially extended crystal defects. ZPLs as narrow as 0.7 nm are found, thus SiV centers display the lowest room temperature linewidth observed at present. These spectral properties render SiV centers promising candidates for room temperature single photon sources. Future investigations will have to address the distribution of emission wavelengths with the aim of producing photons with identical wavelength from different emitters. First, stress reduction in the diamond may be achieved by annealing and thus narrow the wavelength distribution [140]. Second, tuning procedures using external fields may be implemented [35].

5.2.2 Linear electron-phonon coupling: vibronic sidebands

As visible from Figs. 5.2(b), 5.3(b) and 5.4(b), the vibronic sidebands of individual SiV centers vary significantly: The position of the sideband features as well as the relative intensity differ, witnessing preferential coupling to different modes as well as possible shifts of mode frequencies. These observations are in accordance with several reports in the literature hinting at an environment dependent electron-phonon coupling for the SiV center, i.e., washed-out sideband features for larger ensembles

and sideband features found only in limited areas on samples. For a detailed discussion, see page 17. The sideband features reported in the literature are summarized in detail in Tab. 1.1. Commonly, for the SiV center low energy local modes at approx. 40 meV and 65 meV are observed. In the energy region of lattice modes, coupling has been mainly reported to three modes with energy 125 meV, 155 meV and 165 meV. In the region exceeding the lattice phonon energies, local modes around 185 meV have been predicted by simulations. Figure 5.7(a) displays a histogram of the observed sideband features for emitters in the (001) NIs as well as the (001) heteroepitaxial film. The positions of the features are deduced from the fluorescence spectra via a multi peak Lorentzian fit to baseline-corrected spectra. Figures 5.3(b) and 5.4(b) show examples of these fits. Subtracting a baseline is necessary due to broadband background fluorescence especially in the heteroepitaxial film. First, subtracting the baseline enables the multi-peak fitting. Second, it enables estimating the intensity of the sidebands as discussed below. The investigation of NDs or NIs that do not contain SiV centers reveals that the background fluorescence within the measured spectral interval is significantly stronger at shorter wavelengths and decays toward longer wavelengths. Furthermore, the background level is different for individual NIs or NDs. We thus estimate the baseline from the spectrum using up to 8 anchor points that are connected by straight lines.[3] As a control for the subtracted baseline, we verify that the sideband features are observed on a flat baseline after the subtraction. The observed sidebands reflect all sideband features observed for ensembles (cf. Tab. 1.1). Due to the low overall emission into the sidebands and thus a low overall linear electron-phonon coupling, we consider all features to be due to one-phonon processes (discussion see page 15). We do not observe a clear concentration on distinct sideband energies, except around 170 meV to 180 meV. Low energy local modes around 30 meV to 40 meV, as well as high energy local modes beyond 165 meV are observed. For the first time, we experimentally observe high energy sidebands above 180 meV predicted by simulations (Ref. [143]). In the energy range of lattice phonons, we find only a weak concentration around the critical points (see Sec. 1.3.3). We interpret the observed spread in sideband energies in terms of a varying electron-phonon coupling. As mentioned above, a varying electron-phonon coupling has been reported in the literature for ensembles. The findings are summarized in Sec. 1.3.3. The observations include spectrally washed-out sidebands for large ensembles, whereas distinct sideband features are found upon excitation of small sub-ensembles [112]. Other authors report sidebands that are only found in certain areas on a homoepitaxial sample [111]. We thus conclude that the strongly varying sideband spectra identified for single SiV centers are in accordance with previous ensemble investigations and reflect the 'inhomogeneous electron-phonon coupling' of the SiV centers.

Figures 5.2(b), 5.3(b) and 5.4(b) reveal several spectral features in the sideband region with linewidths comparable to the ZPL. Figure 5.7(b) summarizes the sideband features and their respective widths. An accumulation of narrow features is observed in the spectral range 820 nm to 840 nm. For these very narrow features,

[3] Polynomial interpolation between the anchor points has been tested for several emitters and applied in the evaluation for one emitter, but does not lead to considerably different results.

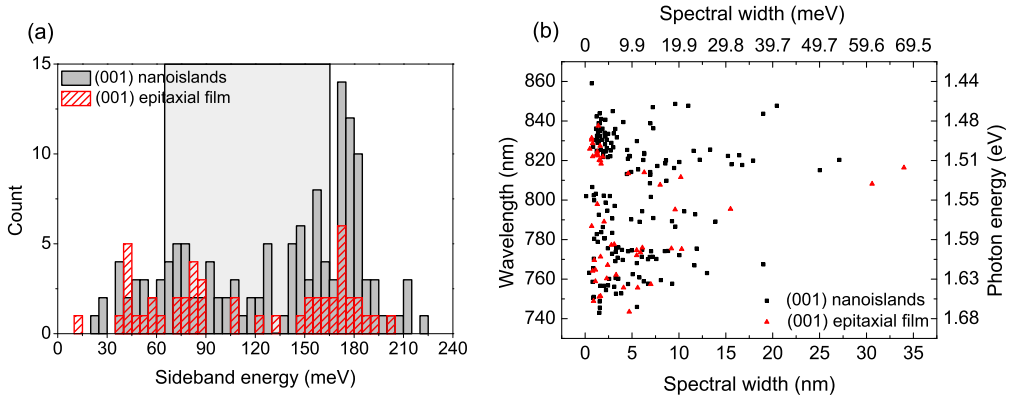

Figure 5.7: (a) Histogram of observed sideband features taking into account emitters observed in the (001) NIs and the (001) epitaxial film. The shaded region indicates the energy range of lattice modes. (b) Width of the observed sideband features plotted versus wavelength (photon energy) of the features. Black squares label features from emitters in (001) NIs, red triangles feature from the (001) epitaxial film Note that the scale for the width in meV gives only approximate values calculated for an absolute energy of 1.57 eV.

it is not clear whether they represent vibronic sideband transitions or additional purely electronic transitions: For color centers involving heavy impurities, the sideband features due to local modes can be as narrow as the ZPL itself [25]. However, an electronic origin of these lines has been suspected in former studies due to the significant narrowing of the lines upon cooling [115]. Recently, strong evidence for the origin of these lines due to electronic rather than vibronic transitions has been reported in the literature: In Ref. [121], absorption of diamond samples containing high densities of SiV centers at wavelengths between 830 nm and 860 nm has been found. Only for purely electronic transitions, emission and absorption occur at the same wavelength (see discussion on page 14). Thus, the results in Ref. [121], together with the observation of narrow fluorescence lines at comparable wavelengths, strongly indicate the existence of electronic transitions of SiV centers at wavelengths between 830 nm and 860 nm. Also for these electronic transitions, a shifting due to local stress is plausible, explaining the spread of wavelengths of the narrow features observed for single centers (for a discussion of the cause of local stress fields, see Sec. 5.2.1). However, it should be emphasized that taking into account only the room temperature luminescence spectra of single centers discussed here, an identification of the lines as electronic transitions is not possible. Further investigations on this narrow near-infrared luminescence will be performed in Chapter 8. For the following discussion of the strength of the electron-phonon coupling, narrow features throughout the sideband spectrum are assumed to be vibronic sidebands, thus potentially leading to an overestimation of the electron-phonon coupling.

The width of the sideband features can also be interpreted in terms of phonon lifetimes [9]. Assuming that the linewidth of the features is due to lifetime broadening [see Eq. (7.8)], we find phonon lifetimes between 0.4 ps (width 0.8 nm) and

approx. 0.02 ps (15 nm). The lifetimes have been calculated for the given width in nm and a center wavelength of 780 nm. These short lifetimes indicate fast vibrational relaxation, most probably also in the excited state. The occurrence of fast excited state relaxation (typically in large molecules) is known as Kasha's rule [9] and is crucial for the description of the excitation processes of single color centers (see Sec. 5.3.2). The short lifetimes indicate that the vibrationally excited states of the SiV centers have even shorter lifetimes than the optical zone center Raman phonon in diamond: In Ref. [216], a lifetime of up to 7 ps is observed for the Raman phonon in diamond.

The strength of the linear electron-phonon coupling is measured either by the Debye-Waller factor (DW) or the Huang-Rhys factor (S). The Debye-Waller factor DW is defined as the integrated luminescence intensity of the ZPL I_{zpl} divided by the integrated luminescence intensity of the color center I_{tot} [27]. The Huang-Rhys factor S is defined by $\frac{I_{zpl}}{I_{tot}} = \exp(-S)$ [84]. DW approaches one for emitters with very low electron-phonon coupling, the higher DW the lower the electron-phonon coupling is. S directly measures the strength of the electron-phonon coupling, for an emitter with full emission into the ZPL it equals zero. It should be noted that for color centers with strong electron-phonon coupling S exceeds one. To obtain S and DW from the spectra, we use baseline-corrected data to avoid background contributions. Nevertheless, due to the possibly incomplete background correction as well as the restricted wavelength range[4] and the fact that the spectra have not been corrected for the detector and monochromator efficiency that vary in the investigated spectral window, the values of S and DW have to be considered as an estimate.

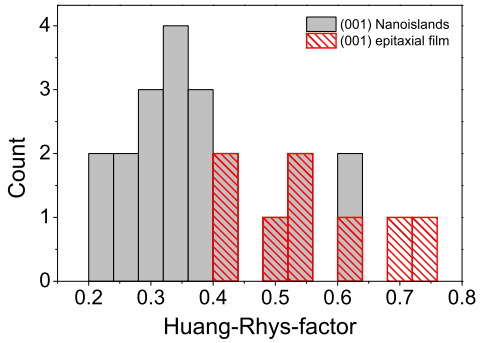

Figure 5.8: Histogram of calculated Huang-Rhys factors S taking into account emission up to 875 nm. For the calculation, baseline-corrected data has been used.

In the following, we try to estimate the error due to a varying detection efficiency. The detection efficiency at 875 nm is only 49% of the efficiency at 740 nm. We furthermore assume that the detection efficiency decreases linearly between 740 nm and 875 nm which is a good approximation taking into account the efficiency curves for the employed grating and the CCD camera. For a sideband spectrum with constant intensity over the spectral range from 740 nm to 875 nm, this variation in detection efficiency then leads to a measured integrated sideband intensity that is 26% too low. Further assuming that on average about 70% of the fluorescence light is concentrated in the ZPL (see discussion below), this error in the integrated sideband

[4](only data up to 875 nm are taken into account due to the low detection efficiency at longer wavelengths)

intensity leads to a DW factor that is underestimated by 6%. We thus conclude, that the main uncertainty for the DW factor (and thus also for the Huang-Rhys factor) stems from the background substraction performed using a baseline correction in the spectra. For this contribution, we cannot estimate whether the phonon sideband contributions are over or underestimated. Figure 5.8 displays the Huang-Rhys factors S calculated for the emitters observed in (001) NIs and in an (001) heteroepitaxial film. For SiV center ensembles, $S = 0.24 \pm 0.02$ is reported in absorption [118]. The observed values of S in the NIs are slightly higher than previously reported for ensembles, the mean value is 0.38 with a standard deviation of 0.12. For the emitters in the heteroepitaxial film, we find 0.56 with a standard deviation of 0.12. This further increased value of S might be partially due to the stronger background contributions in the epitaxial film and their incomplete subtraction. For the majority of the SiV centers, however, more than 70% of the fluorescence is concentrated in the ZPL, thus rendering these SiV centers especially suitable as low bandwidth emitters.

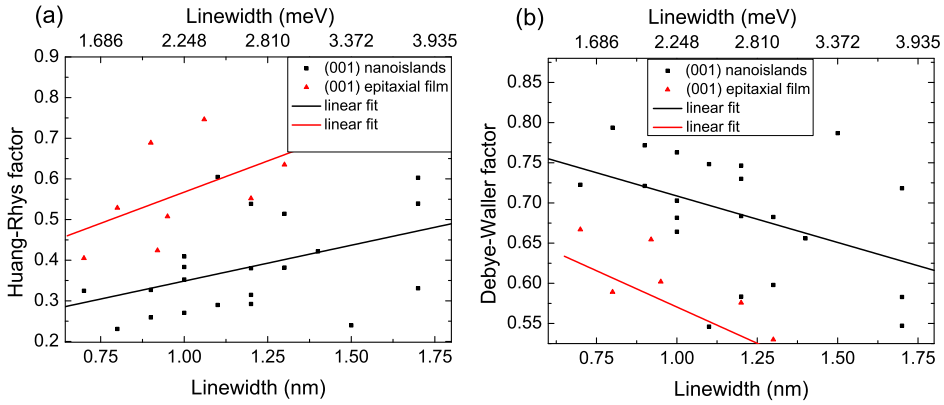

Figure 5.9: Correlation between linear electron-phonon coupling and linewidth (a) Huang-Rhys factors S of emitters from (001) NIs and (001) epitaxial film (b) analogous for the Debye-Waller factors DW. Note that the linewidth in meV has been calculated assuming the mean peak wavelength for emitters in NIs (742.6 nm). Nevertheless, the deviation of the values using the mean wavelength from the film (736.7 nm) is less than 2%.

Quadratic electron-phonon coupling, as introduced in Sec. 1.3.3, influences the linewidth of the ZPL. As outlined in detail in Secs. 1.3.3 and 7.2.2, a quadratic relation between linear and quadratic electron-phonon coupling coefficients is commonly assumed [see Eqs. (1.3) and (1.4) and associated discussion]. Under this assumption, the ZPL linewidth can be calculated taking into account the spectral shape of the one-phonon-assisted absorption transitions of the color center as well as the population of the respective phonon modes. Data on the absorption of single SiV centers is not available. The Huang-Rhys factor S or the Debye-Waller factor DW, in contrast, measure the 'integrated' linear electron-phonon coupling. Taking into account the relation between quadratic and linear electron-phonon coupling, a higher value of $S(DW)$ can indicate a higher quadratic electron-phonon coupling

and thus a higher linewidth. In Ref. [142], an enhancement of up to 15% for DW due to quadratic electron-phonon coupling is suggested. Hence, we try to use the Huang-Rhys factor S and the Debye-Waller factor DW to illustrate a correlation between electron-phonon coupling and room temperature ZPL linewidth. Figure 5.9(a) displays a plot of the ZPL linewidth versus S, while Fig. 5.9(b) plots the linewidth versus DW. In both plots, a similar trend is observed: lower integrated, linear electron-phonon coupling (DW closer to one, lower S) leads to a lower room temperature linewidth of the ZPL. In the plots, this trend is indicated by linear fits. This observation supports the explanation of the varying ZPL width as a consequence of varying electron-phonon coupling in the individual local environments.

5.3 Population Dynamics

The following section discusses the population dynamics of single SiV centers. Single emitter nature of the observed color centers is proven via intensity auto-correlation ($g^{(2)}$) measurements. First, we discuss saturation measurements including maximum photon rates and saturation powers. Second, intensity dependent $g^{(2)}$ measurements are used to identify the level scheme suitable to describe the SiV centers including an estimation of the transition rate coefficients. The last part of the section addresses the collection efficiency for the fluorescence of single SiV centers in NDs on Ir as well as the quantum efficiency of the color centers.

5.3.1 Saturation measurements

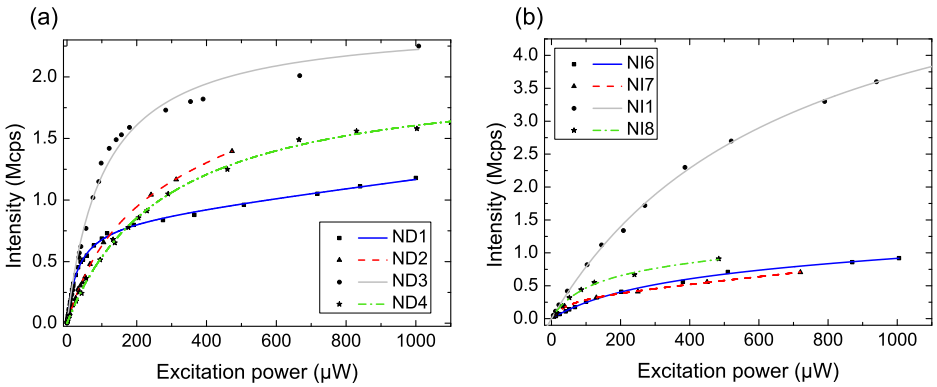

Figure 5.10: Saturation curves (a) emitters in randomly oriented NDs, (b) emitters in (001) NIs. For the randomly oriented NDs, excitation at 671 nm was employed, for the (001) NIs an excitation wavelength of 695-696 nm was used.

An important figure of merit for a single photon source is the photon count rate obtained at saturation. Figure 5.10 exemplarily displays saturation curves of four emitters observed in randomly oriented NDs as well as (001) NIs. Note that the curves have been measured using the optimized excitation polarization (for discus-

sion see Sec. 6.1). Further saturation measurements have been published in Ref. [38]. In principle, the count rate I as a function of the excitation power P is described by

$$I = I_\infty \frac{P}{P + P_{sat}}. \tag{5.1}$$

Fitting parameters are the saturation power P_{sat} and the maximum photon rate I_∞. Note that in Eq. (5.1) I becomes zero for vanishing excitation power P. In the experiment, if the excitation laser source is blocked from entering the setup, about 600 cps are observed. This is mainly due to the dark counts of the APDs. This count rate has been subtracted from all measured values in the saturation curves. As visible, e.g., for emitter ND1 in Fig. 5.10(a) the photon count rate does not asymptotically reach a constant value as suggested by Eq. (5.1). In contrast, it linearly increases at high excitation power. This trend suggests that background fluorescence is present. For a detailed discussion of the origin of the background fluorescence see Sec. 5.3.2. This fluorescence, in contrast to the single emitter fluorescence, does not exhibit saturation but increases linearly with excitation power. To account for the background fluorescence from the diamond host material, we thus add a linear term to Eq. (5.1):

$$I = I_\infty \frac{P}{P + P_{sat}} + c_{backgr} P. \tag{5.2}$$

Figure 5.10 displays fits using Eq. (5.2). As obvious from Fig. 5.10, a distribution of saturation powers P_{sat} and maximum photon rates I_∞ is observed in both sample types investigated. Figure 5.11 summarizes the values of P_{sat} and I_∞ observed for single SiV centers. We find a mean value for I_∞ of 1.5±1.4 Mcps in the randomly oriented NDs and of 1.5±2 Mcps in the (001) oriented NIs. The high standard deviation illustrates the variation in brightness of the emitters. The cause of this large spread of brightness will be discussed in detail in Secs. 5.3.2 and 5.3.4. The highest saturation count rate I_∞ obtained from the fits is 6.2 Mcps. Thus, the single emitters observed here are the brightest color centers to date under continuous laser excitation, surpassing recently investigated single photon sources based on chromium color centers delivering a maximum of 3.2 Mcps [36].

Apparently, also the saturation power P_{sat} varies for different emitters. Figure 5.11(b) displays the saturation intensity obtained for the emitters. The highest value observed is 692 μW, the lowest 14.3 μW. The mean value is $105 \pm 103\,\mu$W for the NDs and $175 \pm 229\,\mu$W for the NIs. Thus, assuming that the SiV centers in the samples exhibit similar excitation properties, one might conclude that the excitation with 671 nm used for the NDs is slightly more efficient compared to the excitation at 695-696 nm used for the NIs. In either case, the observed saturation power is significantly smaller compared to previous studies on single SiV centers implanted into natural diamonds: Wang et al. [37] report a saturation power of 6.9 mW for an excitation wavelength of 685 nm (with comparable or even tighter focussing of the excitation laser). We thus conclude, that the SiV centers observed here are more efficiently excited. First, this might be related to local field enhancements at the site of the color centers: As discussed on page 4, resonant modes of the light field can develop in (spherical) NDs with sizes comparable to the wavelength

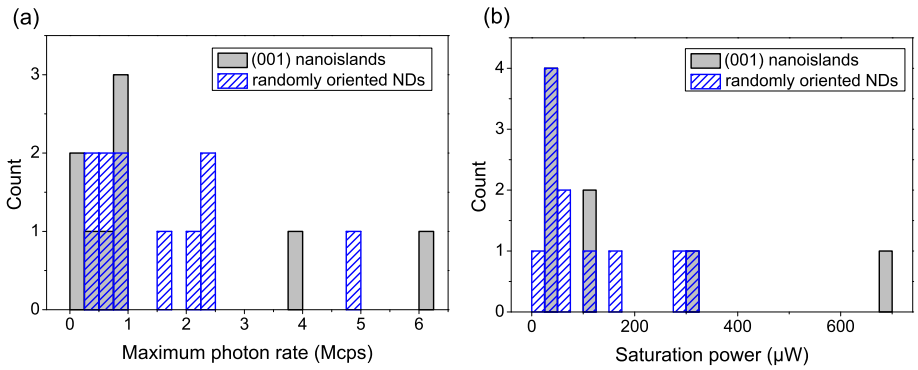

Figure 5.11: Histograms of (a) maximum obtainable photon rates at saturation I_∞ (b) saturation powers P_{sat}. Histograms take into account emitters from randomly oriented NDs and (001) NIs. For the randomly oriented NDs, excitation at 671 nm was employed, for the (001) NIs an excitation wavelength of 695-696 nm was used.

of the excitation/fluorescence light. Ref. [50] points out that the excitation laser light is coupled into such modes of the particle and the resulting field distribution excites the color center. Depending on the position of the color center in the mode field, it experiences a high or low excitation light intensity. This in turn leads to a very efficient excitation if the color center is situated close to an antinode of the field, whereas a significantly less efficient excitation is observed if the color center is situated close to a node of the mode field. The enhanced or reduced intensity, compared to the situation in bulk diamond where the Gaussian focus of the laser determines the local intensity, leads to a lower or higher saturation power. This effect cannot be distinguished from a higher or lower absorption coefficient as the consequence, i.e., a change in saturation power, is exactly the same. However, we point out that as the NDs/NIs used here are not spherical, the formalism used in Ref. [50] cannot be used to calculate and prove the existence of similar modes. The procedure to locate single SiV centers described in Sec. 5.1 would preferably select centers experiencing high local intensity and thus efficient excitation as they appear much brighter in fluorescence maps. Thus, we might observe a more efficient excitation of the SiV centers, even if the local fields discussed above are also capable of leading to a less efficient excitation.

A second cause for a reduced saturation power might be an enhanced absorption coefficient. This enhanced absorption coefficient might, for our experiments, relate to a change in linear electron-phonon coupling: The ground state of the SiV center was reported about 2.05 eV below the conduction band edge [131, 138]. This excludes an excitation of the color center's electrons into the conduction band for our 1.78 eV (695 nm) or 1.85 eV (671 nm) excitation. The excitation, therefore, most probably takes place into excited vibrational states in the electronically excited state. As discussed in Sec. 5.2.2, we observe strongly varying vibronic sideband spectra in emission together with a varying overall emission into the sideband spectrum (Huang-Rhys and Debye-Waller factor). However, as also discussed in Sec.

5.2.2, these changes in the emission spectrum also indicate changes in the absorption spectrum, thus possibly leading to a change in the absorption coefficient for a given excitation wavelength. The excess energy, i.e., the difference between photon energy of the excitation laser and photon energy of the ZPL fluorescence, is approx. 168 meV for 671 nm excitation and 104 meV for 695 nm excitation. These energies correspond to sidebands associated with one-phonon-assisted transitions for the SiV center [see Tab. 1.1 and Fig. 5.7(a)]. Thus, for the low Huang-Rhys and Debye-Waller factors observed, these transitions should have a high probability (compared to transitions to higher vibrationally excited states, see discussion in Sec. 1.3.3). In previous work by Wang [37,74], no sideband spectra were recorded precluding direct comparison.

5.3.2 Intensity auto-correlation ($g^{(2)}$) measurements

To investigate the population dynamics of the color centers as well as to prove the single emitter nature of the observed color centers, we employ the intensity auto-correlation function ($g^{(2)}$ function). The measurements of the $g^{(2)}$ function are performed using the Hanbury Brown and Twiss setup (HBT) setup introduced in Chapter 3. The $g^{(2)}$ function of a two level system can be derived quantum mechanically. The derivation can be found in standard quantum optics textbooks, e.g., Ref. [217] and is not reproduced here. Classically, the $g^{(2)}$ function for a source with constant average intensity is defined by [9, 218]:

$$g^{(2)}(\tau) = \frac{\langle I(t)I(t+\tau)\rangle}{\langle I(t)\rangle^2}. \tag{5.3}$$

Where $\langle\rangle$ denotes temporal averaging. $I(t)$ is the intensity at time t, while $I(t+\tau)$ is the intensity at time $t+\tau$. To represent the correlation function for light emitted by a single emitter, Eq. (5.3) has to be rewritten using the number of photons or photon detection events n, that is proportional to the classical intensity [218]:

$$g^{(2)}(\tau) = \frac{\langle n(t)n(t+\tau)\rangle}{\langle n(t)\rangle^2}. \tag{5.4}$$

For a two-level system, $g^{(2)}(\tau)$ represents the probability to detect two photons separated by a time interval τ. The $g^{(2)}$ function of a two level system can be expressed as [217]:

$$g^{(2)}(\tau) = 1 - e^{-|\tau|/\tau_0}, \tag{5.5}$$

where τ_0 is a constant. More precisely, the $g^{(2)}$ function can be interpreted as follows: Whenever a photon is detected, the observed quantum system has undergone a transition to the ground state to emit the photon (it has been projected to the ground state). To emit a consecutive photon, the system has to undergo an additional cycle of excitation and relaxation. This process takes a certain time. This fact is evident in Eq. (5.5): For $\tau = 0$, $g^{(2)}(\tau)$ vanishes indicating that no two photons can be detected simultaneously. This dip in the $g^{(2)}$ function for τ close to zero is termed *photon-antibunching* and indicates the presence of a single emitter. For times τ large compared to τ_0, $g^{(2)}$ approaches a constant values of one [see Eq. (5.5)].

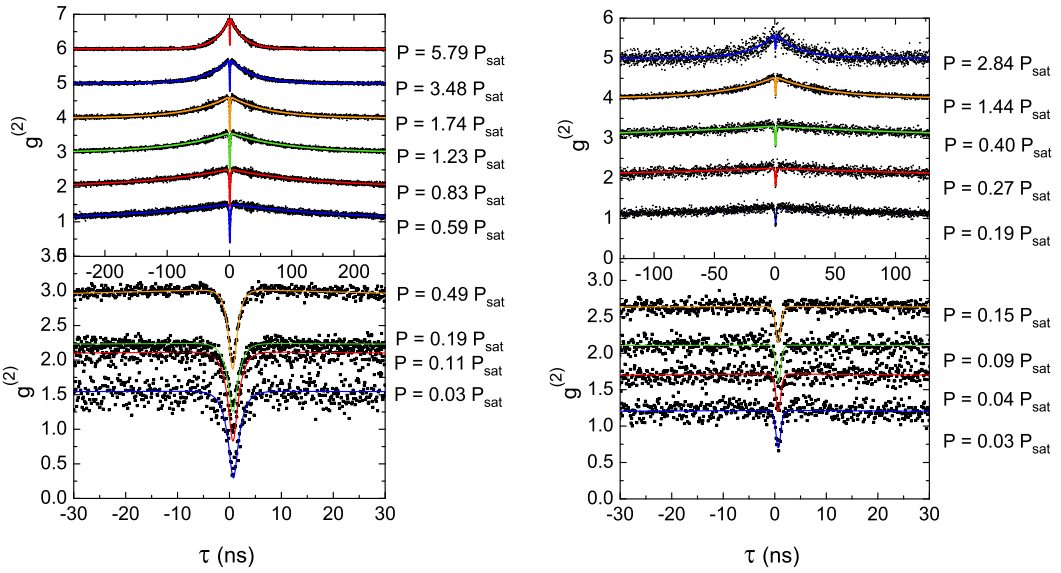

(a) $g^{(2)}$ functions for different excitation powers for emitter ND3. $g^{(2)}$ functions fitted without background correction. Excitation 671 nm.

(b) $g^{(2)}$ functions for different excitation powers for emitter ND2. $g^{(2)}$ functions fitted including background correction. Excitation 671 nm.

Figure 5.12: $g^{(2)}$ functions for varying excitation power fitted with Eq. (5.9) or (5.17) convoluted with the instrument response function. Note that consecutive $g^{(2)}$ functions have been shifted for clarity. The lowest excitation power $g^{(2)}$ function in each graph has not been shifted, the higher excitation power $g^{(2)}$ functions are shifted by 1 each, the lower excitation power functions are shifted by 0.5 each.

Figures 5.12 and 5.13 display $g^{(2)}$ functions of the fluorescence emitted by single SiV centers in randomly oriented NDs as well as oriented NIs. The $g^{(2)}$ functions are measured at different excitation powers P given in units of the respective saturation power P_{sat}. Also for the emitters found in the (001) epitaxial film, $g^{(2)}$ functions have been measured. These $g^{(2)}$ functions will not be discussed here as they are often strongly influenced by background fluorescence (see discussion below).

Figures 5.12 and 5.13 show normalized $g^{(2)}$ functions. From the raw data, we first obtain a histogram of events with a certain delay τ. This histogram is proportional to the $g^{(2)}$ function, to obtain the $g^{(2)}$ function it has to be normalized. Normalization of the $g^{(2)}$ function can be accomplished by two standard methods [218]: First, comparison with the number of histogram events for a classical Poissonian light source ($g^{(2)}(\tau) = 1$ for all delays τ) with count rate equal to the count rate of the investigated light field can be used for normalization [23]: For long measurement times T, with count rates N_1 and N_2 on the detectors in the HBT setup, a constant number of $N = TN_1N_2w$ detection events will be found in any histogram bin of width w for a Poissonian source. Dividing the measured number of histogram events in each time bin by N yields the normalized $g^{(2)}$ function. Second, the histogram can be normalized assuming that $g^{(2)}(\tau) = 1$ for long delay times τ. The first method has been tested but fails for the $g^{(2)}$ functions measured for the fluorescence of single

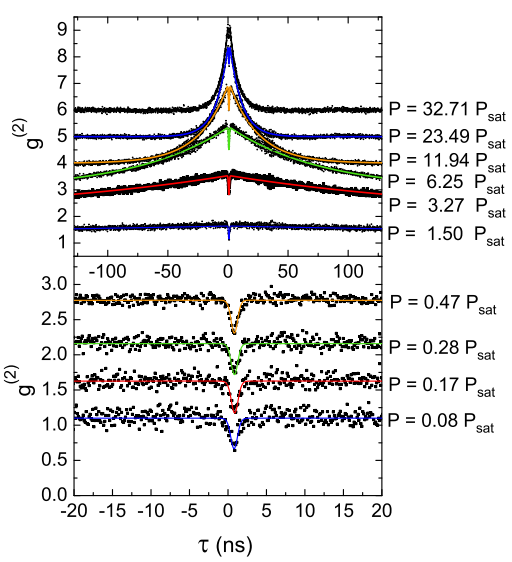

(a) $g^{(2)}$ functions for different excitation powers for emitter ND1. $g^{(2)}$ functions fitted without background correction (discussion see text.) Excitation 671 nm.

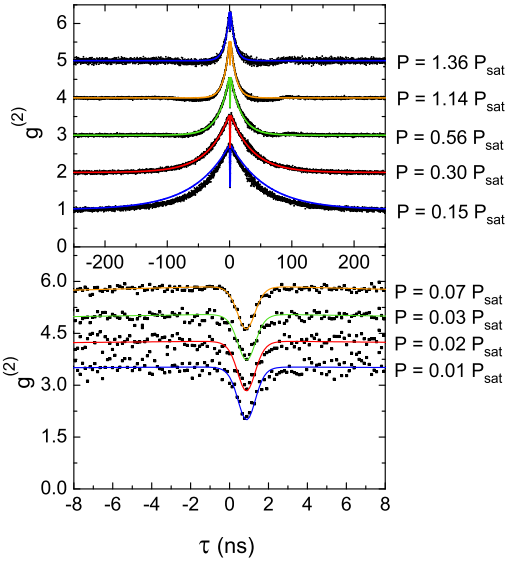

(b) $g^{(2)}$ functions for different excitation powers for emitter NI1. $g^{(2)}$ functions fitted without background correction. Excitation 695 nm.

Figure 5.13: $g^{(2)}$ functions for varying excitation power fitted with Eq. (5.9) or (5.17) convoluted with the instrument response function. Note that consecutive $g^{(2)}$ functions have been shifted for clarity. The lowest excitation power $g^{(2)}$ function in each graph has not been shifted, the higher excitation power $g^{(2)}$ functions are shifted by 1 each, the lower excitation power functions are shifted by 0.5 each.

SiV centers: As discussed below, the measured $g^{(2)}$ functions strongly deviate from the $g^{(2)}$ function of a Poissonian light source ($g^{(2)}(\tau) = 1$ for all delay times τ). The $g^{(2)}$ function exceeds one for a significant fraction of the examined delay times τ, thus normalization using the comparison to a Poissonian light source fails. However, for long delay times τ, we find that the number of histograms events converges to a constant value, the histograms become flat. This is visible, e.g., in Fig. 5.13(a) especially for higher excitation powers. Thus, we perform the normalization by dividing the number of histogram events in each tim bin by the average number of histogram events in this long delay region, thus setting the long delay limit for $g^{(2)}$ to one.

For all displayed $g^{(2)}$ functions, the discussed dip in the $g^{(2)}$ function (antibunching) is observed close to zero delay. Three observations contrasting with the discussion above are evident:

- $g^{(2)}$ does not directly converge to one, but exceeds one for intermediate delay times τ and converges to one for long delay times τ. Note that consecutive $g^{(2)}$ functions in Figs. 5.12 and 5.13 have been shifted for clarity, see figure caption for details. The effect of $g^{(2)}$ exceeding one is differently pronounced for the emitters, e.g., for emitter ND2 [Fig. 5.12(b)] it is comparably weak,

while for emitter ND1 [Fig. 5.13(a)] it is much stronger. It is also clear from the $g^{(2)}$ functions that deviations of $g^{(2)}$ from one are more pronounced for higher excitation powers.

- Despite revealing an antibunching behavior, $g^{(2)}(0)$ does not vanish. Especially for emitter NI1 [Fig. 5.13(b)], $g^{(2)}(0)$ is not close to zero. For higher excitation powers, especially for emitters NI1 and ND1 the dip in the $g^{(2)}$ function mostly vanishes.

- The minimum of the $g^{(2)}$ functions does not exactly coincide with $\tau = 0$ as visible especially in the plots showing a narrow range of delay times τ. This is due to a systematic error in the measurements, i.e., different signal run-times for the detector signals in the HBT setup. In the fits to the $g^{(2)}$ functions, this has been taken into account by introducing an offset τ_{off} for the delay time. The parameter τ_{off} is treated as a free parameter in the fits and has been found to be constant within fitting errors. As this effect is not important for the further discussion, τ_{off} is not explicitly given in all following equations and will not be further discussed.

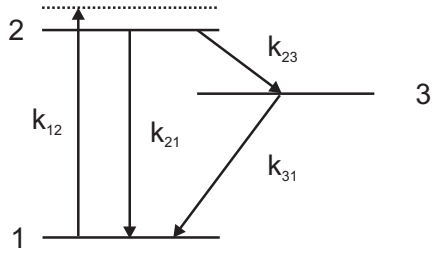

Figure 5.14: Schematic representation of the simplified three level model employed to explain the population dynamics of single SiV centers.

To explain the first observation of $g^{(2)}$ exceeding one, termed *photon-bunching*, a three level system including a *shelving state* instead of the two level system discussed above has to be considered to describe the investigated SiV center. In a first approach, we use a simplified model depicted in Fig. 5.14: Levels 1 and 2 are coupled via a fast radiative transition with the rate coefficient k_{21}, the photons emitted on this transition are measured in our HBT setup. In contrast to that, level 3 acts as a shelving state populated via the rate coefficient k_{23} with the possibility of relaxation into the ground state via k_{31}. As long as the emitter resides in state 3, no photons on the radiative transition 2→1 are detected. This simple model has been successfully employed to describe the dynamics of molecules involving shelving states [169]. To obtain the $g^{(2)}$ function of the fluorescence from a color center described by this level scheme, one solves the rate equations describing the system:

$$\frac{dN_1}{dt} = N_2 k_{21} - N_1 k_{12} + N_3 k_{31} \tag{5.6}$$

$$\frac{dN_2}{dt} = -N_2 k_{21} + N_1 k_{12} - N_2 k_{23} \tag{5.7}$$

$$\frac{dN_3}{dt} = N_2 k_{23} - N_3 k_{31} \tag{5.8}$$

We assume that the system is in the ground state at time zero and that the sum of the populations $N_1 + N_2 + N_3 = 1$. The $g^{(2)}$ function is defined by $\frac{N_2(\tau)}{N_2(\tau\to\infty)}$ [24] resulting in

$$g^{(2)}(\tau) = 1 - (1+a)\, e^{-|\tau|/\tau_1} + a\, e^{-|\tau|/\tau_2} \tag{5.9}$$

The parameters a, τ_1 and τ_2 are given by [74]:

$$\tau_{1,2} = 2/(A \pm \sqrt{A^2 - 4B}) \tag{5.10}$$

$$A = k_{12} + k_{21} + k_{23} + k_{31} \tag{5.11}$$

$$B = k_{12}k_{23} + k_{12}k_{31} + k_{21}k_{31} + k_{23}k_{31} \tag{5.12}$$

$$a = \frac{1-\tau_2 k_{31}}{k_{31}(\tau_2 - \tau_1)} \tag{5.13}$$

The parameter τ_1 governs the antibunching of the $g^{(2)}$ function for short delays τ, while the parameter τ_2 governs the bunching at intermediate timescales. The parameter a determines how significant the influence of the third level and thus how pronounced the bunching is. For $a = 0$, Eq. (5.9) reduces to the $g^{(2)}$ function of the two level system. To interpret the excitation power dependent $g^{(2)}$ functions, assumptions for the rate coefficients $k_{12}, k_{21}, k_{23}, k_{31}$ and their dependence on the excitation power P have to be made. Before we develop the different models in detail, we first discuss the second observation of the non-vanishing $g^{(2)}(0)$ value introduced above.

Causes for a non-vanishing $g^{(2)}(0)$ value

A non-vanishing value of $g^{(2)}(0)$, might have several reasons: First, $g^{(2)}(0)$ might exceed zero if several emitters are present in the laser focus. The contrast obtained for the $g^{(2)}$ function scales with $\frac{1}{n_e}$, where n_e is the number of equally bright emitters contributing to the emission [23, 219]. Due to this property, apart from proving single emitter nature, the $g^{(2)}$ function has been used to 'count' NV centers inside NDs [219]. As $g^{(2)}(0)$ is equal to $1 - \frac{1}{n_e}$ [23], $g^{(2)}(0)$ below 0.5 reliably indicates the presence of a single emitter (if one assumes equally bright emitters). However, various emitters within the detection volume might display different brightness, as frequently observed for the SiV centers here. Thus, the question arises how the $g^{(2)}$ function of the fluorescence from a strong emitter is influenced by the contribution of an additional, weak emitter. We assume that the intensity I can be written as $I = I_1 + I_2$, where I_1 (I_2) is the intensity due to emitter 1 (2). This assumption neglects interference effects, thus it is only valid for distinguishable photons that do not interfere. It is thus justified for emitters with differing emission wavelengths. According to Eq. (5.3), to calculate the $g^{(2)}$ function one has to evaluate the time average

$$\langle I(t)I(t+\tau)\rangle \tag{5.14}$$

With $I = I_1 + I_2$ we find

$$\begin{aligned}
\langle I(t)I(t+\tau)\rangle &= \langle [I_1(t) + I_2(t)][I_1(t+\tau) + I_2(t+\tau)]\rangle \\
&= \langle I_1(t)I_1(t+\tau) + I_1(t)I_2(t+\tau) + I_2(t)I_1(t+\tau) + I_2(t)I_2(t+\tau)\rangle \\
&= g_1^{(2)}(\tau)\langle I_1(t)\rangle^2 + 1\langle I_1(t)\rangle\langle I_2(t)\rangle + 1\langle I_2(t)\rangle\langle I_1(t)\rangle + g_2^{(2)}(\tau)\langle I_2(t)\rangle^2
\end{aligned}$$

The first and the last terms can be identified as the $g^{(2)}$ functions of emitter 1 and 2 respectively ($g^{(2)}_{1,2}$, see last line). The terms including both intensities I_1 and I_2 have been simplified assuming that the intensity fluctuations of the different emitters are uncorrelated. To obtain the $g^{(2)}$ function, the equation above has to be divided by $\langle I(t)\rangle^2 = \langle I_1(t) + I_2(t)\rangle^2$. For emitters with equal intensities $I_1 = I_2 = 0.5I$, we find

$$\begin{aligned} g^{(2)}(0) &= \frac{g^{(2)}_1(0)\langle 0.5I(t)\rangle^2 + 1\langle 0.5I(t)\rangle^2 + 1\langle 0.5I(t)\rangle^2 + g^{(2)}_2(0)\langle 0.5I(t)\rangle^2}{\langle I(t)\rangle^2} \\ &= \frac{0.5\langle I(t)\rangle^2}{\langle I(t)\rangle^2} = 0.5 \end{aligned}$$

Thus, under the assumption that emitters 1 and 2 satisfy $g^{(2)}_{1,2}(0) = 0$, we find the results given in the literature for two equally bright emitters. If emitter 1 is much brighter than emitter 2 (e.g. $I_1 = 0.95I$,$I_2 = 0.05I$, $\frac{I_1}{I_2} = 19$) we find

$$g^{(2)}(0) = \frac{g^{(2)}_1(0)\langle 0.95I(t)\rangle^2 + 2\langle 0.95I(t)\rangle\langle 0.05I(t)\rangle + g^{(2)}_2(0)\langle 0.05I(t)\rangle^2}{\langle I(t)\rangle^2} = 0.095$$

Thus, taking into account an uncertainty in the background contribution (see discussion below), it is challenging to detect the presence of additional weak emitters via the $g^{(2)}$ function. Figure 5.15(a) displays $g^{(2)}(0)$ for two emitters with varying relative intensities. Assuming a deviation of $g^{(2)}(0)$ of 0.15 is detectable, it should be possible to identify emitters with an order of magnitude difference in their count rates.

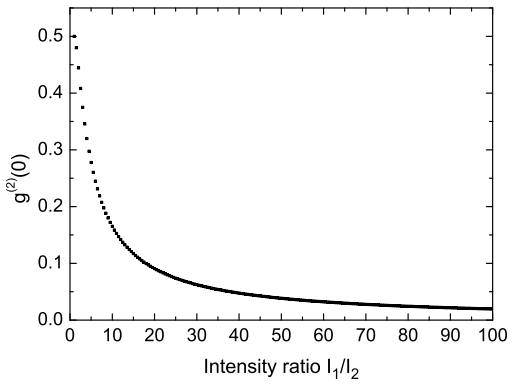

(a) $g^{(2)}(0)$ for two emitters with the intensity ratio $\frac{I_1}{I_2}$. The ratio $\frac{I_1}{I_2}$ is increased in steps of 0.5 from 1 to 105.

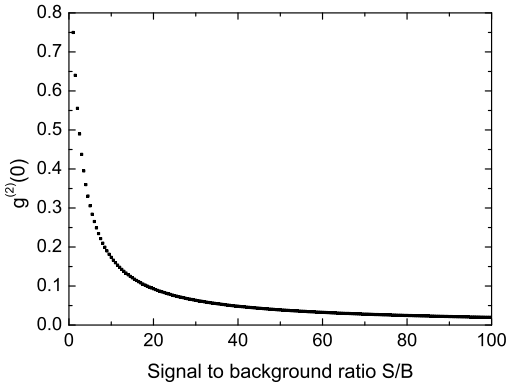

(b) $g^{(2)}(0)$ for one emitter with contribution of non-correlated background with signal to noise ratio $\frac{S}{B}$. $\frac{S}{B}$ is increased in steps of 0.5 from 1 to 105.

Figure 5.15: Influence of additional single emitter and background contribution on $g^{(2)}(0)$

A second cause for a non-vanishing $g^{(2)}(0)$ value is background fluorescence mainly emitted by the diamond material hosting the single color center. This background fluorescence is spectrally broad and has been found to be very strong in

polycrystalline and nanocrystalline diamond films (see, e.g., Fig. 4.3). The most prominent broad luminescence bands of diamond are found in the blue and green region of the spectrum (centered at 2.3 eV and 2.8 eV, [138]). Their origin is not clear; however, they are tentatively attributed to dislocations. Also for the spectral region between 600 nm and 800 nm, there are several reports and explanations of broad luminescence bands in diamond in the literature. Several authors establish a connection between sp^2 bonded disordered carbon in diamond films and broad luminescence. sp^2 bonded disordered carbon introduces electronic states into the bandgap of diamond and thus leads to broad luminescence bands [109, 220, 221]. Other authors trace the broad luminescence back to grain boundaries in the diamond material [222]. Also the recombination of donor acceptor pairs with various spatial distances is considered [223]. Here, donor acceptor pairs seem unlikely for the very pure diamonds used, nevertheless, grain boundaries or even a low level of sp^2 carbon might be present in the diamond films and NDs or NIs. The background level also strongly differs for individual NDs/NIs. This is clear from the observation of saturation curves with significant as well as negligible background contributions in Sec. 5.3.1. This observation also hints at a luminescence background originating from defects in the diamond material.

In the following, we discuss how we estimate the background contributions and how we take them into account when evaluating the data. For emitters residing in a homogeneous bulk material, background estimation is evident: The fluorescence count rates obtained from the diamond material close to the color center can serve as a measure of the background fluorescence [23]. This is mostly not feasible for the emitters discussed here: The background level on the substrate close to the diamonds does not reveal the background observed on the ND or NIs. Estimating the background level from the spectrum of the emitters is challenging, as separation of background and emitter luminescence is often difficult. However, one may use the observed saturation curves to estimate the background: As discussed in Sec. 5.3.1, for several emitters a linearly increasing background has been taken into account. Thus, Eq. (5.2) and the fit parameters therein can be used to separate the background contribution B from the emitter's fluorescence (signal S). From B and S, we calculate p_e according to

$$p_e = \frac{S}{S+B}. \tag{5.15}$$

p_e gives the probability that a detected photon has been emitted by the color center under investigation. p_e can be used to correct for the background contribution in $g^{(2)}$ assuming that the background and color center emission are uncorrelated. This leads to [23]

$$g^{(2)}(\tau) = \frac{1}{p_e^2}\,[g_m^{(2)}(\tau) - (1-p_e^2)]. \tag{5.16}$$

Here, $g^{(2)}(\tau)$ is the ideal $g^{(2)}$ function without background and $g_m^{(2)}(\tau)$ is the measured $g^{(2)}$ function in the presence of background. Thus, this formula can be used to correct measured data for the background contribution. Here, we include p_e obtained from the saturation measurements as a fixed parameter in the fitting of the

measured function $g_m^{(2)}(\tau)$, thus accounting for background contributions:

$$g_m^{(2)}(\tau) = 1 + (g^{(2)}(\tau) - 1)p_e^2 \tag{5.17}$$

To illustrate the influence of background fluorescence, we calculate $g_m^{(2)}(0)$ for different ratios $\frac{S}{B}$. The curve for $g_m^{(2)}(0)$ is displayed in Fig. 5.15(b). A typical value for the fluctuations of the measured datapoints in the $g^{(2)}$ function is about 0.05. Thus, for $\frac{S}{B} > 50$ the background contribution is no longer identified in the measurements as it becomes comparable to the measured fluctuations.

The third cause for a non-vanishing $g^{(2)}(0)$ is not, as discussed before, due to imperfect single photon emission but due to imperfections of the measurement setup. To describe the experimental results correctly, we have to account for the instrument response of the HBT setup. It is mainly due to the APDs used: The photon detection process involves the buildup of an electron avalanche. It does not occur in a well defined time, but includes a temporal uncertainty (jitter). This in turn leads to a reduced timing precision of the photon detection. To quantify this timing jitter of the APDs, we measure the intensity auto-correlation of attenuated ultrashort laser pulses (Titanium-Sapphire laser, 100 fs laser pulses). These laser pulses are sufficiently short, so that the measured width of their correlation function reflects the instrument response function. We find a Gaussian response function featuring a $\frac{1}{\sqrt{e}}$ width of 354 ps (data see Chapter 4 in Ref. [164]). This jitter significantly affects the measured $g^{(2)}$ functions for τ_1 constants comparable to or even smaller than the temporal width of the instrument response function. This situation often occurs for SiV centers. To account for the instrument response, we convolute Eq. (5.9) or Eq. (5.17) (if background is taken into account) with the measured Gaussian response function of our setup and use the resulting function to fit the data.[5] Figures 5.12 and 5.13 show the fitted $g^{(2)}$ functions as solid lines. The excellent agreement of the fits and the measured data proves that for several emitters the observed deviation from $g^2(0) = 0$ is fully explained by the timing jitter (without background correction), thus unambiguously proving single emitter behavior for the observed color centers. For emitters ND3 and NI1, the deviation $\Delta g^{(2)}(0)$ between the fitted value of $g^{(2)}(0)$ and the measured datapoints is less than 0.05 without background correction, witnessing very pure single photon emission with negligible background contribution.

Summarizing this discussion, a non-vanishing value of $g^2(0)$ can be induced by the presence of several emitters, by background fluorescence superimposing the single photon emission as well as a limited timing resolution of the experimental setup. The limited timing resolution as well as the background fluorescence can be included into the fitting function used to evaluate the data. These fits show that the measured $g^{(2)}$ functions are in full agreement with the $g^{(2)}$ functions of single emitters if the experimental issues are taken into account.

[5] Fitting was performed using a Levenberg-Marquardt-Fletcher algorithm implemented in Matlab. Note that convolution with the instrument response function has the same effect on Eq. (5.9) and Eq. (5.17), the terms due to background correction do not influence the convolution (assuming a Gaussian response normalized to 1).

Three level modeling of the intensity dependent $g^{(2)}$ function

From the fits of the $g^{(2)}$ function, we obtain the excitation power dependent values of the parameters a, τ_1 and τ_2 defining the three level $g^{(2)}$ function in Eq. (5.9). In the following, we aim at modeling the power dependence of these parameters and deduce the rate coefficients of the color center's level scheme. Examples of the measured power dependence for four ND emitters are given in Figs. 5.16 and 5.17. Examples for two NI emitters are displayed in Fig. 5.18.

In a first approach, we assume the rate coefficients k_{21}, k_{23}, k_{31} to be constant. Furthermore, we assume that the excitation rate k_{12} of level 2 depends linearly on the excitation power P: $k_{12} = \sigma P$. This is reasonable, as the color center is excited above the ZPL resonance and very fast relaxation processes in the excited state are likely: We assume that the color center is pumped to excited vibrational states in the excited electronic state as discussed on page 67 and in Sec. 6.1. Vibrationally excited states should show a fast relaxation, according to the lifetimes estimated from the sideband spectrum (lifetime less than 1 ps, see page 63). Due to this fast relaxation, no population accumulation is expected in the pumping states or in any intermediate state in the relaxation process to state 2. Thus, stimulated emission due to the excitation laser on the pumping transition is unlikely as the pumping states are effectively not populated. Without stimulated emission, saturation of the pumping transition is not possible, leading to a linear dependence of the pumping rate on the excitation power. Under these assumptions, k_{21}, k_{23}, k_{31} can be derived from the limiting values of the fitted parameters a, τ_1 and τ_2:

$$k_{31} = \frac{1}{(1 + a^\infty)\tau_2^\infty} \tag{5.18}$$

$$k_{23} = k_{31} a^\infty \tag{5.19}$$

$$k_{21} = \frac{1}{\tau_1^0} - k_{23} \qquad \text{for} \qquad k_{21} + k_{23} > k_{31} \tag{5.20}$$

Here, the superscript $^\infty$ denotes the limit for high excitation power and ^{0} denotes the limit for vanishing excitation power.

The last parameter needed to describe the power dependence of a, τ_1 and τ_2 is the proportionality constant σ linking the excitation power and the pumping rate k_{12}. σ can be derived as follows. The fluorescence rate $I(P)$ obtained at power P is proportional to the steady state population of the excited state N_2^∞ multiplied with the transition rate k_{21}. To obtain the steady state population of the excited state, all time derivatives in Eqs. (5.6)–(5.8) are set equal to zero. From these equations and the constraint $N_1 + N_2 + N_3 = 1$ follows,

$$N_2^\infty = \frac{k_{31}k_{12}}{k_{23}k_{12} + k_{31}k_{12} + k_{23}k_{31} + k_{21}k_{31}}. \tag{5.21}$$

Thus, $I(P)$ is proportional to

$$N_2^\infty k_{21} = \frac{k_{21}k_{31}\sigma P}{k_{23}\sigma P + k_{31}\sigma P + k_{23}k_{31} + k_{21}k_{31}}. \tag{5.22}$$

This expression resembles the form of the saturation curve given in Eq. (5.1) if written in a slightly different way:

$$N_2^{\infty} k_{21} = \frac{k_{31} k_{21}}{k_{23} + k_{31}} \frac{P}{P + \frac{k_{23} k_{31} + k_{21} k_{31}}{(k_{23} + k_{31})\sigma}}. \tag{5.23}$$

Here, $N_2^{\infty}(P \to \infty) k_{21} = \frac{k_{31} k_{21}}{k_{23} + k_{31}}$ is proportional to the maximum obtainable photon rate; however, one should keep in mind that the detected photon rate additionally depends on the collection efficiency η_{coll} and the detection efficiency η_{det}^{int} for the light as well as the quantum efficiency of the emitter η_{qe} (see Sec. 5.3.4). On the other hand, $\frac{k_{23} k_{31} + k_{21} k_{31}}{(k_{23} + k_{31})\sigma}$ directly gives the saturation power P_{sat} obtainable from the fitted saturation curve. Thus, we calculate σ as

$$\sigma = \frac{k_{23} k_{31} + k_{21} k_{31}}{(k_{23} + k_{31}) P_{sat}}. \tag{5.24}$$

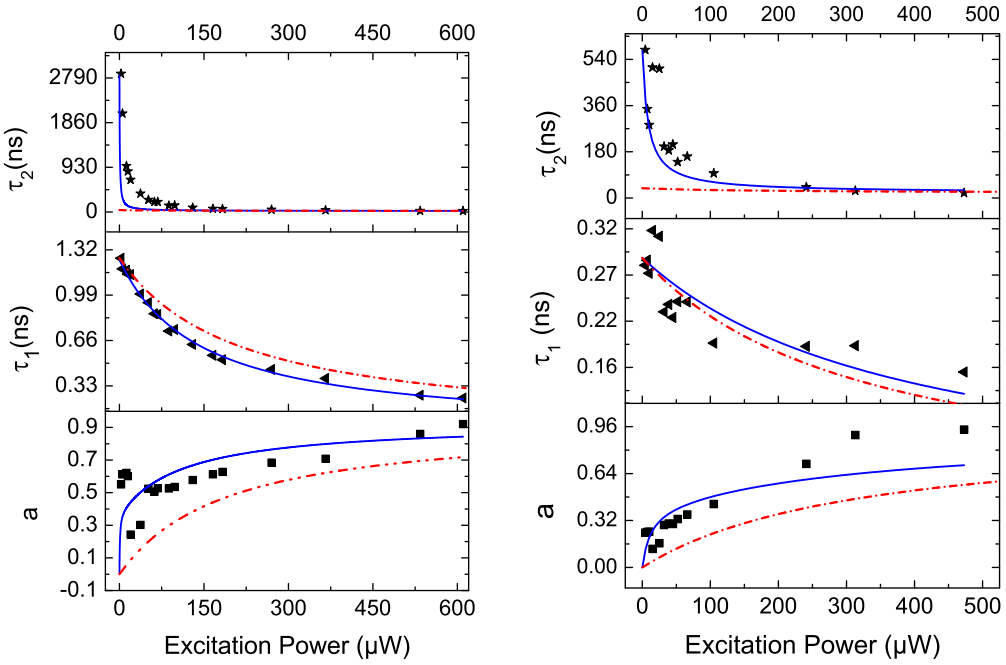

(a) Excitation power dependence for the parameters a, τ_1 and τ_2 for emitter ND3, saturation power 105.3 μW. Excitation 671 nm.

(b) Excitation power dependence for the parameters a, τ_1 and τ_2 for emitter ND2, saturation power 166.8 μW. Excitation 671 nm.

Figure 5.16: Intensity dependence of parameters a, τ_1 and τ_2. Blue solid lines represent fitting curves according to the intensity dependent de-shelving model. Red dashed lines represent the excitation power dependence from the model with constant rates, no fitting was performed to obtain these curves, for explanation see text.

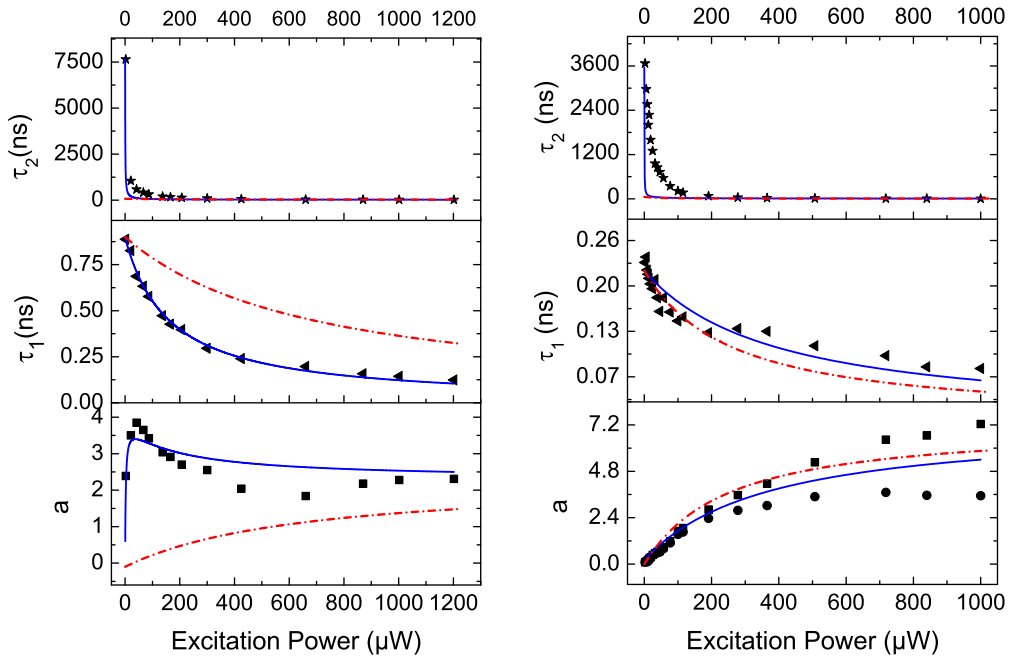

(a) Excitation power dependence for the parameters a, τ_1 and τ_2 for emitter ND4, saturation power 197.3 μW. Excitation 705 nm.

(b) Excitation power dependence for the parameters a, τ_1 and τ_2 for emitter ND1, saturation power 30.6 μW. The power dependence of a includes two datasets: Filled squares obtained using background correction for the $g^{(2)}$ function, filled dots obtained using fitting without background correction. Excitation 671 nm.

Figure 5.17: Intensity dependence of parameters a, τ_1 and τ_2. Blue solid lines represent fitting curves according to the intensity dependent de-shelving model. Red dashed lines represent the excitation power dependence from the model with constant rates, no fitting was performed to obtain these curves, for explanation see text.

As visible from Figs. 5.16, 5.17 and 5.18, the measured power dependence of a, τ_1 and τ_2 allows for the estimation of the limiting values in Eqs. (5.18)–(5.20) necessary to derive the rate coefficients. Using these rate coefficients, the parameter σ, and Eqs. (5.10)–(5.13) we calculate the power dependent curves for a, τ_1 and τ_2, shown in Figs. 5.16, 5.17 and 5.18 as red dashed lines. The rates k_{21}, k_{23} and k_{31} are summarized in Tab. 5.1. The rate k_{21} is found to be the highest of all rates, the shelving rate k_{23} is at least a factor of 33 lower than k_{21}. For emitter NI7, k_{23} is even three orders of magnitude smaller than k_{21}. The rate k_{31} as well as the parameter σ vary by more than an order of magnitude among the emitters shown here. The fact, that k_{21} significantly exceeds all other rates makes these emitters suitable as single photon emitters. The ideal case would be a two level system without a shelving state to obtain the maximum possible photon rate and quantum efficiency. Nevertheless, if the influence of the shelving state is weak, efficient single photon emission is still feasible. Further discussion on the influence of the shelving state is found in Sec.

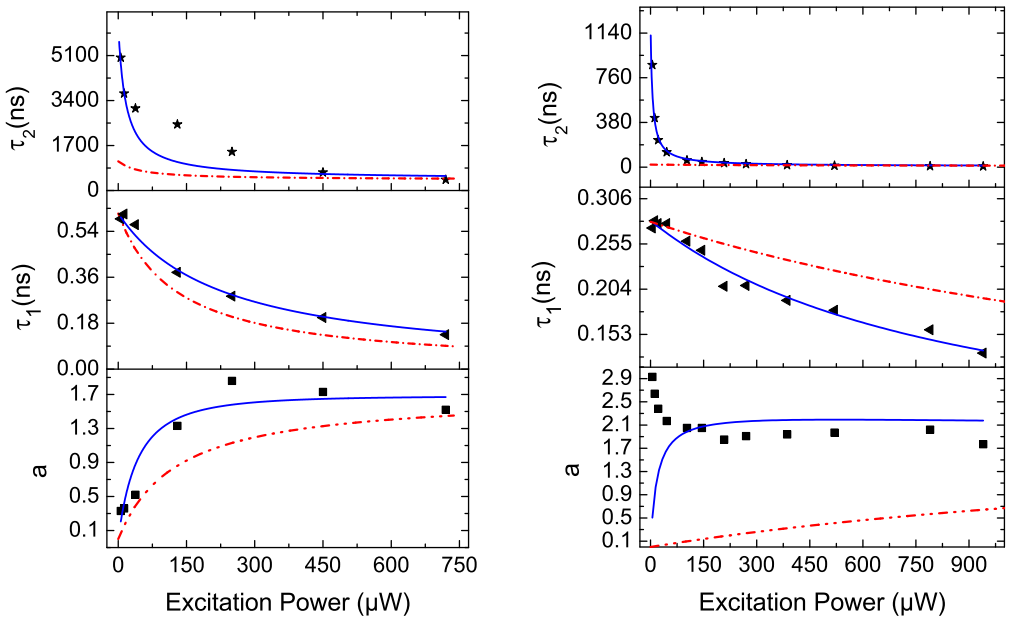

(a) Excitation power dependence for the parameters a, τ_1 and τ_2 for emitter NI7, saturation power 46.9 μW. Excitation 695 nm.

(b) Excitation power dependence for the parameters a, τ_1 and τ_2 for emitter NI1, saturation power 692 μW. Excitation 695 nm.

Figure 5.18: Intensity dependence of parameters a, τ_1 and τ_2. Blue solid lines represent fitting curves according to the intensity dependent de-shelving model. Red dashed lines represent the excitation power dependence from the model with constant rates, no fitting was performed to obtain these curves, for explanation see text.

5.3.4.

As visible from Figs. 5.16, 5.17 and 5.18, it is necessary to perform $g^{(2)}$ measurements at excitation powers far above saturation power to obtain the limiting values of the parameters a, τ_1 and τ_2. Thus, these measurements are only feasible owing to the high photostability of the SiV centers investigated here. For measurements above saturation, great care has to be taken to ensure a defined pump power exciting the emitters: Above saturation, spatial drifts of the setup, changing

Em	k_{21}(MHz)	k_{23}(MHz)	k_{31}(MHz)	σ(MHz/μW)
ND1	4408	137.0	18.9	18.0
ND2	3424	24.6	26.2	10.7
ND3	770	23.6	25.3	3.9
ND4	1079	31.7	13.2	16.6
NI1	3479	92.6	46.3	1.7
NI7	1638	1.5	0.9	12.9

Table 5.1: Rate coefficients deduced from the limiting values of a, τ_1 and τ_2 using the three level model including constant rates. Emitter ND1-ND3 measured under 671 nm excitation, ND4 under 705 nm excitation and NI1, NI7 under 695/696 nm excitation

the intensity impinging onto the emitter, do no longer lead to measurable photon count rate changes. This renders detecting drifts and ensuring a constant excitation intensity/excitation power very challenging.

As evident from Figs. 5.16, 5.17 and 5.18, the model with constant transition rate coefficients reasonably well describes the power dependence of τ_1, and, for some emitters, the power dependence of a. Nevertheless, it totally fails explaining the power dependence of τ_2: All emitters show a significant increase of up to three orders of magnitude for τ_2 at low excitation power. In contrast, the model using constant rates predicts a nearly constant value of τ_2 also at low excitation power.

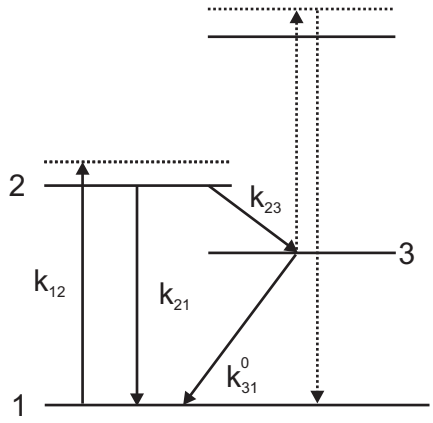

Figure 5.19: Schematic representation of the extended three level model employed to explain the population dynamics of single SiV centers.

In the following, we propose an extension of the simple three level model of Fig. 5.14 allowing to account for these deviations. As a starting point for the discussion, we take the failure of the model to properly describe the power dependence of the parameter τ_2. As the major discrepancy between measured and simulated values of τ_2 occurs at low pump powers, we now use the limiting value τ_2^0 to infer the rate coefficients instead of using τ_2^∞:

$$k_{31} = \frac{1}{\tau_2^0} \tag{5.25}$$

By using Eq. (5.25) instead of Eq. (5.18) together with Eqs. (5.19) and (5.20), we obtain an 'alternative' set of rate parameters. E.g. for emitter ND1 we find $k_{21} = 4543\,\mathrm{MHz}$, $k_{23} = 1.97\,\mathrm{MHz}$, $k_{31} = 0.27\,\mathrm{MHz}$. Whereas the values for k_{21} differ only by 3%, the values of k_{23} and k_{31} seem to be inconsistent if high and low power limiting values are used. Thus, the model with constant rate coefficients is insufficient to describe the investigated SiV centers. To extend the model, an intensity dependent transition process has to be established. Following approaches in the literature [36, 224, 225], we assume that the process reactivating the color centers from the shelving state (de-shelving process), represented by the rate k_{31}, is intensity dependent. In the literature, for color centers as well as molecules, de-shelving processes linearly dependent on the excitation power have been discussed [36, 224, 225]. The assumption of a linearly dependent de-shelving, however, leads to

$$\tau_2^\infty = 0 \qquad a^\infty = 0. \tag{5.26}$$

This is not consistent with our observations even at very high excitation powers:

For the emitters ND1 [Fig. 5.17(b)], ND2 [Fig. 5.16(b)], ND3 [Fig. 5.16(a)] as well as NI1 [Fig. 5.18(b)] and NI7 [Fig. 5.18(a)], a rather tends to a constant value for high excitation powers. Only for emitter ND4 [Fig. 5.17(a)], a decrease of a at high excitation power is observed; however, a does also not decrease to zero. According to these observations, we tentatively model the intensity dependence of the rate k_{31} to follow a saturation law instead of a linear dependence. Additionally, we include an intensity independent rate k_{31}^0:

$$k_{31} = \frac{d \cdot P}{P + c} + k_{31}^0 \tag{5.27}$$

The introduction of a saturating de-shelving process is further motivated by the probable explanation of this process: As depicted in Fig. 5.19, the de-shelving might be realized via an excitation from the shelving state to higher lying states, as, e.g., found for molecules in Ref. [225]. This excitation process might intrinsically exhibit a saturation behavior if population accumulates in the upper state of the de-shelving transition. In this model, as depicted in Fig. 5.19, we assume that the de-shelving process returns the color center back to the ground state (state 1), following the model introduced in Ref. [225]. In Ref. [164], a very similar model employing a de-shelving process ending in the excited state has been proposed. From the experimental data and our model, it cannot be distinguished whether the color centers are excited back to the excited electronic state or if the de-shelving provides a fast relaxation to the ground state. For high excitation powers, however, the two cases cannot be discriminated as the rate k_{12} tends to infinity and thus the color center is 'instantaneously' pumped back to the excited state.

For this new model, we calculate k_{23}, k_{21}, k_{31}^0, d under the assumption $k_{21}+k_{23} > k_{31}^0$:

$$k_{31}^0 = \frac{1}{\tau_2^0} \tag{5.28}$$

$$d = \frac{\frac{1}{\tau_2^\infty} - (1 + a^\infty)\frac{1}{\tau_2^0}}{a^\infty + 1} \tag{5.29}$$

$$k_{23} = \frac{1}{\tau_2^\infty} - k_{31}^0 - d \tag{5.30}$$

$$k_{21} = \frac{1}{\tau_1^0} - k_{23} \tag{5.31}$$

To derive the power dependence of a, τ_1 and τ_2, two additional parameters have to be determined: the parameter c in Eq. (5.27) as the saturation power for the de-shelving process, as well as the proportionality constant σ for the excitation rate $k_{12} = \sigma P$. This parameter can no longer be derived from the saturation curve as it is no longer feasible to link the rate coefficients to the saturation power P_{sat} as in Eq. (5.23). Instead, the parameters c and σ have to be obtained from fits of the power dependent curves of a, τ_1 and τ_2: We employ the definition of the parameters a, τ_1 and τ_2 in Eqs. (5.10)–(5.13), together with the definitions of k_{12} and k_{31} [Eq. (5.27)], as fit functions with free parameters c and σ. Thus, three curves have to be

fitted to obtain two parameters. Fitting the power dependent curves, we find that the power dependence of τ_1 is almost fully determined by σ. Thus, we use $\tau_1(P)$ to determine σ. One way to determine the parameter c is to fit the power dependent curve $\tau_2(P)$, using the value of σ obtained from the fit of $\tau_1(P)$ as a fixed parameter. However, we find that the value of c obtained by this procedure, together with σ obtained from the fit of $\tau_1(P)$, does not at all describe the power dependent curve $a(P)$. Furthermore, we find that if the parameter c is obtained from fitting the power dependent curve $a(P)$, the resulting value of c at least qualitatively describes $\tau_2(P)$. Thus, taking the value of σ from the fit of $\tau_1(P)$ as fixed, we fit the curve $a(P)$ and obtain the value of c. To complete the description, we plot the resulting curve for $\tau_2(P)$ with these parameters. Figures 5.16, 5.17 and 5.18 show the curves obtained with this procedure as solid blue lines. Table 5.2 summarizes the rates and fit parameters obtained for the emitters shown here.

As clearly visible, the extended model describes the power dependence of a, τ_1 and τ_2 much better than the simple model. Especially for emitter NI7 [Fig. 5.18(a)], ND2 [Fig. 5.16(b)] and ND3 [Fig. 5.16(a)] all curves are well described with the intensity dependent de-shelving model. For emitters ND4 [Fig. 5.17(a)] and ND1 [Fig. 5.17(b)], the decrease of τ_2 at intermediate powers is overestimated. This has been observed for several other emitters. Additionally, the power dependence of a can only be qualitatively described using the model with intensity dependent de-shelving for emitter ND4. The same is the case for emitter NI1 [Fig. 5.18(b)], here an extraordinary behavior of a is observed, including an increase of a at very low powers.

Emitter ND1 illustrates one challenge in evaluating the data: In Fig. 5.17(b), the power dependence of a includes two datasets: The dataset marked with filled squares has been obtained including background correction for the $g^{(2)}$ function. The dataset marked with filled dots has been obtained using fitting without background correction. Both fits well describe the measured $g^{(2)}$ function and yield very similar values for τ_1 and τ_2, respectively, but yielding differing values for a. Thus, an uncertainty in the background correction translates into an uncertainty in a and thus into an uncertainty in a^∞ used to estimate the rate coefficients. This is due to the fact that, for the $g^{(2)}$ function corrected for the instrument response function, a higher value of a has a comparable effect on the depth of the antibunching dip as a higher background level. The effect is illustrated in Fig. 5.20(a): For larger

Em	k_{21}(MHz)	k_{23}(MHz)	k_{31}^0(MHz)	d (MHz)	σ(MHz/μW)	c (μW)	P_{sat} (μW)
ND1	4408	137.0	0.27	18.6	12.0	11.9	30.6
ND2	3424	24.6	1.7	24.4	8.9	177	167
ND3	771	23.3	0.35	24.7	5.7	57	105.3
ND4	1084	31.7	0.12	13.1	7.0	2743	282
NI1	3479	92.6	0.82	45.5	4.2	1067	692
NI7	1638	1.5	0.16	0.7	7.2	300	46.9

Table 5.2: Rate coefficients deduced from the limiting values of a, τ_1 and τ_2 using the three level model including intensity dependent de-shelving and parameters c and σ obtained from the fits. For comparison also P_{sat} is given.

values of a, the depth of the antibunching dip is reduced, i.e., the value of $g^{(2)}(0)$ is increased. This is not the case for the ideal $g^{(2)}$ function given in Eq. (5.9) as displayed in Fig. 5.20(b). Due to the APD timing jitter a step slope of the $g^{(2)}$ function in combination with a high absolute value close to zero delay times leads to an increase of $g^{(2)}(0)$ as the timing jitter washes out the $g^{(2)}$ function.

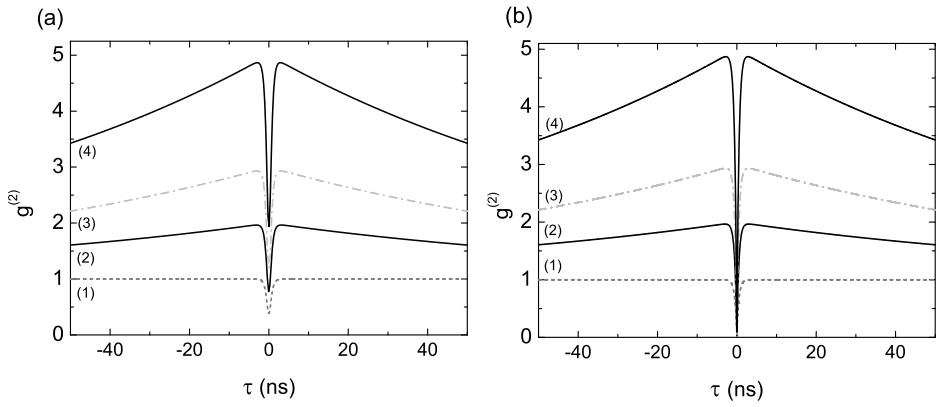

Figure 5.20: (a) $g^{(2)}$ function including instrument response, (b) $g^{(2)}$ function without instrument response. Curves drawn for $\tau_1 = 0.5\,\text{ns}$, $\tau_2 = 100\,\text{ns}$ (1) $a = 0$, (2) $a = 1$, (3) $a = 2$, (4) $a = 4$,

Even more challenging is the estimation of the limiting value τ_2^0: As the curves are very steep for low excitation powers, interpolation of τ_2 to zero excitation power is critical. Thus, measurements at very low excitation power are necessary. But as also a is often rather small at low excitation power, the bunching is weak rendering proper fitting of the parameter τ_2 challenging. This uncertainty in the estimation of τ_2^0 directly leads to an uncertainty for k_{31}^0 [see Eq. (5.28)]. In contrast to the estimation of τ_2^0, the limiting values τ_1^0 and τ_2^∞ can be more reliably determined: The curve $\tau_1(P)$ has a smaller slope for low excitation powers than $\tau_2(P)$, facilitating a more precise interpolation. τ_2^∞ can be extracted reliably from the measured data as a very clear convergence toward a constant value is observed for most emitters. The estimation of a^∞, however, is influenced by the uncertainty in the background correction as discussed above. The rate coefficient k_{21} given in Eq. (5.31) is mostly determined by τ_1^0 as the rate coefficient k_{23} is found to be much smaller than $\frac{1}{\tau_1^0}$. Thus, the rate k_{21} can be mostly reliably determined. Examining Eq. (5.29), it is apparent that as τ_2^∞ is much smaller than τ_2^0, the rate coefficient d is mostly determined by τ_2^∞ and a^∞. Thus, the uncertainty in a^∞ leads to an uncertainty in d. This in turn influences the rate coefficient k_{23} given in Eq. (5.30). As d can be comparable to $\frac{1}{\tau_2^\infty}$, this influence can be significant, whereas as k_{31}^0 is much smaller than $\frac{1}{\tau_2^\infty}$ the uncertainty in τ_2^0 does not lead to a large error in k_{23}. However, in the cases where d is small compared to $\frac{1}{\tau_2^\infty}$, e.g, for emitter ND1, k_{23} is mostly determined by the parameter τ_2^∞. Summarizing, the intensity independent de-shelving rate k_{31}^0 involves a large error, whereas the ZPL transition rate coefficient k_{21} can be more

reliably determined, the other rate coefficients involving the shelving state show a varying uncertainty depending on the influence of background and the ratio of the different rates.

In summary, the measurements unambiguously reveal the presence of a shelving state and also strongly suggest the existence of an intensity dependent de-shelving path. However, at present we cannot identify the nature of the shelving state or its position nor the transition responsible for the de-shelving. The rate coefficients obtained from the intensity dependent de-shelving model for 14 emitters are summarized in Fig. 5.21. It is clear that, for all emitters, the rate k_{21} is significantly higher than the other rates in the three level model. The significant spread of the rates k_{21} might be due to the local environment (proximity to the metal surface) as well as a varying quantum efficiency of the transition (for a detailed discussion see Sec. 5.3.4). The rate k_{31}^0 is lower than 1 MHz for the majority of the emitters, indicating a long lived shelving state. The rate d, indicating the high power limit of the de-shelving rate, is at least a factor of 4.6 higher than k_{31}^0 for all emitters. For the majority of emitters, d is even an order of magnitude larger than k_{31}^0. Comparing the parameter c, indicating the saturation power for the de-shelving process, with the measured saturation power P_{sat}, we find that for several emitters c and P_{sat} have a similar value. The values are summarized in Tab. 5.2. One thus might suspect, that the saturation of the de-shelving transition determines the saturation of the fluorescence of the SiV center. For the rate coefficient k_{23}, a large spread is observed ranging from 137 MHz to 1.5 MHz, thus we conclude that the coupling to the shelving state is strongly modified for the different emitters. It is also apparent from Fig. 5.21 as well as Tab. 5.2 that the rate coefficient populating the shelving state k_{23} is comparable to or even larger than the intensity dependent rate coefficient depopulation the shelving state k_{31}, even at high excitation powers. Thus, population accumulates in the shelving state. The influence of the shelving state will be further addressed in Sec. 5.3.4.

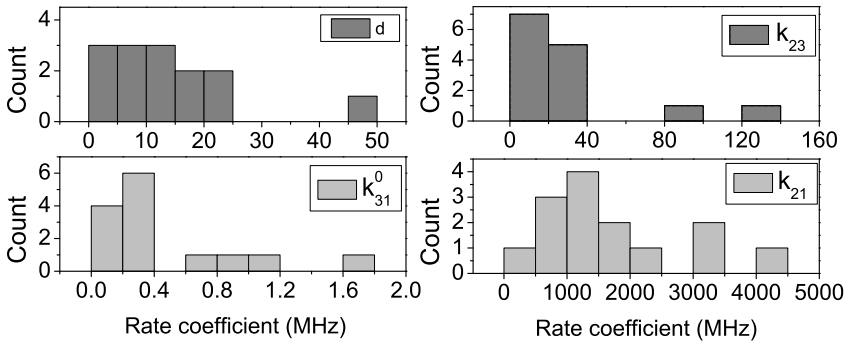

Figure 5.21: Histograms of rate coefficients k_{21}, k_{23}, k_{31} and d obtained from the model of saturating de-shelving. The histograms take into account emitters from NIs as well as randomly oriented NDs. Also the room temperature parameters for the emitters investigated in Chapter 7 are taken into account.

5.3.3 Photostability of single SiV centers

For single photon generation using optical excitation, the photostability of the emitter is crucial. If a single photon source is perfectly photostable it produces a stable photon rate under arbitrarily high excitation power for an infinitely long time. In practice, due to photoinduced processes, permanent or temporal loss of single photon emission under optical excitation can occur, thus limiting the applicability of the single photon source. A permanent loss of fluorescence due to optical excitation is termed *photobleaching*. This effect is known, e.g., for single dye molecules due to photochemical reactions of the molecules [225–228]. The photochemical reaction may occur preferably if the molecule is in the excited electronic state [227, 228], thus the probability for photobleaching has been found to be enhanced at elevated power, complicating the observation of single molecules at excitation powers above the saturation power of the molecule. However, embedding single molecules in a suitable matrix significantly enhances the photostability by protecting them against quenching reactions (see, e.g., Ref. [229] and Refs. therein). Also for single color centers in diamond, observations of photobleaching are found in the literature: Permanent photobleaching has been reported for single color centers emitting in the near-infrared spectral region [137], for single NV centers in NDs [230] and for a center emitting at 736.8 nm [74] (see also discussion below). However, the origin of this permanent bleaching has not been discussed in the publications mentioned above.

In addition to permanent bleaching, also fluorescence intermittence, termed *blinking*, is possible. This effect is well known for colloidal quantum dots, e.g., CdS quantum dots [231] or CdSe-ZnS quantum dots [232, 233]. In these systems, it is induced by charging of the quantum dot and subsequent suppression of luminescence. For single color centers in NDs, blinking has also been observed in Ref. [230] and is attributed to trapping and release of charges on the surfaces of the NDs.

To analyze the photostability of single SiV centers, we obtain time traces of the fluorescence rate from the lists of photon arrival times (time tags) that are usually employed to calculate the $g^{(2)}$ function. For a description of the measurement procedure, see Chapter 3. Figure 5.22 displays examples of these fluorescence time traces. The count rate of each emitter has been calculated in time windows of 100 ms for the lowest excitation power, while for the higher excitation powers time intervals of 50 ms are employed. As the data is retrieved from the lists of photon arrival times recorded to calculate the $g^{(2)}$ function, the total observation intervals decrease for higher excitation power and therefore higher countrates: Here, shorter measurement times were employed as they are sufficient to obtain good statistics in the $g^{(2)}$ histograms.

Based on the observed fluorescence stability, we can very roughly arrange the observed emitters into three classes as discussed below. Note that emitters may belong to class 2 and 3 simultaneously.

Class 1: emitters with fully photostable emission

An example for the fluorescence time trace of such a photostable emitter (ND4) is given in Fig. 5.22(a). Here, time traces for excitation up to three times the

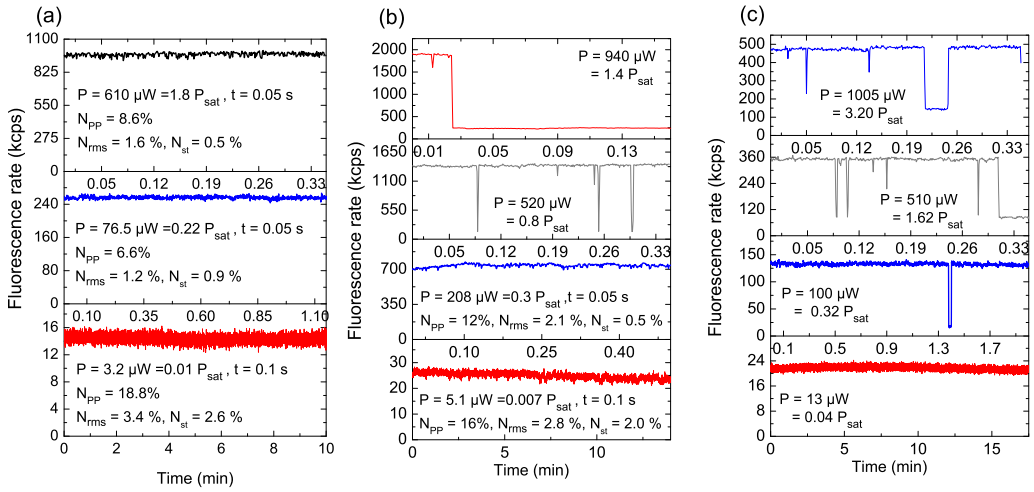

Figure 5.22: Fluorescence timetraces of single SiV centers (a) SiV center with fully photostable emission (emitter ND4, excited at 695 nm). (b) Emitter with destabilization at higher excitation power and permanent photobleaching (emitter NI1). (c) Emitter with longer time intervals of fluorescence intermittence (emitter NI6).

saturation power are given. However, also emitters which are stable at much higher power have been investigated: E.g., emitter ND1 has been shown to be stable under excitation powers up to 32 times the saturation power. The typical observation time for the intensity dependent $g^{(2)}$ measurements discussed above is about one hour, thus these emitters have shown to be photostable for at least one hour under continuous laser excitation. Roughly 20-30% of the emitters investigated in detail show full photostability. As visible, e.g., in the lowermost graph of Fig. 5.22(b), the count rate of the stable emitters nevertheless exhibits slow variations (drift) on timescales exceeding 5 min. Here, a drift of about 10% over approx. 15 min is observed. These drifts become especially important for the $g^{(2)}$ measurements at low power due to extended measurement times of 30 min and more. Most probably this slow variation is due to spatial drifts of the emitter out of the laser focus as no automatic refocussing of the emitter is performed. If a significant drift during extended $g^{(2)}$ measurements was detected, the $g^{(2)}$ measurement was interrupted and manual refocussing of the emitter was performed.

To estimate the fluctuations in the single photon count rate, we evaluate the maximum and minimum count rate, as well as the mean value and the standard deviation of the count rate over a time of 0.5 min to avoid the influence of long term drifts. The difference between maximum and minimum count rate divided by the mean count rate gives the peak to peak noise N_{PP}. N_{rms} is given as the ratio of the standard deviation of the mean value divided by the mean value. As visible in Fig. 5.22, typical values of N_{PP} are about 10%, while N_{rms} amounts to about 2%. For lower excitation powers and therefore lower numbers of detection events in the chosen 50 ms or 100 ms window, statistical measurement errors proportional to the square root of the number of the detection events also significantly contribute to the

noise (N_{st}), see Fig. 5.22(a) and (b). A main source of the observed fluctuations is, at least below the saturation of the single color center, the amplitude noise of the laser used for the excitation. For the emitters shown in Fig. 5.22(a) and (b), a frequency stabilized titanium-sapphire laser was used. According to manufacturer specifications, this laser exhibits an rms noise of 0.75%. For the diode pumped solid state laser used for 671 nm excitation, an rms stability of 5% over 4 hours is given by the manufacturer.

Class 2: emitters exhibiting fluorescence intermittence

Figures 5.22(b) and (c) give time traces for emitters exhibiting only partially stable emission due to fluorescence intermittence. For emitter NI6 in Fig. 5.22(c), long times of fluorescence intermittence have been observed as indicated in the graphs. For an excitation power of 380 μW, a dark period of more than 2 min was observed (fluorescence time trace not shown). Also shorter dark times with only about 100 ms were frequently recorded. The graphs given in 5.22(b) and (c) indicate a general trend: For higher excitation power, the probability for a transition to the dark state is enhanced. For nickel-silicon-related centers, a similar observation has been described in Ref. [164]: As deduced from intensity dependent statistics for on and off times, it is shown that the transition into the dark state is induced by the pump light, while the recovery of fluorescence by a transition to the bright state occurs spontaneously. For the SiV centers investigated here, too few blinking events are observed to employ a similar analysis. However, as the probability for blinking events is apparently higher at higher excitation power, one might suspect that the transition to the dark state is induced by the pump light. For excitation powers below or close to saturation, also for these partially stable emitters an almost constant single photon emission can be obtained as the blinking events are rare. We point out that in the work of Wang [74], an individual blinking color center exhibiting a ZPL wavelength compatible with the emission wavelengths observed here for SiV centers is reported. Thus, also in single crystal bulk diamond evidence for the blinking of SiV centers has been found.

Class 3: emitters for which permanent photobleaching occurred

Figure 5.22(b) shows an emitter for which permanent photobleaching occurred at elevated power. 'Permanent' here means in general that for waiting times of about 10 min no recovery of the fluorescence has been detected. For several emitters, also longer waiting times of more than one hour, partially without laser illumination, did not lead to fluorescence recovery. For emitter NI1, as seen in Fig. 5.22(b), prior to the permanent bleaching event, blinking was observed with a trend to enhanced blinking activity for higher laser powers. However, there are also emitters that were bleached without any prior sign of fluorescence instability/intermittence. E.g., emitter NI3 was bleached at 13 times the saturation intensity after withstanding excitation at 17 times the saturation intensity and an overall observation time exceeding one hour. We point out that in the above mentioned work of Wang [74], permanent bleaching of the investigated blinking center after one week of observation is reported.

Discussion of the observations

Blinking of color centers can be due to photoionization of the color centers as the charge state after ionization emits at a different wavelength and thus does not lead to detectable fluorescence in the preselected spectral window. We here are not able to verify this option as we cannot detect the luminescence at 946 nm originating from an alternative charge state of the SiV center (discussion of SiV charge states see page 8). However, one might also think of non-fluorescent charge states. For NV centers in NDs with only 5 nm size, blinking has been interpreted in terms of the capture of electrons excited to the conduction band in surface traps [230].[6] However, simultaneously it was found that NV^- to NV^0 conversion is not responsible for blinking or bleaching of NV centers as no NV^0 luminescence is observed [230]. The authors of Ref. [230] use the analogy of the optical excitation to an exciton formation to explain this behavior: As long as the electron of the exciton is captured, no fluorescence occurs. However, the authors do not clearly state why this capture of an electron is not equal to the ionization of the color center. Possibly the electron capture cannot be fully interpreted in terms of a color center ionization because the electron is still located close (<5 nm) to the center due to the small size of the NDs. Other authors, in contrast, suspect that the lack of excess electrons needed to charge/recharge NV centers in small NDs leads to photobleaching after photoionization [234]. For quantum dots, it has also been proposed that the blinking reflects a fluctuation in the non-radiative decay rates [232]. This has been suggested as for lower intensity states faster recombination rates, i.e., shorter lifetimes, have been measured.

The observation of photostable SiV centers shows that the SiV complex is, in principle, photostable. For the centers exhibiting blinking or bleaching, modifications in the vicinity of the defect have to trigger the instability. For the SiV centers, the possible channels for blinking as well as permanent photobleaching are not clear. However, due to the enhanced probability for the centers to undergo blinking transitions at elevated excitation powers, we suggest that the transition to the dark state is photoinduced as also found for nickel silicon centers in Ref. [164] or for NV centers in Ref. [230]. It might also be possible that the color center undergoes spontaneous transitions from its excited state to the dark state, thus with a higher excited state population, the rate for a transition to the dark state is enhanced.

We here choose the photon energy of the excitation laser sufficiently low so that the spatially localized electrons bound to the SiV center cannot be excited from the ground state of the SiV center to the conduction band (see discussion on page 10). Thus, for the primary excitation process, the electrons should not be promoted to delocalized conduction band states. These delocalized states enable the capture of electrons by traps in the vicinity of the color centers: An electron in these delocalized states has a finite probability to be found at the spatial site of a trap. In addition to the primary excitation process, one might think of further excitation of the bound electrons from the excited state of the color center (excited

[6] As 532 nm (2.33 eV) excitation light is used and the ground state of the NV^- center is located 2 eV below the conduction band [127], electrons are excited to the conduction band

state absorption), thus promoting them to delocalized conduction band states. Also a simultaneous absorption of two photons is a possible route to photoionization, where the probability for this process is proportional to the square of the incident laser intensity. The existence of two photon absorption processes has been shown for NV centers, e.g., in Ref. [235]. In both cases, trapping of electrons promoted to the conduction band then might lead to fluorescence intermittence. The nature of these trapping states is not clear for the SiV centers investigated here. One might think of surface states as, e.g., in Ref. [230]; however, as we use CVD diamonds, the surfaces of the diamonds should contain significantly less graphite and disordered carbon as compared to the surfaces of the detonation NDs used in Ref. [230]. A second possibility might be trapping of the electrons at other impurity atoms, e.g., nitrogen atom.

Additionally, it is not clear whether the mechanisms responsible for blinking and permanent photobleaching are identical. As very long blinking times have been observed, it is possible that the blinking mechanism is also responsible for the 'permanent' bleaching and that a recovery of the fluorescence after long waiting times is possible but has not been observed. This might especially happen if the laser is not able to free the electrons from their trapping states and if the spontaneous, possibly thermal, escape from these traps is very unlikely. The latter argument suggests trapping states deep within the band gap. The observation of photostable SiV centers is very promising for the application of single SiV centers as single photon sources. Using surface treatments as well as further control of the impurity content might help to enhance the fraction of fully photostable SiV centers.

5.3.4 Collection efficiency and estimated quantum efficiency

This section deals with the maximum single photon rates observed for single SiV centers and the effects limiting this rate and thus the brightness of single SiV centers. In particular, we aim at deducing the quantum efficiency η_{qe} of the SiV centers.

Influence of the shelving state

The maximum obtainable photon count rate I_∞ for continuous laser excitation is given by:

$$I_\infty = \eta_{det}\,\eta_{qe}\,k_{21}\,N_2^\infty(P\to\infty) = \eta_{det}\,\eta_{qe}\,\frac{k_{21}}{1+\frac{k_{23}}{k_{31}^0+d}} \tag{5.32}$$

$N_2^\infty(P\to\infty)$ is the maximum steady state population of the excited state. k_{21}, k_{23}, k_{31}^0 and d are the rates obtained from the intensity dependent de-shelving model. For the simple three level model, k_{31}^0+d has to be replaced by the intensity independent rate k_{31}. η_{det} is the detection efficiency of the experimental setup. It is the product of the collection efficiency η_{coll}, i.e., the probability to collect an emitted fluorescence photon, and the internal efficiency of the detection setup η_{det}^{int}, i.e., the probability to detect a collected photon (optics transmission, detector efficiency). η_{qe} is the quantum efficiency of the SiV center, i.e., the probability for a photon emission upon a transition from state 2 to 1 (see Fig. 5.19). First, we use the rate coefficients

to illustrate the influence of the shelving state on the maximum photon count rate for continuous excitation. For an off-resonantly pumped two level system with decay rate k_{21}, under the assumption that the relaxation to state 2, following the excitation process, is very fast, full population inversion $N_2^\infty(P \to \infty) = 1$ can be obtained. We thus expect a maximum photon rate

$$I_\infty = \eta_{det}\,\eta_{qe}\,k_{21}n_2^\infty = \eta_{det}\,\eta_{qe}\,k_{21} \tag{5.33}$$

for this idealized system. For the emitters discussed in Sec. 5.3.2 and several additional emitters, the rate coefficients obtained from intensity dependent $g^{(2)}$ measurements in the framework of the intensity dependent de-shelving model are summarized in Tab. 5.3. We obtain the maximum excited state populations $N_2^\infty(P \to \infty)$ also summarized in Tab. 5.3. It is clear, that the influence of the shelving state on the maximum photon rate under continuous excitation differs for the individual emitters investigated here: For emitter ND3, the maximum excited state population is only lowered by a factor of two compared to the two level case. On the other hand, for emitter ND1, the maximum excited state population is smaller by nearly an order of magnitude compared to the off-resonantly pumped two level system. As apparent from Tab. 5.3, the shelving rate k_{23} is low compared to k_{21}. However, due to a slow depopulation rate k_{31} of the shelving state, for several SiV centers, the shelving state accumulates most of the population, leading to a significant loss of brightness compared to a two level system.

Internal detection efficiency of the setup

In addition to the maximum excited state population and the transition rate k_{21}, the second factor required to determine the quantum efficiency η_{qe} is the internal detection efficiency η_{det}^{int} of the setup. η_{det}^{int} can be estimated by taking into account the transmission coefficients of all optical components as well as the detector efficiency. We estimate η_{det}^{int} for the setup described in Chapter 3 as follows: According to manufacturer specifications, the microscope objective enables a transmission of 78% at 700 nm. The dichroic mirror, used to separate fluorescence and laser light, transmits approx. 90% of the fluorescence at 740 nm (experimental data see Appendix B, Sec. B.1.1). The bandpass filters that select the spectral window from 730 nm to 750 nm transmit 85%, while the longpass filter used to remove residual laser light transmits about 95%. The lens surfaces in the setup are all equipped with an anti-reflective coating resulting in an overall transmission of 94%. An estimated fraction of 90% is transmitted through the 50:50 beamsplitter in the HBT setup. From test measurements using laser light, we estimate the transmission including the coupling efficiency for the multimode fiber to be 80%. The APDs feature a detection efficiency of 65% at 740 nm according to manufacturer specifications. Thus, the internal detection efficiency η_{det}^{int} of the setup is estimated as 25%. The largest errors in this estimation arise from the efficiency of the fiber coupling, as this could only be measured for reflected laser light and not for the actual fluorescence as well as from the transmission of the microscope objective which is unknown for the fluorescence wavelength of 740 nm.

Em	k_{21} (MHz)	k_{23} (MHz)	k_{31}^0 (MHz)	d (MHz)	N_2^∞ $(P=\infty)$	I_∞ (Mcps)	η_{qe}^{par} (%)	η_{qe}^{perp} (%)
ND1	4408	137	0.27	18.6	0.12	0.84	0.8	2.2
ND2	3424	24.6	1.7	24.4	0.51	1.53	0.4	1.2
ND3	771	23.6	0.35	24.7	0.51	2.46	3.2	8.9
ND4	1084	31.7	0.12	13.1	0.29	2.06	3.3	9.2
NI1	3479	92.6	0.82	45.5	0.33	6.24	2.8	7.7
NI7	1638	1.5	0.16	0.7	0.36	0.34	0.3	0.8
NI9	1181.7	1.8	0.21	3.1	0.65	3.82	2.6	7.1
NI3	161	7.3	0.24	11.9	0.62	0.17	0.9	2.4
NI10	798.8	34.6	0.22	16.2	0.32	0.8	1.6	4.4
NI8	2487	12.5	0.15	5.3	0.30	0.9	0.6	1.7
NI11	1076	13.3	0.32	8.2	0.39	0.52	0.6	1.8
C1	1545.1	17.4	1	11.9	0.43	2.39	1.9	5.2
C3	770.1	11.1	0.79	5.65	0.37	0.78	1.4	3.9
C4	1053.6	21.7	0.11	3.44	0.14	0.59	2.1	5.7

Table 5.3: Rate coefficients k_{ij}, maximum excited state population $N_2^\infty(P \to \infty)$, maximum photon rate I_∞ and quantum efficiency η_{qe} for individual SiV centers. Emitters C1,C3 and C4 are discussed in detail in Chapter 7. NI labels emitters located in nanoislands, ND labels emitters located in randomly oriented nanodiamonds.

Collection efficiency

The third factor required to estimate the quantum efficiency η_{qe} is the collection efficiency η_{coll} for the emitted light. Assuming a single dipole, the collection efficiency critically depends on the orientation of the emitting dipole as well as the material surrounding the dipole. The assumption of a single radiating dipole is justified for SiV centers as discussed in Sec. 6.4. As a first simplified illustration, we discuss the situation of a dipole radiating in air (refractive index approx. 1). In Ref. [45], the collection efficiency η_{coll} is given as:

$$\eta_{coll} = \frac{1}{8}[4 - 3cos\theta_{NA} - cos^3\theta_{NA} + 3(cos^3\theta_{NA} - cos\theta_{NA})cos^2\Phi] \tag{5.34}$$

θ_{NA} gives the maximum collection angle with respect to the optical axis. For our microscope objective with a numerical aperture (NA) of 0.8, this angle amounts to 53.1°. Φ gives the angle of the dipole with respect to the optical axis (laser propagation direction). Figure 5.23 illustrates the obtained collection efficiency. It is clear, that depending on the dipole orientation, the collection efficiency varies by a factor of 2.4 ranging from approx. 10% for a dipole oriented along the optical axis to approx. 25% for a dipole oriented perpendicularly to the optical axis.

However, this simplified picture does not describe the investigated situation: The dipole representing a single SiV center is located within a distance of several hundred nanometers of a metal interface. As discussed, e.g., in Ref. [233], the presence of a metal interface significantly modifies the radiation pattern and thus the collection efficiency of the fluorescence light of single emitters. The following discussion together with Figs. 5.24 and 5.25 is based on a calculation performed by Dr. Mario Agio (CNR Florence) and is reproduced with permission. The radiation properties

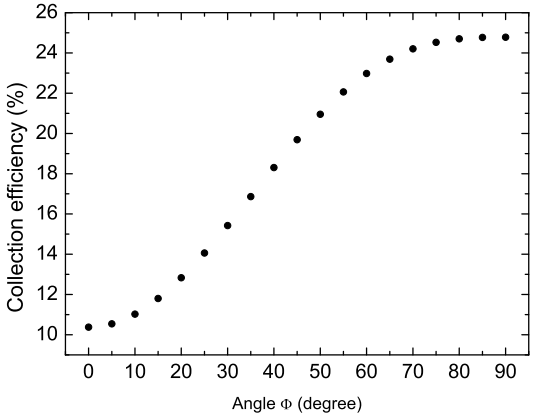

Figure 5.23: Collection efficiency for a single dipole in air using a NA 0.8 objective according to Ref. [45]. Φ gives the angle of the dipole relative to the optical axis.

of the SiV color center are investigated by considering a point-like oscillating dipole in air near an interface [236]. This simplification neglects the fact that the color center is located in a ND/NI with unknown shape and size. The simplification is necessary to perform the calculation and has to be considered as an estimate as discussed below. For the case of an SiV color center in a ND on Ir, the dipole is located in air near a semi-infinite metal substrate (refractive index of Ir $\sqrt{-18 + i \cdot 25}$ at 740 nm according to Ref. [237]). Assuming a semi-infinite metal substrate is reasonable, as the Ir layer is 150 nm thick and no light penetrates the Ir layer and reaches the underlying layers of the multilayer substrate (see Sec. 4.2.4). Here, the collection efficiency calculation is performed by normalizing the detected power, i.e., the fraction of power radiated in the solid angle determined by the NA of the microscope objective, by the radiation emitted in the upper half space. The amount of energy transferred to the metal substrate in the lower half space is absorbed and, for very short distances, it gives rise to the well-known effect of fluorescence quenching [236]. The calculations of the far field radiation pattern are performed by expanding the dipole field in plane waves. Each partial wave fulfills the boundary conditions at the interface through the Fresnel coefficients. Further details can be found in Refs. [238] and [239]. For the calculation of the modification of the radiative decay rate, the total power emitted by the dipole near the interface is divided by the same quantity in vacuo.

The results of the simulation are summarized in Fig. 5.24. Note that in the following, we use the dipole orientation relative to the Ir surface instead of using the orientation relative to the optical axis as introduced above. The optical axis here is perpendicular to the Ir surface. We point out that only the cases of a dipole parallel [Fig. 5.24(a)] and perpendicular [Fig. 5.24(b)] to the Ir surface can be calculated. A dipole perpendicular to the surface is efficiently not excited: The projection of its dipole moment into the sample plane, i.e., the plane perpendicular to the laser propagation direction (optical axis), is zero. The electric field vector of the laser is located in the sample plane, i.e, the polarization vector of the light lies in the sample plane, thus a perpendicularly oriented dipole cannot absorb excitation laser light. We point out that the assumption of a polarization of the laser light in the sample plane is not fully valid taking into account the focussing using a high NA

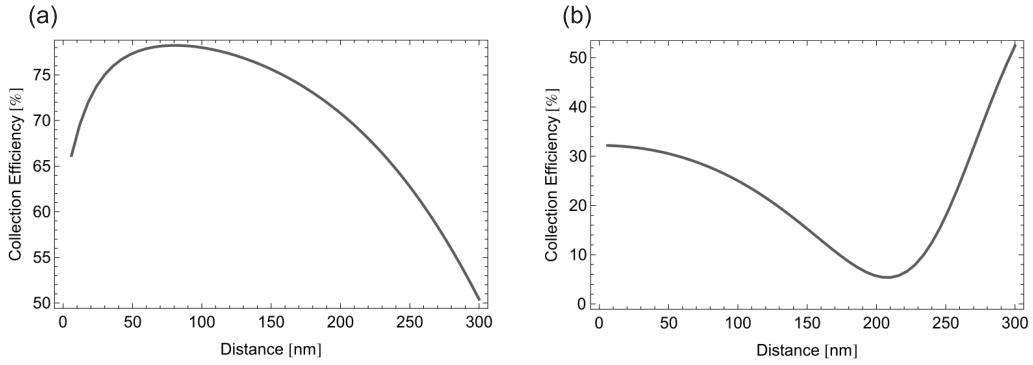

Figure 5.24: Collection efficiency for a single dipole using a NA 0.8 objective for a dipole located above an Ir substrate. (a) dipole parallel to the surface, (b) dipole perpendicular to the surface.

objective [240]. However, exactly in the focus, the polarization lies in the sample plane, thus the deviation will be small for an emitter carefully positioned in the focus. Despite the fact that a perpendicular dipole is efficiently not excited, the two cases of a parallel and perpendicular dipole can be considered as the extreme situations and thus set limits for the quantum efficiency for an unknown dipole orientation.

For a dipole located 75 nm above the Ir surface, we find a collection efficiency of 78% if the dipole is oriented parallel to the surface and 28% for a dipole perpendicular to the surface. For the NIs, 75 nm distance to the Ir surface corresponds to an emitter located as far as possible away from the surface, while for the NDs it corresponds to an emitter roughly in the center of the ND. As discussed below, SiV centers very close to the surface (distance < 20 nm) suffer from strong non-radiative decay channels, thus they are not likely to exhibit bright emission and are thus most probably not selected for investigation. We thus consider a distance of 75 nm as a reasonable estimate. The collection efficiency for a dipole parallel to the surface only changes by about 3% when changing the distance from 20 nm to 150 nm. For a perpendicular dipole, in contrast, the collection efficiency is reduced from 30% to 15%. Thus, for the perpendicular dipole orientation, the dependence of the collection efficiency on the distance to the surface is critical. We emphasize that no experimental method exists to measure the position of an SiV center in a ND.

In the following, we will try to compare our experiments using NDs/NIs on Ir to previous experiments using SiV centers in bulk diamond in Refs. [37, 74]. First, we calculate the collection efficiency of light emitted by a dipole situated in bulk diamond. For the case of SiV centers in bulk diamond, the dipole is located in the high-index medium (diamond, refractive index 2.4 at 740 nm [96]) and collection is performed in air. The collection efficiency is given by the fraction of power radiated in the solid angle determined by the NA of the microscope objective divided by the total emitted power radiated both into the lower and upper half space. The results are given in Fig. 5.25. These calculations have also been implemented by Dr. Mario Agio using the above described model and methods. Depending on the distance to the interface, the collection efficiency oscillates between 3.2 and 3.9%

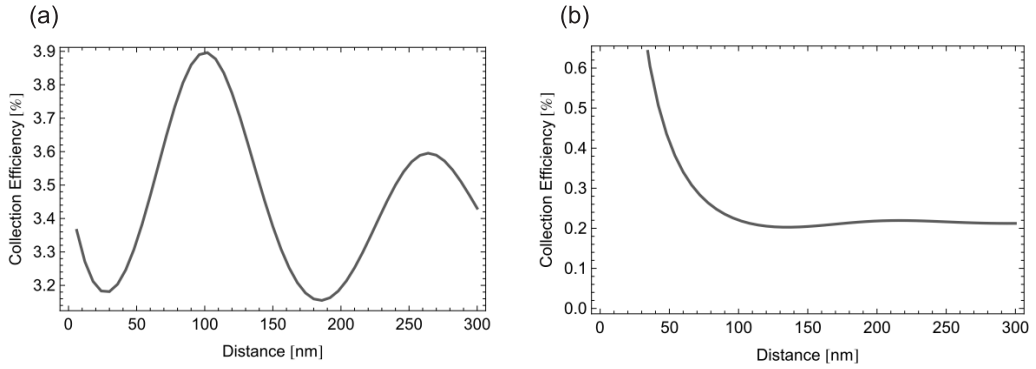

Figure 5.25: Collection efficiency for a single dipole using an objective with NA 0.8 for a dipole in diamond. (a) dipole parallel to the surface, (b) dipole perpendicular to the surface.

for a dipole parallel to the interface [see Fig. 5.25(a)]. For a dipole perpendicular to the interface, positioning close to the interface can lead to a significantly enhanced collection efficiency [see Fig. 5.25(b)]. For positions deeper than 100 nm in the diamond, only 0.2% collection efficiency is obtained. Thus, for a parallel dipole, the collection efficiency in the NDs/NIs on Ir is enhanced by approx. a factor of 20 compared to SiV centers in bulk diamond. On the other hand, the maximum photon rates I_∞ we find are about three orders of magnitude higher than observed in Refs. [37, 74]. The internal detection efficiency given for the setup in Ref. [74] is 19% and thus close to the internal efficiency of our setup (25%). However, it should be noted that Ref. [74] does not include a discussion of the transition rate coefficients similar to the discussion given here. The quantum efficiency of a single SiV center modeled as a two level system is estimated to be 0.5% in Ref. [74]. Therefore, we tentatively suggest that the enhanced brightness of SiV centers in CVD NDs/NIs cannot fully by attributed to an enhanced collection efficiency but it also correlated to a slightly higher quantum efficiency for the *in situ* produced SiV centers as discussed below.

Estimation of the quantum efficiency

We now use the calculated collection efficiencies for a dipole located 75 nm above the Ir surface to estimate the quantum efficiency η_{qe} of the SiV centers according to Eq. (5.32). We find values ranging from 0.3% and 9.2% assuming the two limiting cases of parallel and perpendicular dipole orientations. Thus, the observed quantum efficiency is comparable to previous measurements on SiV ensembles in polycrystalline films yielding $\eta_{qe} = 5\%$ [241]. The values determined here, however, do not straightforwardly represent the internal quantum efficiency of the ZPL transition, i.e., the probability for a radiative decay from the excited state of the SiV center in bulk diamond. First, for the saturation measurements, from which we obtain the maximum photon rate I_∞, only the fluorescence in a spectral window 730 nm to 750 nm is recorded. Thus, a photon emission into most of the spectral range of the

vibronic sidebands (750 nm up to approx. 875 nm) does not lead to a fluorescence detection event. Taking into account the Huang-Rhys factor of single SiV centers (see Sec. 5.2.2), roughly 30% of the fluorescence is emitted into sidebands and is thus not detected in these measurements. Thus, using I_∞ from these measurements, the sideband transitions are erroneously considered as non-radiative in this estimate of the quantum efficiency. The measured value for I_∞ corresponds to roughly 70% of the value that should be obtained for integrating over the full spectral range. Thus, according to Eq. (5.32), the quantum efficiency η_{qe} will be underestimated by 30%. However, we emphasize that the fractional intensity of the emission into the sidebands significantly varies for individual emitters, thus also the error for the estimation of η_{qe} varies. Furthermore, as discussed in Chapter 8, we find additional relaxation paths, linking the pumping levels and the ground state that include radiative near-infrared transitions. As these emission lines are not measured here, these transitions are also considered as non-radiative. In addition to influencing the collection efficiency, the presence of the metal can also influences the quantum efficiency η_{qe} as shown by simulations [242]. However, to estimate this influence, the unknown intrinsic quantum yield of the SiV centers has to taken into account [242]. Thus, the quantum efficiency estimated here is the probability for a photon emission in a restricted spectral range for an SiV center on the metal surface. Furthermore, in addition to our simple model of a dipole in air above the metal surface, the ND can strongly modify the radiation pattern of the emitting dipole: As discussed in Refs. [50, 51] and on page 4 of this thesis, in spherical particles with sizes comparable to the wavelength of the fluorescence and excitation light, resonant modes, so called Mie-resonances, can develop. The coupling to these modes can strongly modify the radiation pattern and thus the collection efficiency: Ref. [51] demonstrates a variation of the collection efficiency between approx. 1% and 20% for spherical NDs on a sapphire substrate if the size is varied from 50 nm to 200 nm. However, the assumption of spherical particles is still a simplification: The real forms of the nanocrystals mostly resemble cubo-octahedral shapes as discussed in Secs. 4.2.4 and 4.2.5. Thus, we cannot estimate the modification of the collection efficiency due to possible resonant modes in the NDs/NIs as the shape and the size of the individual ND/NI is unknown. Following the discussion above, we cannot estimate whether possible coupling to resonant modes leads to an overestimation or underestimation of the quantum efficiency. In addition to these considerations, we emphasize that the rate coefficients and thus the excited state population include uncertainties as discussed on page 83. Furthermore, the measurement of the maximum obtainable photon rates includes an uncertainty due to the contribution of background fluorescence. A quantum efficiency strongly deviating from 100% might have several reasons that will be discussed in the following.

Non-radiative decay: near field coupling to the Ir substrate

First, the proximity to the metal surface can be responsible for non-radiative decay channels. This, effect has, e.g., been discussed for CdSe quantum dots in Ref. [233]. To estimate the influence of the metal layer on radiative and non-radiative decay rates, three-dimensional finite-difference time domain calculations have been per-

formed using a commercial software package (FDTD Solutions, Lumerical). The FDTD numerical method solves Maxwell's equations in the time domain on a discrete spatial grid. By using suitable detector planes, the radiated power is determined and by comparing the results with and without the presence of the Ir layer, the influence on radiative and non-radiative decay rates can be estimated. The results have originally been published in Ref. [38], the calculation has been performed by Janine Riedrich-Möller and is reproduced with permission. To simplify the problem, we assume an emitting dipole in a semi-infinite diamond slab (refractive index n = 2.4) above a semi-infinite iridium (Ir) layer with $\epsilon = -18 + i \cdot 25$ at 740 nm according to Ref. [237]. The dielectric function of Ir indicates the fundamental problem of a close proximity to the surface: The complex part of the dielectric function indicates significant losses in the metal. These losses in turn lead to the occurrence of non-radiative decays, i.e., dissipation of energy via the metal, that are, in this model, not present without the metal.

The orientation of the transition dipole of the SiV center is unknown here. First, this is due to the fact that in some cases randomly oriented NDs have been used. Second, also in oriented diamond, different equivalent directions are possible and the dipole moment corresponding to the SiV center's luminescence transitions is still subject to discussion (see Chapter 6 for discussion). Thus, to illustrate the influence of close proximity to the metal substrate we simulate a dipole parallel to the Ir layer as a first estimate. The influence of the metal layer might roughly be divided into two regimes: At distances $\gtrsim \frac{\lambda}{2}$ (≈155 nm in diamond for the SiV centers), the lifetime mostly exhibits an oscillatory behavior. This is due to far-field interaction of the dipole with its mirror image [233, 243, 244]. Here, we disregard this regime as we are interested in dipoles with close proximity to the metal layer to investigate the quenching.

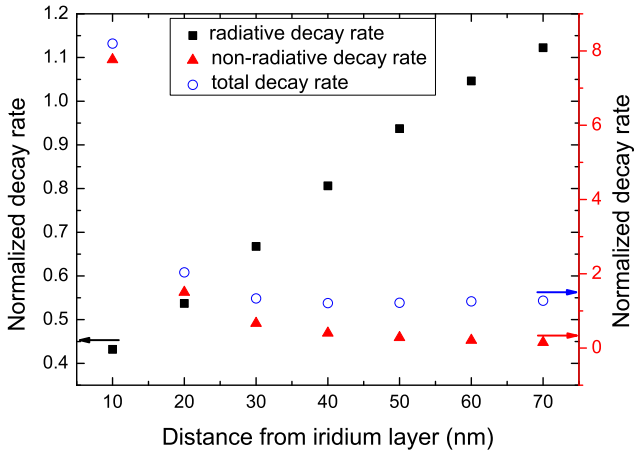

Figure 5.26: Decay rates of an emitting dipole in diamond parallel to an Ir layer for different distances from the layer. The decay rates have been normalized to the rates of the dipole embedded in diamond without the presence of the iridium layer.

Figure 5.26 displays the simulation results for the radiative and non-radiative as well as the total decay rates for a dipole parallel to the Ir layer at distances between

10 nm and 70 nm from the Ir surface. Note that the rates are normalized with respect to the decay rates of an equivalent dipole in bulk diamond. At the distances shown, there is a strong influence of the metal as the dipole near-field components can efficiently couple to evanescent waves in the metal. The modification of the decay rates is especially pronounced for distances of less than 20 nm: Due to the near-field coupling to the lossy metal, the non-radiative decay rate is enhanced by a factor of eight, while the radiative decay is simultaneously lowered by more than a factor of two. For a distance of 60 nm, the decay rates roughly match the rates for the dipole without the presence of the Ir layer. Thus, the presence of the metal layer might account for a spread of approx. a factor of eight in the excited lifetime due to the varying positions of the color centers in the NDs. In our measurements, the lifetime is indicated by the low excitation power limit of the parameter τ_1. However, we note that this lifetime reduction does not lead to an enhanced radiative decay due to the quenching by the metal in accordance with previous observations [243].

Non-radiative decay: phonons and defects

More general, quenching of color center luminescence by the proximity to defect rich crystal areas has been reported in the literature: In Ref. [245], the total lifetime of NV centers in detonation NDs is monitored during several oxidation steps. For detonation NDs, oxidation removes significant amounts of graphite and disordered carbon from the surfaces. After this process, the total lifetime of NV centers in the detonation NDs is prolonged, while the luminescence from the diamonds is enhanced. Thus, the longer lifetime indicates a reduction of non-radiative processes as the total lifetime approaches the radiative lifetime of the system. However, the actual process leading to the quenching is not discussed or identified in Ref. [245]. In Ref. [51], quenching of the luminescence of chromium-related centers due to crystal damage as consequence of heavy ion irradiation is indicated. In Ref. [246], the authors report a decrease by a factor of 20 for the luminescence of *in situ* produced SiV centers upon formation of structural defects and non-diamond carbon phases in the CVD NDs employed. Despite a high crystal quality of the NDs/NIs employed in this work, defects like dislocations are present in the diamonds and might possibly induce a quenching.

In addition to the proximity to metal surfaces or defects, generally, in a solid state host radiative transitions can be quenched by the direct emission of phonons (multi-phonon relaxation). As an estimate for rare earth ions in solids, it has been found that if the transition energy of a luminescent transition is less than 4 times the phonon energy in the crystal, i.e., the emission of 4 phonons can bridge the transition energy, luminescence on this transition will be fully quenched [247]. If the transition energy amounts to between 4 and 10 phonon energies, temperature dependent quenching can be observed. On the other hand, for a transition energy of more than 10 phonon energies, multi-phonon relaxation becomes negligible for rare earth ions. Other authors state that for 5 or less phonon energies non-radiative decay becomes significant (Ref. [141] and references therein). To avoid the quenching due to multi-phonon relaxation, for rare earth ions, host materials with low phonon energies are used [247]. Diamond, however, supports comparably high energy phonons with up

to 165 meV (discussion see 1.3.3). It should be pointed out, that the multi-phonon quenching also depends on the electron-phonon coupling: It increases with stronger electron-phonon coupling [141].

As the diamond lattice supports phonons with energies up to 165 meV, the 1.68 eV transition of the SiV center is equal to 10.2 phonon energies. Thus, quenching due to multi-phonon emission might occur but is not expected to be dominant considering the transition energy and the comparably low electron-phonon coupling. In Ref. [141], the author discusses the possibility of infrared emission from color centers in diamond. It is pointed out that lifetimes for low energy transitions (here energies less than 2 eV), in general, are shorter than lifetimes for transitions in the visible spectral range. The author of Ref. [141] attributed this lifetime shortening to non-radiative decay becoming more important, thus indicating the possibility of phonon-quenching despite the still large number of phonons in a multi-phonon emission process.

Non-radiative decay: the DKR criterion

In addition to this direct quenching due to phonon emission, another quenching mechanism has been introduced by Dexter, Klick and Russel in 1955 (Ref. [248]). The original work deals with so called F-centers, color centers in alkali halide ion crystals (e.g. KCl, NaF, NaCl, NaBr) consisting of an anion vacancy [249]. It is motivated by the observation that F-centers in several alkali halide crystals exhibit quantum efficiencies of only several %; however, the low quantum efficiency is not likely to be due to multi-phonon emission processes [248, 250]. Figure 5.27 depicts the process introduced in Ref. [248] to explain the fluorescence quenching. The system is excited to a high vibrational state in the excited electronic state (point B). For F-centers, a transition to highly excited vibrational states often is the most probable Franck-Condon transition (for further discussion see also page 15). The center subsequently starts to 'cool' by dissipating energy via phonons to reach the excited state equilibrium, point A. This relaxation is fast, e.g., Ref. [250] reports 0.6-10.5 ps as lifetime of vibrationally excited states in F-centers in alkali halide crystals. During this process, the center may cross point C in Fig. 5.27. At this point, the energy of a low lying vibrational state in the electronically excited state matches the energy of a highly excited vibrational state in the ground state. Thus, at this point no activation energy is needed to redistribute the electronic wave function, i.e., a transition to the electronic ground state [248]. Therefore, the color center can undergo a non-radiative transition with high probability. This process, however, is only likely to occur, if point B is higher in energy than point C, i.e., if the color center gains enough excess energy due to the excitation laser field. The energetic position of point C is determined by the configuration coordinate diagram in excited and ground state. The authors of Ref. [248] find evidence that depending on the energetic position of point C high luminescence efficiencies or quenching occur. The observation has later been confirmed, e.g., in Ref. [251] for F-centers in more than 20 alkali halide crystals. In Ref. [251], the authors state that concerning this model it should be possible to obtain luminescence from all F-center systems if the excited state was populated with a low enough excess energy to avoid the

non-radiative process at point C. The criterion that the excitation of a color center has to populate energy levels lower than the crossing point C to enable efficient luminescence is referred to as the *Dexter-Klick-Russel (DKR) criterion for the occurrence of luminescence*. More recent publications [249, 250] confirm this model. Furthermore, using ultrafast laser spectroscopy they find that for F-centers in NaBr the non-radiative process might occur after the relaxation to the equilibrium point A in the excited state, while for F-centers in NaI the non-radiative process occurs during the relaxation [250]. A more general discussion on the origin of non-radiative processes can be found in Ref. [252]. Stoneham and Bartram [253] also extended the model to give branching ratios between radiative and non-radiative transitions.

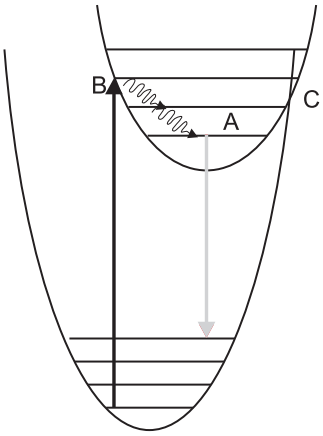

Figure 5.27: Schematic representation of color center excitation and de-excitation processes. Discussion see text.

Similar processes might be possible for SiV centers in diamond. We emphasize that, to our knowledge, the DKR criterion has so far not been applied to color centers in diamond. For SiV centers, the ZPL dominates the spectrum verifying a low linear electron-phonon coupling (see Sec. 5.2.2). A low linear electron-phonon coupling indicates that the vibrations of the color center occur approx. about the same equilibrium position in excited and ground state, i.e., the vibrational parabolas are not significantly shifted and one would expect a very highly energetic position of the crossing point C. We typically use optical excitation with excess energy of 0.1 meV (695 nm) or 0.17 meV (671 nm). For most of the phonon modes coupled to the SiV center as deduced from sideband spectra [see Fig. 5.7(a)], this corresponds to an excitation close to the first vibrationally excited level in the excited electronic state. Due to quadratic electron-phonon coupling, different vibrational frequencies in ground and excited state can occur and the parabolas exhibit different widths (see Sec. 1.3.3). Thus, an intersection of the vibrational parabolas for lower excess energy than in the case of only linear electron-phonon coupling is possible. The models discussed in the literature all assume a single mode model. However, from the sideband spectra, it is clear that the SiV center couples to multiple modes (see Sec. 5.2.2). Therefore, one might also think of crossing points of the vibrational parabolas for different modes in excited and ground state. As the configurational coordinate diagram as well as the different participating modes are not clear, we cannot anticipate wether non-radiative decay processes as described in the DKR

criterion are significant for the SiV center.

Experimental observation of an excitation wavelength dependent quantum efficiency

Experimentally, we find some evidence for the existence of excitation wavelength dependent non-radiative processes as discussed in the DKR criterion: Figure 5.28 displays saturation curves of emitter ND4 under continuous laser excitation with four different wavelengths (spectrum see Fig. 5.2). The excitation wavelengths of 685 nm, 695 nm, 705 nm and 715 nm are created using a tunable titanium sapphire laser system. Note that all curves have been fitted without background correction as the emitter is very bright and displays a negligible background contribution. It is clear from Fig. 5.28 that the saturation power P_{sat} changes with the excitation wavelength. This might be due to a change in the absorption coefficient of the color center but also due to a wavelength dependent polarization rotation of the excitation laser light or changes in the transmission/reflection coefficients of the microscope objective or the dichroic mirror. Due to these experimental issues, the change in saturation power will not be discussed here. Figure 5.28 also lists the maximum obtainable count rates I_∞. It is clear that the maximum obtainable count rates I_∞ show a trend to increase with increasing excitation wavelength and thus with decreasing excess energy in the excited state. For a wavelength change from 685 nm to 715 nm, the obtained maximum count rate more than doubles. We emphasize that the change in count rate cannot be attributed to a change in collection or detection efficiency as the wavelength of the fluorescence does not change. Using power dependent $g^{(2)}$ measurements, we determine the rate coefficients of the three level system involving intensity dependent de-shelving. The rate coefficients are given in Tab. 5.4. From these coefficients, we calculate the excitation wavelength dependent quantum efficiency. The quantum efficiency assuming a parallel dipole more than doubles when the excitation wavelength is changed from 685 nm to 715 nm from 2.0% to 4.3%. For a perpendicular dipole, we find 5.5% (685 nm) and 12.1% (715 nm). Thus, the enhanced brightness reflects an enhanced quantum efficiency for reduced excitation energy. We therefore tentatively attribute the observation of an excitation wavelength dependent brightness of a single center to excitation energy dependent non-radiative processes as introduced in the DKR criterion. To verify this suggestion, the quantum efficiency has to be determined for more emitters using a larger excitation energy range.

Summary of the chapter

In this chapter, we introduced the experimental method employed to locate single SiV centers in confocal scans via the comparison of the fluorescence intensities in two disjunct spectral windows. We performed extensive investigation of the room temperature spectra of single SiV centers, taking into account the ZPL and the sidebands. For the ZPLs, we find an average linewidth of 1.3 ± 0.5 nm in NIs, 1.7 ± 1.2 nm in NDs and 1.0 ± 0.2 nm in a heteroepitaxial (001) film. Linewidths for single centers can be as narrow as 0.7 nm, thus SiV centers show the narrowest

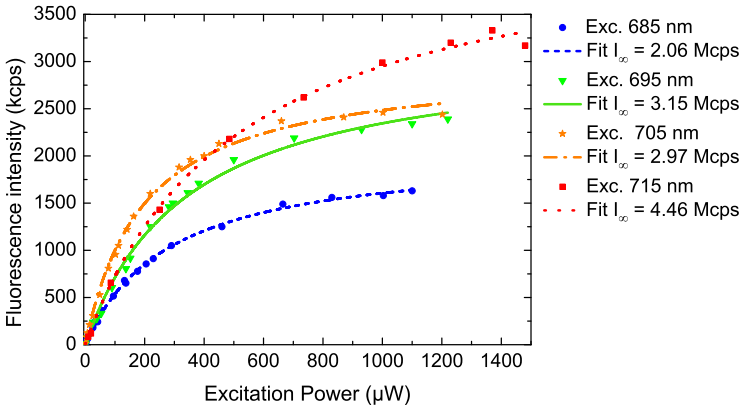

Figure 5.28: Wavelength dependent saturation curves of emitter ND4. Fitting does not include background contribution.

Exc.	k_{21} (MHz)	k_{23} (MHz)	k_{31}^0 (MHz)	d (MHz)	N_2^∞ ($P = \infty$)	I_∞ (Mcps)	η_{qe}^{par} (%)	η_{qe}^{perp} (%)
685	1271	17.73	0.28	12.75	0.42	2.06	2.0	5.5
695	1147	21.8	0.094	15.5	0.42	3.15	3.4	9.4
705	1084	31.7	0.12	13.1	0.29	2.06	3.3	9.2
715	1130	18.9	0.26	16.22	0.47	4.46	4.3	12.1

Table 5.4: Excitation wavelength dependent rate coefficients for emitter ND4. Maximum excited state population, maximum obtainable photon rate as well as quantum efficiency for different excitation laser wavelengths.

room temperature color center emission observed at present. The peak wavelengths of the ZPLs of individual SiV centers spread over approx. 20 nm with an accumulation of emitters that show a ZPL wavelength between 736 nm and 746 nm. Besides the spread in peak wavelengths and the spread in ZPL linewidths, we find a varying fraction of the emission into the ZPL and the sidebands: The observed Huang Rhys factors vary between 0.2 and 0.65 (for NIs). However, for most centers, more than 70% of the fluorescence concentrates in the zero-phonon-line (ZPL). We attribute the varying peak wavelengths, linewidths and sideband emission to the local environment, especially micro stress fields at the site of the individual SiV centers. Alongside the varying spectral properties, we find SiV centers which are fully photostable even for excitation far above saturation but also SiV centers exhibiting blinking or even permanent bleaching under laser excitation. The varying photostability is attributed to the proximity to other defects possibly serving as traps for electrons. All SiV centers investigated in this chapter revealed internal population dynamics of a three level system: In addition to the excited and ground state leading to the ZPL transition, a third longer lived shelving state has to be considered. The nature of the shelving state is unclear at present. From the shelving state, the color center can either relax spontaneously or via a laser induced (intensity dependent) de-shelving pathway. We developed an extended three level model that includes a saturating, intensity dependent de-shelving rate to describe the internal population

dynamics. The rate coefficient for the ZPL transition is significantly higher than the rate coefficient for the transition to the shelving state for all investigated emitters. Nevertheless, the shelving state limits the maximum excited state population and, thus the maximum obtainable photon rate for continuous laser excitation, due to slow depopulation rates.

Due to the Ir layer on which the NDs/NIs or thin heteroepitaxial films are grown, high collection efficiencies for the SiV fluorescence up to 80% can be reached as demonstrated by simulations modeling the SiV center as a radiating dipole in air above an Ir substrate. The quantum efficiencies estimated for the ZPL transition of single SiV centers range from 0.3% to 9.2% (excitation 671 nm and 695 nm). As possible origins for the non-radiative decay, we discuss losses in the Ir layer leading to fluorescence quenching especially for emitters close to the metal layer (distance < 10 nm). Furthermore, quenching due to other defects and multi-phonon emission has to be considered. For one emitter, we observe an excitation wavelength dependent quantum efficiency that might indicate non-radiative processes triggered by the crossing of vibrational parabolas (DKR criterion) in the excited state as a source of the non-radiative decays.

Chapter 6

Polarization spectroscopy at room temperature

This chapter investigates the polarization dependent absorption of single SiV centers as well as the polarization properties of the emitted fluorescence light. The measurements aim at deducing the orientation of the transition dipole moment of the SiV center. Measurements of the polarization properties of SiV centers in randomly oriented nanodiamonds (NDs) have been published in Ref. [38]. Additionally, low temperature polarization studies on centers in randomly oriented NDs are presented in Sec. 7.5. The current chapter focusses on room temperature measurements performed using single SiV centers in (001) nanoislands (NIs) and (001) oriented heteroepitaxial diamond films. In contrast to these studies, measurements on randomly oriented NDs are subject to the following restriction: Generally, in such a system it is only possible to determine relative orientations of emission and absorption dipoles but not the orientation of the transition dipoles with respect to the diamond crystal axes. The orientation relative to the crystal axes, however, gives information about the symmetry of the center and thus may help to deduce the spatial structure of the SiV complex. Additionally, the orientation of the dipole with respect to the crystal axes is crucial for the coupling of SiV centers in single crystal diamond to photonic nanostructures, e.g., nanowires [48] or photonic crystals [69, 254].

6.1 Polarized absorption of single SiV centers

In this section, we first investigate the polarization dependent absorption of single SiV centers. To measure the polarization dependent absorption, a half-wave plate is employed to rotate the excitation laser polarization. The polarization state of the light is slightly changed upon reflection from the dichroic mirror, for a detailed discussion see Appendix B, Sec. B.1.2. Simultaneously, the emitted fluorescence intensity in the wavelength range from 730 nm to 750 nm is recorded using an avalanche photo-diode and a bandpass filter to select the spectral window. For a detailed discussion of the experimental realization, see description in Chapter 3. Such a measurement only reveals the polarized absorption properties of the color center if

the emitted fluorescence is proportional to the absorbed excitation light power. To ensure this, excitation powers far below the saturation power of the color center are employed.

First, we discuss the processes responsible for absorption of light by a single color center. In general, different absorption pathways have to be considered. For a defect-to-band excitation, electrons bound to the color center are excited to the conduction band of diamond and relax via the electronic states of the color center. However, this can also lead to ionization of the color center if the electron is not re-trapped by the color center after excitation but by other defects in the crystal. As discussed in detail in Sec. 1.3.1, we avoid this excitation path by choosing a suitable wavelength: The ground state of the SiV center was reported 2.05 eV below the conduction band edge in Ref. [138]. Thus, by employing excitation with 695 nm (1.78 eV) laser light for the NIs and 671 nm (1.85 eV) laser light for the heteroepitaxial film, we exclude this excitation path. The light absorbing transition can also be provided via transitions to higher vibrational states of the excited electronic state or higher excited electronic states of the color center. Ref. [255] presents absorption and emission spectra of diamonds containing SiV center ensembles at 80 K. Here, absorption peaks are found at 30 meV, 85 meV, 126 meV and 156 meV above the ZPL energy. The maxima correspond to excitation wavelengths of 724 nm, 702 nm, 686 nm and 675 nm. The absorption peaks show widths of approx. 15 meV to 50 meV, thus the absorption does not decrease to zero between the maxima. The authors of Ref. [255] do not identify the origin of the absorption transitions. However, taking into account the width of the peaks as well as the correspondence to sideband energies of the SiV center in luminescence (see Tab. 1.1), absorption due to higher vibrational states of the excited state seems plausible. We emphasize that taking into account this discussion, the 695 nm and 671 nm lasers address two differing absorption transitions.

If the SiV centers exhibit a single transition dipole in absorption a sinusoidal variation of the observed fluorescence $A(\theta_p)$ with minima A_0 close to zero is expected upon rotating the polarization direction θ_p of the linearly polarized excitation light. $A(\theta_p)$ is given by

$$A(\theta_p) = A_0 + A_a \sin^2(\theta_p - \alpha). \tag{6.1}$$

A_a is the amplitude of the oscillation and corresponds to the maximum fluorescence intensity. However, for a better comparison of different emitters, the intensity data are generally normalized to one. α is a phase shift, were $\alpha + 90°$ or $\alpha - 90°$ give the directions of maximum absorption. Note, that the periodicity of the function in Eq. (6.1) is 180°. The sinusoidal variation (with $A_0 = 0$) can be understood as no light is absorbed if its polarization is perpendicular to the absorption dipole axis. We introduce the visibility V

$$V = \frac{I_{max} - I_{min}}{I_{max} + I_{min}} = \frac{A_a}{A_a + 2A_0}, \tag{6.2}$$

where I_{max} and I_{min} are the maximum and minimum of the measured fluorescence. We emphasize that for the calculation of the visibility, we use the parameters A_a and A_0 obtained from fitting Eq. (6.1) to the measured data throughout this work. Using the parameters from the fit helps to gain enhanced accuracy in comparison to

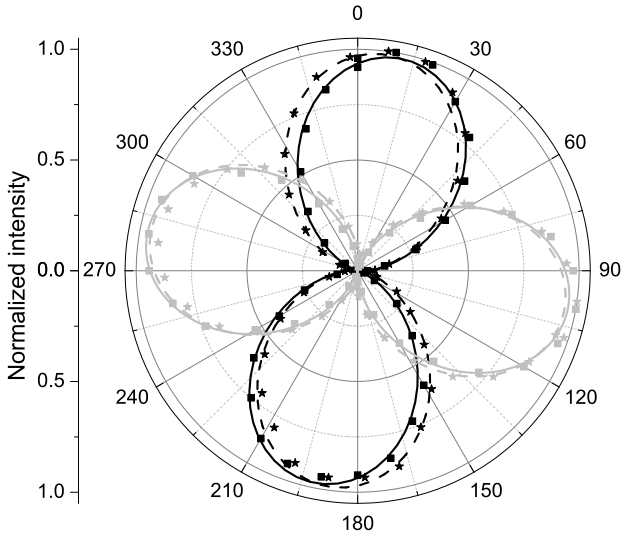

Figure 6.1: Polarization measurements for two individual SiV centers, center 1 black curves, center 2 gray curves. The fluorescence intensity has been normalized to one for both emitters. The polarized absorption (emission polarization) data is shown as filled squares (stars). The corresponding fits are shown as solid (dashed) lines.

using the measured values I_{max} and I_{min}: As the excitation polarization direction θ_p has been rotated by 360°, two minima and maxima are observed. The fit now enables an effective averaging over these maxima and minima as well as the other data points and thus enables an enhanced accuracy as compared to using only two datapoints (I_{max} and I_{min}) to calculate the visibility. For a single dipole, A_0 is zero, thus we can state that the visibility V of a single dipole in absorption amounts to one or 100% respectively. However, when deducing dipole orientations from polarized absorption measurements the following has to be considered. Polarized absorption only addresses the dipole component in the sample plane, i.e., the plane perpendicular to the excitation laser propagation direction [240]. For the (001) oriented samples employed here, the sample plane is a (001) plane of the diamond lattice. Dipoles oriented in this plane lead to maximum absorption. In contrast, dipoles oriented perpendicularly to this plane are effectively not excited. The direction of maximum absorption gives the orientation of the dipole axis projected into the sample plane.

Figure 6.1 exemplarily displays the polarization measurements for two individual SiV centers. The polarized absorption data is given by the filled squares, the sinusoidal fit to the data is indicated by solid lines. As apparent from Fig. 6.1, the curves exhibit a high visibility V: Absorption very close to zero is observed for the direction perpendicular to the direction of maximum absorption. Using the parameters A_a and A_0 obtained from the fit, both SiV centers pictured in Fig. 6.1 show 100% visibility.

Like the two emitters displayed in Fig. 6.1, all SiV centers investigated in NIs as well as in the (001) heteroepitaxial film show very high visibility V in absorption between 87% and 100%. Thus, according to the preceding discussion we conclude

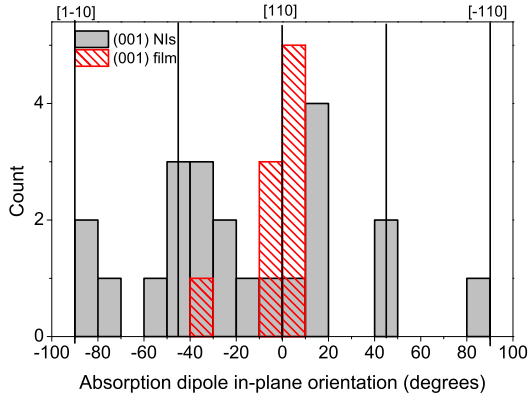

Figure 6.2: In plane dipole orientation deduced from the polarized absorption measurements on SiV centers in (001) NIs and a heteroepitaxial (001) oriented film.

that SiV centers exhibit a single dipole in absorption. Such a transition is commonly termed a π type transition (see, e.g., [256]). We attribute the deviations from 100% visibility for individual emitters to experimental imperfections. First, to determine the visibility V from the polarized absorption measurements it is necessary to correct for background luminescence of the diamond material. As the background varies spatially in the vicinity of the defects (especially for the NIs), this procedure introduces an uncertainty of approx. 5-10%. Second, the dichroic mirror used in the confocal setup to separate the excitation laser light and the SiV center luminescence induces polarization changes of the excitation light. This leads to an orientation dependent loss of linear polarization: For s and p polarization, reflected laser light maintains 100% polarization visibility. For light linearly polarized with a direction of 45°, we measure a reduction to about 90%. The experimental data for the linear polarization loss of the excitation laser light due to the dichroic mirror is summarized in Appendix B, Sec. B.1.2.

The preferred absorption of a defined linear polarization enables optimized excitation of the single color centers. Thus, choosing a suitable excitation polarization allows for low background single photon emission. The saturation curves presented in Sec. 5.3.1 have been measured using the optimized polarization deduced from the polarized absorption measurements. Partially as a result of the optimized excitation polarization, these curves show negligible background contributions to some extent. Figure 6.2 summarizes the angles of maximum absorption obtained for individual SiV centers, i.e., the absorption dipole orientation in the sample plane. As clear from Fig. 6.2, a spread in orientations is observed. The orientation of the dipole with respect to the crystal axes will be deduced in Sec. 6.4.

6.2 Polarization of single SiV center fluorescence

We measure the linear polarization degree of the emitted light by rotating a linear polarization analyzer (polarizing film, Edmund Optics, TechSpec) in the detection path of our confocal setup. Bandpass filters transmitting light between 730 nm and 750 nm select mainly the zero-phonon-line emission for these measurements. The choice of a polarizer film is motivated by experimental considerations: The thin film

can be inserted and removed without causing misalignment due to beam displacement. Using fully polarized, attenuated laser light, we verify that the polarization extinction ratio of the polarizer film amounts to 214:1 corresponding to a visibility of 99.1% (transmission of 0.47% for polarizer at 90° to polarization direction) at 740 nm. Thus, we measure almost full contrast for linearly polarized light within the experimental errors, e.g., laser intensity fluctuations. For the measurements of the emission polarization, the excitation polarization is kept fixed: Either the linear polarization corresponding to maximum absorption of the individual center or circular polarization is used. We point out that no difference in the polarization of the emitted light for both excitation methods has been found for several tested emitters. Figure 6.1 displays the emission polarization measurements for two selected emitters. The data is given as filled stars, the sinusoidal fits are drawn as dashed lines. From the fits, we obtain a visibility of 86% for the SiV center represented by the gray curves and 90% for the SiV center represented by the black curves.

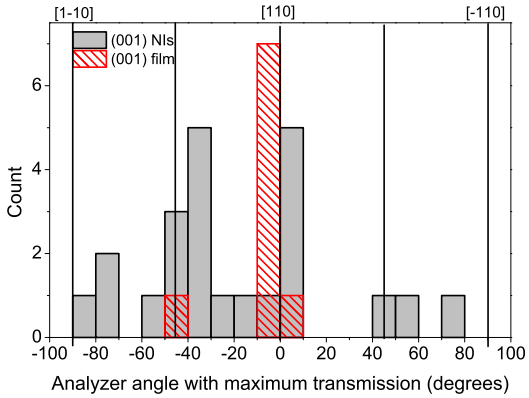

Figure 6.3: Polarization analyzer angle corresponding to maximum transmission of the fluorescence, i.e., direction of linear polarization.

Similar to the absorption measurements, we observe a high visibility V for the fluorescence polarization in the range of 85% to 100% for all SiV centers investigated in NIs as well as in the (001) heteroepitaxial film. Thus, the fluorescence light is linearly polarized. The high degree of polarization is a first hint at a negligible influence of reorientation processes of the electron wave function in the excited state of the color center as these might lead to depolarization of the emitted light as suggested for color center ensembles in Ref. [257]. Furthermore, the creation of linearly polarized single photons renders SiV centers especially suitable as single photon sources. Linearly polarized photons are, e.g., directly applicable in the frequency conversion of single photons aiming at the transformation of photons to wavelengths suitable for long range, low loss fiber transmission [258].

Figure 6.3 gives the polarization analyzer positions of maximum transmission, i.e., the polarization direction of the emitted light. However, care has to be taken when interpreting the measured emission polarization with respect to emission dipole orientations: First, the presence of the metal surface might distort the polarization of the emitted light due to varying reflection coefficients for different polarization directions. Second, due to the collection of the fluorescence light using a high numerical aperture (NA) microscope objective, loss of polarization contrast occurs for the emission of a single dipole [259]. This effect is called polarization anisotropy: In the

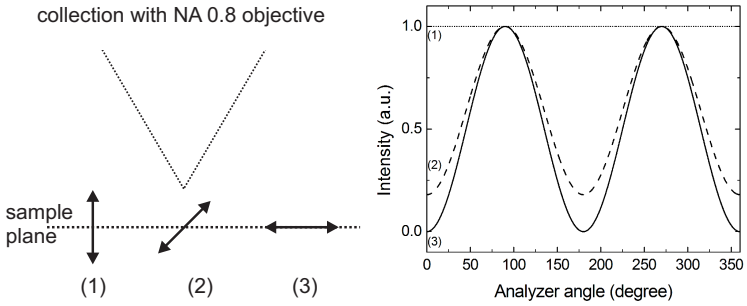

Figure 6.4: Illustration of the loss of visibility V for different tilts of the emission dipole with respect to the sample plane using imaging with an NA 0.8 objective. For simplicity, we assume the same azimuthal angle for the dipole (here 90°). Objective collection angle not drawn to scale.

imaged beam, a spatially varying polarization is observed. Thus, our measurements integrating over the beam's cross section may yield a reduced polarization contrast. The effect is illustrated in Fig. 6.4, simulated for the employed NA 0.8 objective: For a dipole oriented in the sample plane, according to Ref. [259], 100% visibility is expected. In contrast, for a dipole perpendicular to the sample plane the polarization visibility fully vanishes, whereas a 45° tilt yields 70% visibility. Thus, in principle, assuming a single dipole, one may use the visibility V as well as the position of maximum and minimum transmission to determine the three-dimensional orientation of the transition dipole [259]. However, the findings in Ref. [259] are only valid for a dipole located in an isotropic medium. This assumption does not hold for SiV centers in NIs or thin diamond films on Ir: The dipoles located close to the air-metal interface are in a highly anisotropic situation that leads to a modified radiation pattern including modified collection efficiencies (see Sec. 5.3.4). Experimentally, one also has to consider the influence of the dichroic mirror that leads to a loss of linear polarization also for the transmitted fluorescence light. We observe a loss of visibility of up to 10% for the dichroic used for 695 nm excitation depending on the polarization direction (for discussion and experimental data see Appendix B, Sec. B.1.3). Taking also into account the issue of background subtraction as discussed in the preceding section, we conclude that the polarization contrast of the emitted light is not a reliable measure to determine the tilt of the dipole with respect to the sample plane in our case. This becomes evident taking into account the orientation with respect to crystal axes discussed in Sec. 6.4: For the orientation deduced there (using the more reliable polarized absorption measurements), it is clear that dipoles oriented at -90 °, 0° and 90° lie in the sample plane, while dipoles oriented at -45° and 45° should be tilted by 45°, due to the orientation of equivalent $\langle 110 \rangle$ directions. For an illustration, see Fig. 6.6. In contrast to that expectation, we do not find a reduced visibility for the emitters with dipoles oriented at -45° and 45°. However, the measurements are compatible with a single dipole in emission and exclude the existence of two (equally strong) dipoles.

6.3 Relative orientation of emission/absorption dipoles

In the next section, we discuss the relative orientation of emission and absorption dipoles. Figure 6.1 indicates that for the displayed emitters the direction of maximum absorption and the polarization direction of the emitted light almost coincide. Figure 6.5 summarizes the observed deviations for the angle of the maximum polarized absorption and the polarization direction of the emitted light in a histogram. As the polarized absorption measurements only access the dipole component in the sample plane and the emission measurements here do not allow the assignment of the dipole's tilt in the sample plane, this comparison only holds for the component in the sample plane, i.e., the azimuthal orientation of the dipole. From the histogram in Fig. 6.5, we deduce that emission and absorption dipoles of the SiV centers are almost parallel in the sample plane. The maximum deviation is 13.9°, the mean value is 3.0°. For a purely statistical measurement error, we would expect the mean value of the deviations to be zero. We thus interpret this result as an offset of 3.0° of the polarization scale for absorption and emission. The scale for the polarization analyzer angle was calibrated by measuring polarization curves of laser light with defined polarization. Here, it should also be noted that the rotation mounts containing the polarization optics can be positioned with a precision of approx. 1.0°.

The observation of a parallel orientation of absorption and emission dipoles is very common, e.g., for organic molecules (Ref. [240]) and has also been discussed for other vacancy-based color centers for π-type absorption and emission dipoles [256]. Recent studies on chromium-related centers also found parallel orientations for emission and absorption dipoles [35].

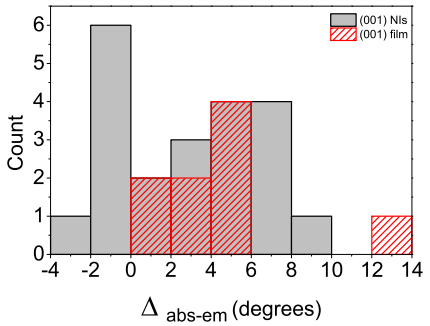

Figure 6.5: Deviation of the azimuthal angle of maximum polarized absorption and polarization direction of the emission.

6.4 Dipole orientation with respect to the crystal axes

As discussed above, the polarized absorption measurements only access the dipole component in the sample plane and its orientation (azimuthal angle). As further detailed above, in principle, emission measurements additionally allow to determine the dipole's tilt but they are not reliable for our measurements. Thus, we will focus the discussion on the orientation of the SiV center transition dipole in the sample plane deduced from our absorption measurements. The dipole orientation is equal to the direction of maximum absorption. A histogram of the obtained values is given in Fig. 6.2. To interpret these orientations with respect to crystal axes, one has to

consider that the nanoislands' ⟨110⟩ crystal directions in the (001) plane (sample plane) align with the sample edges. This has been verified using scanning electron microscope images. We identify a 0° orientation of the azimuthal angle with the [110] direction. The same considerations hold for the (001) oriented heteroepitaxial diamond film.

In the following, we try to deduce the dipole orientation of the SiV center's transition dipole as well as the underlying symmetry of the defect. A detailed discussion of the symmetry properties of color centers and of the models proposed for the SiV center is found in Chapter 2. Generally, point defects in diamond may have their highest symmetry axis, i.e., the axis with the highest rotational symmetry, oriented along ⟨100⟩, ⟨110⟩ or ⟨111⟩ crystal axes [152]. Due to the symmetry of the crystal, the defects may align along different equivalent directions. A single center thus will be oriented along one of the possible equivalent directions. For ⟨100⟩ oriented defects, three equivalent sites have to be considered. In contrast, there are six equivalent sites for ⟨110⟩ and four equivalent sites for ⟨111⟩ oriented defects [154]. Due to symmetry considerations, transition dipoles are either parallel to the high symmetry axis (z-dipole) or perpendicular (x,y-dipoles) [154]. Using measurements of polarized luminescence of ensembles of SiV centers, Brown et al. [154] assigned a single z-dipole to the ZPL transition of the SiV center. We here follow their line of argument and assume a single z-dipole for the interpretation of the orientation data. For our (001) oriented sample, considering the different equivalent directions, one expects dipole orientations in the sample plane of -45° and 45° for ⟨100⟩ oriented transition dipoles. For defects with their high symmetry axis along ⟨111⟩, -90°, 0° and 90° occur as orientations in the sample plane. ⟨110⟩ oriented defects on the other hand, lead to measured dipole orientations of -90°, -45°, 0°, 45° and 90° in the (001) plane. This is illustrated in Fig. 6.6: The in-plane oriented dipoles correspond to 0° and ±90°, while the out-of-plane directions correspond to a projected orientation of ±45°.

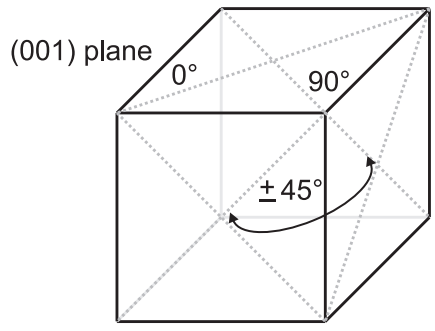

Figure 6.6: Illustration of the equivalent directions for a ⟨110⟩ oriented dipole in a (001) oriented sample and their respective projections.

As apparent from Fig. 6.2, we observe a certain scatter in orientations. The data obtained from the (001) film indicate an accumulation around an azimuthal angle of 0°. However, we point out that only 9 SiV centers have been investigated in the film, whereas 22 color centers have been investigated in the NIs, thus the following discussion focusses on the NIs. For the NIs, -90°, -45°, 0°, 45° and 90° are observed. Furthermore, an accumulation of centers with orientation between 0° and -90° is observed. This is in contrast to the fact that 90° (45°) and -90° (−45°)

are equivalent directions in the crystal. However, this observation is explained by an experimental issue: To select centers with all azimuthal dipole angles with equal probability, circularly polarized laser light is produced, to be used for the confocal scans identifying the color centers. However, as a consequence of the polarization modification of the dichroic mirror, the resulting polarization impinging onto the sample has been measured to be elliptic (ratio of approx. 2:1 semimajor to semiminor axis). This might lead to the effect described above as color centers with orientation closer to the direction of the semimajor axis might appear brighter and are thus more often selected for investigation. Despite the scatter, the measured data best match a $\langle 110 \rangle$ defect orientation. They additionally exclude $\langle 100 \rangle$ and $\langle 111 \rangle$ orientations due to the occurrence of $\pm 45°$ as well as $\pm 90°$ orientations. The scatter in orientations might be suspected to be due to an incomplete orientation of the diamond. However, SEM images imply that the spread of dipole orientations is not due to misorientation (twist and tilt) of the diamond nanoislands. The findings discussed above are thus similar to those of Brown et al. [154]: They identify the SiV center as a $\langle 110 \rangle$ oriented defect with a z-dipole. Considering the symmetry, Brown et al. assign the defect to be of monoclinic I or rhombic I symmetry [154]. According to Ref. [84], this symmetry together with a π dipole along $\langle 110 \rangle$ direction corresponds to point groups C_2 or D_2.

We now compare these observations with theoretical models. Goss et al. [122,155] model the SiV center as a negatively charged color center with D_{3d} symmetry. The silicon atom is located in the split-vacancy configuration. Their calculations identify a ${}^2E_g \rightarrow {}^2E_u$ transition as the 1.68 eV ZPL. As observed experimentally in Chapter 7, at low temperature, the ZPL splits into four components. This splitting is attributed to a Jahn-Teller effect in the model of Goss. The light emitted by a ${}^2E_g \rightarrow {}^2E_u$ transition (D_{3d}), however, should be unpolarized according to Kaplyanskii [152]. Thus, this model does not fit the linearly polarized emission and also not the $\langle 110 \rangle$ orientation. An alternative model introduced by Moliver in Ref. [123], on the other hand, assumes the center being in the neutral charge state (SiV^0). The silicon atom is shifted off center along the [111] direction resulting in a $C_{3\nu}$ symmetry. The splitting is explained in terms of a tunneling of the Si atom between equivalent sites of the $C_{3\nu}$ configuration. The 1.68 eV ZPL is associated with a ${}^3A_2, {}^3E \rightarrow {}^3A_2$ transition [123]. Here, the transition between A_2 states would be linearly polarized [152]. Thus, our polarization data would support this model of the SiV^0. Nevertheless, the measured orientation data does also not fit the symmetry proposed in the model of Moliver. Furthermore, the interpretation as SiV^0 defect is questionable, as the SiV^0 defect has recently been identified as the source of 1.31 eV emission using optical and electron paramagnetic resonance techniques [121].

Summarizing our findings, the investigated SiV centers show preferred absorption of linearly polarized light. The emission from the single color centers is also linearly polarized. Considering the findings on the dipole orientation, our results imply a lower symmetry as predicted by theoretical models discussed in the literature. However, we observe a scatter in orientations for individual centers. As other properties of single centers, e.g., lineposition and linewidth are also highly dependent on the local environment (see Chapter 5), especially on the local stress field,

one might tentatively suggest that also the spread in orientations is induced by the local environment. Furthermore, the orientation of the dipole does not match the models predicted in the literature. Further discussion of the polarization properties is found in Sec. 7.5 including the polarization of the four fine structure components. However, as randomly oriented nanodiamonds are used, no further information on the orientation with respect to crystal axis will be obtained. Further theoretical as well as experimental work is necessary to reliably determine the dipole orientation of the SiV center. A more precise determination of the dipole orientation of single SiV centers might be obtained using single SiV centers located deeply in bulk, single crystal diamond with defined orientation, thus constituting an isotropic medium surrounding the dipole.

Chapter 7

SiV centers at cryogenic temperature

This chapter discusses the spectroscopy of SiV centers at cryogenic temperature, in particular the fine structure of the ZPL observed below approx. 70 K. Sample temperatures down to approx. liquid helium temperature are achieved using the cryostat setup described in Chapter 3. First, we investigate the properties of SiV ensembles in polycrystalline CVD diamond (PCD) films and in a high quality homoepitaxial single crystalline CVD diamond (SCD) film. Second, we observe the spectra of individual SiV centers in randomly oriented CVD nanodiamonds (NDs) on Ir or NDs produced via the BASD method from diamond films. We determine the temperature dependent line positions, shifts and widths for single emitters. In the second part of the chapter, we investigate the temperature dependent population dynamics of single SiV centers, discussing temperature dependent brightness and $g^{(2)}$ functions as well as excited state thermalization. The last part of the chapter deals with the polarization properties of the emitted light, as well as the polarized absorption of single SiV centers.

7.1 ZPL fine structure at cryogenic temperature

In previous work (Refs. [111, 140]), the SiV center ZPL has been shown to split into two doublets at low temperature. This unique four line pattern may be regarded as a 'spectral fingerprint' of the SiV center in high quality, low stress diamond. The origin of this fine structure is not clear at present. However, an empirical model has introduced a level scheme where excited and ground state are split into two sub-states to describe the experimental observations [140]. As discussed in Sec. 2.3, several models for the spatial structure of the SiV complex have been discussed in the literature. Depending on the assumed symmetry, the four line fine structure can be explained in terms of a splitting of degenerate electronic eigenstates due to a Jahn-Teller effect or in terms of a tunneling between different spatial realizations of the center leading to the splitting of states. Moreover, as the spin state of the center is not clear at present, one might also suspect a splitting due to spin-orbit or

spin-spin interactions. In the following, we will briefly introduce the concept of line splitting for the case of tunneling between spatial configurations.

The concept of tunnel splitting has been introduced to explain the fine structure of electronic transitions of organic dye molecules in a solid matrix. In this context, spatial rearrangement processes on a microscopical level can lead to the splitting of electronic transitions. The problem has been intensively investigated in the literature (e.g., Refs. [260–263]). The models introduced in the literature assume that the fluorescence transition of the molecule can be described as an optical two level system (OTLS). Inside the solid matrix, this OTLS is coupled to a two level system with low excitation energy (TLS). The two energy states in the latter system arise due to the fact that atoms or molecules tunnel between local minima in the potential energy surface [262]. This tunneling corresponds to a spatial rearrangement. In general, the two possible spatial configurations have a slightly different energy. In the case of the SiV center, the described situation could occur, e.g., due to the tunneling of the Si atom between different spatial configurations of the SiV center as suggested by Moliver in Ref. [123]. The resulting level system can be described using the picture of an asymmetric double well potential for the excited state $|e\rangle$ and the ground state $|g\rangle$ as depicted in Fig. 7.1 [261]. As a result of the two different configurations, two states $|R\rangle$ and $|L\rangle$, generally with slightly different energies, exist in the two potential wells. Depending on the tunneling, the system can also be described by delocalized states in the double well indicated by gray lines [261]. Four optical transitions are possible in this system, as indicated by solid arrows [261].

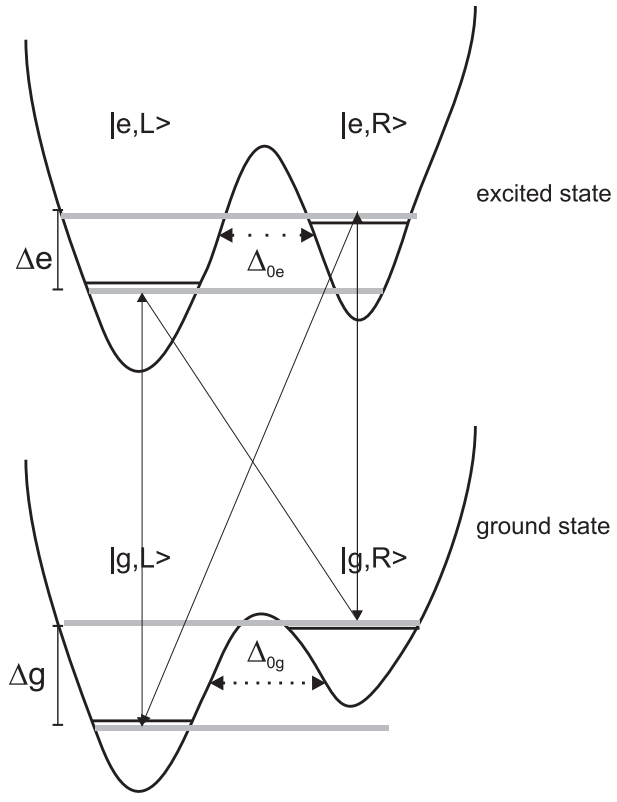

Figure 7.1: Illustration of an optical two level system with ground state $|g\rangle$and excited state $|e\rangle$ coupled to a low energy two level system (states $|R\rangle$ and $|L\rangle$). Discussion see text.

The scheme depicted in Fig. 7.1 can lead to a variety of different fine structure spectra (see Ref. [261]):[1] First, the tunneling or exchange constants Δ_{0g} and Δ_{0e}, describing the exchange between the spatial configurations, determine the dwell time τ_e in the states $|R\rangle$ and $|L\rangle$ [261]. Only if $\tau_e \cdot \Delta\omega \gg 1$ four transitions are observed. Here, $\Delta\omega$ is the energy splitting between the states $|R\rangle$ and $|L\rangle$ in frequency units. It should be emphasized that the model described in Ref. [261] assumes equal tunnel constants Δ for ground and excited state. If $\tau_e \cdot \Delta\omega \gg 1$ is satisfied the linewidth of the four transitions is determined by the intrinsic relaxation properties of the participating states. On the other hand, if $\tau_e \cdot \Delta\omega$ is close to one, only one strongly broadened line would be observed [261, 264, 265]. For the SiV center, population transfer between the excited state sublevels can be deduced from temperature dependent luminescence spectra [140]. Results for single SiV centers will be discussed in Sec. 7.4.3.

Furthermore, the asymmetry of the double well potential, i.e., the energy difference between the two spatial configurations in excited state and ground state, Δg and Δe, influences the spectral fine structure as demonstrated by simulations in Ref. [261]. Depending on the asymmetries, either two or four lines with varying intensities occur [261]. Such a varying number of fine structure components has been observed in the literature for single dye molecules in a solid state matrix [263]. As observed in Refs. [262, 263] for molecules, the asymmetry can be strongly modified by external electric fields. Assuming that the described model holds for SiV centers, also intrinsic fields due to the proximity of other charged defects in the diamond lattice might introduce significant variations in the fine structure spectra of single centers. In Sec. 7.1.2, fine structure spectra of single SiV centers will be discussed. The question arises whether the measurement of additional properties of the luminescence spectra can give information to support or disprove the model introduced above. In Ref. [262], the authors point out that a common polarization of fluorescence lines indicates that the lines belong to the fine structure of the same molecule in the case of tunnel coupling. Thus, observing a common polarization for the fluorescence lines might hint at a splitting due to tunnel coupling.

In the following, we first investigate the fine structure for SiV ensembles in poly- and single crystalline CVD diamond films. From this, we gain information on the fine structure of ensembles as well as the inhomogeneous effects influencing the ZPL. Second, we investigate for the first time the ZPL fine structure of single SiV centers. These measurements aim at the unambiguous identification of single color centers as SiV centers.

7.1.1 Spectra of SiV center ensembles

As discussed in Sec. 4.2.2, polycrystalline CVD diamond (PCD) films grown on Si substrates contain high densities of SiV centers, permitting only ensemble investigations. In ensemble measurements in PCD films, inhomogeneous broadening of the

[1] The spectra calculated in Ref. [261] are absorption spectra. However, the authors point out that these spectra are proportional to the excited state population, thus they also indicate the structure of the fluorescence spectra.

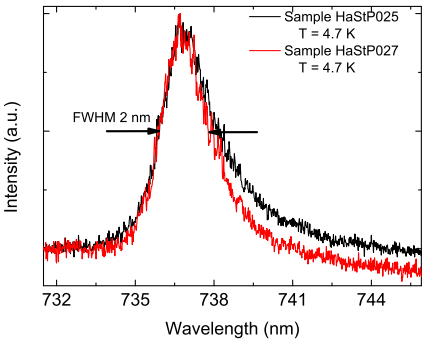

Figure 7.2: SiV ZPL in PCD films at 4.7 K excited with 532 nm laser light (for further information on samples see Appendix A). Spectra have been normalized and intensity matched at the left edge of the spectrum to compensate for different background levels of the samples.

observed lines is predominant: For SiV centers in PCD films, it leads to a linewidth of approx. 2 nm even close to liquid helium temperature as displayed in Fig. 7.2. This linewidth is comparable to or even smaller than linewidths observed in the literature: Feng et al. [139] report 10 meV (4.4 nm) at 10 K, while Clark et al. [140] find 16.8 meV (7.4 nm) at 77 K, with a reduction to 8.4 meV (3.7 nm) after an HPHT annealing step. This temperature independent inhomogeneous broadening illustrates the sensitivity of the SiV center ZPL transition energy to the individual environment. As already discussed in Sec. 5.2.1, the main source of lineshifts and thus inhomogeneous broadening in an ensemble is stress in the diamond lattice. Again, a tail toward longer wavelengths, indicating a preferential red shift, is observed. The temperature independent residual broadening easily dominates over an underlying ZPL fine structure, thus PCD films are not suitable for ZPL fine structure investigations of SiV centers.

To investigate the ZPL fine structure of an ensemble of SiV centers, we employ a high quality single crystal CVD film (sample HaStP070, fabrication see Sec. 4.2.1). As mentioned before, mechanical stress is the main source of lineshifts and thus inhomogeneous broadening of the SiV center ZPL. To avoid stress arising from thermal expansion mismatch of substrate and diamond and to obtain single crystalline, homoepitaxial growth, a (001) Ib HPHT diamond substrate is used. Further enhancement of the crystalline quality is achieved by applying optimized growth conditions involving a low methane fraction and slow growth (approx. 10 nm/h). SiV centers are created *in situ*, most probably due to residual Si contamination of the CVD reactor. We point out that the HPHT substrate does not contain SiV centers, thus all observed SiV centers reside in the high quality CVD diamond.

Figure 7.3 displays temperature dependent spectra of the SiV ZPL recorded using 532 nm excitation in the temperature range from 295 K to 6.4 K. At temperatures below approx. 70 K, a four component fine structure evolves. This structure is in accordance with the work of Clark et al. [140] and Sternschulte et al. [111]. Ref. [140] introduces an empirical level scheme with a split excited and ground state to describe the fine structure. The level scheme and the identification of the transitions is depicted in Fig. 7.4. It should be emphasized that this level scheme only leads to a four component fine structure when assuming that all four possible transitions are allowed. From the spectrum, it is not clear which line splittings give the sublevel splitting in the excited state and in the ground state. Clark et al. [140] use temper-

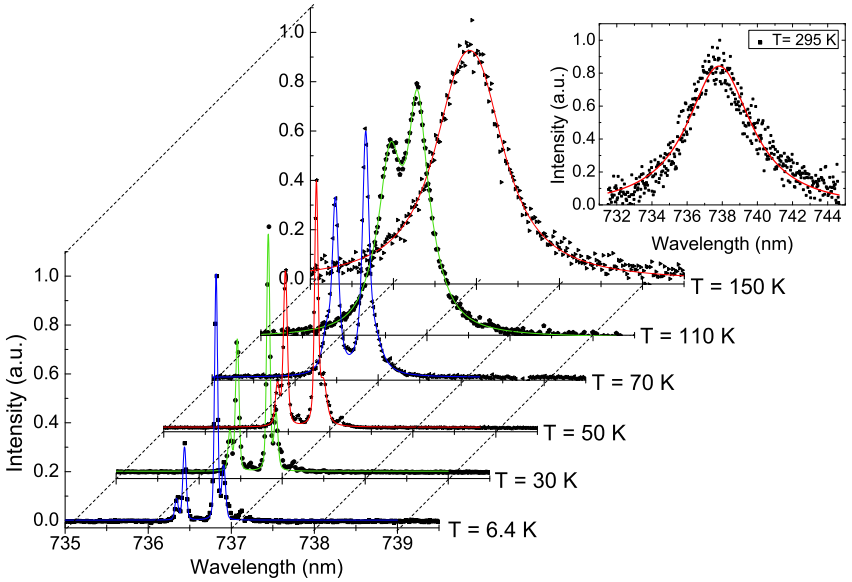

Figure 7.3: Temperature dependence of the ZPL fluorescence in a thin, homoepitaxial CVD diamond film (sample HaStP070) excited with 532 nm laser light. Spectra up to 150 K allow for the observation of the temperature dependent changes of the fine structure. The inset shows the ZPL at room temperature for comparison, note the different wavelength scales.

ature dependent measurements to assign the splittings: Fluorescence measurements indicate population transfer (thermalization) between the excited state sublevels, absorption measurements reveal the same in the ground state, thus the splittings can be assigned and the model depicted in Fig. 7.4 is established. As the splitting in the excited state is found to be approx. five times larger than in the ground state, the lines arrange in two well separated doublets. To analyze the fine structure in detail, we fit the measured data using four Voigt lines. This line form accounts for homogeneous and inhomogeneous broadening as well as the spectrometer response. The line form and the broadening mechanisms are discussed in detail in Sec. 7.2.1.

From our measurements at 6.4 K, we infer a ground state splitting of $\Delta E_g = 53\,\mathrm{GHz} = 1.77\,\mathrm{cm}^{-1} = 0.219\,\mathrm{meV}$ from the spacing of peaks 1 and 2 (see Fig. 7.4 for nomenclature). A consistent spacing of $\Delta E_g = 50\,\mathrm{GHz}$ is calculated from peaks 3 and 4 respectively. The excited state splitting amounts to $\Delta E_e = 263\,\mathrm{GHz} = 8.77\,\mathrm{cm}^{-1} = 1.09\,\mathrm{meV}$ (peaks 1 and 3) and $\Delta E_e = 260\,\mathrm{GHz}$ (peaks 2 and 4). The level splittings are therefore consistent with previous observations in Ref. [140] within 10%. The splitting values are summarized for comparison with single SiV centers in Tab. 7.2.

The spectra in Fig. 7.3 also clearly indicate a blue shift of the ZPL upon cooling. This observation is in accordance with the literature: Gorokhovsky et al. [112] report a blue shift of

$$\Delta\lambda = 1.4\,\mathrm{nm} \qquad \Delta E = -26\,\mathrm{cm}^{-1} = -3.2\,\mathrm{meV},$$

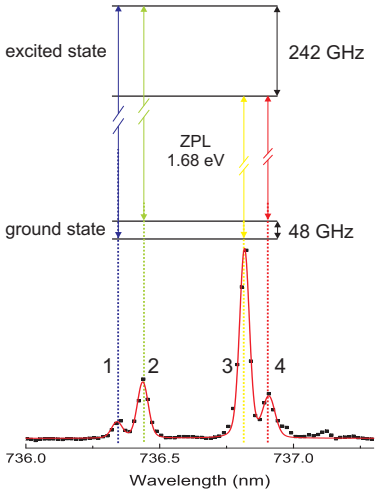

Figure 7.4: Spectrum of SiV ZPL at 6.4 K, nomenclature and identification of peaks. Level scheme according to Ref. [140].

while Feng et al. [139] report

$$\Delta\lambda = 1.2\,\mathrm{nm} \qquad \Delta E = -22\,\mathrm{cm}^{-1} = -2.7\,\mathrm{meV}.$$

Here, the lines shift from 736.82 nm (peak 3) to 737.82 nm, thus we find

$$\Delta\lambda = 1.0\,\mathrm{nm} \qquad \Delta E = -18.4\,\mathrm{cm}^{-1} = -2.3\,\mathrm{meV}.$$

confirming the shifting range in Ref. [139] within 20%. At 6.4 K the observed linewidths are fully determined by the resolution of the grating spectrometer used for spectrum acquisition (for a discussion on the measurement of the spectrometer resolution see Appendix B, Sec. B.2). Thus, reliable determination of the linewidth from the spectra is not possible as it is significantly lower than the spectrometer resolution. For the same sample, fluorescence linewidths down to approx. 10 GHz have been measured by high resolution spectroscopy using a Fabry-Perot interferometer [266], confirming low inhomogeneous broadening. The temperature dependence of the linewidth will be discussed in Sec. 7.2. The linewidth at room temperature, assuming a Lorentzian shape, is 4.45 nm. The measured value corresponds well to the room temperature linewidth of 5 nm reported for single SiV centers by Wang et al. [37, 74].

Summarizing this section, we observe a four component ZPL fine structure with spectrometer resolution limited linewidth of the components for an ensemble of SiV centers in high quality, single crystalline CVD diamond. In contrast, for PCD films, a low temperature linewidth of 2 nm illustrates the sensitivity of the ZPL transition energy to local stress fields.

7.1.2 Spectra of single SiV centers in NDs

Single centers in BASD NDs

As discussed above, PCD films on Si show high densities of SiV centers, enabling only ensemble investigations. One approach to isolate single SiV centers is the production

of NDs from PCD films containing SiV centers via the BASD method [190,191]. The employed method, the starting material and the resulting NDs are described in detail in Secs. 4.2.2 and 4.2.3. The NDs are spin coated onto various substrates to enable the observation of fluorescence from individual NDs in a confocal microscope. Figure 7.5 displays four spectra obtained from individual BASD NDs at 30 K using 671 nm laser excitation. In Fig. 7.5(a), two spectra of small SiV ensembles are shown. In contrast to the spectra from the starting material of the BASD process [Fig. 7.2 and gray curve 7.5(a)], single lines are resolved. These lines spread over the wavelength range covered by the inhomogeneously broadened ZPL in PCD films as indicated by the gray curve in Fig. 7.5(a). Nevertheless, no clear fine structure as displayed for the ensemble in single crystalline diamond in Fig. 7.3 evolves. We interpret these spectra in terms of overlapping ZPL fine structure components of single emitters or small sub-ensembles under different stress conditions. A comparably large inhomogeneous spread of ZPLs (approx. 8 nm) has also recently been observed for NV centers in mechanically crushed diamond and is attributed to the different stress fields in the NDs of different sizes and shapes [99].

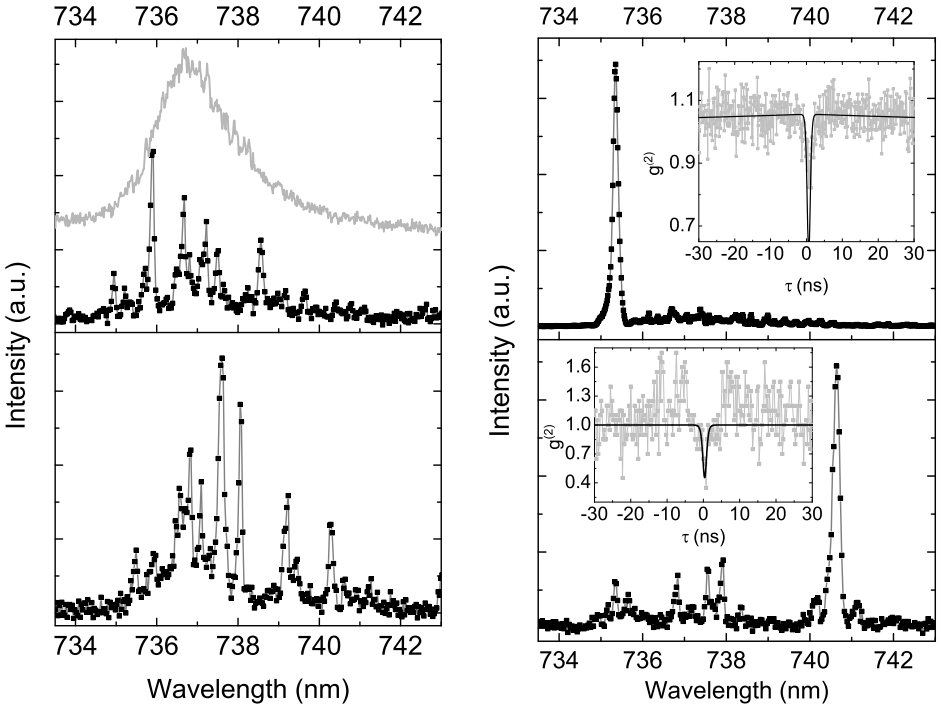

(a) Spectra of BASD NDs containing ensembles of SiV centers, spectrum of ensemble in PCD for comparison (gray curve, shifted for clarity)

(b) Spectra of BASD NDs with dominant emission from single SiV center, inset $g^{(2)}$ functions of emitters

Figure 7.5: Spectra of SiV centers in BASD NDs. All spectra measured at T=30 K under excitation with 671 nm laser light. Note that all four graphs show the same wavelength range.

In addition to the spectra of small ensembles, we observe spectra where a single line dominates the emission [Fig. 7.5(b)]. $g^{(2)}$ measurements show an antibunching dip, indicating that this intense line originates from a single emitter [insets Fig. 7.5(b)]. The emission of the underlying ensemble adds an uncorrelated background, reducing the depth of the antibunching dip (for further discussion see Sec. 5.3.2). Due to the underlying ensemble, identification of the fine structure components of these bright emitters is not feasible: Lines from other emitters might be mistaken as fine structure components. Nevertheless, analyzing the linewidth as well as the temperature dependent shift of the main peak is possible. Figure 7.6 shows the temperature dependent spectra of the dominant emitter in the upper graph of Fig. 7.5(b), in the following named emitter C5. In contrast to the spectra from the high quality homoepitaxial CVD film, the lines of emitter C5 do not reach the linewidth given by the spectrometer resolution at low temperature. This indicates an additional broadening mechanism. We attribute the additional broadening to a fluctuating charge environment in the diamond nanocrystals and the resulting fluctuations in the transition frequency (*spectral diffusion*). This effect will be further discussed at the end of this section and analyzed quantitatively in Sec. 7.2.3. The dominant line blue shifts by 1.4 nm upon cooling from room temperature to 5 K, thus reproducing the observations of Gorokhovsky et al. [112] (for detailed discussion see Sec. 7.3). Furthermore, the spectra in Fig. 7.5(b) demonstrate that bright emitters can be found with emission wavelengths in the long and short wavelength range of the inhomogeneously broadened ensemble ZPL. The mechanism enhancing the brightness of these emitters as compared to the other emitters of the underlying ensemble in the same ND is not clear at present. The fact that emitter C5 was not destroyed by several oxidation steps that repeatedly reduce the size of the NDs hints at an incorporation in the core of the NDs [267]. This incorporation in a 'high quality' crystalline region might aid in reducing non-radiative processes, thus enhancing the effective brightness of the emitter.

Single centers in CVD NDs on Ir: identification via $g^{(2)}$ measurements

In contrast to the observations in BASD NDs, in CVD NDs on Ir single SiV centers without underlying ensemble emission have been observed at room temperature (sample description see Sec. 4.2.4, room temperature spectroscopy see Sec. 5.2). Figures 7.7–7.10 display the temperature dependent spectra of four single SiV centers in CVD NDs. The emitters are labeled C1-C4. Emitter C1 is located in sample MFDIA865A, while emitters C2-C4 are located in sample MFDIA957_2. $g^{(2)}$ measurements reveal a distinct antibunching feature for C1-C4 respectively. The measurements are discussed in Sec. 7.4.2. However, the question has to be raised whether a $g^{(2)}$ measurements provides sufficient evidence to ensure that all the fine structure lines observed stem from the same emitter. Emitters C1 to C3 show a four component fine structure comparable to the observations in single crystal diamond. However, for emitter C3, the short wavelength doublet is badly resolved. In contrast, emitter C4 also exhibits four lines but without the ordering into doublets. Especially for emitter C4, one of the line components dominates the spectrum. Following the discussion starting on page 72, we determine the relative intensity of the

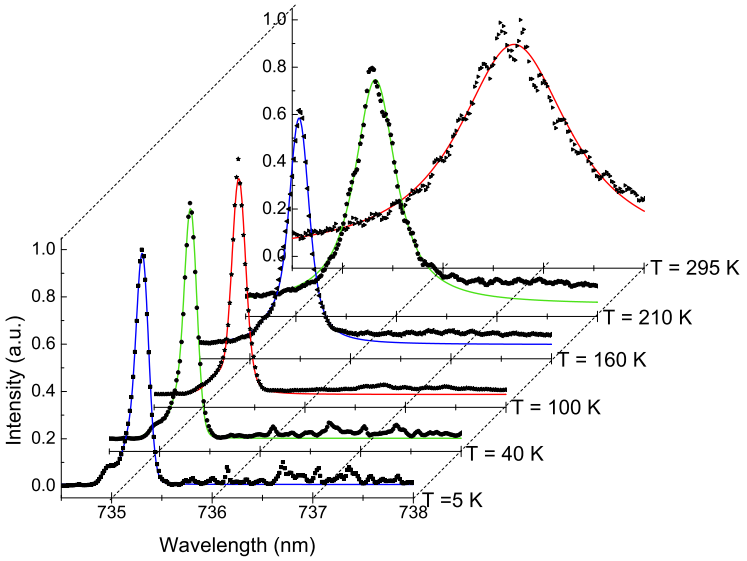

Figure 7.6: Temperature dependent spectra of emitter C5 found in a BASD ND, excitation 671 nm. Shifted to longer wavelength from the main line, the underlying ensemble is clearly visible. At temperatures above 160 K the lines of the ensemble are no longer separated from the lines of emitter C5.

line components to estimate whether a $g^{(2)}$ measurement can reliably prove that the lines originate from the same color center. Table 7.1 summarizes the intensity contributions of the different peaks. For better comparison of the emitters, the total intensity has been normalized to one. According to the discussion on page 72, additional weak emitters can be detected via deviations in the $g^{(2)}$ function if their intensity contribution to the total intensity exceeds approx. 10%. Assuming that all lines except one originate from the same emitter, for emitter C1 peak 3 and for emitters C3 peak 4 would be to weak to lead to a measurable deviation in the $g^{(2)}$ function if only this line is due to an independent emitter. However, it might be reasonable to assume that not only a single line is due to a second emitter, but that the two line doublets originate from different emitters. In this case, a clear deviation in the $g^{(2)}$ function should be observed for the fluorescence of C1 and C3. The $g^{(2)}$ function measurements for emitter C1 and C3, however, are compatible with single emitters. Thus, considering the $g^{(2)}$ measurements as well as other properties of the spectrum, e.g., the polarization discussed in the following, these spectra most probably originate from single emitters. For emitter C2 and C4, the situation is different: For emitter C2, the longer wavelength doublet dominates the spectrum, for emitter C4 a single line dominates the spectrum. Here, the $g^{(2)}$ measurements do not allow to verify the origin of the additional weak lines. Thus, we cannot conclude that the weak lines originate from the same emitters as the dominating line(s). However, additional properties, e.g., the polarization indicate that all lines belong to the same emitter for C2. For C4, the situation is even more ambiguous. The evaluation of the data for emitter C4 will thus focuss on the properties of the main line.

C1	0.17	0.52	0.08	0.24
C2	0.01	0.01	0.25	0.74
C3	0.21	–	0.73	0.07
C4	0.97	0.02	0.01	0.01

Table 7.1: Intensity contributions of the fine structure components to the overall intensity ($I_{tot} = 1$) of the spectrum. The line intensity is the area of the Voigt-peaks (discussion see Sec. 7.2.1) fitted to the spectrum at the lowest measured temperature for each emitter. Rising peak number corresponds to longer wavelength, for emitter C3 the badly resolved short wavelength doublet is termed peak 1.

Spectral properties of single SiV centers in NDs on Ir

For the single emitter spectra displayed in Fig. 7.7–7.10, three major differences compared to the ensemble spectrum in single crystalline homoepitaxial CVD diamond arise:

- absolute positions as well as spacing and intensity of the fine structure components are altered and vary between different emitters
- room temperature linewidths are significantly smaller than for the ensemble in the single crystal
- linewidths at low temperature do not reach the resolution limited linewidth of the spectrometer

The last observation, like for the BASD NDs, is attributed to a fluctuating charge environment in the NDs (spectral diffusion, see end of this Section and Sec. 7.2.3). The possible cause for a varying linewidth at room temperature is discussed in detail in Sec. 5.2.

The first observation can be attributed to stress inside the NDs: As discussed in Sec. 5.2, SiV centers in CVD NDs exhibit a spread of line positions due to stress shifting. Stress may also change the splittings ΔE_e, ΔE_g of the excited and ground state respectively. Simultaneously, positions and spacings of fine structure components change as observed in Ref. [111] for externally applied stress in $\langle 100 \rangle$ direction: E.g., for a stress of 0.4 GPa, ΔE_e amounts to 4.5 times ΔE_e without stress, whereas ΔE_g even increases to a value of 11 times ΔE_g without stress. These changes are accompanied by relative intensity changes of the fine structure components [111]. As no measurements of stress shift coefficients of the fine structure components for stress in other crystal directions exist and the single SiV centers experience an unknown stress state, we cannot directly infer the influence of stress. Nevertheless, the modified spectra might be attributed to stress induced changes in the level scheme. For comparison of the single SiV centers in CVD NDs and the SiV ensemble in the single crystal, homoepitaxial CVD film, we summarize the level spacings for emitters C1-C3 calculated from the low temperature spectra in Tab. 7.2.

Despite significant deviations, the spectrum of emitter C2 most closely matches the spectrum of SiV centers in high quality single crystal diamond: ΔE_g is approx. twice the spacing in the single crystal. Additionally, the ratio of the energy splitting in the excited and ground state $\Delta E_e / \Delta E_g$ deviates only by 6% from the value derived from the single crystal spectrum (Tab. 7.2). This is also the case for emitter

Emitter	$\Delta E_{g^{1,2}}$	$\Delta E_{g^{3,4}}$	$\Delta E_{e^{1,3}}$	$\Delta E_{e^{2,4}}$	$\Delta E_e/\Delta E_g$	$\Delta E_s(\Delta\lambda)$
HaStP070	0.22 meV 1.77 cm^{-1} 53 GHz	0.21 meV 1.68 cm^{-1} 50 GHz	1.09 meV 8.77 cm^{-1} 263 GHz	1.08 meV 8.68 cm^{-1} 260 GHz	5.1	−1.0 nm 18.4 cm^{-1}
C1	0.63 meV 5.1 cm^{-1} 153 GHz	0.73 meV 5.9 cm^{-1} 176 GHz	2.67 meV 21.5 cm^{-1} 646 GHz	2.77 meV 22.3 cm^{-1} 669 GHz	4.0	−1.4 nm 25.6 cm^{-1}
C2	0.43 meV 3.5 cm^{-1} 104 GHz	0.37 meV 3.0 cm^{-1} 88 GHz	1.94 meV 15.6 cm^{-1} 469 GHz	1.88 meV 15.1 cm^{-1} 454 GHz	4.8	−1.2 nm 22.9 cm^{-1}
C3	0.23 meV 1.9 cm^{-1} 56 GHz	0.33 meV 2.9 cm^{-1} 80 GHz	3.22 meV 26.0 cm^{-1} 780 GHz	3.32 meV 26.8 cm^{-1} 804 GHz	11.7	−0.8 nm 14.7 cm^{-1}

Table 7.2: Level spacing assuming the model depicted in Fig. 7.4 for emitters C1-C3 and for the SiV ensemble in sample HaStP070. For emitters C1 and C2, the spectra at 5 K are used, for emitter C3 the spectrum at 50 K is employed as the doublet at shorter wavelength is best resolved in that spectrum. Nomenclature: $\Delta E_{g^{1,2}}$, e.g., gives the ground state splitting calculated from the spectral positions of peaks 1 and 2, excited space splittings are labeled with a subscript e. $\Delta E_e/\Delta E_g$ gives the ratio of the mean spacing of excited and ground state. $\Delta E_s(\Delta\lambda)$ gives the overall shift rates of the highest intensity peak with temperature changing from 5 K to room temperature. For a more detailed analysis of the temperature dependent lineshift, see Sec. 7.3.

C1: Despite the fact that ΔE_e and ΔE_g are approx. three times the spacing in the single crystal, $\Delta E_e/\Delta E_g$ differs only by 22%. Thus, from the spectrum of these two emitters one might deduce that ground and excited state splitting are influenced nearly equally by stress in the crystal, e.g., doubling of the excited state splitting also leads to a doubling of the ground state splitting. Here, it is important to point out that the absolute transition energy (e.g., of peak 1) is red shifted by −5.9 meV (2.6 nm) for emitter C1 and blue shifted by 2.3 meV (−1 nm) for emitter C2 compared to the SiVs in single crystalline diamond. Despite this absolute shift exceeding the level splitting observed in a single crystal, the level scheme still is comparable to the 'ideal case' in the single crystal. We point out that similar patterns were observed for even further shifted emitters, as displayed in Fig. 7.11(d). The observations in the literature suggest a contradictory trend for stress applied in ⟨100⟩ direction: Here, ΔE_e and ΔE_g become comparable when stress is applied [111]. At no stress applied, the ratio $\Delta E_e/\Delta E_g$ is 3.7, at 0.4 GPa stress applied $\Delta E_e/\Delta E_g$ is 1.5. An explanation for the differing trend we observe lies in the unknown stress state in our measurements.

In contrast to the observations described above, the spectrum of emitter C3 indicates a strongly altered level scheme: First, the short wavelength doublet is not well resolved, only at 50 K a clear indication of two peaks is visible. Second, three peaks are needed to fit the long wavelength doublet (see Fig. 7.9). Assuming the peak hidden in the long wavelength edge of the main peak to be the second line in this doublet (marked with an arrow in Fig. 7.9), the spacings obtained are mainly consistent (see Tab. 7.2). Here, one has to take into account larger errors due to the badly resolved peaks. For emitter C3, ΔE_g differs from the single crystal value

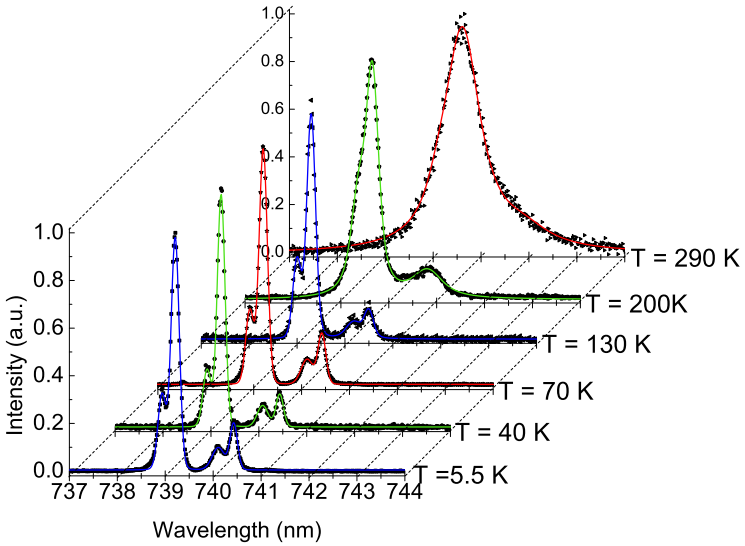

Figure 7.7: Temperature dependent spectra of emitter C1 recorded under 671 nm excitation at an excitation power corresponding to $0.92\,P_{Sat}$

by 32% (mean values), while ΔE_e is three times larger than in the single crystal. This observation would support a strong influence of stress on the excited state, while the ground state remains unaffected. Other examples for this type of altered level scheme have also been observed for single SiV centers. A stronger influence of stress on the excited state is in accordance with observations on NV centers in the literature, e.g., in Ref. [268, 269], revealing a significant influence of stress on the excited state level structure. Nevertheless, it does not fit previous observations on SiV centers under stress in ⟨100⟩ direction (Ref. [111], discussion see above).

The spectrum of emitter C4 is red shifted by $-15.3\,\text{meV}$ (6.8 nm) compared to the spectrum in single crystal diamond and thus represents a strongly shifted emitter. Here, the doublet structure is no longer identified. A main peak dominates the spectrum, therefore $g^{(2)}$ measurements cannot trace back the weak lines to the same emitter (see preceding discussion). Stress measurements in the literature [111] show that already under a moderate stress of 0.33 GPa in ⟨100⟩ direction a single line dominates the spectrum, while other fine structure components mostly vanish. Thus, also the significantly modified spectrum of emitter C4 might originate from a strongly stressed SiV center. We point out that several other emitters featuring a comparably altered spectral pattern have been observed, including spectra dominated by a doublet line, like displayed in Fig. 7.11(b) or dominated by single lines (like emitter C4). For these emitters, the ZPL fine structure cannot be used to clearly identify them as SiV centers. But, on the other hand, the spectral patterns do not exclude that these emitters are SiV centers too. To fully understand the spectral changes induced by stress and to compare them to single emitter results, knowledge of the stress response of SiV centers for stress in different directions is necessary. Additionally, charges in the vicinity of the defect leading to static electric

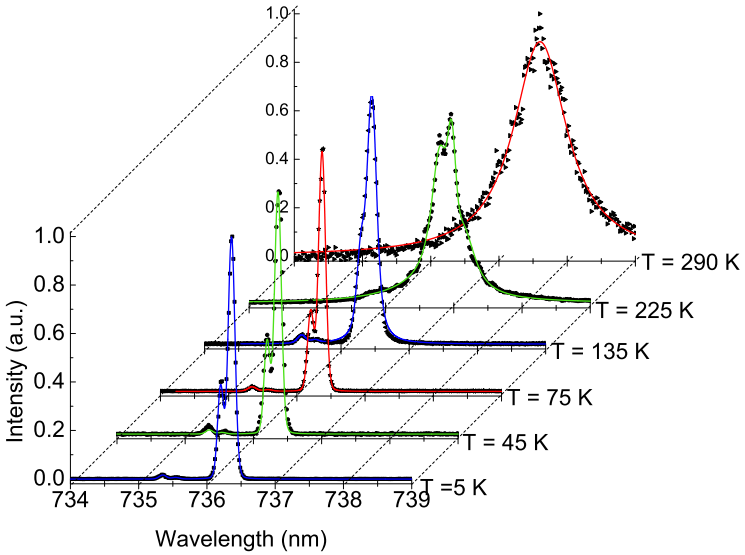

Figure 7.8: Temperature dependent spectra of emitter C2 recorded under 671 nm excitation at an excitation power of 0.16 mW

fields might influence the spectrum via the Stark effect. As there is no data on the Stark effect for the SiV center in the literature, also this influence on the spectra has to be investigated. In spite of all the differences in the spectra of emitters C1-C4 described above, it should be noted, that the overall shift with temperature is comparable: All spectra blue shift upon cooling with shifts of the main peak between 0.8 and 1.4 nm, where the blue shift in the homoepitaxial single crystal CVD diamond is 1 nm. Section 7.3 discusses the temperature dependent shift in more detail.

Irrespective of a mostly distinct fine structure, identification of lines observed in the spectra is not always unambiguous, i.e., a varying number of line components is needed to fit spectra at different temperatures: E.g., the spectrum of emitter C2 at 225 K exhibits kinks in the wings of the main line that are fitted best introducing two peaks not present in the spectra at lower temperature. The occurrence of these peaks remains unclear.

Single SiV centers in CVD NDs on Ir: additional observations

In addition to the spectral properties discussed above, we observe non-stable emission from SiV centers: Fig. 7.11(a) displays three spectra integrated for 60 s or 180 s each. The emitter observed here shows very narrow lines, with linewidth limited by the spectrometer resolution, in contrast to emitters C1-C4. Nevertheless, the relative intensity of the observed lines isn't stable. Also emitters undergoing spectral jumps have been found, as shown in Fig. 7.11(c). Three spectra are given, each integrated for 5 s and normalized to the maximum peak value. Note, that these are not successive spectra, but spectra that have been chosen to best reveal the observations described in the following. In two of the spectra, either the long or

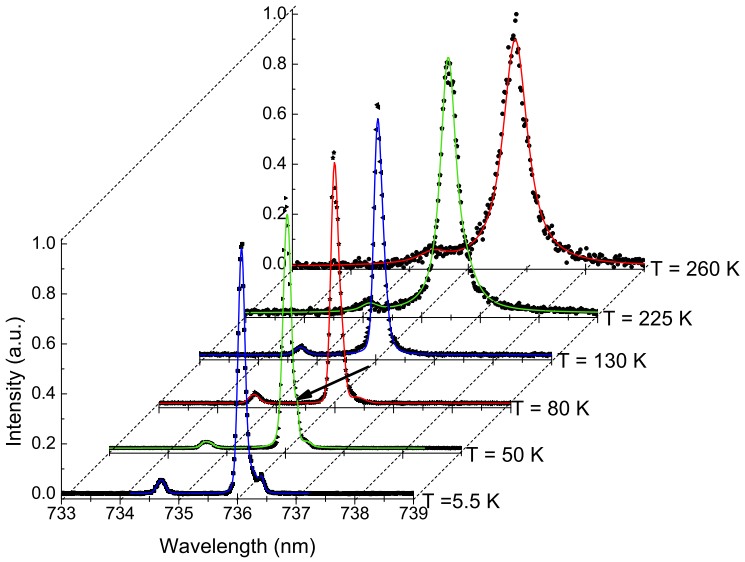

Figure 7.9: Temperature dependent spectra of emitter C3 recorded under 671 nm excitation at an excitation power corresponding to 1.6 P_{Sat}. The arrow indicates the second line in the long wavelength edge of the main line of the long wavelength doublet.

short wavelength ZPL is present [lower (blue) and central (red) curve], while in the third spectrum both ZPLs are present [upper (black) line]. Spectra of the latter kind were observed most of the time. This observation witnesses spectral jumps on a time scale of several seconds: Spectra revealing only one of the ZPLs arise if the emitter resides in one of the states for most of the integration time, while spectra revealing both ZPLs occur if the emitter resides in both states for comparable times. Remarkably, the spectra in both states resemble a very similar ZPL fine structure. An explanation for these jumps might be the transfer of an electron between SiV centers under different stress conditions: Luminescence is only observed from the momentarily charged center, thus leading to the spectral jumps of the fluorescence. Similar spectral jumps have been reported by Siyushev et al. [137] for color centers emitting around 770 nm in NDs as well as by Müller et al. [35] for chromium-related centers in IIa bulk diamond. Also spectra with a slow frequency drift have been observed: Fig. 7.11(d) shows spectra recorded for 20 s exhibiting drifts of approx. 20 GHz. As discussed in Sec. 5.3.3, temporary or permanent bleaching of SiV centers occurred at room temperature. For measurements at cryogenic temperatures, similar observations are made. These observations confirm reports in the literature: For NDs, a significant spread of emitter properties, including spectrally stable and non-stable emission, bleaching and strongly varying linewidths are reported for NV centers (Ib NDs, [269]). Ref. [137] reports comparable effects for color centers emitting at 770 nm. These emission instabilities, including the line broadening observed for emitters C1–C4 in CVD grown NDs as well as emitter C5 in BASD NDs, might arise from charges trapped inside the NDs. The line broadening due to fluctuating charges is commonly referred to as *spectral diffusion*. Sources of fluctuating charges

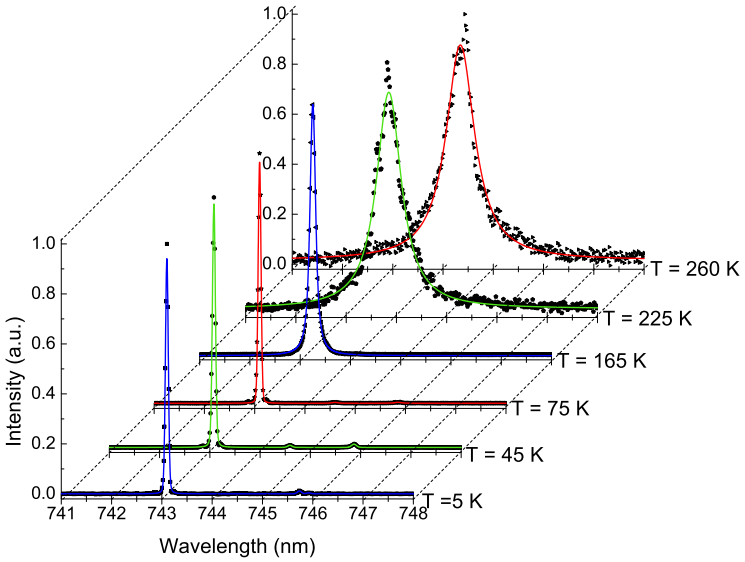

Figure 7.10: Temperature dependent spectra of emitter C4 recorded under 671 nm excitation at an excitation power corresponding to 1 P_{Sat} (5 − 10 K) and 0.7 P_{Sat} (above 10 K).

inside the NDs might be:

- **Ionization of other impurities inside the NDs** A major impurity in diamond is substitutional nitrogen [N_s]. It forms a donor with an ionization energy of approx. 1.7 eV [124–126, 269–271]. Thus, nitrogen donors in the focal volume of the excitation laser can be optically excited and photoionized, leading to positively charged $[N_s]^+$ and an electron promoted to the conduction band, given the excitation laser wavelength is shorter than 729.3 nm. Additionally, very recent experiments show that substitutional nitrogen impurities can also act as acceptors, trapping photoexcited electrons to form $[N_s]^-$, releasing the electrons again after several nanoseconds [272]. Due to these processes, fluctuating charges in the conduction band of diamond are created [270, 273]. These charges have been shown to influence the transition energy of NV centers via the Stark effect [273] and lead to linewidths of up to 90 GHz for single NV centers in nitrogen rich type Ib diamond, while in purer IIa diamond lifetime limited lines (13 MHz, both at 1.8 K) have been observed [270]. For chromium-related centers in IIa diamond ($[N_s] < 1$ ppm), also linewidths of 60 GHz were found (exc. 1.75 eV, 710 nm), witnessing significant spectral diffusion in IIa diamond [35]. Here, for the SiV centers, similar effects have to be considered as the excitation laser at 671 nm (1.85 eV) or 532 nm (2.33 eV) supplies the photon energy to ionize nitrogen donors. For the CVD NDs on Ir, we infer a concentration of single substitutional nitrogen of 40 ppb from former measurements on samples grown in the group of M. Schreck (see Sec.

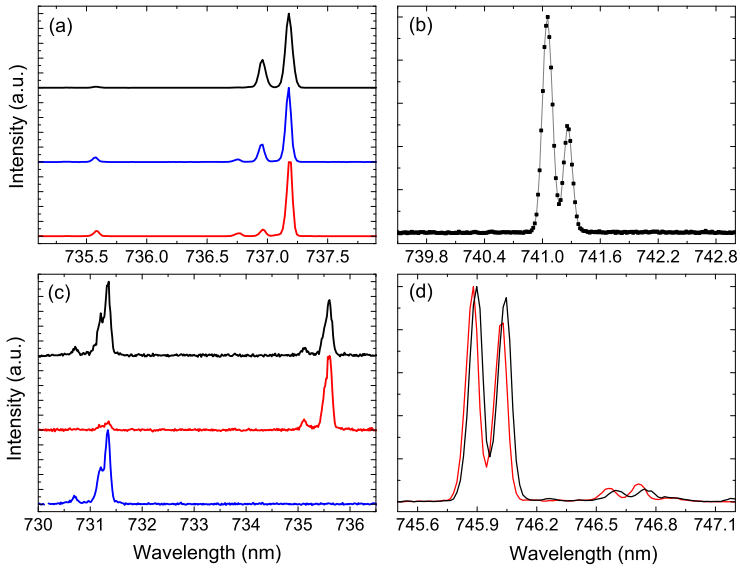

Figure 7.11: Low temperature spectra for different emitters [(a) 8 K, (b)-(d) 30 K]. All spectra are normalized to the peak value. Spectra in (a) and (c) are displaced for clarity. Note that these emitters have not been fully characterized, i.e., no temperature dependent measurements and $g^{(2)}$ measurements have been performed. Nevertheless, the spectra serve to illustrate different characteristics of the observed spectra: (a) spectrum of an emitter with resolution limited lines, but unstable relative intensity (integration time 60 s blue and red curves, 180 s black curve). (b) emitter exhibiting doublet structure instead of four lines. (c) emitter with spectral jumps, but similar spectral pattern in both states (integration time 5 s). (d) strongly shifted four line pattern exhibiting spectral drifts (integration time 20 s).

4.2.4, [197]). For the BASD NDs, we cannot estimate the nitrogen content.[2] Thus, for the CVD NDs, we expect about 10 donors to be present inside a single ND[3] available for ionization. Considering the small ND volume in which these charges are confined, the influence on the color center transitions might be significant: 10 elementary charges at a distance of 130 nm lead to fields of roughly estimated 9×10^5 V/m, while a single electron at a distance of 3.5 nm (10 lattice constants) leads to fields reaching 1×10^8 V/m.[4] Apart from nitrogen donors, other impurities in diamond exist in multiple charge states switching their charge state continuously under laser excitation (photochromism). This effect has, e.g., been observed for NV centers [125]. Also for the SiV center, charge state conversion has been discussed (see page 8). Thus, one might also assume that the charging or discharging of other color centers contributes to the fluctuating charge background and might lead to line broadening or unstable emission. Investigations of the spectral diffusion

[2] As no measures have been taken to avoid nitrogen contamination, we assume a nitrogen content higher than that of the CVD NDs.

[3] ND assumed as sphere with diameter 130 nm.

[4] Field E estimated for charge Q at distance r in vacuum with $E = \frac{Q}{4\pi\epsilon_0 r^2}$, $\epsilon_0 = 8.85 \times 10^{-12}$ As/Vm.

properties of SiV centers in various NDs with significantly different but known impurity content might assist in clarifying that issue.

- **Trapping and release of charges on the surfaces of NDs** Another aspect discussed in the literature are charging effects on the surfaces of diamond: Santori et al. [126] find a charge depletion layer below the surface of implanted CVD diamond, where nitrogen donors are ionized and NV^- centers are converted to neutral NV^0. In high purity diamond, this layer may extend up to microns below the surface. Fu et al. [274] suspect the common hydrogen surface termination of CVD diamonds, leading to a p-type conductive surface layer, to cause this effect. Recent work on 5 nm detonation NDs identifies surface charge traps due to impurities, dislocations and dangling bonds as the major cause of fluorescence blinking of NV centers [230]. Similarly, in Ref. [274], NV centers implanted close to the surface of CVD diamond show strong spectral diffusion compared to *in situ* formed centers deeper in the same sample. These findings suggest that also (possibly light induced) fluctuating charges at surfaces might be responsible for spectral diffusion and non-stable emission. However, we point out that the SiV centers in the 100 nm thick homoepitaxial film also experience a close proximity to the surface without suffering from spectral diffusion. To decrease the influence of surfaces, one might think of using larger NDs, thus increasing the average distance to the surface. A second approach might be cleaning the surface and changing the surface termination by oxidizing the ND surfaces [275]. First tests have been performed yielding the stability of room temperature SiV emission after surface oxidation [267]. To investigate the influence of the surface termination on spectral diffusion, low temperature measurements using these samples have to be performed.

- **Influence of the substrate** In addition to free charges created in the diamond, one might think of charges transferred to the diamond from the metal substrate. This process seems to be unlikely: Due to the high work function of Ir (5.3 eV [276], 4.9 eV for thin films [277]) photoionization of electrons is rather improbable, however, due to the finite temperature the probability does not fully vanish.

The origin of spectral diffusion and spectral/intensity instabilities could not be conclusively determined. The linewidth arising from spectral diffusion will be quantitatively analyzed in Sec. 7.2.3 and compared for different emitters.

Summarizing this section, we were able to unambiguously identify single color centers as single SiV centers due to the four line fine structure of the ZPL. The line patterns, however, are significantly modified due to stress without a trend to preferred distortions of the spectra. Spectral diffusion leads to an additional line broadening at low temperature for most of the single emitters, in contrast to the ensemble in the homoepitaxial, single crystal CVD diamond film.

7.2 Temperature dependence of linewidth and lineform

7.2.1 Broadening mechanisms and lineform

As visible from Figs. 7.3 and 7.6–7.10, the observed ZPLs show a temperature dependent linewidth. In general, two types of line broadening may occur: A spectral line either of an ensemble or of a single emitter might be broadened by inhomogeneous or homogeneous effects. For an ensemble, homogeneous line broadening includes all processes that broaden the line without leading to different resonance frequencies within the ensemble, e.g., pressure broadening in a gas or phonon broadening in a solid as well as the broadening due to excited state lifetime. The broadening occurs due to dephasing processes [137]. The same holds for single color centers: Dephasing due to phonons leads to homogeneous broadening resulting in a Lorentzian lineshape $I_L(\lambda)$ [94, 95]

$$I_L(\lambda) = \frac{2A}{\pi} \frac{w_L}{4(\lambda - \lambda_c)^2 + w_L^2} \tag{7.1}$$

Here, w_L is the full width at half maximum (FWHM) of the line, λ_c is the peak wavelength and A is proportional to the area of the line. As discussed, e.g., in Refs. [94, 95], quadratic electron-phonon coupling introduces a temperature dependent homogeneous phonon broadening (see also Sec. 1.3.3). In the following, we will thus interpret the homogeneous broadening in terms of quadratic electron-phonon coupling and discuss it in detail in Sec. 7.2.2.

On the other hand, inhomogeneous broadening may occur. For an ensemble, this mechanism involves different resonance frequencies for different emitters in the ensemble. Examples are the Doppler broadening in gases, leading to different resonance frequencies for atoms/molecules with different velocities or the inhomogeneous broadening due to varying stress shifts in an ensemble of color centers. For a single emitter, a similar effect occurs if the resonance frequency of the emitter experiences spectral jumps in time. This effect is called spectral diffusion and leads to a Gaussian emission line shape $I_G(\lambda)$ [137].

$$I_G(\lambda) = \frac{A}{w_G \sqrt{\frac{\pi}{4\ln(2)}}} e^{\frac{-4\ln(2)(\lambda-\lambda_c)^2}{w_G^2}} \tag{7.2}$$

Here, w_G is the full width at half maximum (FWHM) of the line, λ_c is the peak wavelength and A is proportional to the area of the line. Possible causes of spectral diffusion have already been discussed in Sec. 7.1.2, including charge fluctuations at surfaces and ionization of impurities. If these processes are not thermally activated one would expect the spectral diffusion broadening to be temperature independent. On the other hand, it might depend on the excitation laser power and wavelength, as these might influence the charge density created. The experimental findings on spectral diffusion will be discussed in Sec. 7.2.3.

If both line broadening types occur the line shape is given by the convolution of a Gaussian and a Lorentzian line. This line shape is termed a Voigt-profile

$I_V(\lambda)$ [179, 278]

$$I_V(\lambda) = \frac{2A\ln(2)}{\pi^{\frac{3}{2}}}\frac{w_L}{w_G^2}\int_{-\infty}^{\infty}\frac{e^{-t^2}}{\left(\frac{\sqrt{\ln(2)}w_L}{w_G}\right)^2+\left(\frac{\sqrt{4\ln(2)}(\lambda-\lambda_c)}{w_G-t}\right)^2}\,dt \tag{7.3}$$

Analogous to Eqs. (7.1) and (7.2), w_G and w_L are the full width at half maximum (FWHM) of Gaussian as well as Lorentzian line contributions, λ_c is the peak wavelength and A is proportional to the area of the line. By fitting a Voigt-profile to the measured line shapes, we separate homogeneous and inhomogeneous line broadening contributions for the ZPL.

In the experiment, one also has to take into account the spectrometer lineform. By observing a spectral line much narrower than the spectrometer resolution, we are able to determine the spectrometer instrument response function. We find that it is also best described by a Voigt-profile, although the Gaussian width is dominant (see Appendix B, Sec. B.2 for the widths). For SiV centers in single crystalline diamond, the measured linewidth at low temperature matches this spectrometer limited linewidth, thus indicating lines much narrower than the spectrometer resolution. For emitter C1-C5, on the contrary, also at low temperature broader lines are observed. The broadened line shape of emitter C1-C5 is dominated by Gaussian contributions. At higher temperatures, however, Lorentzian contributions increase and the lineform changes. As the very complex spectral pattern in combination with the large number of free parameters for each Voigt-profile often hinders stable convergence of least χ^2 fitting for all parameters variable[5], we find the following strategy to fit the line patterns: At low temperature, we fix w_L to the value obtained from the spectrometer lineform as we assume the homogeneous broadening to be far below the spectrometer resolution at low temperature. From the fits, we obtain a constant value for w_G often up to about 50 K. We assume that this value describes the spectral diffusion linewidth for the respective line. As mentioned before, spectral diffusion might be assumed to be temperature independent, thus for higher temperature we fix w_G to the (mean) value obtained for each line at low temperature and fit w_L for the peaks. This value now gives the increasing contribution of homogeneous broadening.

In a last step, we separate the homogeneous linewidth due to phonon broadening w_L^h and the inhomogeneous linewidth due to spectral diffusion w_G^{sd} from the linewidths stemming from the spectrometer resolution w_L^{sp}, w_G^{sp}. The measured line form is given as the convolution of the actual line form emitted by the SiV centers convoluted with the response function of the spectrometer [179]. The convolution of the Voigt-profile of the spectrometer and the Voigt-profile describing the spectral line again resembles a Voigt-profile as deduced in Appendix B, Sec. B.3. From the fits, we obtain the values of the total Lorentzian width w_L and the total Gaussian width w_G. These parameters can be used to derive the widths w_L^h and w_G^{sd} if w_L^{sp}, w_G^{sp} are known by using the properties of the convolution of Gauss and Lorentz function (see also Appendix B, Sec. B.3). The following equations for the convolutions of

[5] Least χ^2 fitting performed using Levenberg-Marquardt algorithm of Origin 8.x

Gaussian and Lorentzian functions hold [179]:

$$w_L = w_L^h + w_L^{sp} \qquad w_G = \sqrt{\left(w_G^{sp}\right)^2 + \left(w_G^{sd}\right)^2} \tag{7.4}$$

For simplicity, in the following discussion w_L and w_G label the homogeneous and inhomogeneous linewidth corrected for the spectrometer induced linewidths.

7.2.2 Homogeneous broadening

As mentioned before, quadratic electron-phonon coupling leads to a temperature dependent broadening and shifting of the ZPL [94, 95] as observed in all displayed spectra. The broadening can be regarded as the uncertainty in transitions energy of the ZPL due to energy exchange between different vibrational modes (mode mixing) in the presence of quadratic electron-phonon coupling [95]. Other authors emphasize that the broadening in the presence of quadratic electron-phonon coupling arises due to an enhanced dephasing of the ZPL by quadratically coupled modes [279]. Maradudin derives a quantitative model for the broadening as a consequence of quadratic electron-phonon coupling in Ref. [95].[6] The temperature dependent linewidth $w_L(T)$ is given by:

$$w_L(T) = \beta_1 \int_0^{\omega_m} g^2(\omega)\omega^2 n(\omega)[n(\omega)+1]d\omega \qquad \text{with} \qquad n(\omega) = \left(e^{\frac{\hbar\omega}{k_B T}} - 1\right)^{-1} \tag{7.5}$$

Where ω is the phonon frequency and $g(\omega)$ is the phonon spectrum of the perturbed crystal, i.e., the crystal including the color center. $n(\omega)$ gives the phonon population term, where k_B is the Boltzmann constant and T the absolute temperature. β_1 summarizes several constants, ω_m gives the maximum vibrational frequency at the defect [94]. As the phonon spectrum of the perturbed crystal is not directly accessible in fluorescence measurements, we cannot use this formula straightforwardly to describe the temperature dependent broadening. Nevertheless, treating the crystal in Debye approximation, Maradudin derives that the width of the ZPL changes with T^7 for low temperature. Here, low temperature means low compared to the Debye temperature of the crystal [283]. In diamond, the Debye temperature is approx. 1900 K [283], thus one would expect that the low temperature model is valid up to room temperature.

Alternatively, Maradudin suggests to use the bandshape of the electronic transitions involving a one-phonon absorption (absorption coefficient $K(\omega)$) to describe the temperature dependent broadening. Assuming a quadratic relation between linear and quadratic electron-phonon coupling coefficients [see Eqs. (1.3) and (1.4) and associated discussion], as well as introducing the auxiliary function $\rho(\omega)$, Eq. (7.5)

[6] We point out that the model derived by Maradudin uses several approximations (e.g., the adiabatic approximation [280]) and has been developed for the ZPLs of color centers in Alkali Halides observed in absorption. Nevertheless, several works successfully applied the model to describe ZPLs of color centers in diamond in absorption [215, 281] and emission [215, 282].

transfers to

$$w_L(T) = \beta_2 \int_0^{\omega_m} \rho^2(\omega) n(\omega)[n(\omega)+1] d\omega \tag{7.6}$$

$$\text{with} \qquad n(\omega) = \left(e^{\frac{\hbar\omega}{k_B T}} - 1 \right)^{-1}, K(\omega) \propto [n(\omega)+1] \frac{\rho(\omega)}{\omega^2} \tag{7.7}$$

Note that these equations are only valid in the absence of local modes [95] . In Ref. [215], Davies finds good agreement of the observed linewidths for several color centers including the NV center with the model of Maradudin (indicating a T^7 dependence [274]). This result, which is in accordance with a crystal treated in Debye approximation, is interpreted in terms of a weak quadratic electron-phonon coupling in Ref. [284].

For our measurements, this second approach is also not feasible. First, we observe only emission and no absorption spectra. In the presence of quadratic electron-phonon coupling the emission and absorption spectra do not exhibit mirror symmetry about the ZPL, thus we cannot use the one-phonon spectrum in emission to deduce the one-phonon spectrum in absorption [94]. This effect is emphasized in the literature: Lawson et al. [281] list several examples that, in general, for vacancy-related centers in diamond the observed energetic shifts of vibronic sidebands with respect to the ZPL, i.e., the phonon energies of the corresponding modes, in absorption are higher than those in emission. A lack of mirror symmetry has also been observed for emission and absorption spectra of SiV centers in Ref. [255]. Second, the significant spread of vibronic sideband spectra discussed in Sec. 5.2.2 hints at a strong variation of linear and thus, as suggested by Maradudin due to a quadratic relation between linear and quadratic electron-phonon coupling [Eqs. (1.3) and (1.4)], also quadratic electron-phonon coupling. Therefore, deducing a general trend for several color centers is not possible with this approach.

Besides the model of Maradudin, more recently, Hizhnyakov et al. [283, 285, 286] postulated a model including the effect that the bonds and therefore the springs responsible for the vibration of the color center strongly soften upon the transition to the excited state. Thus, the local phonon density of states may strongly differ for a color center in excited and ground state of the center. Including this effect, Hizhnyakov et al. find a $aT^3 + cT^7$ ($a, c = const.$) dependence and verify for an NV center ensemble a dominant influence of the T^3 dependence. It is important to point out that the theory by Hizhnyakov et al. takes into account the participation of degenerate electronic states [283, 285, 286], in contrast to the theory introduced by Maradudin. For degenerate electronic states, phonon interactions can induce transitions between degenerate sublevels of electronic states (dynamic Jahn-Teller effect). Thus, in the case of degenerate electronic states, phonon interactions can results in additional dephasing mechanisms. A dominant T^3 dependence has also been observed by Halperin et al. [287] for an ensemble of color centers with emission at 415 nm or by Lenef et al. [265] for the excited state dephasing of NV centers. On the other hand, Hizhnyakov and Reineker [288] also explain a T^3 dependence in terms of fluctuating fields due to crystal defects: As a phonon modulates the distance between the color center and other defects in the crystal, oscillating fields are created.

The authors also emphasize, that the T^3 dependence has been observed in systems exhibiting a significant inhomogeneous broadening of ensembles. Hizhnyakov et al. [283] also mention a T^5 dependence of the linewidth at low temperature if the dynamic Jahn-Teller effect is the dominant dephasing process. In contrast to the above discussed treatment of the dynamic Jahn-Teller effect, the T^5 law is derived from perturbation theory and may thus be only valid for a restricted temperature range [283]. Moreover, in full contrast to the experimental findings of Hizhnyakov [283], Davies [215] and Lenef [265], Fu et al. [289] find a T^5 dependence of the ZPL width of single NV centers. While, again contradictory, Dräbenstedt et al. [264] observe a nearly linear dependence for $150 - 250\,\mathrm{K}$. The varying broadening trends observed in the literature for NV centers may be attributed to a significant influence of the crystalline environment on the ZPL broadening. In Ref. [289], the T^5 broadening indicating a dynamic Jahn-Teller effect is found for an NV center under low stress conditions. Under significant stress, degenerate states might split up, thus limiting the influence of a Jahn-Teller effect. Additionally, as introduced above, the impurity content of the diamond can influence the observed ZPL broadening. In principle, taking into account the discussion above, it should be possible to derive the line broadening mechanism from the dominant term in the polynomial $aT^3 + bT^5 + cT^7$ ($a, b, c = const.$) dependence of the linewidth on temperature. Nevertheless, the example of the NV center illustrates how critical these measurements are: Either dominant T^3, T^5 or T^7 broadening has been observed in the literature [215, 265, 283, 289].

Figure 7.12 shows the temperature dependent homogeneous linewidth of the emitters C1-C5 as well as for the ensemble of SiV centers in the homoepitaxial CVD diamond film. The single emitters show a similar temperature dependent broadening, while for the ensemble two main differences are recognizable: The broadening in the ensemble starts already at 75 K, while for the single emitters C1-C4 broadening becomes visible at temperatures above 100 K. In addition, the difference in room temperature linewidth is clearly visible. Fitting the temperature dependent linewidth to either a T^3, T^5 or T^7 dependence, it is clear from Fig. 7.12 that the latter does not describe at all the temperature dependent broadening observed here. For the ensemble in the single crystal as well as emitter C1 and C3-C5, the T^3 dependence gives the lowest χ^2, while only for emitter C2 T^5 leads to the best fit. The T^5 dependence, as discussed above, is attributed to a dynamic Jahn-Teller effect. As polarization measurements of the SiV centers (see Sec. 6.4) tentatively suggest non-degenerate electronic states, the interpretation of the T^5 or T^3 broadening as arising from a dynamic Jahn-Teller effect is questionable. However, a T^3 dependence, as experimentally reported in Ref. [287], has also been attributed to broadening by crystal defects [288]. As the low temperature linewidth is strongly influenced by spectral diffusion (see next section) also ascribed to interaction with charges from, e.g., other crystal defects, this might support the explanation of the T^3 dependence as due to crystal defect.

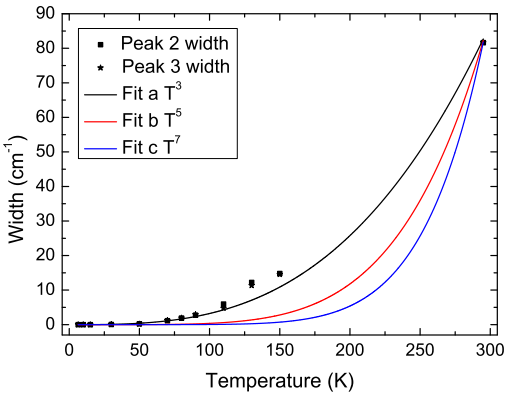

(a) Linewidth of the SiV ensemble in homoepitaxial diamond. Fit takes into account data from Peak 2

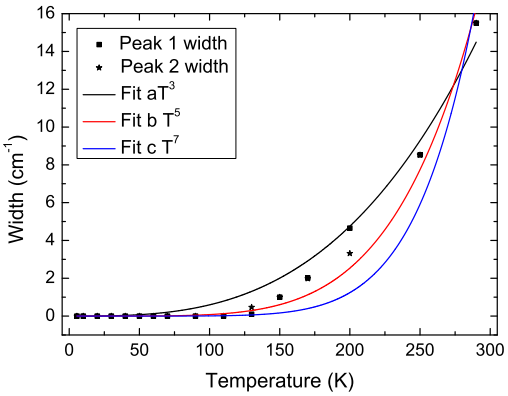

(b) Linewidth of emitter C1. Fit takes into account data from Peak 1

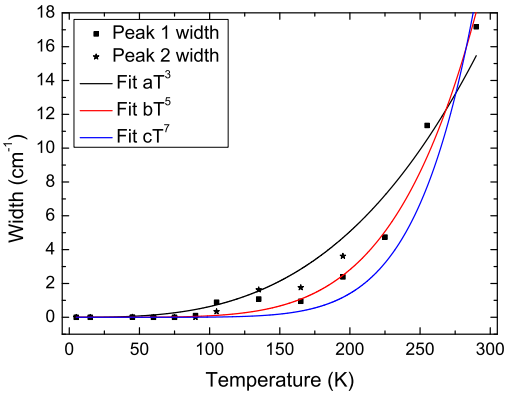

(c) Linewidth of emitter C2. Fit takes into account data from Peak 1

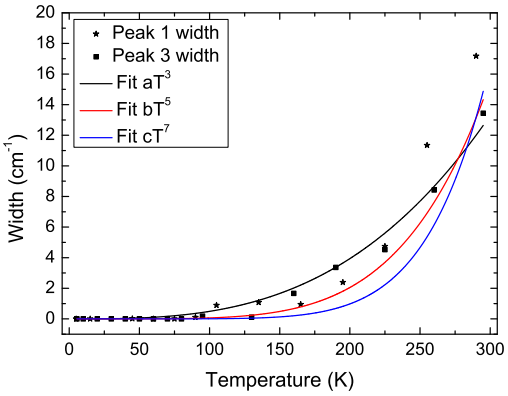

(d) Linewidth of emitter C3. Fit takes into account data from Peak 3

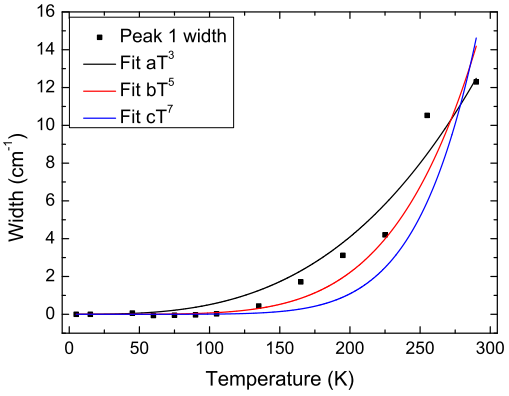

(e) Linewidth of emitter C4. Fit takes into account data from Peak 1

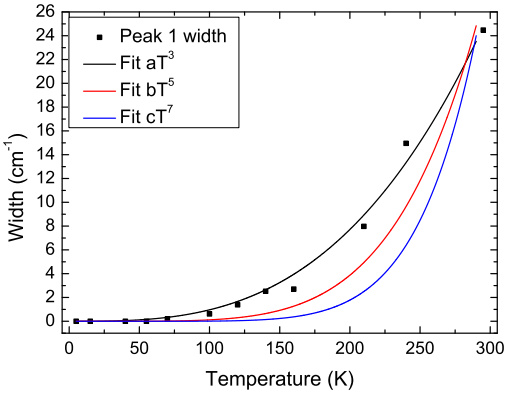

(f) Linewidth of emitter C5. Fit takes into account the main peak

Figure 7.12: Summary of the observed temperature dependent homogeneous linewidths for emitter C1-C5 and the SiV center ensemble observed in the homoepitaxial CVD diamond film. Only those peaks clearly visible over a large temperature range are shown. For some emitters, the data of several peaks is shown. Due to the similarity of the curves for different peaks of the same emitter, fitting takes into account only one peak, as given in the caption.

7.2.3 Spectral diffusion

In addition to the homogeneous broadening discussed above, inhomogeneous broadening attributed to spectral diffusion is observed for the majority of emitters in NDs. Table 7.3 summarizes the spectral diffusion linewidths for different emitters, determined using Eq. (7.4) from the fitted Gaussian width of the Voigt-profiles at low temperature. Figure 7.13 shows the spectral diffusion linewidths of emitters C1-C5 for direct comparison. For emitter C3, only the short wavelength peak and the main peak of the red shifted doublet are taken into account. As pointed out before, the short wavelength peak showed a doublet structure in some spectra. This observation, together with an unclear, three peak structure of the long wavelength doublet leads to significant errors for this emitter. For emitter C4, only the main peak is considered as the spectrum of the weaker peaks is inconsistent for spectra taken at different temperatures. Similar considerations hold for emitter C5. Emitter C4 noticeably shows the lowest Gaussian (spectral diffusion) linewidth, despite the strongly modified spectral pattern. For all emitters, the measured linewidths vary between 25 GHz and 160 GHz. Emitters C2, C4 and C5, in general, show a lower spectral diffusion linewidth compared to emitter C1 and C3. For emitter C5, this is remarkable as it is found in a BASD ND supposed to have a higher impurity concentration, i.e., other SiV centers and substitutional nitrogen. Furthermore, significant differences between individual lines of the same emitter also occur with linewidth differences up to nearly 50%. This might indicate that different transitions of the color centers can show a different susceptibility to spectral diffusion. The difference between individual emitters indicates a strong dependence on the local environment, i.e., proximity to possibly ionized impurities or surfaces (discussion see page 127). This behavior has also been reported for NV centers in NDs [269].

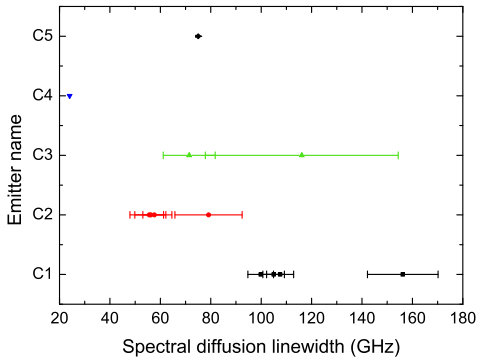

Figure 7.13: Spectral diffusion linewidths of emitters C1-C5 in GHz. Note the differences between the emitters as well as between the linewidths for individual lines of the same emitter. Emitters C1-C4 are located in CVD NDs, emitter C5 in a BASD ND.

The fitted linewidth and thus the spectral diffusion linewidth is constant at low temperature (see Tab. 7.3), thus supporting the assumption of a temperature independent spectral diffusion. Since spectral diffusion is particularly low for C4/C5, the increasing homogenous broadening starts to affect the lineform at lower temperature for these emitters. This in turn leads to an earlier onset of the observed homogeneous broadening (see Tab. 7.3).

The general lower limit of a transition linewidth is the so called lifetime limited width $\Delta\nu_{FT}$. This width is induced by the finite lifetime of the excited state which,

Emitter	Peak1	Peak 2	Peak 3	Peak 4	const.
C1	0.20(1) nm 3.6(2) cm^{-1} 1.08(6) $\cdot 10^2$ GHz 0.44(2) meV	0.191(8) nm 3.5(2) cm^{-1} 1.05(5) $\cdot 10^2$ GHz 0.43(2) meV	0.29(3) nm 5.2(5) cm^{-1} 1.6(2) $\cdot 10^2$ GHz 0.65(6) meV	0.18(1) nm 3.3(2) cm^{-1} 1.00(6) $\cdot 10^2$ GHz 0.41(2) meV	110 K
C2	0.104(9) nm 1.9(2) cm^{-1} 58(5) GHz 0.24(2) meV	0.14(3) nm 2.6(5) cm^{-1} 8(2) $\cdot 10^1$ GHz 0.33(6) meV	0.10(2) nm 1.9(3) cm^{-1} 56(9) GHz 0.23(4) meV	0.10(1) nm 1.9(2) cm^{-1} 56(6) GHz 0.23(3) meV	45 K
C3	0.21(7) nm 4(2) cm^{-1} 1.2(4) $\cdot 10^2$ GHz 0.5(2) meV		0.13(2) nm 2.4(4) cm^{-1} 0.7(1) $\cdot 10^2$ GHz 0.30(4) meV		80 K
C4	0.044 nm 0.8 cm^{-1} 24 GHz 0.1 meV				10 K
C5	0.136(2) nm 2.52(4) cm^{-1} 76(1) GHz 0.312(5) meV				40 K

Table 7.3: Analysis of spectral diffusion linewidths for different emitters. Up to the temperature value given in the column 'const.' no significant increase in the linewidth is observed (with w_L fixed to w_L^{sp} in the fit). The error values denote the standard deviation of the linewidths for the different temperatures up to the temperature value given in the last column.

via Heisenberg's uncertainty principle, leads to an uncertainty in energy/frequency for the transition. This simple consideration only holds for transitions for which the final state is the ground state. If the transition ends in an unstable state, the lifetime of both states, initial and final state, contributes to the broadening. Although, the method employed here does not offer the resolution to measure this lifetime induced broadening, we compare the measured linewidths to this theoretical limit. $\Delta\nu_{FT}$ can be calculated from the lifetime τ [9, 137]

$$\Delta\nu_{FT} = \frac{1}{2\pi\tau}. \tag{7.8}$$

As indistinguishable photons are required for several applications in quantum information, reaching this limit of so called Fourier-transform limited photons is an important goal. From the $g^{(2)}$ functions, we estimate the excited state lifetime of the emitters (C1, C3, C4) which ranges from $0.72 - 1.28$ ns yielding a lifetime limit of $0.12 - 0.22$ GHz. Thus, even the lowest measured spectral diffusion linewidth corresponds to $450 \cdot \Delta\nu_{FT}$ for emitters C1, C3 and $170 \cdot \Delta\nu_{FT}$ for emitter C4. Nevertheless, spectrometer resolution limited lines are feasible in CVD NDs as shown in Fig. 7.11 and linewidths of approx. 10 GHz have been observed for SiV ensembles in high quality, homoepitaxial CVD films [266], thus indicating that narrow lines might be obtained at low temperature for SiV centers in low-defect environments, promising the possibility of enhanced low temperature properties for single emitters.

Light induced spectral changes

For the generation of indistinguishable photons, not only the temperature dependence and the absolute value of the linewidth is crucial but also its stability with excitation power. Figure 7.14(a) shows spectra of emitter C1 at 25 K and different excitation powers. Significant changes in the spectrum arise at elevated excitation powers: The red shifted doublet gains intensity compared to the short wavelength doublet, while simultaneously both doublets broaden at the blue edge. A first approach to explain these effects might be an increased temperature of the ND due to absorption of laser light. This is possible, as the cryostat system uses a cold finger, where only the temperature of the substrate holder can be controlled. The NDs are cooled only via the substrate. Nevertheless, this approach is not conclusive, if one compares Fig. 7.14(a) to the temperature dependent spectra of emitter C1 in Fig. 7.7: For increasing temperature, the red shifted doublet does not gain intensity nor a change on the blue edge of the lines is observed. Emitter C4 also exhibits light induced spectral changes: The inhomogeneous linewidth changes from 20 GHz at $0.3\,P_{Sat}$ to 55 GHz at $14\,P_{Sat}$ [see Fig. 7.14(b)]. Similar to emitter C1, the low intensity lines are enhanced at high power, an effect not observed for elevated temperatures. We point out that for emitter C3 no significant changes are observed for excitation powers up to $2.2\,P_{Sat}$. Thus, spectral changes might be observed both, for emitters strongly affected by spectral diffusion (C1) or for emitters with low inhomogeneous linewidth (C4). Furthermore, a strong influence of spectral diffusion does not herald light induced spectral changes (C3). We tentatively attribute the observed changes to free charges created by the laser light. The observation of so called light assisted spectral diffusion has been reported for single quantum dots [290, 291] but also for single NV centers [55, 292]: In Ref. [55], the authors find a broadening of the NV ZPL by more than an order of magnitude when green laser light (532 nm) is applied in addition to the resonant red (637 nm) excitation as green laser light can ionize impurities, especially substitutional nitrogen, in the vicinity of the NV center. Light assisted spectral diffusion might be connected to the observation of spectra with unstable relative intensity as well as spectral drifts shown in Fig. 7.11.

Summarizing this section, we have intensively investigated the temperature dependent ZPL width of single SiV centers. The lineform indicates both homogeneous and inhomogeneous broadening mechanisms. Homogeneous broadening is found to depend on T^3, while inhomogeneous broadening due to spectral diffusion seems to be temperature independent. At low temperature, for most emitters, spectral diffusion defines the linewidth of approx. 20-100 GHz. Enhanced inhomogeneous broadening at elevated excitation power indicates light assisted spectral diffusion. Future experiments will have to address the reduction of spectral diffusion to enable the creation of indistinguishable single photons.

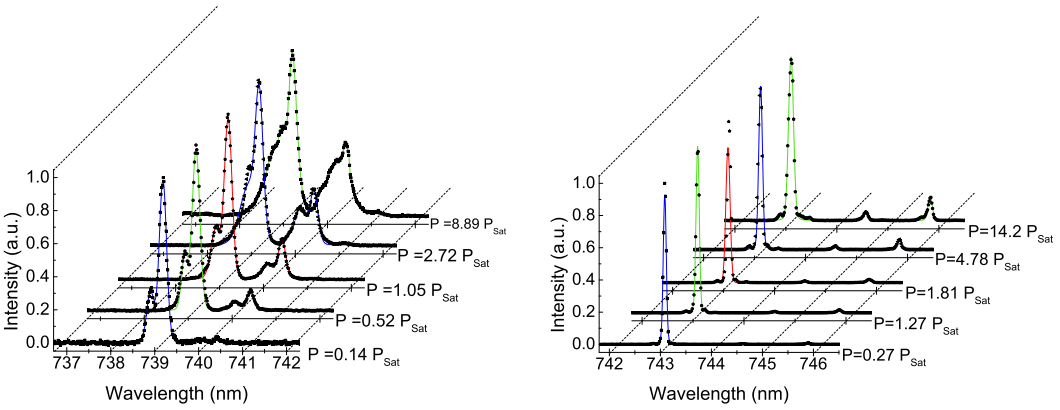

(a) Excitation power dependent spectra of emitter C1 recorded at 25 K. Spectra (except the highest excitation power spectrum) have been fitted with four Voigt-profiles, keeping w_L fixed to the spectrometer resolution value.

(b) Excitation power dependent spectra of emitter C4 recorded at 10 K. Spectra have been fitted with four Voigt-profiles, keeping w_L fixed to the spectrometer resolution value.

Figure 7.14: Light induced spectral changes for emitter C1 ($P_{Sat} = 0.416\,\mathrm{mW}$) and C4 ($P_{Sat} = 0.103\,\mathrm{mW}$.)

7.3 Temperature dependent ZPL shifts

Besides the linewidth, the exact position of the ZPL is crucial regarding the production of indistinguishable photons as well as for the coupling of SiV centers to resonant photonic structures. Figure 7.16 summarizes the temperature dependent lineshifts of emitters C1-C4 in the CVD NDs. Figure 7.15 shows the data for emitter C5 and for the ensemble in the homoepitaxial CVD diamond film. As the above mentioned applications also require cooling of the emitter to reduce the linewidth, detailed knowledge of the temperature dependent shifting of the ZPL is important.

All observed SiV ZPLs show a similar blue shift upon cooling. The overall shift ranges from $-19\,\mathrm{cm}^{-1}$ for one peak in the ensemble, to $-31\,\mathrm{cm}^{-1}$ for a peak of emitter C1. We point out that the overall shift is only an estimate as, due to the coalescence of peaks at higher temperature, an uncertainty in determining the peak positions is introduced. The observation of a blue shift and its magnitude is in accordance with reports in the literature on SiV centers as discussed before ($-26\,\mathrm{cm}^{-1}$, [112]; $-22\,\mathrm{cm}^{-1}$, [139]). Blue shifting of the ZPL upon cooling has also been observed for a variety of other color centers, e.g., Ni-N complexes [293], N_2-V (H2) centers [281], NV centers [215, 283] and several others [215]. Despite that general trend, the cause of the lineshift as well as the exact temperature dependence are discussed controversially in the literature. There are three main contributions to the ZPL shift mentioned in the literature:

- temperature dependent bandgap changes
- temperature dependent lattice expansion

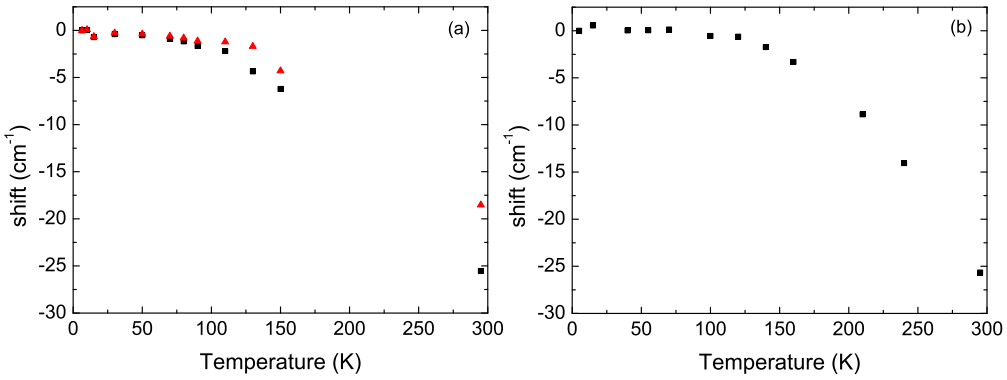

Figure 7.15: Temperature dependent lineshift for (a) the ensemble ZPL in homoepitaxial diamond and (b) for emitter C5 in a BASD ND.

- quadratic electron-phonon coupling

Feng et al. [139] explain the shifting of the ZPL in terms of a change in the bandgap E_G of diamond that is given by the empirical formula:

$$E_G(T) = E_G(0) - \frac{\alpha T^2}{T + \beta} \tag{7.9}$$

where $E_G(0)$ is the bandgap energy at 0 K and $\alpha = -1.979 \cdot 10^4$ and $\beta = -1437$ have been experimentally determined (see Ref. in [139]). Thus, if diamond is heated from 0 to 300 K the bandgap decreases by about 15.7 meV. As the dependence of the ZPL position on the bandgap change is unknown, additional assumptions have to be made to quantitatively explain the shifting. The simplest assumption would be that the change in ZPL position is proportional to the band gap change. Thus, one should observe a shift $c_1 \frac{\alpha T^2}{T+\beta}$ (c_1 proportionality constant). This dependence does not at all describe the observed temperature dependent shift, thus we conclude that the bandgap change cannot be straightforwardly used to describe the temperature dependence of the ZPL shift.

When diamond is cooled down the lattice constant and thus the volume changes. For color centers, this change in lattice constant introduces lineshifts similar to shifts due to mechanical stress. In the literature, often the linear thermal expansion coefficient α is measured which, for an isotropic medium, can be converted to a volume expansion coefficient α_v via $\alpha_v = 3\alpha$ [294]. For measurements of α see, e.g., Ref. [295] or for more recent measurements Ref. [296]. The shift ΔE_l induced by lattice contraction can be calculated by [94]

$$\Delta E_l = A(c_{11} + 2c_{12}) \int_0^T \alpha_v(T) dT \tag{7.10}$$

where c_{11} and c_{12} are the elastic moduli of the diamond lattice with $c_{11} + 2c_{12} = 1327$ GPa [281] and A is the shift rate of the ZPL under hydrostatic compression. The parameter A has not been measured for the SiV center. Thus, we cannot quantify the influence of lattice contraction on the ZPL position. Assuming a significant

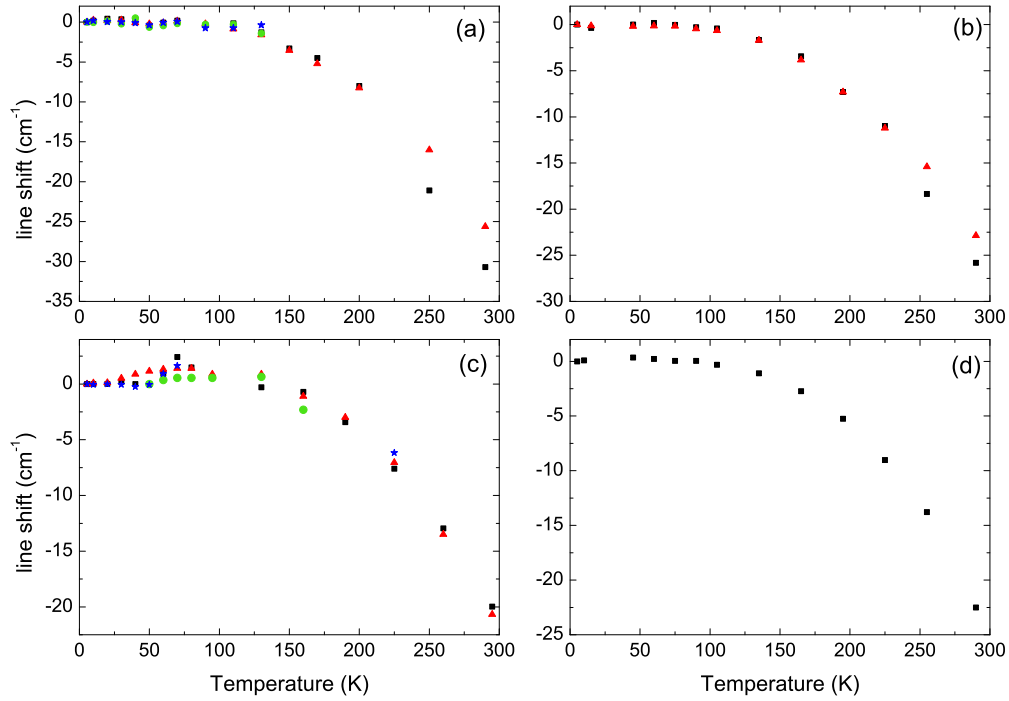

Figure 7.16: Temperature dependent lineshift for emitters C1-C4 (a)-(d) in the CVD grown NDs on Ir. Peaks clearly resolved over a sufficiently broad temperature range are taken into account.

influence of lattice contraction, the very similar temperature dependent shifting rate of the different fine structure components would imply a similar shift rate under hydrostatic compression, in contrast to the shifting behavior under uniaxial stress in $\langle 100 \rangle$ direction [111]. Ref. [296] gives an empirical formula for the linear thermal expansion coefficient α of diamond. It is pointed out, that below approx. 100 K the temperature dependence of α matches the model of a Debye solid predicting a T^3 dependence [296]. In Eq. (7.10), this leads to a T^4 dependence of the lineshift. Figure 7.17 shows the lineshifts observed for the strongest line of emitter C2 fitted with a T^4 dependence. In the following, we will use the shifting rate of this peak to exemplarily discuss the temperature dependent shifting of the ZPL as the shifting rates are very similar for the different emitters. The T^4 fit describes the curve reasonably but shows deviations at temperatures above 200 K. This might be partially due to the larger error in determining the position of coalescing line components. Nevertheless, assuming that only lattice expansion is responsible for the lineshift isn't reasonable: As a temperature dependent homogenous linewidth is observed (see Sec. 7.2), a quadratic electron-phonon coupling is present [94] that also contributes to the lineshift as discussed below. Without knowledge of the stress shift of the SiV center under hydrostatic compression, separation of phonon and lattice contributions is not feasible. Additionally, one might observe a different shifting rate for emitters in diamond which is in close contact with a substrate consisting of

a different material and for emitters in a system consisting only of diamond: The different coefficients of thermal expansion might introduce additional stress during cooling. This additional stress might lead to a modified lineshifting. As no significant difference is observed between the emitters in NDs on a foreign substrate and the SiV centers in the homoepitaxial CVD diamond, we conclude that the additional stress buildup is negligible compared to the intrinsic effects.

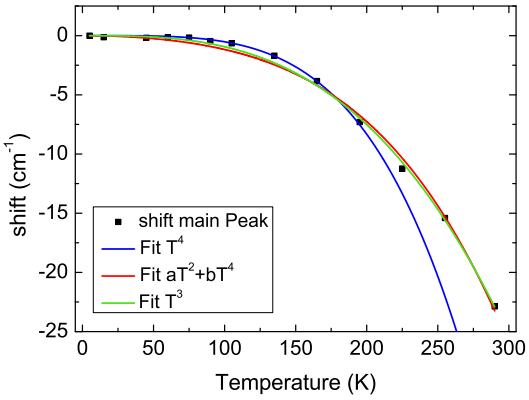

Figure 7.17: Temperature dependent lineshift of emitter C2 fitted with different models, explanation see text.

As mentioned before, quadratic electron-phonon coupling not only broadens but also shifts the ZPL. Maradudin finds in his work [95] that the shift is proportional to the internal energy of the crystal. This derivation also leads to a T^4 dependence at temperatures small compared to the Debye temperature T_D, with a change to a linear dependence at high temperatures $T > T_D$. The restricted validity of this model might explain the deviation from the T^4 dependence at temperatures above 200 K. On the other hand, 200 K is still a factor of eight lower than the Debye temperature of diamond, thus on might expect only minor deviations. Additionally, in analogy to the temperature dependence of the linewidth [Eq. (7.7)], one can use the one-phonon absorption spectrum $K(\omega)$ together with the phonon population term $n(\omega)$ to calculate the auxiliary function $\rho(\omega)$ and with this the shift rate ΔE_{ph} [95]:

$$\Delta E_{ph} = \beta_3 \int_0^\infty \rho(\omega)[n(\omega) + \frac{1}{2}]d\omega \tag{7.11}$$

$$\text{with} \qquad n(\omega) = \left(e^{\frac{\hbar\omega}{k_B T}} - 1\right)^{-1}, K(\omega) \propto [n(\omega) + 1]\frac{\rho(\omega)}{\omega^2} \tag{7.12}$$

Due to the same line of argument as for the line broadening, using this approach is not feasible to evaluate our data as determining $\rho(\omega)$ is not possible.

The overall lineshift is given as the sum of the phonon dependent parts ΔE_{ph} and the lattice contribution ΔE_l. Several publication have successfully employed Eq. (7.10) and (7.11) to describe the temperature dependent lineshift of the ZPL [281, 282, 293]. In addition to this model, Hizhnyakov and coworkers [283, 285, 286] predict a $aT^2 + bT^4$ dependence. To obtain these results, they again take into account the softening of bonds when the color center resides in the excited state and the resulting change in the local phonon density of states (see also discussion page 133). The shift of the main peak of emitter C2 has been also fitted with this

model in Fig. 7.17. This model more closely fits the measured data as compared to the T^4 model. Nevertheless, as Hizhnyakov and coworkers do not comment on the influence of the lattice expansion in their work, this model does not allow for the separation of lattice and phonon contribution either. We point out that a fit to the measured data assuming a T^3 dependence given in Fig. 7.17 also yields a very good description of the measured curve. This result agrees with the reports of Halperin et al. [287] who experimentally find a T^3 dependence of the line position for color centers with emission at 415 nm, but do not theoretically motivate it.

In summary, the origin of the dominant process responsible for the lineshift, either due to phonon dependent processes or due to lattice contraction, and its precise temperature dependence could not be determined. To separate the processes, precise knowledge of the shifting coefficients for the SiV center ZPL fine structure components under hydrostatic compression is necessary. Nevertheless, the measured curves are consistent for different emitters and the overall shift agrees with previous observations on SiV centers.

7.4 Temperature dependent population dynamics

This section features the temperature dependent population dynamics of single SiV centers. As discussed in Sec. 5.3.2, all observed single SiV centers involve three level population dynamics. The following temperature dependent effects might occur:

- **Deactivation of non-radiative channels** For color centers in a solid host, non-radiative de-excitation channels may lead to a low quantum efficiency of the ZPL transition (for further discussion see Sec. 5.3.4). Non-radiative channels might be thermally activated: For SiV centers, Feng et al. [139] report a strong quenching of SiV luminescence at temperatures above approx. 100 K: The luminescence of the SiV centers decreases by a factor of approx. 8 between 50 K and room temperature. From the experimentally observed temperature dependence of the quenching, Feng et al. deduce an activation energy for the responsible non-radiative process of 70 meV. An observation possibly connected to temperature dependent non-radiative transitions is reported by Sternschulte et al. [111]: The excited state lifetime of SiV centers in bulk diamond decreases from 4 ns to 2.7 ns upon heating from 5 K to 300 K, indicating possible lifetime shortening due to non-radiative quenching. For single emitters, an enhanced quantum efficiency due to the suppression of non-radiative decay channels might influence the maximum obtainable photon rates at low temperature.

- **Changes in shelving dynamics** All observed SiV centers show three level dynamics. Nevertheless, the energetic position of the shelving state is unknown. Thus, depending on the energy difference between excited state and shelving state, one might think of a thermally activated shelving or de-shelving process. Such an effect has, e.g., been shown for NV centers by Dräbenstedt et al. [264]: For NV centers, the shelving state is found only 37 meV below the

excited state. Thus, at elevated temperatures NV centers can be thermally re-excited from the metastable shelving state leading to an efficient de-shelving mechanism. At low temperatures, the thermal energy is no longer sufficient and deactivation of the thermal de-shelving mechanism leads to a decrease of the fluorescence at low temperatures. Changes in shelving dynamics induce changes of the shelving and de-shelving rates deduced from $g^{(2)}$ measurements and might also lead to changes in maximum obtainable photon rates.

- **Change in absorption cross section** The levels responsible for the pumping transition of the SiV centers could so far not be reliably identified. Most probably, the pumping transitions take place via vibrationally excited states in the excited electronic state (discussion see page 67). One might suspect that the absorption coefficient changes due to the narrowing or shifting of pumping transitions and a possible change in effective detuning. This would lead to changes in the laser power needed to saturate the color centers.

7.4.1 Temperature dependent saturation

Figure 7.18 summarizes the saturation curves of emitters C1, C3 and C4 measured at room temperature and cryogenic temperature ($20 - 30\,\mathrm{K}$).[7] At low temperature, lower maximum photon rates I_∞ and higher saturation powers P_{sat} are observed (general discussion of saturation curves Sec. 5.3.1). Nevertheless, this mostly reflects technical problems: When working in the cryostat, the performance of the confocal setup (spot size and collection efficiency) is changed compared to the setup at room temperature. For a detailed discussion of these effects and a correction routine, see Appendix B, Sec. B.4. After correcting I_∞ and P_{sat} for these effects, we find the values given in Tab. 7.4 for the low temperature measurements.

Emitter	P_{sat} RT	I_∞ RT	T_{low}	P_{sat}	I_∞	ΔP_{sat}	ΔI_∞
C1	$73\,\mu$W	2.39 Mcps	25 K	$97\,\mu$W	2.17 Mcps	-33%	9%
C3	$65\,\mu$W	0.775 Mcps	20 K	$57\,\mu$W	0.713 Mcps	13%	7%
C4	$32\,\mu$W	0.593 Mcps	30 K	$18\,\mu$W	1.08 Mcps	45%	-82%

Table 7.4: Saturation power P_{sat} and maximum photon count rate I_∞ for emitters C1, C3, C4 at room temperature and corrected saturation power P_{sat} and maximum photon count rate I_∞ at cryogenic temperature (temperature given in column T_{low}, see Appendix B, Sec. B.4 for discussion of correction of P_{sat} and I_∞). ΔP_{sat} and ΔI_∞ give the deviation of the low temperature value from the room temperature value in %, calculated from $\Delta I_\infty = \frac{I_\infty(RT) - I_\infty(lowT)}{I_\infty(RT)}$[%] and analogous for ΔP_{sat}.

The corrected maximum photon count rates I_∞ for emitters C1 and C3 agree within less than 10% at room temperature and at 25 K/20 K. I_∞ for emitter C4 changes considerably, indicating a higher count rate at low temperature. However,

[7] Note that emitter C5 is not included in the discussion of saturation and population dynamics, as the underlying ensemble influences the measurements. For emitter C2, technical problems inhibited low temperature saturation and $g^{(2)}$ measurements.

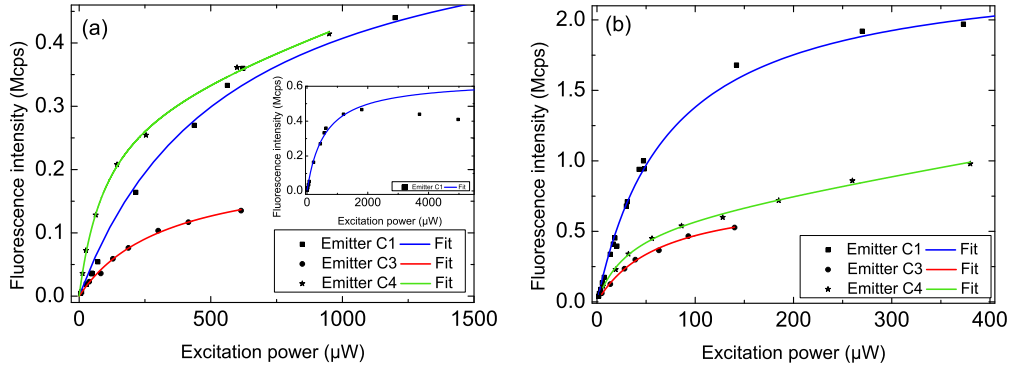

Figure 7.18: Saturation curves for emitters C1, C3 and C4 (excitation 671 nm). (a) Saturation curves at low temperature (Emitter C1 25 K, Emitter C3 20 K, Emitter C4 30 K). The inset shows the full saturation curve for emitter C1, measured up to 5.5 mW. Note that the last two points are not taken into account for the fit, as they show a clear decrease in intensity. (b) Saturation curves at room temperature.

we point out that this is no clear evidence for enhanced emission at low temperature: For emitter C4, background fluorescence had to be taken into account. This background fluorescence was especially pronounced at room temperature. Thus, over-accounting for the background might explain a too low value of I_∞ at room temperature. From these measurements, we conclude that no significant de-activation of non-radiative channels occurs. This conclusion is also supported by the temperature dependent $g^{(2)}$ measurements in the next section.

The question arises whether the missing thermal de-activation of non-radiative processes can help to identify the cause of the non-radiative transitions. In Sec. 5.3.4, different causes for non-radiative processes have been discussed. FDTD simulations suggest that non-radiative processes might be introduced by near field coupling if the emitter is close to the lossy Ir substrate. However, for this process, the lack of temperature dependence seems not reasonable, as losses in the metal should be temperature dependent [297, 298]. However, as no experimental data for the temperature dependent dielectric function of Ir are found in the literature, we cannot estimate if a significant temperature dependence would be expected. Also for the process of quenching due to multi-phonon emission [247], a reduction at lower temperature would be expected. For processes involving quenching due to the presence of lattice defects (e.g., Ref. [245]), the temperature dependence has not been discussed in the literature. For tunnel processes, as discussed in the DKR-criterion, only minor temperature dependence should be expected. Summarizing, the absence of temperature dependent quenching does not allow to reliably determine the cause of non-radiative processes. The observation of temperature independent brightness, however, is contradictory to previous ensemble investigations [139].

The observed saturation powers P_{sat} are in the same order of magnitude for room and cryogenic temperature. Thus, we conclude no significant influence of the temperature on the excitation process. The deviations here might be due to slight misalignment of the emitter in the laser focus, as the determination of P_{sat} is very

sensitive to this issue, while I_∞ is not.

7.4.2 Temperature dependent $g^{(2)}$ measurements

Intensity dependent measurements of the $g^{(2)}$ function were carried out for emitters C1, C3 and C4 at room temperature and cryogenic temperature ($20-30\,\mathrm{K}$). Figure 7.19 exemplarily shows the $g^{(2)}$ functions measured for emitter C1.

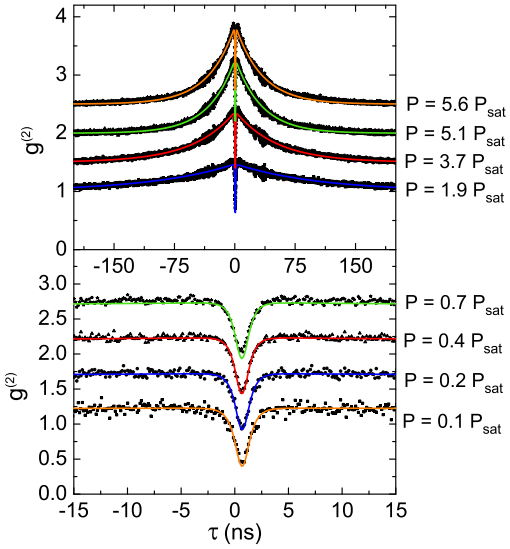

(a) Room temperature $g^{(2)}$ functions of emitter C1

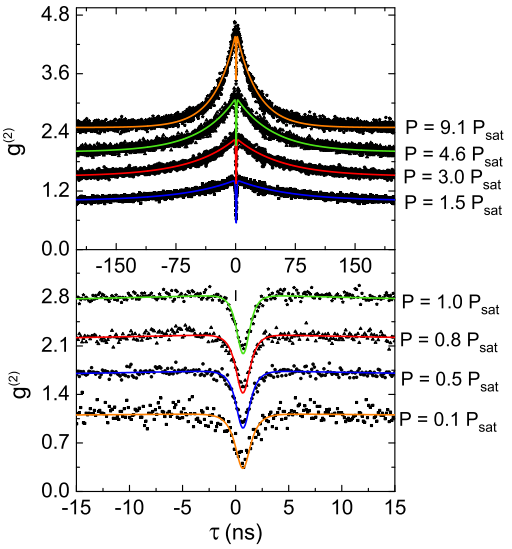

(b) $g^{(2)}$ functions of emitter C1 at 30 K

Figure 7.19: Intensity dependent $g^{(2)}$ functions of emitter C1 (excitation 671 nm). Note that the excitation power given in units of P_{sat} is rounded to the first digit after the decimal point.

The measured $g^{(2)}$ data are fitted with the $g^{(2)}$ function of a three level system taking into account the instrument response and possible background radiation (see Sec. 5.3.2). The fits agree well with the measured data for short as well as long delay time τ and identify all color centers as single emitters. The deviation of $g^{(2)}(0)$ from 0 is induced by the instrument responses of the setup as confirmed by the fitted $g^{(2)}$ functions taking into account the instrument response (see Sec. 5.3.2). The deviation $\Delta g^{(2)}(0)$ between the fitted value of $g^{(2)}(0)$ and the measured datapoints is below 0.07 for emitter C1 and below 0.15 for emitter C3 and is mainly governed by the noise of the $g^{(2)}$ function. For these emitters, consideration of background radiation was not necessary to obtain these results confirming a very high signal to noise ratio. For emitter C4, the background level estimated from the saturation measurement was taken into account, leading to a maximum deviation of fitted and measured value of $\Delta g^{(2)}(0) = 0.04$. We point out that the three level system used to discuss the population dynamics marks a significant simplification for SiV centers as, instead of a single radiative transition assumed in the model, we observe four

radiative transitions in the experiments at low temperature. Our $g^{(2)}$ measurements correlate photons from all four different transitions, as we do not spectrally filter out individual transitions. Thus, we observe an 'effective' $g^{(2)}$ function for the color center, dominated by the properties of the lines with high relative intensity. For the full system, the appropriate description is unsettled: Are the excited state sublevels pumped with the same pumping rate k_{12}? Do they couple to the same shelving state with the same rate k_{23}? Coupling to several shelving states has been observed for dye molecules. However, this leads to multiple time constants for the decay of the long time part of $g^{(2)}$ for shelving states with significantly different lifetimes [299]. This has not been observed in the $g^{(2)}$ functions measured for single SiV centers. Furthermore, population transfer takes place in the excited state (see Sec. 7.4.3). Additionally, for the multi-level system, finding an analytical expression for the $g^{(2)}$ function is not feasible. Therefore, in the following we analyze the population dynamics using an effective three level system analogous to the room temperature case. The full conformity of the measured $g^{(2)}$ data with the fitted three level $g^{(2)}$ function justifies this approach.

From the fits of the $g^{(2)}$ functions, we obtain the parameters a, τ_1 and τ_2 as discussed in detail in Sec. 5.3.2. The excitation power dependence of these parameters is displayed in Fig. 7.20. To estimate the rate coefficients of the three level system, we obtain the limiting values τ_1^0, τ_2^0, τ_2^∞ and a^∞ from the data (for detailed discussion see Sec. 5.3.2). The values determined for emitters C1, C3 and C4 are given in Tab. 7.5. The rate coefficients k_{21}, k_{23}, k_{31} and d obtained from the limiting values using the model of intensity dependent de-shelving, as well as the parameters σ and c obtained from the power dependence of a, τ_1 and τ_2 (see Sec. 5.3.2) are summarized in Tab. 7.6.

Em C1	τ_1^0(ns)	τ_2^0(ns)	τ_2^∞(ns)	a^∞
RT	0.64	1000	33.1	1.35
30 K	0.72	100.8	26.5	1.97
Em C3	τ_1^0(ns)	τ_2^0(ns)	τ_2^∞(ns)	a^∞
RT	1.28	1335	57	1.74
20 K	1.12	1950	105	1.5
Em C4	τ_1^0(ns)	τ_2^0(ns)	τ_2^∞(ns)	a^∞
RT	0.93	9137	39.6	6.1
30 K	1.12	4151	44.6	5.2

Table 7.5: Limiting values of the fitting parameters a, τ_1 and τ_2 obtained from the fits of the intensity dependent $g^{(2)}$ functions (for explanation of the parameters see Sec. 5.3.2)

The observed τ_1^0 values range from $0.64 - 1.28$ ns confirming the room temperature observations in Sec. 5.3.2. The deviation of τ_1^0 at room temperature and cryogenic temperature in relation to the room temperature value of τ_1^0 is 13% for emitter C1 and C3 and 20% for emitter C4, thus evidencing the absence of significant lifetime changes upon cooling. From observations in the literature, a lifetime change of approx. 50% (in relation to the room temperature lifetime) would have been expected [111]. Other authors report a luminescence quenching by a factor of 8 due to non-radiative decay, this in turn should induce a significant shortening of

the lifetime at room temperature which has not been observed here. As the rate k_{21} is mainly determined by τ_1^0, it is also mainly unaffected by temperature (deviations between 12% and 17%). Moreover, the deviations show no clear trend toward a lifetime increase or decrease. These findings correspond to the observations for the saturation of the emitters in Sec. 7.4.1, where also no significant changes of emitter brightness are observed. We find that the maximum photon rate is not exclusively determined by the rate k_{21} as it would be for a two level system (see Sec. 5.3.4 for further discussion): Emitter C1 exhibits the highest maximum photon rate and also the highest value of k_{21}. On the other hand, for emitters C4 we find a higher k_{21} (at room temperature) compared to emitter C3, but nevertheless a lower maximum photon rate I_∞.

From the values given in Tab. 7.5 as well as the curves in Fig. 7.20, it is clear that the emitters exhibit different bunching dynamics: Emitters C3 and C4 show very long τ_2 times at low excitation power indicating a slow intensity independent de-shelving rate k_{31}^0. For emitter C1, the shelving dynamics at low excitation power are not well-defined: We notice significant differences between low temperature and room temperature observations. As visible in Fig. 7.20(a), at 25 K no significant increase of τ_2 at low excitation power is observed in contrast to the room temperature observation. If one assumes a thermal deactivation of de-shelving as discussed above, one would expect an inverse trend. We point out that this discrepancy might be due to the following fact: The high brightness of emitter C1 enables using powers down to $0.02\,\mathrm{P_{sat}}$ at room temperature, while for cryogenic temperature (due to the decrease in collection efficiency) the lowest power used is $0.1\,\mathrm{P_{sat}}$. For all other emitters, the lowest powers used are $0.1 - 0.2\,\mathrm{P_{sat}}$. The measurements at low power determine the estimation of τ_2^0, thus the different minimum powers introduce significant errors. Apart from emitter C1, k_{31}^0 is in the same order of magnitude at room temperature and cryogenic temperature decreasing by 32% for emitter C3, but increasing by 120% for emitter C4 upon cooling (in relation to the room temperature value). Similarly, the rate k_{23} is found to be in the same order of magnitude deviating by 14-49% without a clear trend for increase or decrease with temperature.

In the following, the power dependence of the parameters a, τ_1 and τ_2 displayed in Fig. 7.20 and its concurrence with the three level intensity dependent de-shelving

Em C1	k_{21}(MHz)	k_{23}(MHz)	k_{31}^0(MHz)	d (MHz)	σ(MHz/μW)	c (μW)
RT	1545.1	17.4	1.0	11.9	5.21	80.4
30 K	1363.9	25	10	2.79	1.07(6.3)	350(60)
Em C3	k_{21}(MHz)	k_{23}(MHz)	k_{31}^0(MHz)	d (MHz)	σ(MHz/μW)	c (μW)
RT	770.1	11.1	0.749	5.65	3.79	217
20 K	889.5	5.73	0.513	3.3	0.525(3.1)	3285(558)
Em C4	k_{21}(MHz)	k_{23}(MHz)	k_{31}^0(MHz)	d (MHz)	σ(MHz/μW)	c (μW)
RT	1053.6	21.7	0.11	3.44	1.83	201
30 K	874.8	18.8	0.24	3.4	1.87(11.0)	47(8.1)

Table 7.6: Rate coefficients deduced from the limiting values of a, τ_1 and τ_2 using the three level model including intensity dependent de-shelving. Values of σ and c given in brackets denote the values corrected for the decreased performance of the confocal setup.

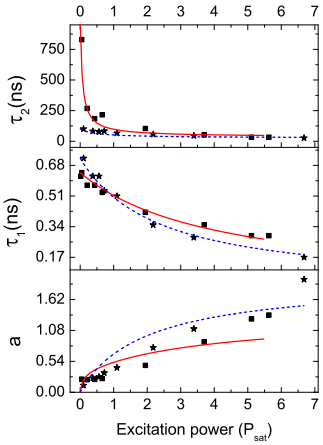

(a) $g^{(2)}$ parameters a, τ_1 and τ_2 for emitter C1 at room temperature and 30 K. x-scale given in units of saturation power (75 μW RT, 569 μW uncorr. 25 K)

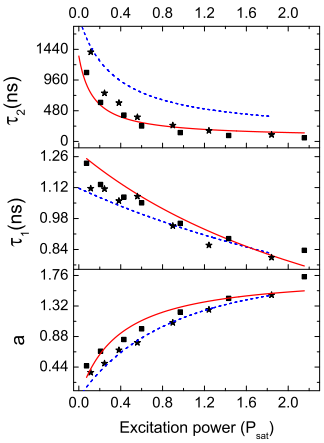

(b) $g^{(2)}$ parameters a, τ_1 and τ_2 for emitter C3 at room temperature and 20 K. x-scale given in units of saturation power (32 μW RT, 103 μW uncorr. 20 K)

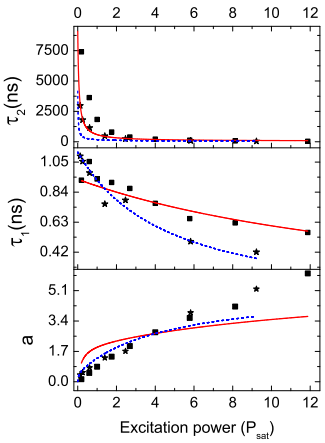

(c) $g^{(2)}$ parameters a, τ_1 and τ_2 for emitter C4 at room temperature and 30 K. x-scale given in units of saturation power (65 μW RT, 334 μW uncorr. 30 K)

Figure 7.20: $g^{(2)}$ parameters a, τ_1 and τ_2 at room temperature and cryogenic temperature. Filled squares: data points at room temperature (Fit red curve), filled stars: cryogenic temperature (Fit blue curve).

model is discussed in detail. Note that the excitation power is given in units of the saturation power P_{sat} measured at the respective temperature. This accounts for the change in laser power needed to saturate the emitters at cryogenic temperature for technical reasons (see Sec. 7.4.1). This re-scaling allows for direct comparison of the curves. As visible from Fig. 7.20, the model including an intensity dependent de-shelving reasonably describes the power dependence of the parameters a, τ_1 and τ_2 for room temperature as well as cryogenic temperature. This agreement allows to draw the conclusion that intensity dependent de-shelving processes are present at both temperatures. For emitter C4, the model overestimates the decrease of τ_2 for intermediate power, while for emitter C3 at 20 K the decrease is underestimated over the whole power range.

Similar to the change in saturation power P_{sat}, the fitting parameters σ and c will also be subject to changes introduced by the altered performance of the confocal setup when using the cryostat, i.e., a reduced effective intensity impinging onto the emitter, as these parameters are linking the excitation power to the intensity dependent transition rate coefficients in the system (discussion of power dependence see page 81). Correcting the values of σ with the same factor as deduced for P_{sat} yields (values see also Tab. 7.6): emitter C1 $\sigma_{30\,\mathrm{K}} = 6.3\,\mathrm{MHz}/\mu\mathrm{W}$, emitter C3 $\sigma_{20\,\mathrm{K}} = 3.1\,\mathrm{MHz}/\mu\mathrm{W}$, thus matching the room temperature values within 21% and 19% respectively. Similar considerations hold for the parameter c: As it indicates the saturation power for the de-shelving process, a correction analogous to P_{sat} should be feasible. For emitter C1, the correction leads to $c_{20\,\mathrm{K}} = 60\,\mu\mathrm{W}$ matching

the room temperature value within 26%. Nevertheless, for emitter C3, correcting the low temperature value leads to $c_{30\,\mathrm{K}} = 558\,\mu\mathrm{W}$ and thus a mismatch of 158%. An unusual behavior of the fitting parameters σ and c is observed for emitter C4: Applying the correction factors to emitter C4, we find that the effective pumping rate σ is enhanced by nearly a factor of 6, while c is even lowered by a factor of 25. For emitter C4, also a 45% decrease of P_{sat} has been observed (Sec. 7.4.1). We thus might assume that emitter C4 is more effectively pumped a cryogenic temperatures.

Summarizing, all emitters are reasonably described in the framework of the three level intensity dependent de-shelving model at cryogenic as well as room temperature. No clear evidence for temperature dependent processes including de-activation of non-radiative processes and changes in shelving or de-shelving dynamics is found. Emitters C1 and C3 show no temperature dependent absorption properties, while for emitter C4 absorption enhancement at low temperature is indicated.

7.4.3 Excited state thermalization

The low temperature spectra of single SiV centers shown in Figs. 7.7–7.10 suggest an excited state splitting between 1.9 meV and 3.3 meV. This raises the question of population transfer between the excited state sublevels. For coherent manipulation of SiV centers, e.g., via optical Rabi Oscillations, fast population transfer processes would be a detrimental source of decoherence. As a first estimate, one might consider the excited state energy spacing ΔE in comparison to $k_B T$ as the Boltzmann-factor $exp(-\frac{\Delta E}{k_B T})$ determines the possible thermal population of the higher lying excited state component. At 20 K, $k_B T$ amounts to 1.7 meV and hence is still comparable to the energy spacing. Thus, one might expect a significant population transfer between the excited state sublevels, depending on the initial population distribution. Moreover, one has to consider the exchange time τ_e of the population between the states: Only if $\tau_e \cdot \Delta\omega \gg 1$ two distinct spectral lines are observed ($\Delta\omega$ is the excited state splitting in frequency units). The linewidth of these lines is then determined by the intrinsic relaxation properties of the states. On the other hand, if $\tau_e \cdot \Delta\omega$ is close to one, only one strongly broadened line would be observed [264, 265]. From the spectra, we conclude that $\tau_e \cdot \Delta\omega \gg 1$ as separated narrow lines are observed. Nevertheless, this does not exclude excited state population transfer before radiative decay takes place: The lifetime of the excited state is approx. 1 ns. If τ_e is in the same order of magnitude $\tau_e \cdot \Delta\omega \gg 1$ is still satisfied and at least some population transfer is possible. In the following, we try to estimate the influence of thermalization in the excited state of emitters C1 and C2. These two emitters have been chosen as they display a clear four level structure without additional peaks for temperatures up to 130 K.

In the literature, excited state thermalization of SiV ensembles has already been investigated. Moreover, Clark et al. [140] utilize the thermalization behavior to support their proposed level scheme: They use the fact that luminescence spectra reflect the population distribution in the excited state, while absorption spectra reproduce the population distribution in the ground state, both including temperature dependent thermalization. Thus, one can use the thermalization behavior in absorption

and emission to distinguish between lines from the same ground and excited state respectively. We point out that the thermalization in accordance with Ref. [140] has also been observed for the SiV ensemble in the single crystalline CVD diamond film introduced in Sec. 7.1.1 in our previous work [88].

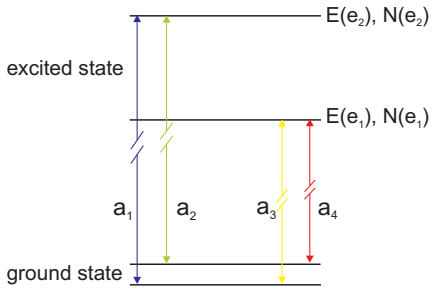

Figure 7.21: Schematic level scheme of the SiV center after Clark et al. [140]. E(e_i) denote the energy of the excited state components, while N(e_i) denote the population of the respective component. a_i are the transition dipole moments of the four fine structure lines.

Considering the level scheme depicted in Fig. 7.21, Clark et al. [140] find the following relations for the intensities of the four fine structure components in emission (represented by the peak areas A_i, i=1-4)

$$\frac{A_1}{A_3} = \frac{a_1\,N(e_2)}{a_3\,N(e_1)} = \frac{a_1\,g(e_2)}{a_3\,g(e_1)}\,\exp\left(\frac{E(e_1)-E(e_2)}{k_BT}\right) \tag{7.13}$$

$$\frac{A_2}{A_4} = \frac{a_2\,N(e_2)}{a_4\,N(e_1)} = \frac{a_2\,g(e_2)}{a_4\,g(e_1)}\,\exp\left(\frac{E(e_1)-E(e_2)}{k_BT}\right) \tag{7.14}$$

$$\frac{A_1}{A_2} = \frac{a_1\,N(e_2)}{a_2\,N(e_2)} = \frac{a_1}{a_2} \tag{7.15}$$

$$\frac{A_3}{A_4} = \frac{a_3\,N(e_1)}{a_4\,N(e_1)} = \frac{a_3}{a_4} \tag{7.16}$$

Here, a_i is the transition dipole moment of peak i. $N(e_1), N(e_2)$ are the populations, $E(e_1), E(e_2)$ are the energies and $g(e_1), g(e_2)$ are the statistical weights of the excited state components. Eqs. (7.13) and (7.14) show that the intensity ratio of peak 1 and 3 and peak 2 and 4, respectively, are temperature dependent. Taking the natural logarithm of Eq. (7.13) yields

$$\ln\left(\frac{A_1}{A_3}\right) = \ln\left(\frac{a_1\,g(e_2)}{a_3\,g(e_1)}\right) + \frac{E(e_1)-E(e_2)}{k_B}\frac{1}{T} \tag{7.17}$$

and analogous for Eq. (7.14). Thus, plotting $\ln(\frac{A_1}{A_3})$ versus the inverse temperature $\frac{1}{T}$ is supposed to resemble a straight line with slope $\frac{E(e_1)-E(e_2)}{k_B}$ if thermalization takes place [and analogous for Eq. (7.14)]. On the other hand, Eqs. (7.15) and (7.16) indicate that the intensity ratio of peaks 1 and 2 as well as 3 and 4 should be constant. Figures 7.22 and 7.23 summarize the plots necessary to verify thermalization via Eqs. (7.13)–(7.16). The positive and negative signs of the logarithmic intensity ratios, apparent from Figs. 7.22 and 7.23, arise due to the different relative intensities of the fine structure components as shown in Figs. 7.7 and 7.8: For emitter C2, the longer wavelength doublet dominates the spectrum. For emitter C1, the intensity of the doublets is rather comparable; however, the shorter wavelength

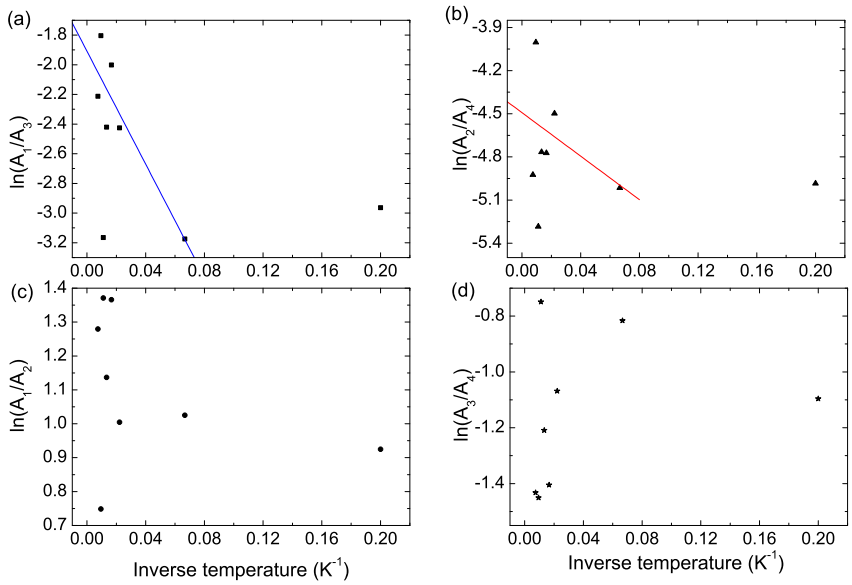

Figure 7.22: Thermalization behavior of emitter C1. (a) logarithm of intensity ratio of peaks 1 and 3 versus inverse temperature, (b) analogous for peaks 2 and 4. Straight lines (red and blue) are fits to the data, further explanation see text. (c) logarithm of intensity ratio of peaks 1 and 2 versus inverse temperature, (d) analogous for peaks 2 and 4

doublet is more intense. From the plots, the validity of excited state thermalization is not unambiguously clear: The ratios $\ln(\frac{A_1}{A_2})$ and $\ln(\frac{A_3}{A_4})$ are not clearly constant. However, the relative variation of $\ln(\frac{A_1}{A_2})$ is smaller than the variation of $\ln(\frac{A_1}{A_3})$ and $\ln(\frac{A_2}{A_4})$, for $\ln(\frac{A_3}{A_4})$ a larger variation is observed. We point out that Clark et al. [140] also report a spread of the ratios $\ln(\frac{A_1}{A_2})$ and $\ln(\frac{A_3}{A_4})$ of up to 300%. Thus, the observation here is consistent with their findings. Nevertheless, the ratios $\ln(\frac{A_1}{A_3})$ and $\ln(\frac{A_2}{A_4})$ show a certain trend: They decrease upon cooling (higher inverse temperature) and become constant at temperatures below 10 K for both emitters. This is in accordance with the observations of Clark et al. [140] reporting the same behavior below 6 K. The authors of Ref. [140] interpret this in terms of a breakdown of thermalization at low temperatures. This possibility to inhibit thermalization at very low temperatures might be important for future applications of SiV centers in quantum information. Figures 7.22 and 7.23 also display the straight line fitted to the data of $\ln(\frac{A_1}{A_3})$ and $\ln(\frac{A_2}{A_4})$. Due to the effects at low temperature discussed above, we exclude the datapoints for 20 K and below from the fit for emitter C1. For emitter C2, fitting straight lines to the datapoints of $\ln(\frac{A_1}{A_3})$ and $\ln(\frac{A_2}{A_4})$ does not yield unambiguous results: Excluding the datapoint at 5 K as well as the datapoint at 90 K that shows a strong deviation especially for $\ln(\frac{A_1}{A_3})$ leads to the most reasonable results. We attribute the larger errors for emitter C2 to uncertainties, fitting the very weak peaks 1 and 2. From the slope c of the linear fit, we try to estimate

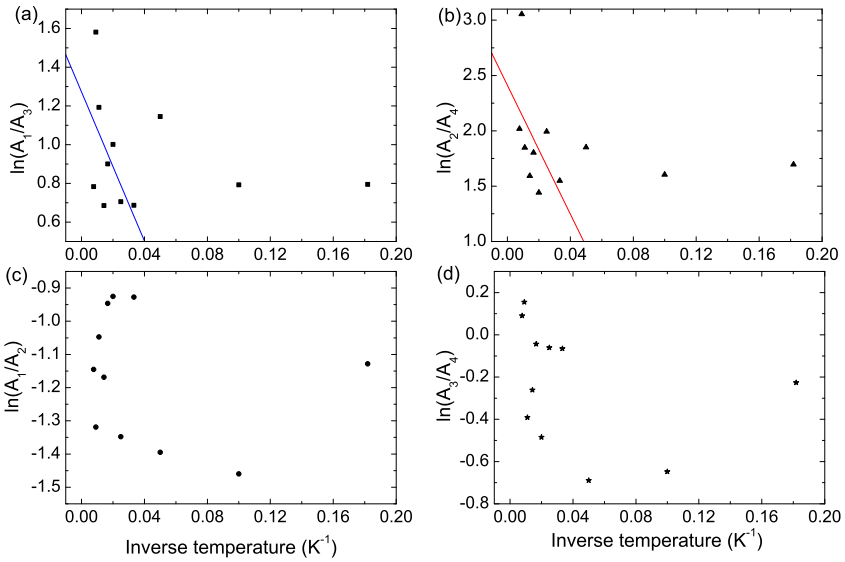

Figure 7.23: Thermalization behavior of emitter C2. (a) logarithm of intensity ratio of peaks 1 and 3 versus inverse temperature, (b) analogous for peaks 2 and 4. Straight lines (red and blue) are fits to the data, further explanation see text. (c) logarithm of intensity ratio of peaks 1 and 2 versus inverse temperature, (d) analogous for peaks 2 and 4

the excited state splitting as

$$c = \frac{E(e_1) - E(e_2)}{k_B} = \frac{\Delta E_e}{k_B}.$$

For emitter C1, we find from fitting $\ln(\frac{A_1}{A_3})$: $\Delta E_e = 1.6\,\text{meV}$ and from fitting $\ln(\frac{A_2}{A_4})$: $\Delta E_e = 2.5\,\text{meV}$. The second value reproduces the excited state splitting derived from the spectra at low temperature ($\Delta E_e = 2.77\,\text{meV}$) with only 10% deviation. For emitter C2, we obtain from $\ln(\frac{A_1}{A_3})$: $\Delta E_e = 1.6\,\text{meV}$ and from $\ln(\frac{A_2}{A_4})$: $\Delta E_e = 0.7\,\text{meV}$. The first being in good agreement with the spectroscopic splitting of 1.6 meV. We emphasize that the fitted values all include an error of at least 50% (as calculated by the fitting algorithm implemented in Origin 8.x). For the SiV ensemble in the single crystal homoepitaxial CVD film discussed in Sec. 7.1.1, previous work (Ref. [88]) has found clear evidence for excited state thermalization; however, it was also not possible to reliably derive the excited state splitting from the thermalization. Summarizing, the observed temperature dependent line intensities tentatively hint at an excited state thermalization above approx. 10 K.

7.5 Polarization properties of the ZPL fine structure components

The following section examines the polarization properties of the ZPL fine structure components. The discussion will be restricted to polarization properties of single emitters. Polarization properties for an ensemble are much more complex as they

simultaneously map the properties of centers oriented along all equivalent directions [257]. Nevertheless, the polarization properties of ensembles have been used to deduce the site symmetry as well as the transition dipole orientation for the SiV center in Ref. [154]. From the data in Ref. [154], the existence of a single transition dipole in ⟨110⟩ direction is inferred. The polarization properties of single SiV centers at room temperature have been discussed in detail in Chapter 6. There, the observation of linearly polarized emission together with a preferential absorption of linearly polarized light revealed the existence of a single dipole oriented most probably in ⟨110⟩ direction, thus confirming the findings of Ref. [154]. Since at room temperature only a single emission line is visible, no information about polarization of fine structure components could be gained. In the following, we retrieve this information from low temperature spectra. However, as the observed emitters C1–C5 are hosted in randomly oriented NDs, no information of alignment with respect to crystal axes can be deduced. In the following sections, we will discuss the polarization properties of the SiV centers in absorption as well as emission.

7.5.1 Polarization properties of the emitted light

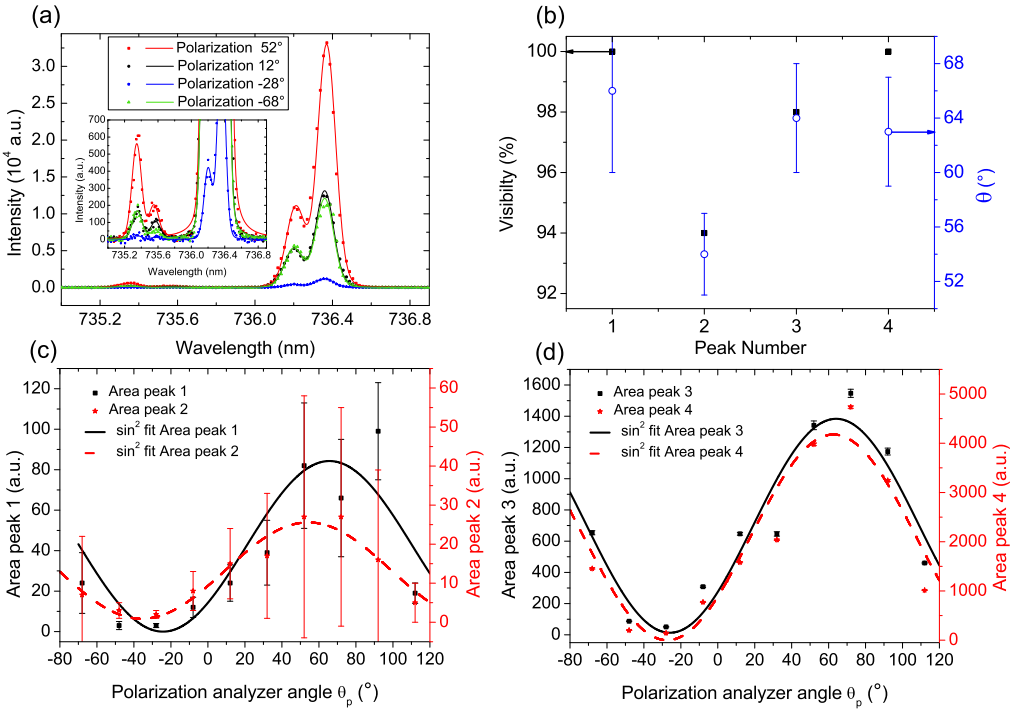

Figure 7.24: Fluorescence polarization of emitter C2. (a) fluorescence spectra of emitter C2 taken at different angles of the polarization analyzer and a temperature of 30 K. The excitation polarization is fixed to the optimal value. The inset of the graph shows an enlarged detail to enable observation of the weaker doublet. (b) summary of visibility (black squares) and linear polarization direction θ (blue circles) obtained from the fits in (c) and (d). (c) and (d) peak areas in dependence of the polarization analyzer angle θ_p fitted with Eq. (7.18).

Figure 7.24 summarizes the investigations on the fluorescence polarization for emitter C2. The spectra in Fig. 7.24(a) reveal a clear dependence of the intensity on the polarization analyzer angle θ_p for both doublet components. To perform a quantitative analysis of the line intensities, all spectra are fitted with Voigt-profiles. For the fits, the widths of the peaks are kept constant for all analyzer angles. The peak positions change slightly by less than 0.02 nm for different spectra, which might be attributed to a spectral inaccuracy of the spectrometer, as this change is less than the width of the instrument response function of the spectrometer. Figures 7.24(c) and (d) summarize the determined peak areas A that serve as a measure of the line intensity. From Fig. 7.24(a), it is clear that the short wavelength doublet is much weaker than the long wavelength doublet. This complicates the determination of the peak areas for peaks 1 and 2 as it leads to an enhanced error of the fit that determines the peak areas, as indicated by the error bars in Fig. 7.24(c).

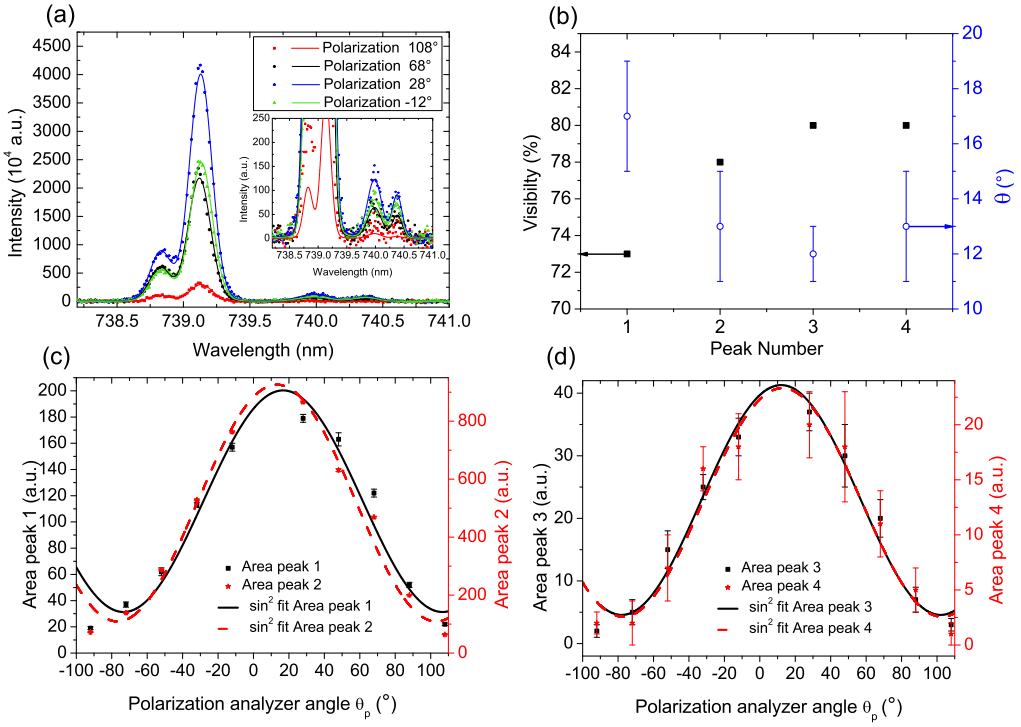

Figure 7.25: Fluorescence polarization of emitter C1. (a) fluorescence spectra of emitter C1 taken at different angles of the polarization analyzer and a temperature of 28 K. The emitter is excited with circularly polarized light. The inset of the graph shows an enlarged detail to enable observation of the weaker doublet. (b) summary of visibility (black squares) and linear polarization direction θ (blue circles) obtained from the fits in (c) and (d). (c) and (d) peak areas in dependence of the polarization analyzer angle θ_p fitted with Eq. (7.18).

The dependence of the measured peak area A of the polarization analyzer angle θ_p is fitted with

$$A(\theta_p) = A_0 + A_a \sin^2(\theta_p - \alpha) \tag{7.18}$$

here A_0 is an offset, A_a is the amplitude of the oscillation and α is a phase shift,

where $\alpha + 90°$ or $\alpha - 90°$ gives the maximum transmission, i.e., the polarization direction here named θ. Note, that the periodicity of the analyzer transmission is 180°, thus also a polarization direction θ shifted by 180°, i.e., $\theta \pm 180°$ can be used. We choose a range of -90 to 90 ° for the polarization directions. For linearly polarized light, one expects an offset A_0 close to zero and thus a visibility V

$$V = \frac{A_a}{A_a + 2A_0} \tag{7.19}$$

close to 100%. For peaks 1, 3 and 4 we find a visibility V between 98% and 100% and a polarization direction θ between 63 ° and 66 ° [see Fig. 7.24(b)]. The errors given for the polarization direction are the errors for the fitting parameter α obtained from the fitting routine. Only the data of peak 2 gives a deviating result: $V = 94\%$ and polarization direction $\theta = 54°$. We attribute this deviation to the high uncertainty in fitting the peak area of peak 2, as it is the weakest of the four peaks. From the above findings, we conclude that all four fine structure components of emitter C2 are linearly polarized with a common polarization direction.

A very similar behavior is found for emitter C1. The results are summarized in Fig. 7.25. Again the peak areas display an oscillation; however, fitting the data yields a slightly lower visibility V between 73% and 80%. A certain loss in linear polarization might be due to experimental considerations (see Appendix B, Sec. B.1.3) or due to a tilt of the emitter's dipole with respect to the sample plane that lowers the visibility (see Sec. 6.2). Therefore, a visibility close to 80% strongly suggests linearly polarized emission. Examining the polarization direction, we find $12 - 13$ ° for peak 2-4, while for peak 1 we find 17 °. We thus conclude, that also for emitter C1 the four fine structure components exhibit parallel linear polarization. Parallel polarization is also observed for emitter C3, however, with a visibility only around 50%. The loss of visibility again might be due to a tilted emission dipole. The corresponding data is given in Appendix C, Sec. C.1. Also the lines associated with emitter C5 in the BASD ND show parallel polarization with nearly full visibility, in contrast to the underlying ensemble showing only weakly polarized emission (data see Appendix C, Sec. C.1). The weakly polarized emission of the ensemble arises due to the emission of SiV centers oriented along different equivalent directions that leads to a very low averaged polarization (see also Ref. [154]). From these observations, we conclude that the four possible transitions, for the observed single SiV centers, are linearly polarized sharing the same polarization. We emphasize that despite the very dissimilar spectra of emitters C1, C2, C3 and C5 we find linearly polarized emission with a common polarization direction for each emitter.

7.5.2 Polarized absorption of single SiV centers

This section analyzes the polarized absorption of single SiV centers. Instead of rotating a linear polarization analyzer in the fluorescence, we now rotate the excitation laser polarization θ_e. Simultaneously, we record spectra of the fluorescence emitted by the single SiV centers. If the color center is excited far below saturation, the fluorescence is proportional to the light intensity absorbed by the color center and thus reveals the polarized absorption of the color center (for a detailed discussion

see also Sec. 6.1). To evaluate the data, we proceed analogous to the data evaluation for the fluorescence. We again use Eq. (7.18), the polarizer analyzer angle θ_p is now replaced by the excitation polarization direction θ_e.

Assuming the two excited state components are populated via the same linearly polarized pumping transition, one might expect polarized absorption with a common direction of maximum absorption for all four fine structure components. This prediction holds for emitters C1 and C5 (see Figs. 7.26 and Appendix C, Fig. C.4): The four line components show a visibility of 67-69% (peak 1,2) and 100% (peak 3,4) for emitter C1 and 100% for emitter C5. The difference of the visibility for peaks 1,2 and peak 3,4 for emitter C1 is not clear. On the other hand, for peaks 1 and 2 a minimum of the curve $A_{1,2}(\theta_e)$ close to zero is observed (see marked datapoints Fig. 7.26 (c)), thus indicating high visibility; however, the fit reveals a visibility of 67-69%. The direction of maximum absorption is estimated between 46 ° and 55 ° for emitter C1 and between -12 and −30 ° for emitter C5. For emitter C3, a different behavior is observed (see Appendix C, Fig. C.3): Although, the four fine structure components show a common direction of maximum absorption between 21 ° and 33 °, the visibility is only 45-13%. The low visibility might partially be due to the high excitation power of $2.0\,P_{Sat}$ used for these measurements: Only for excitation below saturation, the fluorescence is proportional to the absorption of the color center, for excitation above saturation the curve might be distorted. A significantly deviating behavior is observed for emitter C2 (see Fig. 7.27): Peak 1,2 and 4 show polarized absorption featuring a visibility of 90-100% (peak 1,2) and 62% (peak 4) with a common direction of maximum absorption between 75 ° and 77 °. In contrast to that, peak 3 shows a vanishing polarization dependent absorption [visibility 11%, see Fig. 7.27(d)]. In emission, the four peaks show a consistent behavior. From this data, the polarized absorption behavior of the emitters under investigation here is not conclusive. We point out that the spectrally integrated measurements using the APDs for detection, as employed for the discussion in Secs. 6.1 and 6.2, are more precise than the measurements here: They can be performed much faster, thus avoiding drifts of the emitter during the measurements. Drifts of the emitter can influence the measurements as absolute peak values have to be compared to deduce the polarized absorption. Furthermore, measurements using the APDs for detection allow for a better angle resolution due to a larger number of datapoints.

7.5.3 Comparison and interpretation of results

The measurements of the emission polarization yield, within experimental errors, that all fine structure components share a common linear polarization direction. The results obtained for polarized absorption yield partially inconclusive results. Nevertheless, we try to compare the polarization direction for the emission polarization and the maximum of polarized absorption. As discussed in Sec. 6.3, at room temperature the absorption and emission dipoles of single SiV centers excited at $694 - 696\,\text{nm}$ have been found to be nearly parallel. This observation is not fully reproduced in the measurements at cryogenic temperature: For emitter C2, we find the maximum absorption (for the three polarized peaks) at a mean value of 76 °, while

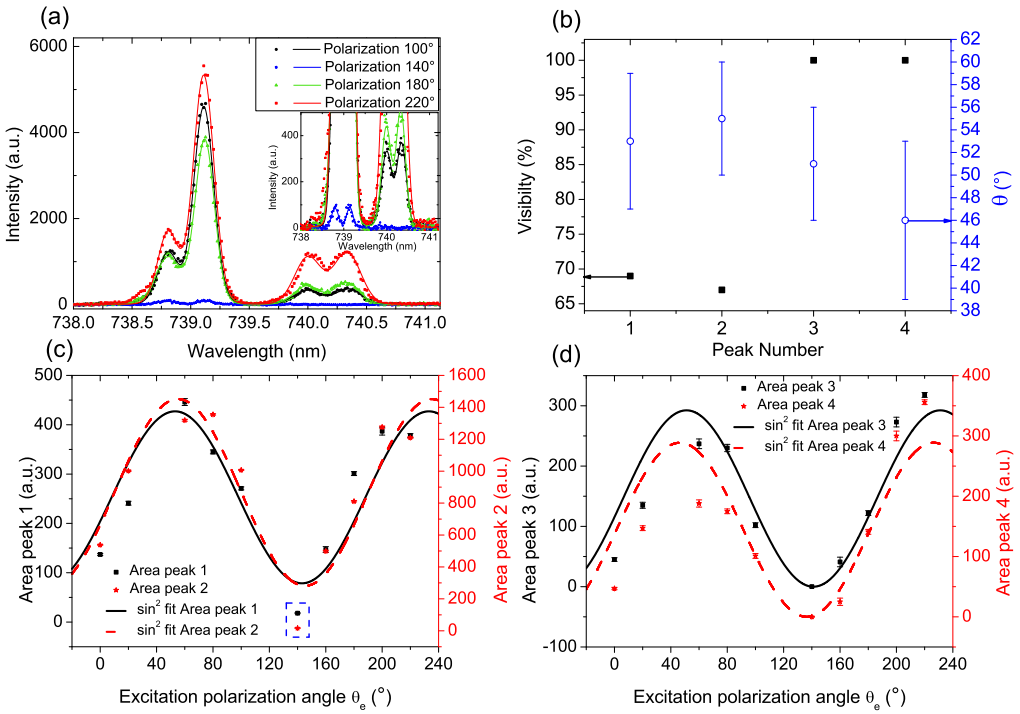

Figure 7.26: Polarized absorption of emitter C1. (a) fluorescence spectra of emitter C1 taken at different angles of incident excitation polarization at a temperature of 27 K. The inset of the graph shows an enlarged detail to enable observation of the weaker doublet. Spectra taken at $0.56\,P_{Sat}$.(b) summary of visibility (black squares) and linear polarization direction corresponding to maximum absorption θ (blue circles) obtained from the fits in (c) and (d). (c) and (d) peak areas in dependence of the excitation polarization fitted with Eq. (7.18).

the emitted light is polarized at 64 °. For emitters C3 and C5, we find deviations of more than 30 °. For emitter C1, we cannot compare the data as noncalibrated polarization optics were used. Thus, we might tentatively suspect that for excitation with 671 nm a reorientation in the excited state might possibly take place leading to deviations in the absorption and emission dipole orientation. On the other hand, as discussed above, for the determination of dipole orientations, spectrally integrated measurements might be more precise, thus the deviations might also be partially due to the inaccuracy of the measurements.

Furthermore, the question has to be raised whether these observations support one of the models suggested for the line splitting mechanism of the SiV center ZPL transition. We here focuss on the emission polarization as the polarized absorption yielded inconclusive results. Measuring the emission polarization, we find linearly polarized light with a common polarization direction for all fine structure components. Measurements at room temperature suggest a single, ⟨110⟩-oriented dipole as discussed in Sec. 6.4. This type of transition dipole only occurs in low symmetry defects with C_2 or D_2 symmetry. According to the discussion in Sec. 2.2, these symmetries do not lead to orbitally degenerate states as they only show one-dimensional

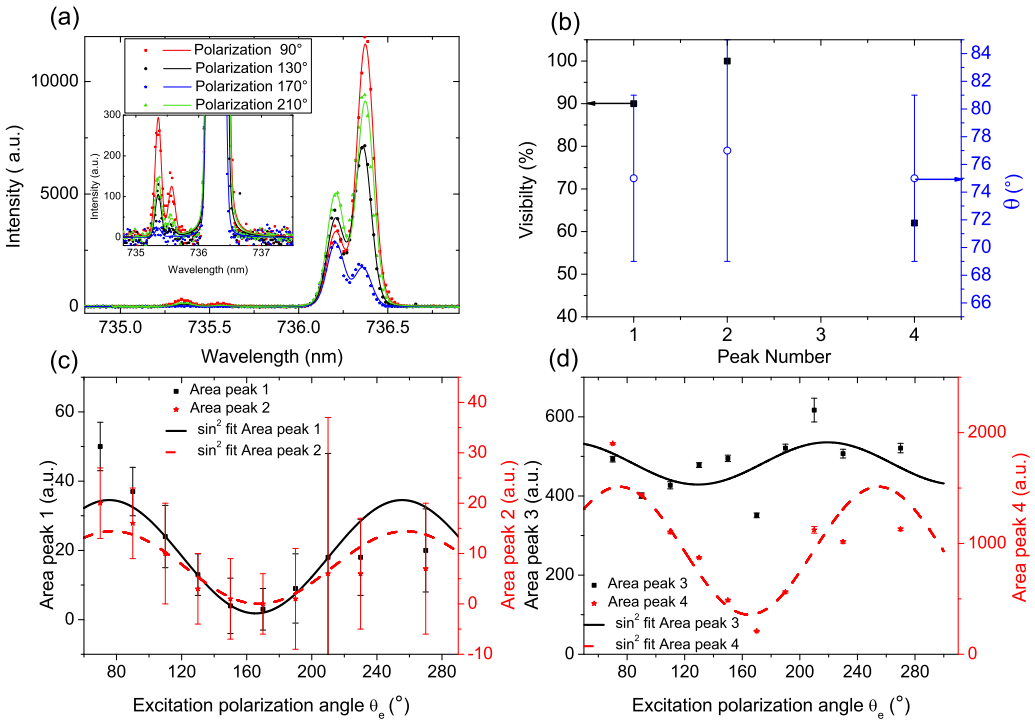

Figure 7.27: Polarized absorption of emitter C2. (a) fluorescence spectra of emitter C1 taken at different angles of incident excitation polarization at a temperature of 30 K. The inset of the graph shows an enlarged detail to enable observation of the weaker doublet. (b) summary of visibility (black squares) and linear polarization direction corresponding to maximum absorption θ (blue circles) obtained from the fits in (c) and (d). (c) and (d) peak areas in dependence of the excitation polarization fitted with Eq. (7.18).

irreducible representations. Therefore, a Jahn-Teller effect seems unlikely for the line splitting as there are no orbitally degenerate states which could split into sublevels. However, one might argue that the low measured symmetry is already the result of a (static) Jahn-Teller effect. However, for line components emerging from the splitting of an orbitally degenerate state one would not expect a common linear polarization direction. For line components that arise due to a splitting via tunneling between two spatial configurations (see discussion at the beginning of this chapter), a common polarization of the fine structure components is expected. However, it has to be emphasized that it is not clear what are the different configurations that would lead to such a tunnel coupling: Moliver has suggested a tunnel coupling in the context of a model for the SiV center involving $C_{3\nu}$ symmetry [123]. This symmetry does not describe the measured dipole orientation. For $C_{3\nu}$ symmetry, the simulations in Ref. [123] indicate the existence of different configurations with low energy barriers (tunnel barriers). As no simulations for the lower symmetries (C_2 or D_2) exist, it is not clear whether different spatial configurations with possible tunneling exist for these symmetries. We thus can only tentatively suspect that the splitting arises due to a tunnel coupling as the polarization properties of the fine structure components

support this model. Further investigations including controlled modifications of the level system using external electric fields might help to support or disprove this model.

Summary of the Chapter

Summarizing this chapter, we were able to unambiguously identify single color centers as single SiV centers due to the four line fine structure of their ZPL. The observed line patterns, however, are significantly altered compared to the line pattern for SiV centers in a single crystalline diamond due to stress without a trend to preferred changes. We observe a temperature dependent homogeneous linewidth best described via a T^3 law, the main cause of the broadening remains uncertain but might be associated to phonon-broadening in the presence of impurities. Spectral diffusion is observed as an additional line broadening mechanism for most of the single emitters, in contrast to the ensemble in the single crystal. We find spectral diffusion linewidths ranging from 25 GHz to 160 GHz. In addition to the linewidth, the line position of the ZPL changes upon cooling, we observe a blue shift of 20-30 cm^{-1} for cooling from room temperature to approx. 5 K. The temperature dependence is close to a T^4 dependence with deviations at elevated temperatures. From the temperature dependence, we cannot infer the dominant mechanism responsible for the blue shift as either due to quadratic electron-phonon coupling or lattice contraction. All emitters reveal population dynamics that are reasonably described in the framework of the three level intensity dependent de-shelving model at cryogenic as well as room temperature. No clear evidence for temperature dependent processes including de-activation of non-radiative processes and changes in shelving or de-shelving dynamics are found. The temperature dependent line intensities indicate thermal population transfer in the excited state in accordance with the literature. Polarization measurements reveal that all fine structure components are linearly polarized with a common polarization direction. In absorption, the behavior is not fully conclusive: Some peaks show polarized absorption, while other peaks, even for the same emitter, do not show preferential absorption of a distinct linear polarization direction.

Chapter 8

Photoluminescence of SiV centers in the spectral region >800 nm

As discussed in Sec. 5.2.2, several spectra of single SiV centers feature very narrow room temperature photoluminescence (PL) lines in the near-infrared spectral region mostly between 820 nm and 840 nm. For simplicity, we will term these lines *near-infrared (NIR) lines* throughout this chapter. The NIR lines might arise from narrow vibronic sidebands or due to additional purely electronic transitions of the SiV centers. However, the sharp emission lines might also belong to other color centers incorporated together with the SiV centers during CVD growth: E.g., Ref. [300] reports ZPL emission of single nickel-related centers between 806 nm and 820 nm after CVD growth on nickel-implanted silica substrates. According to manufacturer specifications, the seed diamonds (HPHT diamonds) used for nanodiamond (ND) growth contain up to 5 ppm mass (5 mg/kg) of nickel. Thus, a nickel contamination of the NDs cannot be excluded and the NIR lines might not originate from the SiV centers giving rise to the 740 nm ZPL. Also for the heteroepitaxially nucleated samples, formation of other color center is conceivable due to impurities in the CVD process.

This chapter deals with more detailed investigations of this near-infrared luminescence. Further information on these additional PL transitions might help in elucidating the full electronic level structure of the SiV center. First, we discuss the spectroscopic properties at room temperature using an emitter displaying especially pronounced luminescence in the region $\lambda > 800$ nm dominated by a distinct single line. Second, we examine the saturation of the fluorescence and the intensity auto-correlation of the ZPL and the additional NIR line. Furthermore, we use cross-correlation measurements to investigate if the additional line originates from the same emitter. Polarization measurements yield further information on polarized absorption and polarization of the fluorescence of the ZPL and the additional NIR line. As a last source of information, we discuss the low temperature properties of the NIR lines for two emitters in NDs.

8.1 Spectroscopic characterization

Figure 8.1 displays the spectrum of emitter EF5. This emitter is located in a (001) heteroepitaxial diamond film (sample MFDIA562). The ZPL is clearly visible at 739.1 nm, a Lorentzian fit yields a linewidth of 0.9 nm (2.0 meV). Figure 8.1(b) shows the sideband region of the spectrum of emitter EF5 in detail. As clearly visible, a single line dominates the spectrum in the region $\lambda > 800$ nm. This line features higher brightness compared to the corresponding NIR lines of most other investigated SiV centers. Thus, this emitter is highly suitable for further investigations of the NIR PL. A Lorentzian fit to the narrow NIR line yields a peak position of 822.7 nm and a linewidth of 1.4 nm (2.6 meV) [see inset of Fig. 8.1(a)]. The energetic difference between the ZPL and the NIR line is 170 meV. It is thus close to the energy of the Raman active, optical, Brillouin zone-center phonon mode in diamond (165 meV, e.g, [147]). However, due to the different spectral widths as well as the different fine structure of the lines that is even more striking at low temperature (investigated for other emitters, see Sec. 8.5), the 822.7 nm NIR line cannot originate from Raman scattering of the 739.1 nm ZPL. For other SiV centers, also multiple lines with wavelengths roughly in the spectral range from 820 nm to 840 nm have been observed, additionally excluding Raman scattered light.

As all SiV centers investigated in this work revealed internal population dynamics of a three level system (see Sec. 5.3.2), one might suggest that the 822.7 nm line is due to a fluorescent transition from the excited state to this third level or due to a transition from the third level to the ground state. For NV centers, radiative transitions between shelving states (singlet states) have been reported at 1046 nm [301]. Furthermore, recent reports have shown an absorption of SiV ensembles between 830 nm and 860 nm [121]. Thus, if the narrow NIR lines indeed originate from an electronic transition, one might suspect the transition takes place from the shelving state to the ground state as absorption can only be detected for transitions involving the ground state of the system.

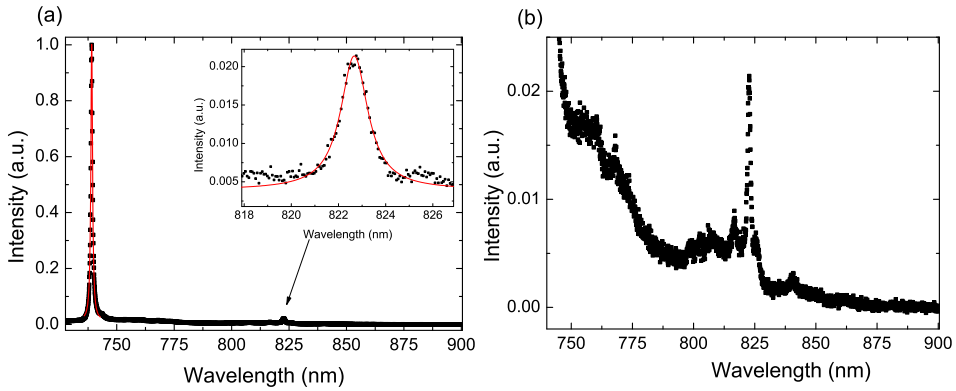

Figure 8.1: Spectrum of emitter EF5 all spectra have been normalized on the ZPL. (a) Overview spectrum, the inset shows a fit of the dominant narrow PL line in the region $\lambda > 800$ nm, (b) zoomed image of the vibronic sideband region of emitter EF5.

8.2 Saturation measurements at room temperature

As already visible from the spectrum, the 822.7 nm line is significantly weaker than the ZPL at 739.1 nm. To quantify the ratio of the luminescence intensities, we perform a simultaneous measurement of the count rates on these lines. Here, bandpass filters (730-750 nm for the ZPL, 815-825 nm for the 822.7 nm PL) in front of the two APDs of the HBT setup enable the concurrent measurement. Note that due to this procedure, the measured count rates represent only the count rate on one detector, while for the saturation measurements discussed in Secs. 5.3.1 and 7.4.1 rates from both detectors have been summed up. Figure 8.2 displays the saturation curves measured on the ZPL and the 822.7 nm line. The fits yield a negligible background contribution for both curves. For the ZPL, we find a saturation power P_{sat} of 61 μW and a maximum photon rate I_∞ of 55.4×10^4 cps. For the 822.7 nm line, we find $P_{sat} = 75\,\mu$W and $I_\infty = 5.8 \times 10^4$ cps. The very similar saturation powers obtained for the two transitions might be considered as a first hint that the luminescence is excited via the same absorptive transition. This in turn indicates that the lines stem from the same emitter. The detection efficiency of the APDs is lower for 820 nm light (approx. 65% for 740 nm, 50% for 820 nm) additionally, the bandpass filter used for the NIR line has a lower transmission (85% for 740 nm, 50% for 820 nm). Thus, the detection efficiency at 820 nm amounts only to 45% of the detection efficiency at 740 nm. A correction for this difference yields $I_\infty^{corr} = 12.8 \times 10^5$ cps for the NIR PL. Thus, the ZPL intensity amounts to 4.3 times the intensity of the 822.7 nm line.

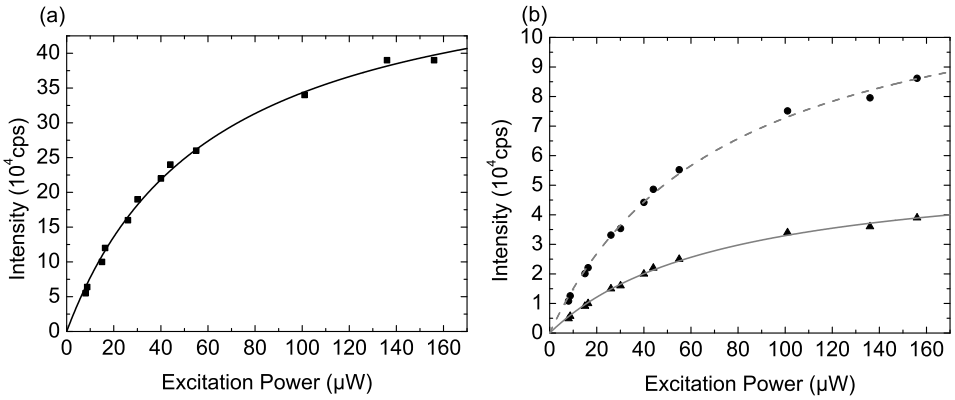

Figure 8.2: Saturation curves of emitter EF5. (a) Saturation curve measured on the ZPL (b) Saturation curve on the 822.7 nm line. The triangles give the measured intensity, the solid line gives the fit to the data. The dashed line and the dots represent the curve corrected for the lower detection efficiency at 822.7 nm. Excitation with 671 nm laser light.

8.3 Intensity correlation measurements

This section aims at deducing additional information on the luminescent transitions by measuring the intensity (auto-)correlation of the emitted light. A detailed discussion on intensity auto-correlation measurements and the evaluation of the data is

given in Sec. 5.3.2. The count rate measured on the 822.7 nm line is approx. an order of magnitude weaker than the count rate measured for the 739.1 nm ZPL, thus cross-correlation measurements for the lines as well as $g^{(2)}$ auto-correlation measurements for the 822.7 nm line are challenging due to the low signal levels. Figure 8.3 summarizes the intensity correlation measurements on emitter EF5. Measurements of $g^{(2)}$ for the 739.1 nm ZPL reveal only a weak bunching [Fig. 8.3(a)]. The parameters obtained from fitting the intensity dependent $g^{(2)}$ functions are summarized in Fig. 8.4. Figure 8.4 also displays the power dependent curves for τ_1, τ_2 and a (for the ZPL $g^{(2)}$ function) obtained from the intensity dependent de-shelving model as solid lines (see Sec. 5.3.2). The obtained rate coefficients are: $k_{23} = 5.8\,\mathrm{MHz}$, $k_{21} = 1.16\,\mathrm{GHz}$, $k_{31}^0 = 0.27\,\mathrm{MHz}$, $d = 18.96\,\mathrm{MHz}$ with the parameters $\sigma = 8.4\,\mathrm{MHz}/\mu\mathrm{W}$ and $c = 66.6\,\mu\mathrm{W}$. Thus, the parameters observed for emitter EF5 are in accordance with the parameters observed for SiV centers in NIs and randomly oriented NDs in Sec. 5.3.2. For this emitter, the increase of τ_2 at low excitation powers is significantly overestimated by the intensity dependent de-shelving model, while the power dependence of τ_1 and a is reasonably described.

Figure 8.3(b) displays the $g^{(2)}$ auto-correlation measurements of the 822.7 nm fluorescence.[1] Fewer measurements have been performed for the 822.7 nm line due to the significantly increased measurement time at low count rates. As it is clear from Figs. 8.3(b) and 8.4, the $g^{(2)}$ functions of the 822.7 nm emission display an almost negligible bunching. We fit these $g^{(2)}$ functions using the same fit function ($g^{(2)}$ function of a three level system corrected for experimental issues) as for the $g^{(2)}$ functions of the ZPL fluorescence. The fitted τ_1 times are about a factor of 2.4 shorter than measured for the 739.1 nm emission.

Using the $g^{(2)}$ measurements discussed above, we try to deduce the origin of the 822.7 nm luminescence: First, it should be emphasized that the fact that a deviating antibunching time constant τ_1 is observed for NIR line and ZPL excludes that the NIR line is a vibronic sideband of the ZPL: Vibronic sidebands originate from the same excited state as the ZPL; however, the sideband transitions end in vibrationally excited states in the ground state (see page 14). These vibrationally excited states decay within picoseconds to the vibrational ground state which is also the final state of the ZPL transition (see discussion page 63). This very fast relaxation following the emission of a photon does not influence the measured $g^{(2)}$ and thus the $g^{(2)}$ function measured for sideband fluorescence is equal to the $g^{(2)}$ function measured for the ZPL fluorescence itself. As discussed in Sec. 5.3.2, the internal population dynamics of single SiV centers have been successfully modeled using the level scheme depicted once more in Fig. 8.5. The ZPL luminescence arises due to the transition between states 2 and 1, while a shelving state (state 3) induces a bunching in the $g^{(2)}$ measurement. The observation of an intensity dependent de-shelving mechanism requires the existence of a fourth state (labeled state 4) that enables the de-shelving. The $g^{(2)}$ function of this system is calculated by solving the coupled rate equations

[1] For these measurements, an asymmetric combination of filters has been used in the HBT: a longpass 800 nm for one diode and a bandpass 815-825 nm for the second diode. As no other intense luminescence is observed in the range $\lambda > 800\,\mathrm{nm}$, this does not impose restrictions on the measurements. Furthermore, the fitting was performed without background correction.

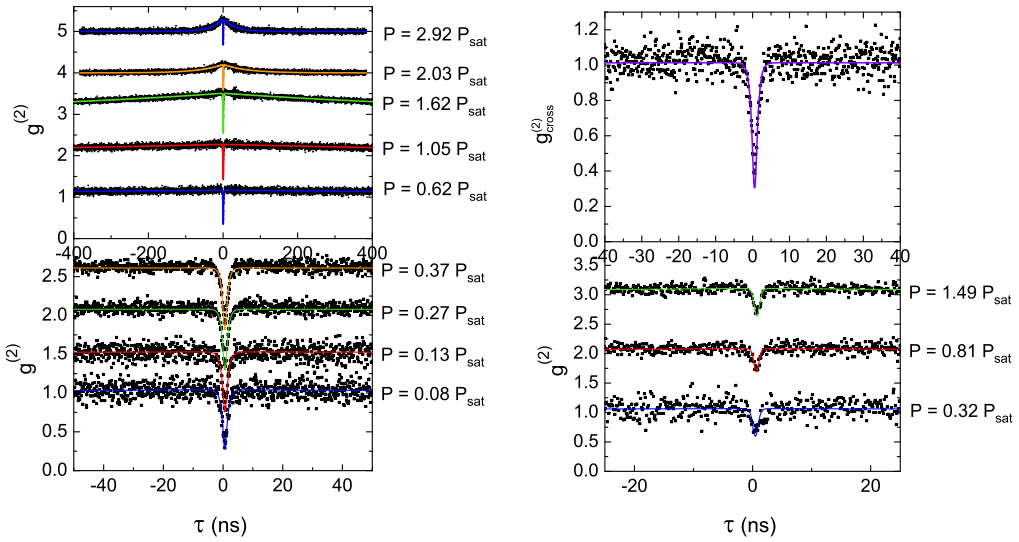

(a) $g^{(2)}$ auto-correlation measurements for the 739.1 nm ZPL with varying excitation power

(b) lower graph: $g^{(2)}$ auto-correlation measurements for the 822.7 nm line with varying excitation power, upper graph: intensity cross-correlation of 739.1 nm and 822.7 nm line.

Figure 8.3: Correlation measurements for emitter EF5

for the populations [see Eqs. (5.6)–(5.8)] using the initial condition that at $\tau = 0$ the system resides in the ground state. This initial condition is justified, as each photon detection event on the ZPL projects the system back into the ground state. The normalized occupation probability of state 2, $\frac{N_2(\tau)}{N_2(\tau\to\infty)}$, gives the $g^{(2)}$ function for the light measured on the transition $2 \to 1$ (ZPL transition) [24]. For this level system, one might suspect that the 822.7 nm luminescence arises due to the transition from state 3 to state 1 (ground state). This assumption is motivated by the observation of absorbing transitions at similar wavelengths in diamonds containing SiV ensembles (see discussion above and Ref. [121]). For this situation, one might calculate the $g^{(2)}$ function for the light emitted on the transition $3 \to 1$ analogous to the $g^{(2)}$ function for the ZPL

$$g^{(2)}_{3\to1} = \frac{N_3(\tau)}{N_3(\tau \to \infty)}, \tag{8.1}$$

as also here each photon detection event projects the system into the ground state and we can use the same initial condition as for the transition $2 \to 1$. It should be emphasized that the rate coefficient for the transition $3 \to 1$ was found to be intensity dependent due to the de-shelving via level 4. We assume that the direct de-excitation of level 3 leads to a radiative transition from $3 \to 1$. In contrast, the intensity dependent de-shelving process can be interpreted as a non-radiative transition to state 1 via state 4. Both processes influence the population in state 3 and thus $g^{(2)}_{3\to1}$. For $g^{(2)}_{3\to1}$, the de-shelving process implies an *intensity dependent non-radiative decay* for the transition $3 \to 1$. Also in the presence of this intensity dependent

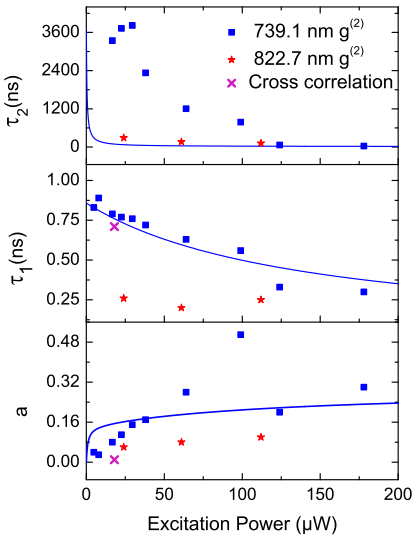

Figure 8.4: $g^{(2)}$ parameters obtained for the $g^{(2)}$ measurements of emitter EF5. Blue solid lines give the intensity dependent curves for the ZPL $g^{(2)}$ function fitted with the intensity dependent de-shelving model (parameters see text).

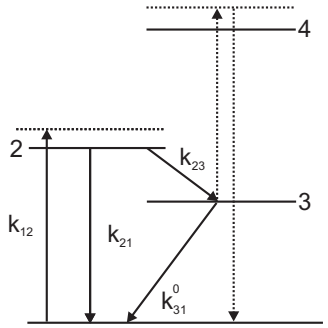

Figure 8.5: Schematic representation of the extended three level model employed to explain the population dynamics of single SiV centers.

non-radiative channel, for each intensity, the probability to detect a photon on the transition $3 \rightarrow 1$ after a delay τ is proportional to the population $N_3(\tau)$ and thus $g^{(2)}_{3\rightarrow 1}$ indeed describes the $g^{(2)}$ function for the emitted light.

We now solve the coupled rate equations [Eqs. (5.6)–(5.8)] using the rate coefficients k_{21}, k_{23}, k^0_{31} and d as well as the parameters c and σ obtained from the $g^{(2)}$ measurements of the ZPL luminescence (definition of the parameters see Sec. 5.3.2).[2] From the solution of the rate equations, we calculate the normalized occupation for state 3 and 2 for different excitation powers P. Figure 8.6 displays the resulting normalized occupation of state 2, i.e., the $g^{(2)}$ function for the ZPL fluorescence, as well as the normalized occupation of state 3, i.e., $g^{(2)}_{3\rightarrow 1}$. We use $P = 7\,\mu$W, $P = 35\,\mu$W, $P = 140\,\mu$W and $P = 210\,\mu$W, roughly corresponding to $0.1\,P_{sat}$, $0.5\,P_{sat}$, $2\,P_{sat}$ and $3\,P_{sat}$. Comparing Figs. 8.3(a) and 8.6, it is apparent that the simulations reasonably describe the $g^{(2)}$ functions measured for the ZPL fluorescence, thus the rate coefficients determined using the intensity dependent de-shelving model appropriately describe the observed SiV center. We emphasize that the simulated functions do not include the correction for the timing jitter of the APDs, thus the simulated functions display $g^{(2)}(0) = 0$, whereas the measured $g^{(2)}$

[2]Solving of the differential equations (analytically) as well as the calculation of the limiting values $N_{2,3}(\tau \rightarrow \infty)$ is performed using Maplesoft's Maple 15.

functions display a non-vanishing value for $g^{(2)}(0)$ due to the timing jitter of the APDs.

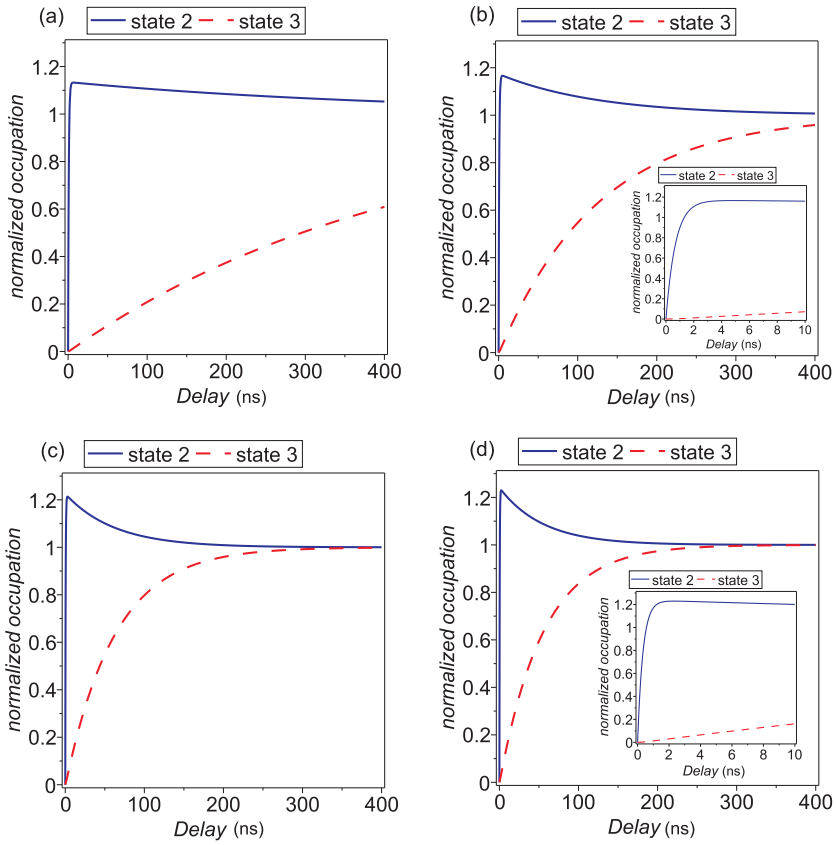

Figure 8.6: Normalized occupation of state 3 and state 2, simulated using $k_{23} = 5.8\,\mathrm{MHz}$, $k_{21} = 1.16\,\mathrm{GHz}$, $k_{31}^{0} = 0.27\,\mathrm{MHz}$, $d = 18.96\,\mathrm{MHz}$ and $\sigma = 8.4\,\mathrm{MHz}/\mu\mathrm{W}$ and $c = 66.6\,\mu\mathrm{W}$. (a) $P = 7\,\mu\mathrm{W}$, (b) $P = 35\,\mu\mathrm{W}$, (c) $P = 140\,\mu\mathrm{W}$, (d) $P = 210\,\mu\mathrm{W}$.

As evident from Fig. 8.6, $g^{(2)}_{3\to1}$ also displays an antibunching behavior; however, the corresponding time constant τ_1^{31} is much longer than τ_1 measured for the ZPL fluorescence: Below saturation [Fig. 8.6(a) and (b)], $g^{(2)}_{3\to1}$ converges to a constant value of one only within several 100 ns as the rate coefficients populating (k_{23}) and de-population (k_{31}) the shelving state are much lower than k_{21}. Thus, the course of $g^{(2)}_{3\to1}$ is in stark contrast to the $g^{(2)}$ functions measured on the 822.7 nm line displayed in Fig. 8.3(b). The $g^{(2)}$ measurements thus exclude that the 822.7 nm line arises due to a transition between the shelving state, identified from $g^{(2)}$ measurements on the ZPL, and the ground state.

As further measurements prove that the NIR line and the ZPL originate from the same emitter as discussed below, a further extended level scheme has to be considered to include the NIR line. Figure 8.7 schematically depicts such a level scheme. In addition to the fluorescent ZPL transition and the possibly non-radiative path via the shelving state, a third relaxation possibility including the excited state of the 822.7 nm NIR transition should be taken into account. However, the $g^{(2)}$

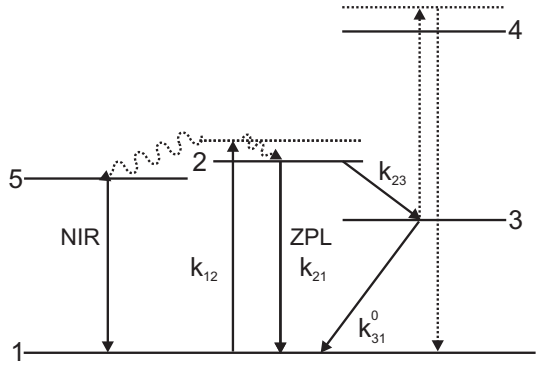

Figure 8.7: Schematic representation of the extended model including the NIR transition. Length of the NIR transition and of the ZPL transition drawn to scale.

function measured for the ZPL fluorescence does not display deviations from the $g^{(2)}$ function of a three level system. Thus, this additional path should not lead to an accumulation of population in state 5, which is the case for the shelving state (state 3), as this would lead to changes in the $g^{(2)}$ function measured on the ZPL. Indeed, the time constant measured for the antibunching of the 822.7 nm line is short compared to the antibunching time constant of the ZPL, thus supporting the assumption of a fast decay path. Thus, this pathway, similar to fast non-radiative decay paths (see discussion Sec. 5.3.4), might not lead to a deviation of the measured $g^{(2)}$ function for the ZPL fluorescence from the $g^{(2)}$ function of a three level system. We assume that the relaxation to state 5 occurs from the intermediate pumping level. If the relaxation path to state 5 would include the excited state (state 2), the antibunching constant for the 822.7 nm line should be at least as long as the antibunching constant of the ZPL, as the filling of state 5 from the excited state 2 would dominate the antibunching time constant. The relaxation rates from the pumping level are not directly accessible in our measurements, they are just assumed to be faster than any other rates in the system so that the pumping level does not accumulate population. This assumption is justified, as the vibrationally excited states that are most probably responsible for the pumping transition feature very short lifetime in the ps range (discussion see page 76). The ratio of the relaxation rates from the pumping state to state 5 and to the excited state 2 should determine the branching ratio for the 740 nm ZPL and the NIR line. However, taking into account also the issue of a varying quantum efficiency (see discussion below), the intensity ratio of the lines does not aid in deducing the branching ratio.

For a two level system at low excitation powers, the time constant of the antibunching indicates the lifetime of the excited state of the radiating transition under the assumption that no longer lived states are populated in the excitation process. Thus, from the $g^{(2)}$ measurements, one might expect a very bright emission from the 822.7 nm line due to a short lifetime. However, it is not clear what excited state population can be reached for the 822.7 nm line due to the unknown branching ratio of the transition from the pumping levels to states 2 and 5. Furthermore, as discussed in Sec. 5.3.4, for the ZPL transition of SiV centers a low quantum efficiency varying between 0.3% and 9.2% for individual emitters is found. Thus, in principle, the lower brightness might also be correlated with a more efficient quenching mechanism for near-infrared luminescence leading to an even lower quantum efficiency: In

Ref. [141], the author discusses the possibility of infrared emission from color centers in diamond. It is pointed out that lifetimes for long wavelength transitions in general are shorter than lifetimes for transitions in the visible spectral range as non-radiative decay due to multi-phonon emission becomes more important. Here, one has to take into account that for a transition with longer wavelength a lower number of phonons is needed to bridge the transition energy. Following the discussing in Sec. 5.3.4, 9.1 phonons with 165 meV, the maximum phonon energy supported by the diamond lattice, are needed to bridge the transition energy of the 822.7 nm line. Thus, the number of required phonons is smaller by one compared to the phonon equivalent of the 739.1 nm ZPL amounting to 10.2 phonons, as a consequence the probability of a non-radiative decay is higher. Non-radiative quenching of low energy transitions has been reported for NV^- centers: For NV^- centers, infrared emission at 1046 nm occurs due to transitions between metastable levels [301]. The infrared emission at 1046 nm is four orders of magnitude weaker than the visible 637 nm emission despite the fact that 30% of the population is available for the transition. To clarify the issue of the quantum efficiency, the population dynamics has to be evaluated in detail for several emitters and the level scheme has to be identified.

In addition to the $g^{(2)}$ auto-correlation measurements, we perform a cross-correlation measurement of the two emission lines: As discussed in Sec. 8.2, bandpass filters in front of the individual detectors in the HBT setup allow for a simultaneous detection of the fluorescence from the 739.1 nm and the 822.7 nm line respectively. If these lines originate from the same emitting color center, a cross-correlation measurement reveals an antibunching: the emission is anti-correlated. If the lines originate from different emitters, one expects no correlation between the fluorescence photons. We point out that the cross-correlation measurement does not enable to discriminate between lines from different charge states of the emitter or lines from different transitions (purely electronic or vibronic) of the same charge state. We emphasize, that the two lines cannot arise from a cascaded emission, as the photon energy of the excitation laser is 1.78 eV and thus does not supply the summed energy for both transitions (1.68 eV and 1.51 eV). Additionally, the linear dependence of the fluorescence on excitation power for both transitions excludes multi-photon processes for the excitation.

Cross-correlation measurements have been used to prove the charge state conversion of a single NV center from NV^- to NV^0, previously only known for ensembles [125]. We assume that the 822.7 nm line observed here is not due to a second charge state, as the emission of SiV^0 has been reported at 946 nm [121]. Nevertheless, also the unlikely case that a single electron alternatively charges an SiV center emitting at 739.1 nm and another color center emitting at 822.7 nm would explain anti-correlated emission. However, one might also expect to observe fluorescence blinking in this case, which has not been observed in the experiments. Figure 8.3(b) displays the measurement of the cross-correlation. We find strong antibunching, the time constant $\tau_1^{cross} = 0.7$ ns is close to the values obtained for the 739.1 nm ZPL. Summarizing, the cross-correlation measurement identifies the 822.7 nm PL as anti-correlated to the SiV ZPL, thus the lines originate from the same emitter. Ref. [302] introduces cross-correlation measurements between disjunct spectral win-

dows of the luminescence transition of a single quantum dot that is broadened by spectral diffusion. To change its emission from one window to the other, the emitter has to undergo a spectral jump. The cross-correlation exhibits an antibunching, the time constant of the antibunching reveals the characteristic time τ_d for the spectral jumps. Interpreting our measurements in the same way, the time constant of the antibunching reveals the characteristic time for the SiV center to change its emission between the two possible transitions. As this characteristic time is comparable to the lifetime of the excited state (state 2, Fig. 8.7), the changes occur in between successive excitation and emission cycles of the ZPL. This short characteristic time also supports the assumption of an alternative decay path connecting the pumping levels and the ground state of the center without involving the long lived shelving state: The longer time windows, in which the emitter resides in the shelving state (state 3) do not influence the measured cross-correlation between the ZPL and the NIR lines if the level scheme in Fig. 8.7 is applicable. Additionally, the cross-correlation indicates that the SiV center changes between the two emission lines very often instead of undergoing a larger number of transitions on either the ZPL or the NIR line before changing its emission wavelength again.

8.4 Polarization measurements

Further information about luminescent transitions can be obtained using polarization spectroscopy. For a detailed discussion on polarization spectroscopy and the measurement procedure, see Chapter 6. First, we measure the polarized absorption of the color centers by rotating the polarization of the excitation light (671 nm) and simultaneously detecting the fluorescence either on the 739.1 nm line or on the 822.7 nm line. Second, we measure the linear polarization degree of the emitted light by rotating a polarization analyzer while the excitation polarization is kept fixed.

Figure 8.8 displays the polarization dependent measurements on emitter EF5 in a polar plot. Figure 8.8(a) [Fig. 8.8(b)] displays the data for the 822.7 nm [739.1 nm] line, details see figure caption. To enable comparison of the data, all measurements have been normalized to one. The polarized absorption indicates the preferential absorption of linearly polarized light with a polarization direction of 89° for both measurements on the 822.7 nm line and the 739.1 nm line. For light perpendicular to that direction, effectively no absorption takes place. Thus, the lines arise due to an absorptive transition with the same in plane dipole moment. Together with the observation of a similar saturation power, this indicates that the lines are excited via the same absorptive transition and thus arise from the same emitter.

Additionally, the linear polarization direction of the emitted light is measured to be 84.0° for the 822.7 nm line and 85.6° for the 739.1 nm line. Thus, the emission shares a common polarization direction within experimental errors. Figure 8.8(a) seems to indicate that the degree of linear polarization is significantly lower for the 822.7 nm line. However, this is due to experimental reasons: The polarization analyzer is intended for use with visible light only. Thus, its performance deteriorates in the near-infrared: At 770 nm for linearly polarized light a loss of contrast of 5% has been measured, for 780 nm even 12% loss have been demonstrated [303]. Longer

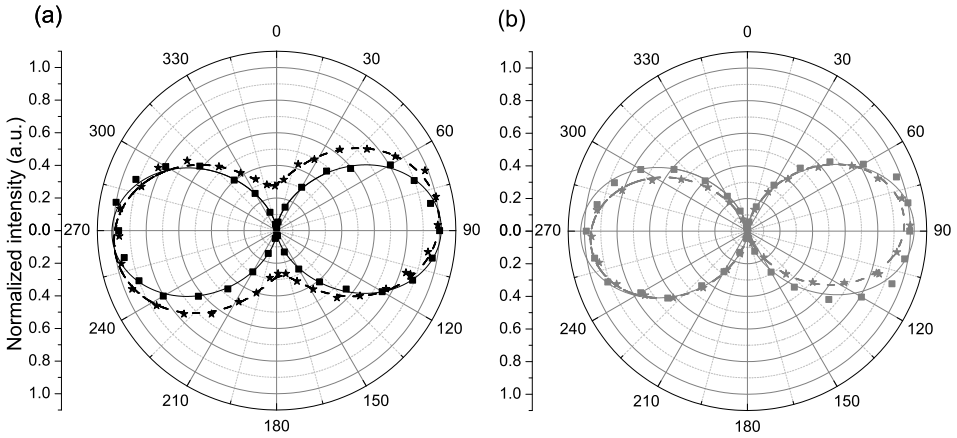

Figure 8.8: Polarization measurements on emitter EF5. (a) measurement on 822.7 nm line (b) measurements on 739.1 nm ZPL. Filled squares (stars) indicate the measured data of polarized absorption (emission polarization). Solid lines (dashed lines) give the fits to the absorption (emission) data.

laser wavelengths were not available for testing. Following the measurements at shorter wavelength, we assume that most of the loss of contrast originates from the polarization analyzer. Background fluorescence has been subtracted for both measurements; however, as discussed in Sec. 6.1 this procedure may introduce an error in the visibility of 5-10% due to a spatially varying background. The observation of a common polarization direction also indicates a common orientation of the emission dipole in the sample plane (see Sec. 6.2). This might also indicate that the emission originates from the same emitter. For the 822.7 nm and the 739.1 nm lines, polarized absorption and emission yield an almost parallel orientation of the emission and absorption dipoles respectively. This also holds for the emission and absorption dipoles corresponding to the ZPL of other SiV centers investigated in this work (see Sec. 6.3).

8.5 Spectroscopic investigation at low temperature

After finding very strong evidence that the NIR lines originate from the same emitter and are due to electronic transitions, we now try to verify the electronic nature of the lines via spectroscopic methods. As discussed in Sec. 5.2.2, previous work by Sittas et al. [115] has shown that an emission line at 812 nm associated with the SiV center significantly narrows upon cooling. The authors, therefore tentatively attribute this line to an electronic rather than vibronic transition. For an electronic transition, as discussed in Sec. 7.2.2, a temperature dependent linewidth arises due to quadratic electron-phonon coupling. Thus, a purely electronic transition significantly narrows upon cooling. In contrast, the linewidth of a vibronic sideband is mostly determined by the lifetime of the vibrationally excited state in the ground state in which the respective transition ends [9] (for a general discussion on side-

band transitions see page 14). As the lifetime of this vibrationally excited state will not prolong significantly upon cooling, sidebands are expected to maintain a broad linewidth compared to electronic transitions upon cooling.

We perform a low temperature investigation of the emission in the spectral range $\lambda > 800\,\mathrm{nm}$ for two emitters: First, we investigate emitter C2 already introduced in Chapter 7. This emitter resides in a CVD ND on Ir. Second, we investigate emitter C5 also introduced in Chapter 7. This emitter resides in a BASD ND. Note that for the latter emitter the measured properties might still be influenced by the underlying ensemble of SiV centers.

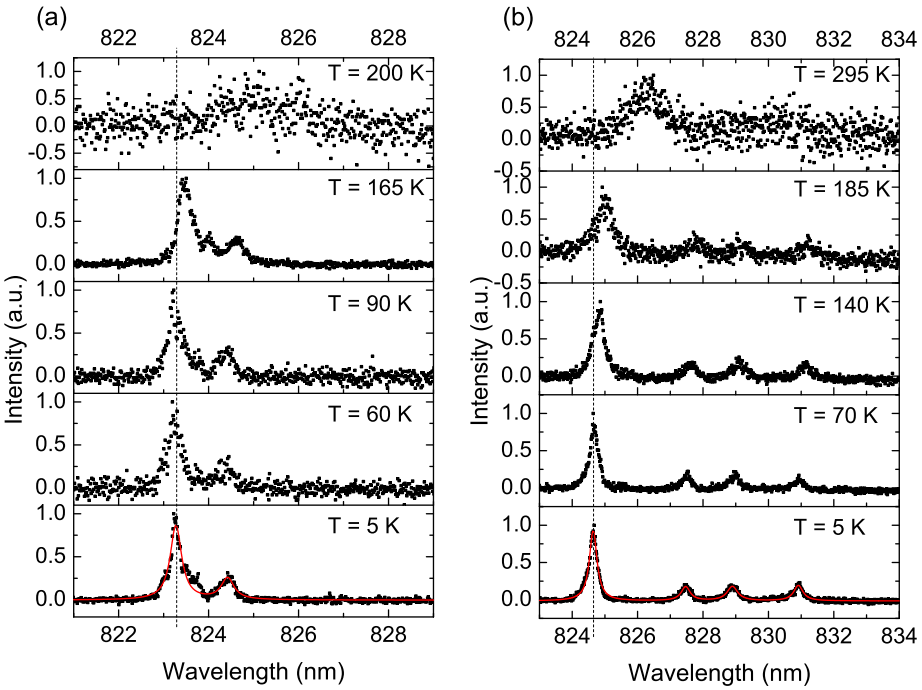

Figure 8.9: Temperature dependent spectra of the $\lambda > 800\,\mathrm{nm}$ luminescence for (a) emitter C2, (b) emitter C5.

Figure 8.9 displays temperature dependent luminescence spectra in the range $\lambda > 800\,\mathrm{nm}$ for emitters C2 and C5. It is clear that, in contrast to emitter EF5 investigated in the previous section, several lines are visible in the spectral region of interest. However, at room temperature the weaker lines disappear and a single line dominates the spectrum. The temperature dependent spectra clearly reveal a narrowing of the lines accompanied by a blue shift upon cooling. The spectra recorded at 5 K have been fitted using Lorentzian lines. For emitter C2, the fits yield two lines with a peak wavelength $\lambda_1 = 823.3\,\mathrm{nm}$ and width $w_1 = 0.4\,\mathrm{nm}$ as well as $\lambda_2 = 824.4\,\mathrm{nm}$ and $w_2 = 0.3\,\mathrm{nm}$ respectively. Each of these lines, furthermore, indicates a badly resolved doublet structure. This structure is similar to the structure observed for the 740 nm ZPL of emitter C2 as displayed in Fig. 7.8 (discussion Sec. 7.1.2), indicating that the NIR line might originate from a similar level scheme involving a split excited and ground state. For the excited state splitting

of emitter C2, i.e. the spacing of the two doublets of the ZPL, we find a splitting of 1.9 meV (see Tab. 7.2). The splitting for the two badly resolved NIR doublets is 2.0 meV. However, the relative intensities are significantly altered compared to the ZPL of this emitter.

For emitter C5, four lines are fitted corresponding to $\lambda_1 = 824.6\,\text{nm}$ ($w_1 = 0.3\,\text{nm}$), $\lambda_2 = 827.5\,\text{nm}$ ($w_2 = 0.3\,\text{nm}$), $\lambda_3 = 828.9\,\text{nm}$ ($w_3 = 0.4\,\text{nm}$) and $\lambda_4 = 830.9\,\text{nm}$ ($w_4 = 0.3\,\text{nm}$). We emphasize that for emitter C5, due to the underlying ensemble emission, it is not clear if all these lines originate from a single emitter. The measured linewidths indicate that the NIR lines are approx. a factor of 2-3 broader than the 740 nm ZPLs. The narrowing of the NIR lines upon cooling strongly indicates that these lines are due to electronic transitions as discussed above. The lineshift, however, does not give clear evidence: The observed NIR lines blue shift by approx. 1.6-1.7 nm (3.1 meV). Especially for emitter C2 this value includes a large error due to weak NIR emission at room temperature. The shift is comparable to the shifts observed for the 740 nm line (1.0-1.4 nm, 2.3-3.2 meV). However, this does not aid to identify electronic transitions or sidebands: An electronic transition might be expected to show such a characteristic shift. However, also the absolute energies of the sidebands shift when the ZPL shifts assuming that the photon energies are not influenced by cooling. Thus, the shifting behavior is also compatible with a sideband 'following' the blue shift of the 740 nm ZPL.

Summarizing, we find strong evidence that, besides the well known 740 nm ZPL, SiV centers exhibit additional electronic transitions in the near-infrared spectral range between 820 nm and 840 nm. For an emitter with a particularly pronounced single line, near-infrared emission we investigate the spectral properties at room temperature and find a very narrow linewidth of 1.4 nm (2.6 meV). The NIR line saturates at similar excitation power as the ZPL. However, despite a shorter excited state lifetime indicated in the $g^{(2)}$ measurements, the NIR line delivers a factor of four lower fluorescence rates. Cross-correlation measurement between the ZPL at 740 nm and the NIR line reveal anti-correlated emission, thus strongly indicating that the emission originates from the same emitter. The short antibunching time constant in the cross-correlation measurements indicates a fast switching between the transitions. $g^{(2)}$ auto-correlation measurements exclude that the NIR emission arises due to a transition from the shelving state to the ground state of the SiV center. They also exclude that the NIR lines are vibronic sidebands of the ZPL. Polarization measurements reveal preferential absorption of linearly polarized light for both transitions. The maximum absorption is observed for the same polarization direction. The emitted fluorescence light shares a linear polarization direction. Low temperature measurements indicate a narrowing of the lines in the spectral region 820 nm to 840 nm. This finding, together with the observation of absorption in diamonds containing SiV ensembles at similar wavelengths in Ref. [121], supports the identification of the NIR lines as electronic transitions.

Chapter 9

Summary and Outlook

In this work, single *in situ* created SiV centers have been investigated with respect to their suitability as single photon sources. Additionally, spectroscopic investigations at low temperature have been performed and previously unknown fluorescent transitions were investigated. Polarization spectroscopy at room as well as cryogenic temperature yielded information on dipole moments and orientations. The results will be briefly summarized in the following and an outlook on possible further work will be given.

In situ production of SiV centers in various materials systems

During this work, SiV centers were successfully introduced *in situ* into chemical vapor deposition (CVD) diamond using microwave plasma (MW) and hot filament (HF) CVD processes. Depending on SiV density, degree of crystal orientation, and stress distribution in the various material systems, the samples have been employed for different investigations:

- **Thin (001) oriented homoepitaxial HFCVD diamond film**: grown on HPHT diamond substrate, high SiV density and low stress level. Enables the observation of low temperature properties of 'unstressed' SiV ensemble ZPL.
- **colloidal BASD nanodiamonds (NDs)**: produced from polycrystalline HFCVD film, most NDs contain multiple emitters, spin coating from solution on various substrates feasible. Investigation of optical properties of SiV centers compared to polycrystalline starting material.
- **randomly oriented MWCVD NDs on Ir**: controlled ND density due to optimized seed process, mostly single, bright SiV centers observed. Characterization of single SiV centers as single photon sources as well as low temperature investigations, undefined stress fields in NDs
- **heteroepitaxial (001) oriented MWCVD nanoislands (NIs) on Ir**: single, bright SiV centers in crystalline environment with defined orientation observed, enhanced background compared to NDs, varying stress fields in individual NI. Characterization of single SiV centers as single photon sources

and investigation of dipole orientation in crystalline environment with defined orientation.

- **heteroepitaxial (001) oriented MWCVD thin film on Ir**: spectral properties of single SiV centers comparable to nanoislands, higher background fluorescence. Similar investigations to NIs.

SiV centers as room temperature single photon sources

Single SiV centers demonstrated highly suitable spectral properties for room temperature single photon emission: For most centers, more than 70% of the fluorescence concentrates in the zero-phonon-line (ZPL) at room temperature. The ZPL is especially narrow at room temperature: We find an average linewidth of 1.3 ± 0.5 nm in NIs and 1.7 ± 1.2 nm in NDs. With linewidths for single centers down to 0.7 nm, SiV centers show the narrowest room temperature color center emission observed at present. This renders single SiV centers highly qualified as narrow bandwidth room temperature single photon sources. The narrow linewidth potentially allows narrow spectral filtering thus SiV centers are interesting as single photon sources for quantum key distribution under daylight conditions where narrow spectral filtering is mandatory to reduce errors introduced by background detection events [39]. The peak wavelengths of the ZPL of individual SiV centers spread over 20 nm with an accumulation of emitters with ZPL wavelengths between 736 nm and 746 nm. Thus, despite a narrow bandwidth, the peak wavelength of individual emitters is subject to a large spread. We attribute this spread in peak wavelengths, the above mentioned spread in ZPL linewidths, as well as the varying fraction of the emission into the ZPL and the sidebands to the influence of the local environment of individual color centers: Micro stress fields at the site of an individual SiV center or other defects in the vicinity of the center might significantly influence the previously mentioned properties. Together with varying spectral properties, we find SiV centers which are fully photostable even for excitation far above saturation, while others exhibit blinking or even permanent bleaching under laser excitation. This varying photostability is also attributed to the proximity to other defects possibly serving as traps for electrons. To enhance the photostability, as well as the predictability of spectral properties of individual SiV centers, diamond host materials with lower stress and impurity/defect levels are desirable. To optimize existing diamond samples, one might, e.g., think of annealing steps that have shown to reduce the inhomogeneous linewidth of the ZPL for SiV center ensembles [140]. Additionally, larger nanodiamonds may be used to create SiV centers farther away from disturbing surface defects.

All SiV centers investigated in this work revealed internal population dynamics of a three level system: Besides the excited and ground state leading to the ZPL transition, a third longer lived shelving state has to be considered. The nature of the shelving state is unclear at present. From the shelving state, the color center can either relax spontaneously or via a laser induced (intensity dependent) de-shelving pathway. We have developed an extended three level model that includes a saturating, intensity dependent de-shelving rate to describe the internal population

dynamics. The rate coefficient for the ZPL transition is significantly higher than the rate coefficient for the transition to the shelving state for all investigated emitters. Nevertheless, the shelving state limits the maximum excited state population and, thus the maximum obtainable photon rate for continuous laser excitation, due to slow depopulation rates. In Ref. [304], the authors suggest to use plasmonic nanoparticles to selectively reduce the lifetime of shelving states and thus enhance the brightness of single emitters, such an approach might also be feasible for single SiV centers. If the shelving state arises due to a second charge state it might also be feasible to decrease the influence of the shelving state by introducing additional charges via doping of the diamond.

The Ir layer on which the NDs/NIs or thin heteroepitaxial films are grown strongly modifies the spatial emission pattern of single color centers as compared to an emitter in bulk diamond. We find that high collection efficiencies for the SiV fluorescence up to 80% can be reached as demonstrated by simulations modeling the SiV center as a radiating dipole in air above an Ir substrate. The collection efficiency is thus comparable to or even superior to the collection efficiency reached via using solid immersion lenses or photonic nanostructures (nanowires) together with color centers in bulk diamond (see also the introduction of this thesis). On the other hand, Ir, which is chosen due to its high inertness in the harsh environment of the CVD process and the feasibility of heteroepitaxy, certainly is not the optimum material for a mirror for visible light: Comparably high losses in the Ir metal layer might lead to fluorescence quenching especially for emitters close to the metal layer (distance $< 10\,\mathrm{nm}$). The presence of the metal layer might thus be related to the large spread in maximum single photon rates that has been observed: Count rates ranging from approx. $10^5\,\mathrm{cps}$ to $6.2 \times 10^6\,\mathrm{cps}$ were found, the latter rendering SiV centers in NIs on Ir the brightest single color centers under cw excitation observed to date. The quantum efficiencies observed for the ZPL transition of single SiV centers range from 0.3% to 9.2% (excitation 671 nm and 695 nm). This finding is comparable to previous measurements on SiV ensembles in polycrystalline films yielding a quantum efficiency of 5% [241]. However, the origin of the non-radiative decay could not be reliably identified. For one emitter, we observe an excitation wavelength dependent quantum efficiency that might indicate non-radiative processes triggered by the crossing of vibrational parabolas (DKR criterion) in the excited state as a source of the non-radiative decays. A small quantum efficiency is detrimental for a single photon source, as it limits the single photon rate obtainable for triggered single photon emission using pulsed (laser) excitation. An ideal single photon source would allow for the generation of photons on demand, i.e., the reliable generation of a single photon following each excitation pulse. Thus, enhancing the quantum efficiency is desirable. To exclude the metal substrate as the source of non-radiative decay, one might think of using nano-manipulation techniques to place randomly oriented nanodiamonds containing single SiV centers on dielectric structures that enable a high collection efficiency, e.g., so called solid immersion lenses (SILs) [56] or direct placement on fiber facets [64]. First experiments in cooperation with the group of Prof. Oliver Benson (Humboldt University, Berlin) have demonstrated that it is possible to remove the CVD grown NDs from the Ir substrate using an atomic force

microscope and to reposition them. Furthermore, one might employ nanophotonic structures, e.g., nanowires [48]: In these cylindrical nanostructures, a high collection efficiency can be reached for color centers with a distance from the metal substrate in the micron range, thus minimizing the influence of the substrate. Structures similar to those described in Ref. [48] have been fabricated in cooperation with the group of Prof. Marco Loncar (Harvard University) in heteroepitaxial diamond films containing isolated SiV centers and are currently under investigation. Coupling SiV centers to resonator structures (defect resonators) in photonic crystals can also shorten the lifetime of the centers (Purcell effect) and modify the radiation pattern [69]. In this context, cavity coupling can also aid in enhancing the radiative quantum yield by increasing radiative transition rates [69].

Measurements of the polarized absorption for single SiV centers show a preferential absorption of linearly polarized light. By using the preferentially absorbed linear polarization, efficient optical (laser) excitation with low background contribution can be obtained. The ZPL fluorescence of single SiV centers is fully linearly polarized. The possibility to create linearly polarized single photons is highly desirable as these photons are, e.g., directly applicable for the encoding of information using the polarization of single photons (quantum key distribution via BB84 protocol [2]) or in the frequency conversion of single photons aiming at the transformation of photons to wavelengths suitable for long range, low loss fiber transmission [258]. We emphasize that very recently, in a first experiment using a sample produced during this work, single photons emitted by an SiV center in a ND on Ir were employed to implement quantum key distribution using the BB84 protocol [2] in the group of Prof. Oliver Benson (Humboldt University, Berlin) [305]. Furthermore, we find parallel absorption and emission dipoles for the SiV centers. From polarization measurements on oriented NIs, we deduce a single $\langle 110 \rangle$-oriented transition dipole for the SiV center. This observation is in contrast to the dipole orientations resulting from the spatial structures suggested for the SiV complex in theoretical models [122, 123, 155] but confirms previous experimental observations for SiV ensembles [154]. Further theoretical as well as experimental work is necessary to reliably determine the spatial structure of the SiV complex.

Low temperature properties of SiV centers

In low temperature measurements using single SiV centers, we observe for the first time for single SiV centers the four component ZPL fine structure characteristic of SiV center ensembles in high quality diamond. This fine structure arises due to a splitting in excited and ground state of the ZPL transition. Due to stress in the employed nanodiamonds, significantly varying line patterns were observed. The energy of the ZPL transitions, as well as the splitting and the relative intensities of the line components vary for individual emitters. In the case of spectra consisting of multiple line components, one has to keep in mind that $g^{(2)}$ measurements might not be able to detect whether all lines, especially weak ones, originate from the same emitter. However, for most spectra taking into account also that the lines share a common linear polarization direction (see discussion below), they most probably originate from the same emitter. To prove reliably that the lines originate from the

same emitter, one may perform cross-correlation measurements between the lines. However, such measurements are extremely challenging due to the required narrow spectral filtering (on the order of 100 GHz) as well as the low signal level for the weak lines.

During cooling from room temperature to liquid helium temperature, the ZPL blueshifts by approx. 1 nm-1.4 nm. At low temperatures, spectral diffusion (SD) is the dominant line broadening mechanism for most observed SiV centers. Typical linewidths amount to approx. 50-100 GHz. With increasing temperature T, the homogeneous broadening due to phonons becomes more pronounced. The homogeneous linewidth is found to increase with T^3; however, the underlying mechanism leading to this dependence is still subject to controversial discussion in the literature. Here, it might be connected to the broadening associated with crystal defects. With regard to single photon emission, SD blurs the intrinsic properties of the fluorescence line and prevents the emission of a train of indistinguishable photons from a single color center. However, the characteristic timescale of the spectral jumps leading to the observed SD linewidth is critical: If the jumps occur on timescales long compared to the lifetime of the emitter a significant number of indistinguishable photons can be extracted between spectral jumps. The measurements discussed here do not allow to estimate the time constants of the jumps due to integration times of at least several seconds up to minutes. Very recently, the stabilization of the ZPL transition of an NV center against spectral jumps occurring on time scales larger than 50 ms has been demonstrated by resonance tuning [306]. Thus, if the critical time can be estimated and is sufficiently long, possible countermeasures to compensate for SD might be taken. Ref. [302] demonstrates a method for the measurement of the characteristic time between spectral jumps using quantum dots: Disjunct spectral windows inside the inhomogeneously broadened fluorescence line are selected via two monochromators and the cross-correlation of the photons emitted into these spectral windows is measured. To change its emission wavelength from one window to the other, the emitter has to undergo a spectral jump. As this happens on average after a characteristic time τ_d, the cross-correlation exhibits an antibunching for shorter timescales: No photons with shorter delay times are observed in the two disjunct windows. The time constant of the antibunching reveals the characteristic time τ_d. This method is also applicable to single SiV centers. Furthermore, one might think of reducing spectral diffusion by using enhanced purity diamonds or larger NDs. Also surface treatments might be favorable. First surface oxidation experiments on SiV center containing NDs have been performed. The low temperature properties of SiV centers in these NDs are currently under investigation.

Temperature dependent $g^{(2)}$ measurements reveal almost temperature independent internal population dynamics of the SiV centers. Neither significantly enhanced absorption nor enhanced brightness at low temperature could be observed. We thus conclude that neither strongly temperature dependent non-radiative channels are significant nor thermal populating or de-populating of the shelving state occurs. Investigating the temperature dependent line intensities, we find evidence for a thermalization of the population between the excited state sublevels which has been previously shown for ensembles.

Low temperature spectra recorded using different orientations of a linear polarization analyzer show that the fine structure components of the ZPL show a common linear polarization. This observation is in accordance with a splitting of the ZPL due to tunneling between two spatial configurations (with slightly different energies) as introduced for molecules, e.g., in Ref. [261]. However, a reliable identification of the splitting mechanism has to include the identification of the participating electronic states, which is not possible at present as theoretical models in the literature and experimental observations are contradictory. The splitting of the ZPL fine structure components either under the influence of externally applied stress or under the influence of external fields (magnetic fields, electric fields) can yield further information on the participating electronic states. Experiments using external magnetic fields are currently performed in cooperation with the group of Prof. Mete Atatüre (Cambridge University).

Additional electronic transitions of SiV centers

Spectra of several single SiV centers feature a very narrow room temperature photoluminescence (PL) line or several narrow lines in the near-infrared (NIR) spectral region mostly between 820 nm and 840 nm. For one emitter, we show that the additional NIR line is connected to an absorption pathway that preferentially absorbs linearly polarized light with the same polarization direction found for the ZPL excitation. Furthermore, a similar saturation power is found for ZPL and NIR line as well as a common linear polarization of the emitted fluorescence light. These findings indicate that the lines originate from the same color center. To unambiguously prove this hypothesis, we use intensity correlation measurements: The intensity cross-correlation measurement shows an antibunching which proves that the emission of the ZPL and the NIR line is anti-correlated. The antibunching time constant of the cross-correlation is 0.7 ns and witnesses fast exchange between the two fluorescent transitions. Intensity auto-correlation ($g^{(2)}$) measurements of either the ZPL fluorescence or the NIR fluorescence exclude that the NIR line arises due to a transition from the shelving state of the SiV center to the ground state. A participation of the ground state in the NIR emission seems reasonable, as in recent work [121] absorbing transitions in diamonds containing large SiV ensembles have been detected at similar wavelengths. Furthermore, low temperature measurements reveal a significant narrowing of the NIR line upon cooling. Together with different population dynamics for NIR line and ZPL, this proves that the line arises due to a purely electronic transition and is not a vibronic sideband of the ZPL. To include the NIR emission, a new level scheme involving an additional fast relaxation pathway from the pumping levels has to be proposed. To further investigate the nature of the NIR transitions, direct excitation on the NIR transition can be used to assure a participation of the ground state and the identification as an electronic transition. However, as the SiV centers are located in nanodiamonds on an opaque metal substrate, observation of absorption, i.e., extinction of excitation laser light, is difficult. Nevertheless, detection of the red shifted fluorescence after excitation on the NIR transition could serve as a measure of the absorption (photoluminescence excitation spectroscopy).

Summarizing, we identified advanced material systems that made available single *in situ* produced SiV centers. This, for the first time, enabled detailed spectroscopy on single SiV centers in CVD diamond gaining new insights into the population dynamics of single centers as well as the level scheme including the electronic transitions and their splittings. Furthermore, we succeeded in determining the orientation of the transition dipole of single SiV centers. We demonstrated high brightness, narrow bandwidth single photon emission from single SiV centers, distinguished by the narrowest room temperature emission lines as well as the brightest emission under cw excitation from single color centers at present. Bright, narrow bandwidth emission of SiV centers found in colloidal nanodiamond solutions furthermore renders SiV centers highly attractive as fluorescence markers for in in-vivo imaging applications. The results of this thesis partially confirm previous results obtained for SiV center ensembles but also obtain new partially contradictory results especially on additional electronic transitions of SiV centers as well as the symmetry properties of SiV centers.

Appendix A

Sample Overview

Samples from two different collaborators were investigated in this work:

- Samples produced by a modified hot filament (HF)CVD process have been supplied by the company Komet rho-Best, Innsbruck. Not all growth parameters are given, as the production process is confidential. Morphology and post growth processing of the samples is analyzed and discussed in Chapter 4. Two types of samples are produced: homoepitaxial single crystalline samples and polycrystalline films grown on seeded Si substrates.
- Samples synthesized by microwave plasma assisted (MW)CVD were supplied by the CVD diamond group at the university of Augsburg headed by Dr. Matthias Schreck. The samples were grown using a commercial CVD reactor manufactured by IPLAS using a CYRANNUS plasma source. Here, heteroepitaxial samples as well as randomly oriented nanodiamonds were grown using on the unique Ir/YSZ/Si material system developed by the group.

The following table summarizes the sample parameters of the samples discussed in this work. All samples were grown using a pure CH_4/H_2 plasma. The fourth column lists the thickness for samples with closed films, while it lists the average nanodiamond (ND) size for samples with spatially isolated CVD nanodiamonds. For samples with isolated CVD nanodiamonds, the seed concentration in the spin coating process is also added in that column.

Sample name	**Process**	**Morphology**	**Thickness/ ND size (seed conc.)**	**Growth time (min)**	**Substrate**	**CH_4 fraction (%)**	**Pressure (mbar)**	**Microwave power (W)**
HaStP070	HFCVD	single crystalline film	$80-100\,\mathrm{nm}$	-	HPHT diamond (001)	0.26	-	-
HaStP027	HFCVD	polycrystalline film	$0.17\,\mu\mathrm{m}$	-	Si (001)	0.26	-	-
HaStP025	HFCVD	polycrystalline film	$1.65\,\mu\mathrm{m}$	-	Si (001)	0.26	-	-
SlGh45	HFCVD	polycrystalline film	$1.9\,\mu\mathrm{m}$	-	Si (001)	0.26	-	-
MFDIA865A(B)	MWCVD	isolated NDs	130 nm (0.0031 ct/kg)	25	Ir/YSZ/Si (001)	1	30	2000
MFDIA943_1	MWCVD	isolated NDs	*approx.* 130 nm (0.0031 ct/kg)	35	Ir/YSZ/Si (001)	1	30	2000
MFDIA957_2	MWCVD	isolated NDs	216 nm (0.0016 ct/kg)	55	Ir/YSZ/Si (001)	0.4	30	2000
MFDIA946	MWCVD	isolated nanoislands	160 nm	20	Ir/YSZ/Si (001)	0.5	40	2000
MF4DIA562_1	MWCVD	heteroepitaxial film	90 nm	20	Ir/YSZ/Si (001)	0.5	30	2000
MFDIA455	MWCVD	heteroepitaxial film	45 nm	20	Ir/YSZ/Si (111)	0.5	160	2100

Appendix B

Supplementary technical information

B.1 Dichroic beamsplitters

This section summarizes the properties of the dichroic beamsplitters used in the confocal microscope. The transmission of the dichroic beamsplitter significantly influences the detection efficiency of the confocal setup and the observable wavelength range. Furthermore, the influence of the beamsplitter on the polarization of transmitted and reflected light is crucial in polarization dependent absorption and emission measurements of color centers.

B.1.1 Transmission curves of dichroic beamsplitters

Figure B.1 gives the transmission curves for the beamsplitters used in the experiments (details see figure caption). The transmission curves are measured using a commercial photospectrometer (Hitachi, U-3501). Briefly describing the operating principle, light from a broadband source is transmitted through a grating monochromator selecting a narrow wavelength band. To measure larger wavelength ranges, the monochromator is scanned thus varying the wavelength. The light from the monochromator is then split in two paths and detected using a photo-detector. The transmission is calculated comparing the signals in the two paths. Before the dichroic is inserted in one of the paths, a reference measurements is performed to correct for differences in the two light paths. As visible in Fig. B.1, for both beamsplitters a second region of unintended high reflectivity is observed. For the beamsplitter XF2083 708DRLP, that transmits light with wavelengths longer than 708 nm and reflects shorter wavelengths this region already starts at approx. 900 nm, thus limiting the observable wavelength range of color center fluorescence. For the dichroic mirror zq670rdc, that transmits light with wavelengths longer than 670 nm and reflects shorter wavelengths the unintended high reflectivity starts above 1100 nm. In this wavelength range, the silicon photo-detectors employed throughout this work (spectrometer CCD and APDs) are not sensitive anymore, thus here the dichroic does not limit the observable spectral range.

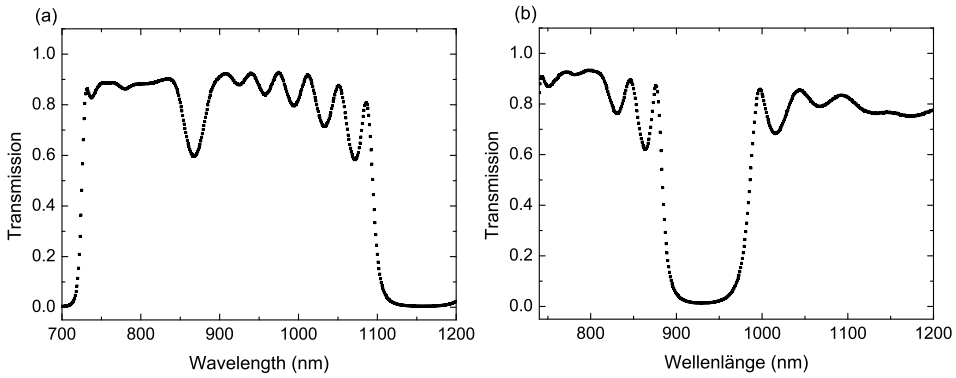

Figure B.1: Transmission curves of dichroic beamsplitters used in the confocal microscope. (a) beamsplitter Chroma Technologies, zq670rdc. This beamsplitter is used, whenever the 671 nm excitation laser is used. (b) beamsplitter Omega Optical, xf2083 708DRLP. This beamsplitter is used whenever excitation at 685 nm or longer wavelength is used. Curves measured using a photospectrometer (Hitachi, U-3501).

B.1.2 Influence on polarization of reflected excitation laser light

The dichroic mirror induces changes in the linear polarization of the reflected laser light. To quantify these polarization changes, the linear polarization degree (visibility) of the light after being reflected of the dichroic is measured using a linear polarization analyzer (Edmund Optics, TechSpec laminated linear polarizer film for visible light). Note that before being reflected of the dichroic, the linear polarization is defined better than 1000:1 by a polarizing beamsplitter cube. A deviation up to 2% might be introduced due to laser intensity fluctuations. Figure B.2 gives the curves for the two dichroics employed. For light polarized under an angle of 45°, a loss of linear polarization up to approx. 10% is observed, while for s and p polarized light (90° and 0°) almost no loss occurs. This has to be taken into account when interpreting data of polarized absorption of color centers.

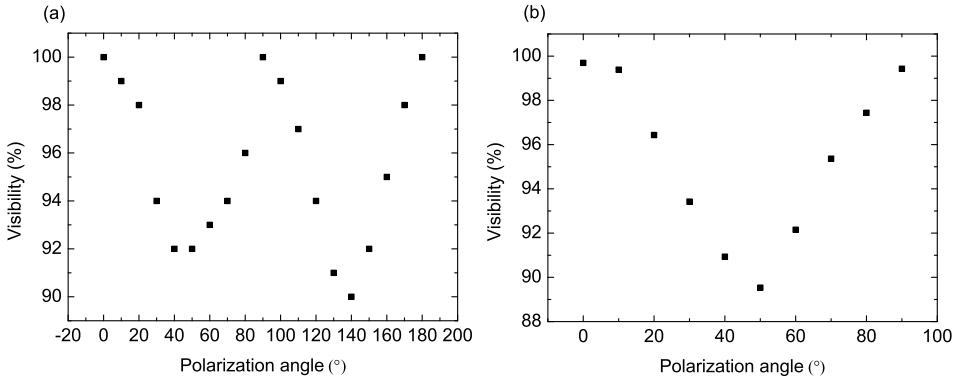

Figure B.2: Linear polarization loss of laser light reflect of dichroic beamsplitters used in the confocal microscope. (a) beamsplitter Chroma Technologies, zq670rdc, reflected laser light 671 nm (b) beamsplitter Omega Optical, xf2083 708DRLP, reflected laser light 685 nm.

B.1.3 Influence on the polarization of transmitted light

The dichroic mirror induces polarization changes of the transmitted fluorescence light. To quantify these polarization changes, first, the linear polarization degree (visibility) of attenuated laser light at 740 nm after being transmitted through the dichroic is measured using a linear polarization analyzer. Note that before being transmitted through the dichroic, the linear polarization is defined better than 1000:1 by a polarizing beamsplitter cube. A deviation up to 2% might be introduced due to laser intensity fluctuations. Figure B.4 gives the curves for one of the dichroics (xf2083 708DRLP) employed in the polarization measurements under 695 nm excitation (discussion see below).

Furthermore, we employ a commercial polarization analyzing system (Thorlabs, PAN5710VIS/IR). This device allows for a full characterization of the transmitted polarization state and not only for the measurement of the linear polarization degree. Additionally, the system allows for the measurement of the influence of the dichroic mirror on circularly polarized light. Figure B.3 summarizes the parameters used to characterize elliptically polarized light: The electric field vector of an elliptically polarized light field rotates on an ellipse in the x-y-plane (propagation direction of the light is the z-direction). The semimajor axis of this ellipse is denoted a, the semiminor axis is denoted b (see Fig. B.3). The polarization analyzing system measures the parameters η (ellipticity) and α (orientation of the semimajor axis). For linearly polarized light, η equals zero and α gives the linear polarization direction. Circularly polarized light is characterized by $\eta = \pm 45°$. Here, $\eta = +45°$ denotes right handed circularly polarized light, $\eta = -45°$ denotes left handed circular polarized light. To test the polarization induced changes due to the dichroic mirror, a defined polarization state is prepared using a polarizing beamsplitter cube and a quarter-wave or half-wave retarder plate. Again, attenuated laser light at 740 nm is employed to simulate fluorescence from SiV centers. Then the dichroic mirror is inserted into the beam path and the change in polarization is measured.

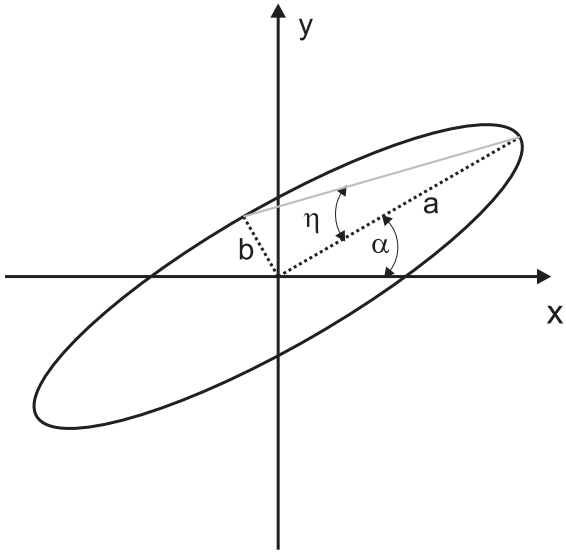

Figure B.3: Parameters used to describe elliptically polarized light. a and b denote the semimajor and semiminor axis of the ellipse on which the electric flied vector moves in the x-y-plane. (z: propagation direction of light). η denotes the ellipticity, α gives the direction of the semimajor axis.

To compare the measurements with the commercial polarization analyzing system to the measurements using only a linear polarization analyzer, we calculate the visibility V from the measured parameter η. η is given by:

$$\tan\eta = \frac{b}{a} \tag{B.1}$$

The maximum and minimum intensity (I_{max},I_{min}) observed for elliptically polarized light correspond to the semimajor and semiminor axes of the ellipse. Therefore, we can write the visibility V

$$V = \frac{I_{max} - I_{min}}{I_{max} + I_{min}} = \frac{a^2 - b^2}{a^2 + b^2} \tag{B.2}$$

Using Eq. (B.1), this can be written as

$$V = \frac{1 - (\tan\eta)^2}{1 + (\tan\eta)^2} \tag{B.3}$$

Figure B.4 summarizes the measured visibility for both dichroics.

Discussion of the results

Figure B.4(a) enables the comparison of the visibility measured for linearly polarized light transmitted through dichroic xf2083 708DRLP using analysis with a linear polarization analyzer and the commercial polarization analyzer system. It is clear, that for s or p polarized light the polarization state is not unaffected: We observe a visibility close to 100% for both measurements. For light polarized with an angle of 45°, a loss of linear polarization is observed. The loss of visibility amounts to 2% for the measurements with the commercial system and 9% using the polarization analyzer. We thus assume a loss of approx. 9% as a worst case estimate. We also give the data obtained for the zq670rdc beamsplitter in Fig. B.4(b). The loss of contrast here is only measured using the commercial system. The maximum loss in visibility corresponds to 2.5%, here for a polarization direction of 90°. We point out that for both dichroics, the polarization direction α of the transmitted light remains almost unchanged. This indicates, that s and p components do not suffer from significantly different intensity reflection coefficients as this would lead to a rotation of the polarization direction. Furthermore, we check the influence of the dichroic on circularly polarized light transmitted through the dichroic. For the dichroic xf2083 708DRLP, right handed circularly polarized light exhibits $\eta = 43.3°$ after transmission through the dichroic, left handed light exhibits $\eta = -44.1°$. For the dichroic zq670rdc, right handed circularly polarized light exhibits $\eta = 29.3°$ after transmission through the dichroic, left handed light exhibits $\eta = -35.2°$. These measurement show that circularly polarized light becomes elliptically polarized upon transmission through the dichroic probably due to different phase shifts for s and p polarized components. However, as the observed color centers mostly display a linear polarized emission (see Chapter 6) this is not critical. It is only crucial to know that the polarization change for circularly polarized light is not so significant that circularly polarized

emission might be misinterpreted as linearly polarized after transmission through the dichroic. The lowest value of η observed here still corresponds to a visibility of only 52% and thus is easily distinguishable from linearly polarized light.

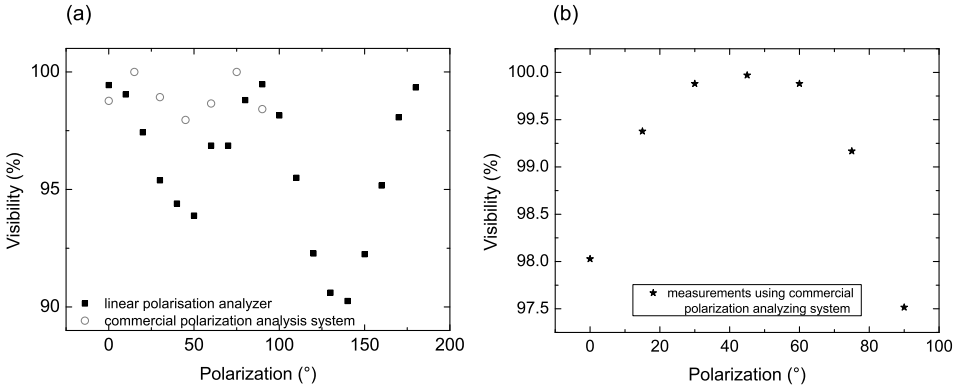

Figure B.4: Loss of linear polarization due to transmission through dichroic mirror (a) xf2083 708DRLP (b) zq670rdc. For the dichroic mirror xf2083 708DRLP, two measurements using a linear polarization analyzer as well as a commercial polarization analysis system are given.

B.2 Resolution of the employed spectrometer

To measure fluorescence spectra, we employ a grating spectrometer (iHr 550, Horiba Jobin Yvon). The spectrometer is equipped with three gratings featuring 600, 1200 and 1800 grooves/mm. For spectroscopy at low temperatures, we employ the 1800 grooves/mm grating to enable maximum resolution, while at room temperature where the observed linewidths exceed 0.5 nm we use the 600 grooves/mm spectrometer to enable a higher wavelength coverage. Furthermore, the width of the entrance slit influences the resolution, thus at low temperature a narrow entrance slit of 70 μm or less is used. As the fluorescence is imaged into the spectrometer from am 62.5 μm core multimode glass fiber, a slit width below approx. 60 μm leads to a significant loss of signal due to clipping by the entrance slit. Additionally, we find experimentally that closing the slit further does not significantly enhance the resolution. Furthermore, the spectrometer is an imaging spectrometer, i.e., the optics used image the entrance slit onto the detector, here a CCD camera (Symphony CCD, 1024x256 Pixel, back illuminated, deep depletion, Horiba Jobin Yvon). Thus, positioning the CCD camera in the focal plane of the spectrometer is crucial to obtain maximum resolution. Due to these technical considerations, we determine the spectrometer resolution experimentally from the linewidth of a spectral line from a mercury gas discharge ($\lambda = 546.07$ nm) rather than calculating it. This line is supposed to be sufficiently narrow such that the actual linewidth does not influence the measurement but only the spectrometer transfer function is measured. The result is shown in Fig. B.5. The instrument response function of a grating spectrometer

can be complicated as it is determined both by the transfer function of the grating as well as the diffraction due to the apertures (gratings, slits) in the spectrometer (see, e.g., Ref. [97]). To obtain an instrument response function that allows for the correction of the measured data by separating the linewidths due to instrument response and emission linewidth of the color centers, an approximate function has to be found. As pointed out in Ref. [179], the instrument response function can often be reasonably approximated using a Gaussian line form. To test this approximation, we employ a Gaussian and Lorentzian line as well a the more general case, a Voigt profile which is the convolution of a Gaussian and a Lorentzian function, to fit the line (for further explanation on the Voigt profile see section 7.2.1). We find that a Lorentzian lineshape does not fit the measured data. Fitting the data with a Gaussian line yields much better results. On the other hand, by introducing a small Lorentzian contribution better results are obtained (χ^2 reduction about 30%). We therefore follow a pragmatic approach and use this optimized Voigt-profile as the instrument response function throughout this work. We employ the linewidths given in the caption of Fig. B.5 to correct for the spectrometer resolution. The formulas used to correct for the spectrometer instrument response are given in Eq. (7.4) and are deduced in the next section.

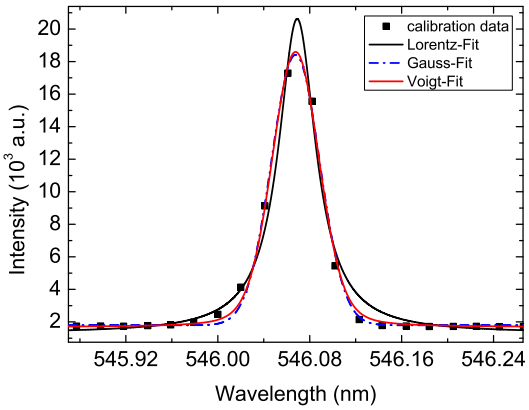

Figure B.5: Mercury spectral line used to test the spectrometer resolution fitted with different line forms (entrance slit width 30 μm). Linewidth (FWHM) Lorentz: 0.040 nm, Gauss 0.042 nm, Voigt $w_L = 0.010 \pm 0.002$ nm, $w_G = 0.043 \pm 0.002$ nm

B.3 Convolution of Voigt-profiles

Aim of this short section is to show that the convolution of two Voigt-profiles again results in a Voigt-profile and that the Gaussian and Lorentzian parts of this new Voigt-profile can be treated via the equations that hold for the convolution of Gaussian and Lorentzian functions. We start from the Voigt-profile $V(\nu)$

$$V(\nu) = \int_{-\infty}^{+\infty} L_1(\nu - x) G_1(x) dx \tag{B.4}$$

where L and G denote Gaussian and Lorentzian peak functions. We now convolute $V(\nu)$ with a Gaussian function:

$$W(\nu) = \int_{-\infty}^{+\infty} V(\nu - y) G_2(y) dy = \int_{-\infty}^{+\infty} \int_{-\infty}^{+\infty} G_1(\nu - y - x) L_1(x) dx G_2(y) dy \tag{B.5}$$

$G_2(y)$ does not depend on x thus we can write.

$$W(\nu) = \int_{-\infty}^{+\infty} \int_{-\infty}^{+\infty} G_1(\nu - y - x) L_1(x) G_2(y) dx \; dy \tag{B.6}$$

Changing the order of the integration and regrouping the terms yields:

$$W(\nu) == \int_{-\infty}^{+\infty} \underline{\int_{-\infty}^{+\infty} G_1(\nu - y - x) G_2(y) dy} L_1(x) dx \tag{B.7}$$

The underlined term again gives a Gaussian function G_3 as it is the convolution of two Gaussian functions being invariant under convolution. The parameter of the new Gaussian function can be calculated via the rules for the convolution of Gaussian functions. We find:

$$W(\nu) = \int_{-\infty}^{+\infty} G_3(\nu - x) L_1(x) dx \tag{B.8}$$

This in turn shows that $W(\nu)$ again is a Voigt-profile. The same can be shown for the convolution of $V(\nu)$ with a Lorentzian L. Furthermore, an associative law exist for the convolution operation $*$:

$$v * (l * g) = (v * l) * g \tag{B.9}$$

In our case, this means to convolute a Voigt-profile v with another Voigt-profile $l*g$ (l and g are the Gaussian and Lorentzian parts of the profile), we first convolute v with l this leads to a new Voigt-profile with the changed Lorentzian contribution. This again is convoluted with the remaining Gaussian part leading to a changed Gaussian contribution. This justifies the assumption made in Sec. 7.2.1 that different Gaussian and Lorentzian contributions to a Voigt-profile can be separated according to the rules for convoluted Gaussian and Lorentzian functions.

B.4 Correction of confocal imaging through the cryostat window

As described in Chapter 3, a Janis Research ST500-LN microscope cryostat is used to perform spectroscopic measurements at temperatures down to liquid helium temperature. The sample is mounted on a cold finger and isolated by a vacuum chamber. Thus, imaging the sample inside the cryostat demands focussing the laser light as well as collecting the fluorescence through an optical window terminating the isolation vacuum. As the microscope objective used in the confocal setup (Olympus, LMPLFLN100, NA=0.8) is optimized for imaging a sample in air, the imaging through the window degrades the performance of the confocal microscope. Two effects are conceivable: First, focussing the laser through the window corrupts the spot size in the focus. This in turn leads to the excitation of a larger volume and, therefore, especially in bulk diamond to a decreased signal to noise ratio. The larger spot size also reduces the resulting excitation intensity for the same excitation power compared

to focussing without the glass. Second, the imaging of the fluorescence through the objective is deteriorated. Therefore, the confocal setup experiences an effective loss of collection efficiency. To quantify these effects, we measure the fluorescence of a bright, stable emitter as a function of excitation power first without the cryostat glass then with the glass brought into the beam line (without evacuating the cryostat). From the parameters of the saturation curve, i.e., the maximum photon rate I_∞ and the saturation power P_{Sat} we can determine the effect on collection efficiency and effective excitation intensity, respectively. Figure B.6 shows the saturation curve of emitter C1 (see Chapter 7) with and without the cryostat glass. Fitting the saturation curves yields $I_\infty = 2.4\,\text{Mcps}$ and $P_{Sat} = 73.4\,\mu\text{W}$ without imaging through the cryostat window and $I_\infty = 0.71\,\text{Mcps}$ and $P_{Sat} = 416\,\mu\text{W}$ imaging the light through the cryostat window. Thus, the saturation intensity measured inside the cryostat has to be corrected with a factor of 0.17, while the maximum photon rate should be multiplied by 3.4 to enable comparison of room temperature and low temperature results.

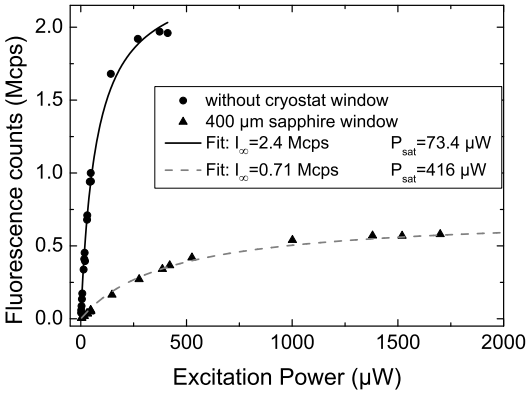

Figure B.6: Saturation curves of emitter C1 with and without cryostat window. Note that with the cryostat windows powers up to 3.3 mW have been used. For better comparison of the curves, the measurement inside the cryostat is only shown up to 2.2 mW.

Appendix C

Supplementary experimental data

C.1 Fluorescence polarization at cryogenic temperature

Figures C.1 and C.2 give additional data on the polarization properties of the emitters C3 and C5. For more details, see figure caption and discussion in section 7.5.

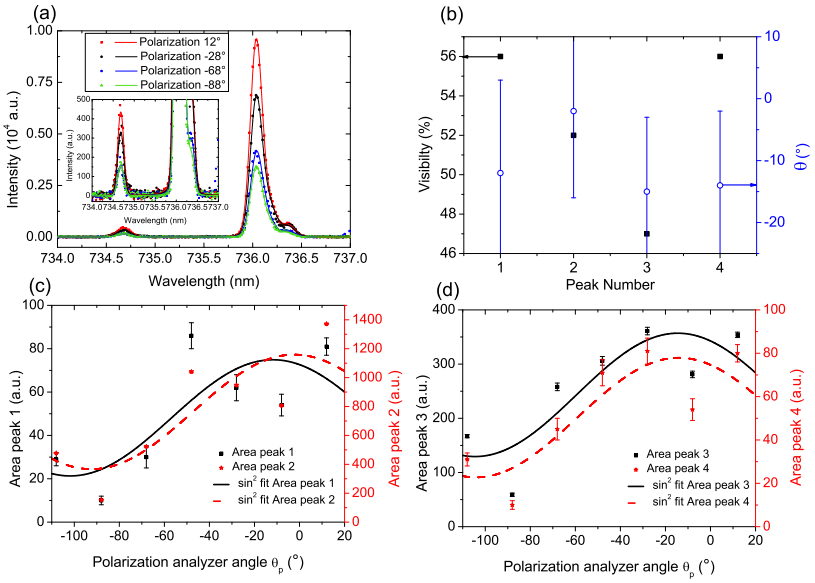

Figure C.1: Fluorescence polarization of emitter C3. (a) fluorescence spectra of emitter C3 taken at different angles of the polarization analyzer and a temperature of 20 K. The excitation polarization is fixed to the optimal values. The inset of the graph shows an enlarged detail to enable observation of the weaker line components. (b) summary of visibility (black squares) and linear polarization direction θ (blue circles) obtained from the fits in (c) and (d). (c) and (d) peak areas in dependence of the polarization analyzer angle θ_p fitted with Eq. (7.18). Peak 1, 2 and 4 are the main peaks visible in the spectrum, while peak 3 is an additional peak to describe the asymmetric flank of peak 2.

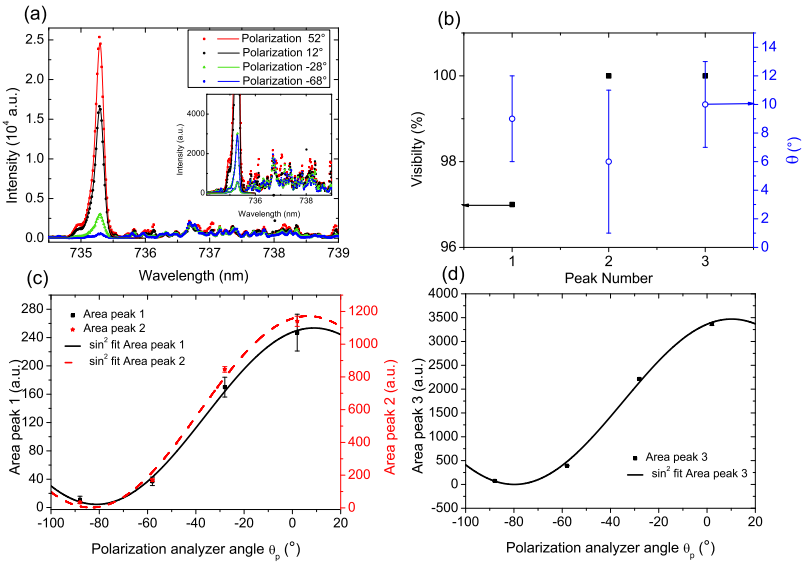

Figure C.2: Fluorescence polarization of emitter C5. (a) fluorescence spectra of emitter C5 taken at different angles of the polarization analyzer and a temperature of 15 K. The excitation polarization is fixed to the optimal values. The inset of the graph shows an enlarged detail to enable observation of the weaker line components. Note the different behavior of the ensemble and of emitter C5: While the lines attributed to emitter C5 show a strong intensity oscillation with the polarizer angle, most lines in the ensemble exhibit no significance intensity variation. (b) summary of visibility (black squares) and linear polarization direction θ (blue circles) obtained from the fits in (c) and (d). (c) and (d) peak areas in dependence of the polarization analyzer angle θ_p fitted with Eq. (7.18). The position of the peaks are: peak 1 734.94 nm, Peak 2 735.18 nm, Peak 3 735.3 nm.

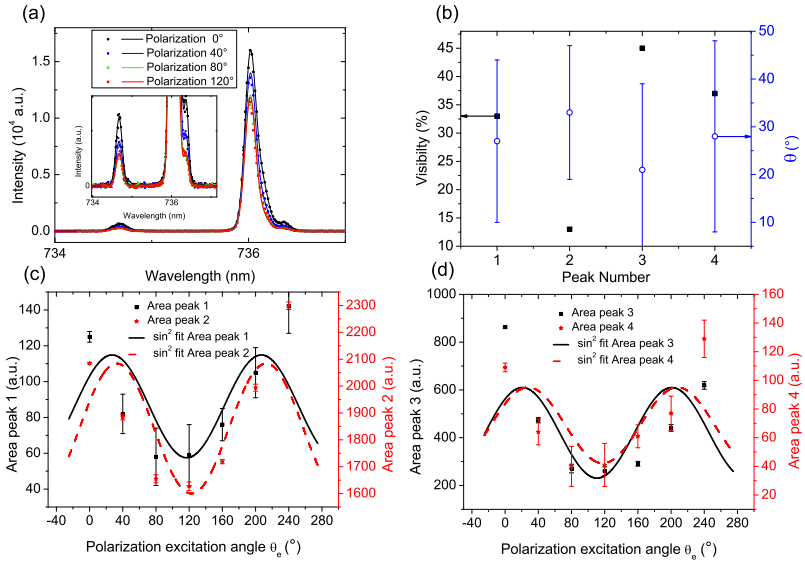

Figure C.3: Polarized absorption of emitter C3. (a) fluorescence spectra of emitter C3 taken at different angles of incident excitation polarization at a temperature of 20 K. The inset of the graph shows an enlarged detail to enable observation of the weaker doublet. Spectra taken at 2.0 P_{Sat}.(b) summary of visibility and linear polarization direction corresponding to maximum absorption θ obtained from the fits in (c) and (d). (c) and (d) peak areas in dependence of the excitation polarization fitted with Eq. (7.18)

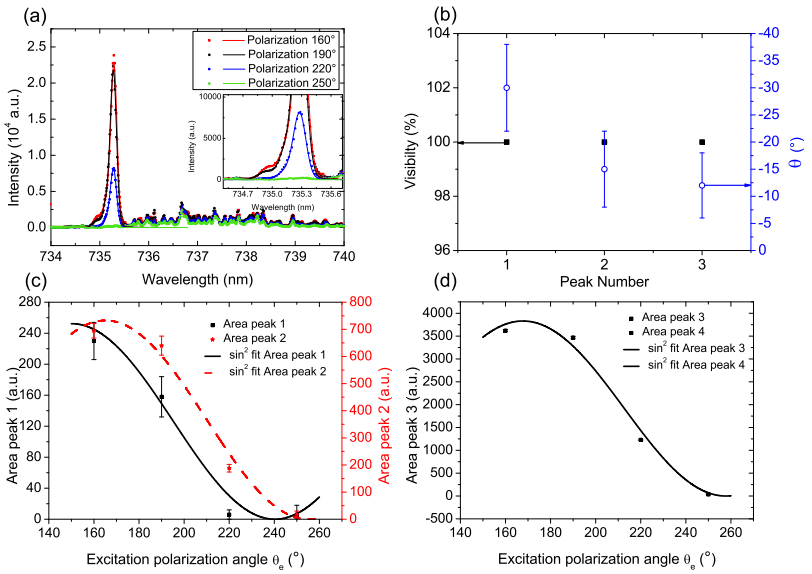

Figure C.4: Polarized absorption of emitter C5. (a) fluorescence spectra of emitter C3 taken at different angles of incident excitation polarization at a temperature of 15 K. Spectra taken at 0.18 mWThe inset of the graph shows an enlarged detail to enable observation of the weaker doublet.(b) summary of visibility and linear polarization direction corresponding to maximum absorption θ obtained from the fits in (c) and (d). (c) and (d) peak areas in dependence of the excitation polarization fitted with Eq. (7.18)

Bibliography

[1] P. Zoller, T. Beth, D. Binosi, R. Blatt, H. Briegel, D. Bruss, T. Calarco, J. Cirac, et al. *Eur. Phys. J. D* **36**, 203 (2005).

[2] C. Bennett, G. Brassard, et al. *Proceedings of IEEE International Conference on Computers, Systems and Signal Processing, Bangalore, India* **175** (1984).

[3] N. Gisin, G. Ribordy, W. Tittel, and H. Zbinden. *Rev. Mod. Phys.* **74**, 145 (2002).

[4] T. Ladd, F. Jelezko, R. Laflamme, Y. Nakamura, C. Monroe, and J. O'Brien. *Nature* **464**, 45 (2010).

[5] E. Knill, R. Laflamme, and G. Milburn. *Nature* **409**, 46 (2001).

[6] H. Kimble. *Nature* **453**, 1023 (2008).

[7] Y. Lim, A. Beige, and L. Kwek. *Phys. Rev. Lett.* **95**, 30505 (2005).

[8] S. Benjamin, B. Lovett, and J. Smith. *Laser & Photonics Reviews* **3**, 556 (2009).

[9] B. Lounis and M. Orrit. *Rep. Prog. Phys.* **68**, 1129 (2005).

[10] M. Eisaman, J. Fan, A. Migdall, and S. Polyakov. *Rev. Sci. Instrum.* **82**, 071101 (2011).

[11] S. Scheel. *J. Mod. Opt.* **56**, 141 (2009).

[12] B. Huttner, N. Imoto, N. Gisin, and T. Mor. *Phys. Rev. A* **51**, 1863 (1995).

[13] G. Brassard, N. Lütkenhaus, T. Mor, and B. C. Sanders. *Phys. Rev. Lett.* **85**, 1330 (2000).

[14] W.-Y. Hwang. *Phys. Rev. Lett.* **91**, 057901 (2003).

[15] N. Gisin, S. Pironio, and N. Sangouard. *Phys. Rev. Lett.* **105**, 070501 (2010).

[16] N. Sangouard and Zbinden. *Arxiv preprint arXiv:1202.0493v1* (2012).

[17] B. Lounis, W. Moerner, et al. *Nature* **407**, 491 (2000).

[18] V. Zwiller, T. Aichele, W. Seifert, J. Persson, and O. Benson. *Appl. Phys. Lett.* **82**, 1509 (2003).

[19] H. J. Kimble, M. Dagenais, and L. Mandel. *Phys. Rev. Lett.* **39**, 691 (1977).

[20] F. Diedrich and H. Walther. *Phys. Rev. Lett.* **58**, 203 (1987).

[21] C. Brunel, B. Lounis, P. Tamarat, and M. Orrit. *Phys. Rev. Lett.* **83**, 2722 (1999).

[22] P. Michler, A. Kiraz, C. Becher, W. Schoenfeld, P. Petroff, L. Zhang, E. Hu, and A. Imamoglu. *Science* **290**, 2282 (2000).

[23] R. Brouri, A. Beveratos, J. Poizat, and P. Grangier. *Opt. Lett.* **25**, 1294 (2000).

[24] C. Kurtsiefer, S. Mayer, P. Zarda, and H. Weinfurter. *Phys. Rev. Lett.* **85**, 290 (2000).

[25] A. M. Zaitsev. *Phys. Rev. B* **61**, 12909 (2000).

[26] B. Naydenov, R. Kolesov, A. Batalov, J. Meijer, S. Pezzagna, D. Rogalla, F. Jelezko, and J. Wrachtrup. *Appl. Phys. Lett.* **95**, 181109 (2009).

[27] T. Gaebel, I. Popa, A. Gruber, M. Domham, F. Jelezko, and J. Wachtrup. *New J. Phys.* **6**, 98 (2004).

[28] E. Wu, J. R. Rabeau, G. Roger, F. Treussart, H. Zeng, P. Grangier, S. Prawer, and J.-F. Roch. *New J. Phys.* **9**, 434 (2007).

[29] E. Wu, J. R. Rabeau, F. Treussart, H. Zeng, P. Grangier, S. Prawer, and J. F. Roch. *J. Mod. Opt.* **55**, 2893 (2008).

[30] I. Aharonovich, C. Zhou, A. Stacey, J. Orwa, S. Castelletto, D. Simpson, A. Greentree, F. Treussart, et al. *Phys. Rev. B* **79**, 235316 (2009).

[31] J. Rabeau, Y. Chin, S. Prawer, F. Jelezko, T. Gaebel, and J. Wrachtrup. *Appl. Phys. Lett.* **86**, 131926 (2005).

[32] G. Marshall, T. Gaebel, J. Matthews, J. Enderlein, J. O'Brien, and J. Rabeau. *New J. Phys.* **13**, 055016 (2011).

[33] I. Aharonovich, S. Castelletto, D. A. Simpson, A. Stacey, J. McCallum, A. D. Greentree, and S. Prawer. *Nano Lett.* **9**, 3191 (2009).

[34] I. Aharonovich, S. Castelletto, B. C. Johnson, J. C. McCallum, D. A. Simpson, A. D. Greentree, and S. Prawer. *Phys. Rev. B* **81**, 121201 (2010).

[35] T. Mueller, I. Aharonovich, L. Lombez, Y. Alaverdyan, A. N. Vamivakas, S. Castelletto, F. Jelezko, J. Wrachtrup, et al. *New J. Phys.* **13**, 075001 (2011).

[36] I. Aharonovich, S. Castelletto, D. A. Simpson, A. D. Greentree, and S. Prawer. *Phys. Rev. A* **81**, 043813 (2010).

[37] C. Wang, C. Kurtsiefer, H. Weinfurter, and B. Burchard. *J. Phys. B: At. Mol. Opt. Phys.* **39**, 37 (2006).

[38] E. Neu, D. Steinmetz, J. Riedrich-Möller, S. Gsell, M. Fischer, M. Schreck, and C. Becher. *New J. Phys.* **13**, 025012 (2011).

[39] J. Duligall, M. Godfrey, K. Harrison, W. Munro, and J. Rarity. *New J. Phys.* **8**, 249 (2006).

[40] Z. Yuan, B. Kardynal, R. Stevenson, A. Shields, C. Lobo, K. Cooper, N. Beattie, D. Ritchie, et al. *Science* **295**, 102 (2002).

[41] M. Nothaft, S. Höhla, F. Jelezko, N. Frühauf, J. Pflaum, and J. Wrachtrup. *Nat. Comm.* **3**, 628 (2012).

[42] S. Pezzagna, D. Rogalla, D. Wildanger, J. Meijer, and A. Zaitsev. *New J. Phys.* **13**, 035024 (2011).

[43] A. Zaitsev, A. Bergman, A. Gorokhovsky, and M. Huang. *Phys. Status Solidi A* **203**, 638 (2006).

[44] A. Lohrmann, S. Pezzagna, I. Dobrinets, P. Spinicelli, V. Jacques, J. Roch, J. Meijer, and A. Zaitsev. *Appl. Phys. Lett.* **99**, 251106 (2011).

[45] T. Plakhotnik, W. Moerner, V. Palm, and U. Wild. *Opt. Comm.* **114**, 83 (1995).

[46] W. Barnes, G. Bjork, J. Gerard, P. Jonsson, J. Wasey, P. Worthing, and V. Zwiller. *Eur. Phys. J. D* **18**, 197 (2002).

[47] S. Reitzenstein and A. Forchel. *J. Phys. D: Appl. Phys.* **43**, 033001 (2010).

[48] T. Babinec, B. Hausmann, M. Khan, Y. Zhang, J. Maze, P. Hemmer, and M. Loncar. *Nature Nanotech.* **5**, 195 (2010).

[49] A. Beveratos, R. Brouri, T. Gacoin, J. Poizat, and P. Grangier. *Phys. Rev. A* **64**, 61802 (2001).

[50] J. Greffet, J. Hugonin, M. Besbes, N. Lai, F. Treussart, and J. Roch. *Arxiv preprint arXiv:1107.0502* (2011).

[51] S. Castelletto and A. Boretti. *Opt. Lett.* **36**, 4224 (2011).

[52] P. Siyushev, F. Kaiser, V. Jacques, I. Gerhardt, S. Bischof, H. Fedder, J. Dodson, M. Markham, et al. *Appl. Phys. Lett.* **97**, 241902 (2010).

[53] J. Hadden, J. Harrison, A. Stanley-Clarke, L. Marseglia, Y. Ho, B. Patton, J. O'Brien, and J. Rarity. *Appl. Phys. Lett.* **97**, 241901 (2010).

[54] L. Marseglia, J. P. Hadden, A. C. Stanley-Clarke, J. P. Harrison, B. Patton, Y.-L. D. Ho, B. Naydenov, F. Jelezko, et al. *Appl. Phys. Lett.* **98**, 133107 (2011).

[55] H. Bernien, L. Childress, L. Robledo, M. Markham, D. Twitchen, and R. Hanson. *Phys. Rev. Lett.* **108**, 043604 (2012).

[56] T. Schröder, F. Gädeke, M. Banholzer, and O. Benson. *New J. Phys.* **13**, 055017 (2011).

[57] K. Lee, X. Chen, H. Eghlidi, P. Kukura, R. Lettow, A. Renn, V. Sandoghdar, and S. Götzinger. *Nature Photon.* **5**, 166 (2011).

[58] X. Chen, S. Götzinger, and V. Sandoghdar. *Opt. Lett.* **36**, 3545 (2011).

[59] E. Ampem-Lassen, D. Simpson, B. Gibson, S. Trpkovski, F. Hossain, S. Huntington, K. Ganesan, L. Hollenberg, et al. *Opt. Express* **17**, 11287 (2009).

[60] T. Van der Sar, E. Heeres, G. Dmochowski, G. De Lange, L. Robledo, T. Oosterkamp, and R. Hanson. *Appl. Phys. Lett.* **94**, 173104 (2009).

[61] S. Schietinger, M. Barth, T. Alchele, and O. Benson. *Nano Lett.* **9**, 1694 (2009).

[62] M. Barth, N. Nuesse, B. Loechel, and O. Benson. *Opt. Lett.* **34**, 1108 (2009).

[63] S. Schietinger, T. Schroeder, and O. Benson. *Nano Lett.* **8**, 3911 (2008).

[64] T. Schröder, A. Schell, G. Kewes, T. Aichele, and O. Benson. *Nano Lett.* **11**, 198 (2011).

[65] M. Barth, S. Schietinger, T. Schroeder, T. Aichele, and O. Benson. *J. Lumin.* **130**, 1628 (2010).

[66] C. K. Hong, Z. Y. Ou, and L. Mandel. *Phys. Rev. Lett.* **59**, 2044 (1987).

[67] L. C. Bassett, F. J. Heremans, C. G. Yale, B. B. Buckley, and D. D. Awschalom. *Phys. Rev. Lett.* **107**, 266403 (2011).

[68] A. Faraon, P. Barclay, C. Santori, K. Fu, and R. Beausoleil. *Nature Photon.* **5**, 301 (2011).

[69] J. Riedrich-Möller, L. Kipfstuhl, C. Hepp, E. Neu, C. Pauly, F. Mücklich, A. Baur, M. M Wandt, et al. *Nature Nanotech.* **7**, 69 (2012).

[70] Y.-R. Chang, H.-Y. Lee, K. Chen, C.-C. Chang, D.-S. Tsai, C.-C. Fu, T.-S. Lim, Y.-K. Tzeng, et al. *Nature Nanotech.* **3**, 284 (2008).

[71] N. Mohan, C.-S. Chen, H.-H. Hsieh, Y.-C. Wu, and H.-C. Chang. *Nano Lett.* **10**, 3692 (2010).

[72] F. Neugart, A. Zappe, F. Jelezko, C. Tietz, J. P. Boudou, A. Krueger, and J. Wrachtrup. *Nano Lett.* **7**, 3588 (2007).

[73] R. Weissleder and V. Ntziachristos. *Nat. Med.* **9**, 123 (2003).

[74] C. Wang. *A Solid-State Single Photon Source Based on Color Centers in Diamond*. Ph.D. thesis, Technische Universität München (2007).

[75] R. S. Balmer, J. R. Brandon, S. L. Clewes, H. K. Dhillon, J. M. Dodson, I. Friel, P. N. Inglis, T. D. Madgwick, et al. *J. Phys.: Condens. Matter* **21**, 364221 (2009).

[76] F. Bundy, H. Hall, H. Strong, and R. Wentorf. *Nature* **176**, 51 (1955).

[77] A. Krüger. *Neue Kohlenstoffmaterialen: Eine Einführung*. Teubner (2007).

[78] S. Ferro. *J. Mater. Chem.* **12**, 2843 (2002).

[79] S. Koizumi, C. Nebel, and M. Nesladek, editors. *Physics and Applications of CVD Diamond*. Wiley-VCH (2008).

[80] C. Wild, N. Herres, and P. Koidl. *J. Appl. Phys.* **68**, 973 (1990).

[81] A. Gicquel, K. Hassouni, F. Silva, and J. Achard. *Curr. Appl. Phys.* **1**, 479 (2001).

[82] A. Fuchs. Herstellung von Nanodiamanten durch hemische Gasphasenabscheidung, Bachelorarbeit am Fachbereich Physik der Universität des Saarlandes (2011).

[83] R. Robertson, J. Fox, and A. Martin. *Philos. Trans. Roy. Soc. A* **232**, 463 (1934).

[84] J. Walker. *Rep. Prog. Phys.* **42**, 1605 (1979).

[85] M. Markham, J. Dodson, G. Scarsbrook, D. Twitchen, G. Balasubramanian, F. Jelezko, and J. Wrachtrup. *Diam. Relat. Mater.* **20**, 134 (2010).

[86] G. Balasubramanian, P. Neumann, D. Twitchen, M. Markham, R. Kolesov, N. Mizuochi, J. Isoya, J. Achard, et al. *Nature Mater.* **8**, 383 (2009).

[87] R. Mildren, J. Butler, and J. Rabeau. *Opt. Express* **16**, 18950 (2008).

[88] C. Hepp. Spektroskopische Untersuchungen an optisch aktiven Defektzentren in CVD-Diamantfilmen, Diplomarbeit am Fachbereich Physik der Universität des Saarlandes (2008).

[89] P. Achatz, J. Garrido, M. Stutzmann, and O. Williams. *Appl. Phys. Lett.* **88**, 101908 (2006).

[90] M. Nesládek, K. Meykens, L. M. Stals, M. Vaněček, and J. Rosa. *Phys. Rev. B* **54**, 5552 (1996).

[91] W. Saslow, T. K. Bergstresser, and M. L. Cohen. *Phys. Rev. Lett.* **16**, 354 (1966).

[92] K. Bharuth-Ram, U. Vetter, H. Hofsäss, C. Ronning, and M. Dietrich. *Nucl. Inst. Meth. B* **190**, 835 (2002).

[93] K. Bharuth-Ram, A. Burchard, M. Deicher, H. Quintel, M. Restle, H. Hofsäss, and C. Ronning. *Phys. Rev. B* **64**, 195207 (2001).

[94] G. Davies. *Rep. Prog. Phys.* **44**, 787 (1981).

[95] A. A. Maradudin. *Solid State Phys.* **18**, 273 (1966).

[96] A. Zaitsev. *Optical Properties of Diamond: A Data Handbook*. Springer (2001).

[97] W. Demtröder. *Experimentalphysik 2: Elektrizität und Optik*. Springer (2009).

[98] M. Barth, J. Kouba, J. Stingl, B. Löchel, and O. Benson. *Opt. Express* **15**, 17231 (2007).

[99] C. Santori, P. E. Barclay, K.-M. C. Fu, R. G. Beausoleil, S. Spillane, and M. Fisch. *Nanotechnology* **21**, 274008 (2010).

[100] C. Kreuzer, J. Riedrich-Moeller, E. Neu, and C. Becher. *Opt. Express* **16**, 1632 (2008).

[101] I. Friel, S. Clewes, H. Dhillon, N. Perkins, D. Twitchen, and G. Scarsbrook. *Diam. Relat. Mater.* **18**, 808 (2009).

[102] M. Zhi, X. Wang, and A. Sokolov. *Opt. Express* **16**, 12139 (2008).

[103] V. Vavilov, A. Gippius, A. Zaitsev, B. Deryagin, B. Spitsyn, and A. Aleksenko. *Sov. Phys. Semicond.* **14**, 1078 (1980).

[104] L. H. Robins, L. P. Cook, E. N. Farabaugh, and A. Feldman. *Phys. Rev. B* **39**, 13367 (1989).

[105] J. Barjon, E. Rzepka, F. Jomard, J. Laroche, D. Ballutaud, T. Kociniewski, and J. Chevallier. *Phys. Status Solidi A* **202**, 2177 (2005).

[106] D. Musale, S. Sainkar, and S. Kshirsagar. *Diam. Relat. Mater.* **11**, 75 (2002).

[107] M. Stammler, H. Eisenbeiß, J. Ristein, J. Neubauer, M. Göbbels, and L. Ley. *Diam. Relat. Mater.* **11**, 504 (2002).

[108] J. Ruan, W. Choyke, and W. Partlow. *J. Appl. Phys.* **69**, 6632 (1991).

[109] L. Bergman, B. Stoner, K. Turner, J. Glass, and R. Nemanich. *J. Appl. Phys.* **73**, 3951 (1993).

[110] C. Clark and C. Dickerson. *Surf. Coat. Tech.* **47**, 336 (1991).

[111] H. Sternschulte, K. Thonke, R. Sauer, P. C. Münzinger, and P. Michler. *Phys. Rev. B* **50**, 14554 (1994).

[112] A. Gorokhovsky, A. Turukhin, R. Alfano, and W. Phillips. *Appl. Phys. Lett.* **66**, 43 (1995).

[113] G. Dollinger, A. Bergmaier, C. Frey, M. Roesler, and H. Verhoeven. *Diam. Relat. Mater.* **4**, 591 (1995).

[114] J. Ruan, W. Choyke, and W. Partlow. *Appl. Phys. Lett.* **58**, 295 (1991).

[115] G. Sittas, I. Kiflawi, H. Kanda, and P. Spear. *Diam. Relat. Mater.* **5**, 866 (1996).

[116] C. A. Breeding and W. Wang. *Diam. Relat. Mater.* **17**, 1335 (2008).

[117] A. Collins, M. Kamo, and Y. Sato. *J. Mater. Res.* **5**, 2507 (1990).

[118] A. Collins, L. Allers, C. Wort, and G. Scarsbrook. *Diam. Relat. Mater.* **3**, 932 (1994).

[119] Y. Bar-Yam and T. Moustakas. *Nature* **342**, 786 (1989).

[120] L. Allers and A. Mainwood. *Diam. Relat. Mater.* **7**, 261 (1998).

[121] U. F. S. D'Haenens-Johansson, A. M. Edmonds, B. L. Green, M. E. Newton, G. Davies, P. M. Martineau, R. U. A. Khan, and D. J. Twitchen. *Phys. Rev. B* **84**, 245208 (2011).

[122] J. P. Goss, R. Jones, S. J. Breuer, P. R. Briddon, and S. Öberg. *Phys. Rev. Lett.* **77**, 3041 (1996).

[123] S. Moliver. *Tech. Phys.* **48**, 1449 (2003).

[124] A. Collins. *J. Phys.: Condens. Matter* **14**, 3743 (2002).

[125] T. Gaebel, M. Domhan, C. Wittmann, I. Popa, F. Jelezko, J. Rabeau, A. Greentree, S. Prawer, et al. *Appl. Phys. B: Lasers Opt.* **82**, 243 (2006).

[126] C. Santori, P. E. Barclay, K.-M. C. Fu, and R. G. Beausoleil. *Phys. Rev. B* **79**, 125313 (2009).

[127] G. Iakoubovskii, K.and Adriaenssens, M. Nesladek, and L. Stals. *Diam. Relat. Mater.* **8**, 717 (1999).

[128] K. Iakoubovskii, G. Adriaenssens, and M. Nesladek. *J. Phys.: Condens. Matter* **12**, 189 (2000).

[129] U. F. S. D'Haenens-Johansson, A. M. Edmonds, M. E. Newton, J. P. Goss, P. R. Briddon, J. M. Baker, P. M. Martineau, R. U. A. Khan, et al. *Phys. Rev. B* **82**, 155205 (2010).

[130] D. Hayward, I.P.And Baldwin, D. Batchelder, and G. Pitt. *Diam. Relat. Mater.* **4**, 617 (1995).

[131] K. Iakoubovskii and G. Adriaenssens. *Diam. Relat. Mater.* **9**, 1349 (2000).

[132] I. Vlasov, A. Barnard, V. Ralchenko, O. Lebedev, M. Kanzyuba, A. Saveliev, V. Konov, and E. Goovaerts. *Adv. Mater.* **21**, 808 (2008).

[133] J. Ruan, K. Kobashi, and W. Choyke. *Appl. Phys. Lett.* **60**, 1884 (1992).

[134] G. Davies. *Mater. Sci. Forum* **143-147**, 21 (1993).

[135] X. Liang, L. Wang, X. Ma, D. Li, P. Cheng, and D. Yang. *Appl. Phys. Lett.* **90**, 161123 (2007).

[136] M. Rossi, S. Salvatori, F. Galluzzi, R. Montereali, and F. Somma. *Diam. Relat. Mater.* **6**, 1564 (1997).

[137] P. Siyushev, V. Jacques, I. Aharonovich, F. Kaiser, T. Mueller, L. Lombez, M. Atatuere, S. Castelletto, et al. *New J. Phys.* **11**, 113029 (2009).

[138] K. Iakoubovskii and G. J. Adriaenssens. *Phys. Rev. B* **61**, 10174 (2000).

[139] T. Feng and B. Schwartz. *J. Appl. Phys.* **73**, 1415 (1993).

[140] C. D. Clark, H. Kanda, I. Kiflawi, and G. Sittas. *Phys. Rev. B* **51**, 16681 (1995).

[141] L. Rogers. *Physics Procedia* **3**, 1557 (2010). 10th International Meeting On Hole Burning, Single Molecule, And Related Spectroscopies, 2009, Palm Cove, Australia.

[142] Osad'ko, I. *Sov. Phys. Usp.* **22**, 311 (1979).

[143] P. J. Lin-Chung. *Phys. Rev. B* **50**, 16905 (1994).

[144] R. Wehner, H. Borik, W. Kress, A. Goodwin, and S. Smith. *Solid State Commun.* **5**, 307 (1967).

[145] W. Windl, P. Pavone, K. Karch, O. Schütt, D. Strauch, P. Giannozzi, and S. Baroni. *Phys. Rev. B* **48**, 3164 (1993).

[146] J. Warren and J. Yarnell. *Phys. Rev.* **158**, 805 (1967).

[147] S. A. Solin and A. K. Ramdas. *Phys. Rev. B* **1**, 1687 (1970).

[148] R. Brout and W. Visscher. *Phys. Rev. Lett.* **9**, 54 (1962).

[149] M. H. Grimsditch, E. Anastassakis, and M. Cardona. *Phys. Rev. B* **18**, 901 (1978).

[150] M. S. Dresselhaus, G. Dresselhaus, and A. Jorio. *Group Theoory- Application to the Physics of Condensed Matter.* Springer Berlin Heidelberg (2008).

[151] J. Maze, A. Gali, E. Togan, Y. Chu, A. Trifonov, E. Kaxiras, and M. Lukin. *New J. Phys.* **13**, 025025 (2011).

[152] A. Kaplyanskii. *Opt. Spec* **16**, 329 (1963).

[153] W. Demtröder. *Experimentalphysik 3 : Atome, Moleküle und Festkörper.* Springer (2009).

[154] S. Brown and S. Rand. *J. Appl. Phys.* **78**, 4069 (1995).

[155] J. Goss, P. Briddon, and M. Shaw. *Phys. Rev. B* **76**, 75204 (2007).

[156] K. V. Kaplyanskii, A. and V. Medvedev. *Sov. Phys.-Solid State* **12**, 1193 (1970).

[157] A. Collins. *J. Phys.: Condens. Matter* **1**, 439 (1989).

[158] M. Nazaré, A. J. Neves, and G. Davies. *Phys. Rev. B* **43**, 14196 (1991).

[159] A. Neves, L. Rino, and H. Kanda. *Diam. Relat. Mater.* **12**, 526 (2003). 13th European Conference On Diamond, Diamond-like Materials, Carbon Nanotubes, Nitrides And Sililcon Carbide (diamond 2002), Granada, Spain.

[160] A. Smith, K. Johnston, A. Collins, G. Davies, and A. Mainwood. *Diam. Relat. Mater.* **12**, 495 (2003).

[161] P. Mason, F. Ham, and G. Watkins. *Phys. Rev. B* **60**, 5417 (1999).

[162] H. Sternschulte, K. Thonke, J. Gerster, W. Limmer, R. Sauer, J. Spitzer, and P. Munzinger. *Diam. Relat. Mater.* **4**, 1189 (1995).

[163] H. Sternschulte. *Lumineszenzuntersuchungen an dotiertem und undotiertem Diamant.* Ph.D. thesis, Universität Ulm (1999).

[164] D. Steinmetz. *Ni Si-basierte Farbzentren in Diamant als Einzelphotonenquellen.* Ph.D. thesis, Universität des Saarlandes (2011).

[165] R. Webb. *Rep. Prog. Phys.* **59**, 427 (1996).

[166] C. Arend. Kontinuierliche und zeitabhängige Spektroskopie an Farbzentren in Diamant, Diplomarbeit am Fachbereich Physik der Universität des Saarlandes (2011).

[167] R. Hanbury Brown and R. Twiss. *Nature* **178**, 1046 (1956).

[168] R. Hanbury Brown and R. Twiss. *Nature* **177**, 27 (1956).

[169] S. Kitson, P. Jonsson, J. Rarity, and P. Tapster. *Phys. Rev. A* **58**, 620 (1998).

[170] A. C. Ferrari and J. Robertson. *Phys. Rev. B* **63**, 121405 (2001).

[171] E. Zscherpel. Raman Spektroskopie an poly- und nanokristallinen Diamanten, Bachelor Arbeit am Fachbereich Physik der Universität des Saarlandes (2010).

[172] D. Steinmetz, E. Neu, J. Meijer, W. Bolse, and C. Becher. *Appl. Phys. B: Lasers Opt.* **102**, 451 (2011).

[173] P. Menon, A. Edwards, and C. Feigerle. *Diam. Relat. Mater.* **8**, 101 (1999).

[174] W. Banholzer. *Surf. Coat. Technol.* **53**, 1 (1992).

[175] M. Kamo, Y. Sato, S. Matsumoto, and N. Setaka. *J. Cryst. Growth* **62**, 642 (1983).

[176] H. Okushi. *Diam. Relat. Mater.* **10**, 281 (2001).

[177] L. Bergman and R. Nemanich. *Annu. Rev. Mater. Sci.* **26**, 551 (1996).

[178] L. Bergman and R. Nemanich. *J. Appl. Phys.* **78**, 6709 (1995).

[179] D. Kirillov and G. Reynolds. *Appl. Phys. Lett.* **65**, 1641 (1994).

[180] C. Raman and K. Krishnan. *Nature* **121**, 501 (1928).

[181] J. O. Orwa, K. W. Nugent, D. N. Jamieson, and S. Prawer. *Phys. Rev. B* **62**, 5461 (2000).

[182] C. Fritzen, N. Balzaretti, R. Livi, J. de Souza, and J. da Jornada. *Diam. Relat. Mater.* **8**, 2110 (1999).

[183] G. Yang and M. Aslam. *Appl. Phys. Lett.* **66**, 311 (1995).

[184] A. Kromka, B. Rezek, M. Kalbacova, V. Baresova, J. Zemek, C. Konak, and M. Vanecek. *Adv. Eng. Mater.* **11**, B71 (2009).

[185] I. Koenka, Y. Kauffmann, and A. Hoffman. *Appl. Phys. Lett.* **99**, 201907 (2011).

[186] A. Bochow. Strukturelle und spektroskopische Untersuchungen an CVD-Diamantfilmen, Diplomarbeit am Fachbereich Physik der Universität des Saarlandes (2007).

[187] S. Harris, A. Weiner, S. Prawer, and K. Nugent. *J. Appl. Phys.* **80**, 2187 (1996).

[188] H.-J. Hinneberg, M. Eck, and K. Schmid. *Diam. Relat. Mater.* **1**, 810 (1992).

[189] V. Sedov, I. Vlasov, V. Ralchenko, A. Khomich, V. Konov, A. Fabbri, and G. Conte. *Bulletin of the Lebedev Physics Institute* **38**, 291 (2011).

[190] M. Ozawa, M. Inaguma, M. Takahashi, F. Kataoka, A. Krueger, and E. Osawa. *Adv. Mater.* **19**, 1201 (2007).

[191] Y. Liang, M. Ozawa, and A. Krueger. *ACS Nano* **3**, 2288 (2009).

[192] E. Neu, C. Arend, E. Gross, F. Guldner, C. Hepp, D. Steinmetz, E. Zscherpel, S. Ghodbane, et al. *Appl. Phys. Lett.* **98**, 243107 (2011).

[193] A. Stacey, I. Aharonovich, S. Prawer, and J. Butler. *Diam. Relat. Mater.* **18**, 51 (2009).

[194] S. Gsell, T. Bauer, J. Goldfuß, M. Schreck, and B. Stritzker. *Appl. Phys. Lett.* **84**, 4541 (2004).

[195] S. Gsell. *Wachstum von großflächigen einkristallinen Diamantschichten mittels Heteroepitaxie auf Silizium: Entwicklung von Pufferschichtsystemen und Untersuchung der Nukleationsmechanismen.* Ph.D. thesis, Universität Augsburg (2007).

[196] S. Gsell, M. Fischer, M. Schreck, and B. Stritzker. *J. Cryst. Growth* **311**, 3731 (2009).

[197] M. Schreck. personal communication (2011).

[198] J. Perriere. *Vacuum* **37**, 429 (1987).

[199] R. Samlenski, C. Haug, R. Brenn, C. Wild, R. Locher, and P. Koidl. *Appl. Phys. Lett.* **67**, 2798 (1995).

[200] M. Schreck, T. Bauer, S. Gsell, F. Hörmann, H. Bielefeldt, and B. Stritzker. *Diam. Relat. Mater.* **12**, 262 (2003).

[201] C. Wild, P. Koidl, W. Müller-Sebert, H. Walcher, R. Kohl, N. Herres, R. Locher, R. Samlenski, et al. *Diam. Relat. Mater.* **2**, 158 (1993).

[202] E. Neu, M. Fischer, S. Gsell, M. Schreck, and C. Becher. *Phys. Rev. B* **84**, 205211 (2011).

[203] E. Wu, V. Jacques, H. Zeng, P. Grangier, F. Treussart, and J.-F. Roch. *Opt. Express* **14**, 1296 (2006).

[204] R. Brescia, M. Schreck, J. Michler, S. Gsell, and B. Stritzker. *Diam. Relat. Mater.* **16**, 705 (2007).

[205] M. Schreck, H. Roll, J. Michler, E. Blank, and B. Stritzker. *J. Appl. Phys.* **88**, 2456 (2000).

[206] S. Gsell, M. Fischer, and M. Schreck. unpublished (2011).

[207] H. Windischmann and G. F. Epps. *Diam. Relat. Mater.* **1**, 656 (1992).

[208] M. Fischer, S. Gsell, M. Schreck, and A. Bergmaier. *Appl. Phys. Lett.* **100**, 041906 (2012).

[209] C. Santori, P. Tamarat, P. Neumann, J. Wrachtrup, D. Fattal, R. Beausoleil, J. Rabeau, P. Olivero, et al. *Phys. Rev. Lett.* **97**, 247401 (2006).

[210] C. Santori, D. Fattal, S. M. Spillane, M. Fiorentino, R. G. Beausoleil, A. D. Greentree, P. Olivero, M. Draganski, et al. *Opt. Express* **14**, 7986 (2006).

[211] X. Jiang and C. Jia. *Appl. Phys. Lett.* **69**, 3902 (1996).

[212] J. Michler, Y. Von Kaenel, J. Stiegler, and E. Blank. *J. Appl. Phys.* **83**, 187 (1998).

[213] R. Brescia, M. Schreck, M. Gsell, S.and Fischer, and B. Stritzker. *Diam. Relat. Mater.* **17**, 1045 (2008).

[214] M. I. Heggie, C. P. Ewels, N. Martsinovich, S. Scarle, R. Jones, J. P. Goss, B. Hourahine, and P. R. Briddon. *J. Phys.: Condens. Matter* **14**, 12689 (2002).

[215] G. Davies. *J. Phys. C: Solid State* **7**, 3797 (1974).

[216] K. Lee, B. J. Sussman, J. Nunn, V. Lorenz, K. Reim, D. Jaksch, I. Walmsley, P. Spizzirri, et al. *Diam. Relat. Mater.* **19**, 1289 (2010).

[217] R. Loudon. *The Quantum Theory of Light.* Oxford University Press (2000).

[218] M. Fox. *Quantum Optics: an introduction.* Oxford University Press (2006).

[219] J. Rabeau, A. Stacey, A. Rabeau, S. Prawer, F. Jelezko, I. Mirza, and J. Wrachtrup. *Nano Lett.* **7**, 3433 (2007).

[220] L. Bergman, M. McClure, J. Glass, and R. Nemanich. *J. Appl. Phys.* **76**, 3020 (1994).

[221] M. Rossi, S. Salvatori, F. Galluzzi, F. Somma, and R. Montereali. *Diam. Relat. Mater.* **7**, 255 (1998).

[222] A. Mora, J. Steeds, and J. Butler. *Diam. Relat. Mater.* **12**, 310 (2003).

[223] R. Graham, T. Moustakas, and M. Disko. *J. Appl. Phys.* **69**, 3212 (1991).

[224] E. Wu, V. Jacques, H. Zeng, P. Grangier, F. Treussart, and J.-R. Roch. *Opt. Express* **14**, 1296 (2006).

[225] L. Fleury, J. Segura, G. Zumofen, B. Hecht, and U. Wild. *Phys. Rev. Lett.* **84**, 1148 (2000).

[226] F. Treussart, A. Clouqueur, C. Grossman, and J. Roch. *Opt. letters* **26**, 1504 (2001).

[227] R. Zondervan, F. Kulzer, M. A. K. o, , and M. Orrit. *The Journal of Physical Chemistry A* **108**, 1657 (2004).

[228] C. Eggeling, J. Widengren, R. Rigler, and C. Seidel. *Anal. Chem.* **70**, 2651 (1998).

[229] C. Toninelli, K. Early, J. Bremi, A. Renn, S. Götzinger, and V. Sandoghdar. *Arxiv preprint arXiv:1002.0920* (2010).

[230] C. Bradac, T. Gaebel, N. Naidoo, M. J. Sellars, J. Twamley, L. J. Brown, A. S. Barnard, T. Plakhotnik, et al. *Nature Nanotech.* **5**, 345 (2010).

[231] R. Verberk, A. M. van Oijen, and M. Orrit. *Phys. Rev. B* **66**, 233202 (2002).

[232] X. Wu, Y. Sun, and M. Pelton. *Phys. Chem. Chem. Phys.* **11**, 5867 (2009).

[233] C. Vion, P. Spinicelli, L. Coolen, C. Schwob, J.-M. Frigerio, J.-P. Hermier, and A. Maitre. *Opt. Express* **18**, 7440 (2010).

[234] J. Tisler, G. Balasubramanian, B. Naydenov, R. Kolesov, B. Grotz, R. Reuter, J. Boudou, P. Curmi, et al. *ACS Nano* **3**, 1959 (2009).

[235] T.-L. Wee, Y.-K. Tzeng, C.-C. Han, H.-C. Chang, W. Fann, J.-H. Hsu, K.-M. Chen, and Y.-C. Yull. *J. Phys. Chem. A* **111**, 9379 (2007).

[236] R. Chance, A. Prock, and R. Silbey. *Adv. Chem. Phys.* **37**, 1 (1978).

[237] J. H. Weaver, C. G. Olson, and D. W. Lynch. *Phys. Rev. B* **15**, 4115 (1977).

[238] E. Hellen and D. Axelrod. *JOSA B* **4**, 337 (1987).

[239] L. Novotny and B. Hecht. *Principles of Nano-Optics.* Cambridge University Press (2006).

[240] T. Ha, T. Laurence, D. Chemla, and S. Weiss. *J. Phys. Chem. B* **103**, 6839 (1999).

[241] A. V. Turukhin, C.-H. Liu, A. A. Gorokhovsky, R. R. Alfano, and W. Phillips. *Phys. Rev. B* **54**, 16448 (1996).

[242] M. Agio. personal communication (2012).

[243] B. Buchler, T. Kalkbrenner, C. Hettich, and V. Sandoghdar. *Phys. Rev. Lett.* **95**, 063003 (2005).

[244] W. Lukosz and R. Kunz. *J. Opt. Soc. Am.* **67**, 1607 (1977).

[245] B. Smith, D. Gruber, and T. Plakhotnik. *Diam. Relat. Mater.* **19**, 314 (2010).

[246] S. Grudinkin, N. Feoktistov, A. Medvedev, K. Bogdanov, A. Baranov, A. Vul, and V. Golubev. *J. Phys. D: Appl. Phys.* **45**, 062001 (2012).

[247] A. Kenyon. *Prog. Quant. Electron.* **26**, 225 (2002).

[248] D. Dexter, C. Klick, and G. Russell. *Phys. Rev.* **100**, 603 (1955).

[249] G. Baldacchini, D. Pan, and F. Lüty. *Phys. Rev. B* **24**, 2174 (1981).

[250] M. Leblans. *Radiat. Eff. Defects Solids* **134**, 39 (1995).

[251] R. Bartram and A. Stoneham. *Solid State Commun.* **17**, 1593 (1975).

[252] M. Henderson and R. Bartram. *Crystal Field engineering of solid state laser materials.* Cambridge University Press (2000).

[253] A. Stoneham and R. Bartram. *Solid-State Electron.* **21**, 1325 (1978).

[254] D. Englund, B. Shields, K. Rivoire, F. Hatami, J. Vucckovic, H. Park, and M. D. Lukin. *Nano Lett.* **10**, 3922 (2010).

[255] K. Iakoubovskii, G. Adriaenssens, N. Dogadkin, and A. Shiryaev. *Diam. Relat. Mater.* **10**, 18 (2001).

[256] A. A. Bergman, A. M. Zaitsev, and A. A. Gorokhovsky. *J. Lumin.* **125**, 92 (2007).

[257] C. Clark, E. Mitchell, and G. Maycraft. *J. Appl. Phys.* **33**, 378 (1962).

[258] S. Zaske, A. Lenhard, and C. Becher. *Opt. Express* **19**, 12825 (2011).

[259] J. Fourkas. *Opt. Lett.* **26**, 211 (2001).

[260] A. Boiron, P. Tamarat, B. Lounis, R. Brown, and M. Orrit. *Chem. Phys.* **247**, 119 (1999).

[261] C. Hofmann and M. Orrit. *J. Phys. Chem. B* **110**, 18925 (2006).

[262] M. Bauer and L. Kador. *J. Chem. Phys.* **118**, 9069 (2003).

[263] M. Bauer and L. Kador. *J. Lumin.* **107**, 32 (2004).

[264] A. Dräbenstedt, L. Fleury, C. Tietz, F. Jelezko, S. Kilin, A. Nizovtzev, and J. Wrachtrup. *Phys. Rev. B* **60**, 11503 (1999).

[265] A. Lenef, S. W. Brown, D. A. Redman, S. C. Rand, J. Shigley, and E. Fritsch. *Phys. Rev. B* **53**, 13427 (1996).

[266] M. Hausschild. Hochauflösende Spektroskopie an SiV-Zentren in Diamant, Diplomarbeit am Fachbereich Physik der Universität des Saarlandes (2009).

[267] F. Guldner. Untersuchung des Einflusses der Oberflächenterminierung von Nanodiamanten auf die Fluoreszenzeigenschaften von SiV-Zentren, Bachelorarbeit am Fachbereich Physik der Universität des Saarlandes (2011).

[268] A. Batalov, V. Jacques, F. Kaiser, P. Siyushev, P. Neumann, L. J. Rogers, R. L. McMurtrie, N. B. Manson, et al. *Phys. Rev. Lett.* **102**, 195506 (2009).

[269] Y. Shen, T. Sweeney, and H. Wang. *Phys. Rev. B* **77**, 33201 (2008).

[270] P. Tamarat, T. Gaebel, J. Rabeau, A. Greentree, H. Wilson, L. Hollenberg, S. Prawer, P. Hemmer, et al. *Phys. Rev. Lett.* **97**, 083002 (2006).

[271] M. V. Hauf, B. Grotz, B. Naydenov, M. Dankerl, S. Pezzagna, J. Meijer, F. Jelezko, J. Wrachtrup, et al. *Phys. Rev. B* **83**, 081304(R) (2011).

[272] R. Ulbricht, S. T. van der Post, J. P. Goss, P. R. Briddon, R. Jones, R. U. A. Khan, and M. Bonn. *Phys. Rev. B* **84**, 165202 (2011).

[273] F. Jelezko, I. Popa, A. Gruber, C. Tietz, J. Wrachtrup, A. Nizovtsev, and S. Kilin. *Appl. Phys. Lett.* **81**, 2160 (2002).

[274] K.-M. C. Fu, C. Santori, P. E. Barclay, and R. G. Beausoleil. *Appl. Phys. Lett.* **96**, 121907 (2010).

[275] L. Rondin, G. Dantelle, A. Slablab, F. Grosshans, F. Treussart, P. Bergonzo, S. Perruchas, T. Gacoin, et al. *Phys. Rev. B* **82**, 115449 (2010).

[276] H. Michaelson. *J. Appl. Phys.* **48**, 4729 (1977).

[277] M. Pawlak, T. Schram, K. Maex, and A. Vantomme. *Microelectron. Eng.* **70**, 373 (2003).

[278] B. Armstrong. *J. Quant. Spectrosc. Radiat. Transfer* **7**, 61 (1967).

[279] M. Toutounji. *J. Phys. Chem. C* **114**, 20764 (2010).

[280] K. Rebane. *Impurity Spectra of solids.* Plenum Press, New York (1970).

[281] S. Lawson, G. Davies, A. Collins, and A. Mainwood. *J. Phys.: Condens. Matter* **4**, 3439 (1992).

[282] M. Nazare, G. Woods, and M. Assuncao. *Mat. Sci. Eng. B: Solid.* **11**, 341 (1992). Symp at the 1990 Fall Meeting of the European Materials Research Soc. Strasbourg, France.

[283] V. Hizhnyakov, H. Kaasik, and I. Sildos. *Phys. Status Solidi B* **234**, 644 (2002).

[284] G. Davies and M. Hamer. *Philos. Trans. Roy. Soc. A* **348**, 285 (1976).

[285] V. Hizhnyakov, V. Boltrushko, H. Kaasik, and I. Sildos. *J. Chem. Phys.* **119**, 6290 (2003).

[286] V. Hizhnyakov, V. Boltrushko, H. Kaasik, and I. Sildos. *J. Lumin.* **107**, 351 (2004).

[287] A. Halperin and O. Nawi. *J. Phys. Chem. Solids* **28**, 2175 (1967).

[288] V. Hizhnyakov and P. Reineker. *J. Chem. Phys.* **111**, 8131 (1999).

[289] K.-M. C. Fu, C. Santori, P. E. Barclay, L. J. Rogers, N. B. Manson, and R. G. Beausoleil. *Phys. Rev. Lett.* **103**, 256404 (2009).

[290] H. D. Robinson and B. B. Goldberg. *Phys. Rev. B* **61**, R5086 (2000).

[291] I. Favero, A. Berthelot, G. Cassabois, C. Voisin, C. Delalande, P. Roussignol, R. Ferreira, and J. Gérard. *Phys. Rev. B* **75**, 73308 (2007).

[292] L. Robledo, H. Bernien, I. van Weperen, and R. Hanson. *Phys. Rev. Lett.* **105**, 177403 (2010).

[293] L. Rino, A. Neves, J. Lopes, and H. Kanda. *Diam. Relat. Mater.* **14**, 383 (2005). 15th European Conference On Diamond, Diamond-like Materials, Carbon Nanotubes, Nitrides, And Silicon Carbide, Riva Del Garda, Italy.

[294] W. Demtröder. *Experimentalphysik 1: Mechanik und Wärme*. Springer (2008).

[295] G. Slack and S. Bartram. *J. Appl. Phys.* **46**, 89 (1975).

[296] S. Stoupin and Y. V. Shvyd'ko. *Phys. Rev. B* **83**, 104102 (2011).

[297] P. Johnson and R. Christy. *Phys. Rev. B* **11**, 1315 (1975).

[298] S. Roberts. *Phys. Rev.* **100**, 1667 (1955).

[299] A. Boiron, B. Lounis, and M. Orrit. *J. Chem. Phys.* **105**, 3969 (1996).

[300] I. Aharonovich, C. Zhou, A. Stacey, F. Treussart, J.-F. Roch, and S. Prawer. *Appl. Phys. Lett.* **93**, 243112 (2008).

[301] L. J. Rogers, S. Armstrong, M. J. Sellars, and N. B. Manson. *New J. Phys.* **10**, 103024 (2008).

[302] G. Sallen, A. Tribu, T. Aichele, R. André, L. Besombes, C. Bougerol, M. Richard, S. Tatarenko, et al. *Nature Photon.* **4**, 696 (2010).

[303] E. Gross. Spektroskopische Untersuchung von Farbzentren in Diamant im sichtbaren und infraroten Spektralbereich, Diplomarbeit am Fachbereich Physik der Universität des Saarlandes (2011).

[304] S. Kena-Cohen, A. Wiener, Y. Sivan, P. N. Stavrinou, D. D. C. Bradley, A. Horsfield, and S. A. Maier. *ACS Nano* **5**, 9958 (2011).

[305] T. Schroeder. personal communcation (in preparation for publication) (2012).

[306] V. Acosta, C. Santori, A. Faraon, Z. Huang, K. Fu, A. Stacey, D. Simpson, S. Tomljenovic-Hanic, et al. *Arxiv preprint arXiv:1112.5490* (2011).

List of publications

Refereed journal publications

- J. Riedrich-Möller, L. Kipfstuhl, C. Hepp, E. Neu, C. Pauly, F. Mücklich, A. Baur, M. Wandt, S. Wolff, M. Fischer, S. Gsell, M. Schreck and C. Becher *One- and two-dimensional photonic crystal microcavities in single crystal diamond* Nature Nanotechn. **7**, 69 (2012)

- E. Neu, M. Fischer, S. Gsell, M. Schreck and C. Becher, *Fluorescence and polarization spectroscopy of single silicon vacancy centers in heteroepitaxial nanodiamonds on iridium* Phys. Rev. B **84**, 205211 (2011)

- E. Neu, C. Arend, E. Gross, F. Guldner, C. Hepp, D. Steinmetz, E. Zscherpel, S. Ghodbane, H. Sternschulte, D. Steinmüller-Nethl, Y. Liang, A. Krueger, C. Becher *Narrowband fluorescent nanodiamonds produced from chemical vapor deposition films*, Appl. Phys. Lett., **98**, 243107 (2011)

- D. Steinmetz, E. Neu, J. Meijer, W. Bolse und C. Becher, *Single photon emitters based on Ni/Si related defects in single crystalline diamond*, Appl. Phys. B **102**, 45 (2011)

- E. Neu, D. Steinmetz, J. Riedrich-Möller, S. Gsell, M. Fischer, M. Schreck und C. Becher, *Single photon emission from silicon-vacancy colour centres in chemical vapour deposition nano-diamonds on iridium*, New J. Phys. **13**, 025012 (2011)

- J. Riedrich-Möller, E. Neu and C. Becher *Design of microcavities in diamond-based photonic crystals by Fourier- and real-space analysis of cavity fields* Photonics and Nanostructures **8**, 150 (2010)

- C. Kreuzer, J. Riedrich-Möller, E. Neu and C. Becher, *Design of photonic crystal microcavities in diamond films*, Opt. Express **16**, 1632 (2008).

Refereed conference proceedings

- M. Grün, P. Miska, E. Neu, D. Steinmetz, F. Montaigne, H. Rinnert, C. Becher and M. Vergnat, *Towards spectroscopy of a few silicon nanocrystals embedded in silica*, E-MRS 2008 Spring Meeting, Strasbourg, France, May 26-30, 2008; published in: Physica E, Physica E **41**, 998 (2009)

- D. Steinmetz, E. Neu, C. Hepp, R. Albrecht, W. Bolse, J. Meijer, D. Rogalla und C. Becher, *Single-photon emission from Ni-related color centers in CVD diamond*, Proc. SPIE **7727**, 77270P (2010)

International Conference Proceedings

- E. Neu, M. Fischer, S. Gsell, M. Schreck, and C. Becher, *Spectroscopy of single SiV centers in oriented diamond nanocrystals: new insights into promising single photon sources* , Hasselt Diamond Workshop 2012, SBDD XVII, Hasselt, Belgium, March 14-16, 2012.

- E. Neu, J. Riedrich-Möller, L. Kipfstuhl, C. Hepp, C. Arend, D. Steinmetz, and C. Becher, *Bright single photon emission from color centers in diamond and coupling to photonic crystal cavities*, International Conference on Quantum Information Processing and Communication, QIPC 2011, Zurich, Switzerland, September 5-9, 2011

- E. Neu, D. Steinmetz, C. Arend, J. Riedrich-Möller, M. Fischer, S. Gsell, M. Schreck, and C. Becher, *Narrow-bandwidth high-brightness single photon emission from silicon-vacancy colour centres in CVD-nano-diamonds*, 2011 Conference on Lasers and Electro-Optics Europe and 12th European Quantum Electronics Conference, CLEO EUROPE/EQEC 2011, art. no. 5943585, 2011

- E. Neu, D. Steinmetz, C. Arend, J. Riedrich-Möller, M. Fischer, S. Gsell, M. Schreck and C. Becher, *Narrow-bandwidth high-brightness single photon sources based on silicon vacancy colour centres in CVD-nano-diamonds*, Quantum Science and Technologies, Rovereto, Italy, May 9-12, 2011

- E. Neu, D. Steinmetz, C. Arend, J. Riedrich-Möller, M. Fischer, S. Gsell, M. Schreck, and C. Becher, *Single photon emission from silicon-vacancy colour centres in CVD nano-diamonds*, Hasselt Diamond Workshop 2011, SBDD XVI, Hasselt, Belgium, February 21-23, 2011

- E. Neu, D. Steinmetz, J. Riedrich-Möller, R. Albrecht, S. Gsell, M. Fischer, M. Schreck and C. Becher, *Color Centers in Diamond: Artificial Atoms for Quantum Information*, International workshop of the EU-RTN EMALI, Barcelona, Spain, September 23-25, 2010

- E. Neu, D. Steinmetz,J. Riedrich-Möller, S. Ghodbane, D. Steinmüller-Nethl and C. Becher*Color Centers in diamond: artificial atoms for quantum information* 450. WE-Heraeus-Seminar "Mixed States of Light and Matter", Physikzentrum Bad Honnef, Germany, February 07-10, 2010

- E. Neu, D. Steinmetz, C. Hepp, R. Albrecht, W. Bolse, J. Meijer, C. Becher, *Characterization of single Nickel-related color centers created by ion-implantation*, Hasselt Diamond Workshop 2010, SBDD XV, Hasselt, Belgium, February 22-24, 2010

- R. Albrecht, J. Riedrich-Möller, E. Neu, D. Steinmetz, C. Hepp, B. Sauer, M. Hauschild and C. Becher, *Towards optical interfaces for color centers in diamond*, International Conference on Quantum Information Processing and Communication, QIPC 2009, Rome, Italy, September 21-25, 2009

- J. Riedrich-Möller, E. Neu, and C. Becher, *Design of microcavities in diamond-based photonic crystals* (TUE5s.2), 2nd European Topical Meeting on Nanophotonics and Metamaterials (NANOMETA 2009), Seefeld, Austria, January 5-8, 2009

- E. Neu, D. Steinmetz, S. Ghodbane, D. Steinmüller-Nethl, and C. Becher, *Towards spectroscopy of single color centers in CVD-diamond*, Hasselt Diamond Workshop 2009, SBDD XIV, Hasselt, Belgium, March 2-4, 2009

- C. Hepp, E. Neu, J. Riedrich-Möller, D. Steinmetz, S. Ghodbane, D. Steinmüller-Nethl, and C. Becher, *Optical properties of nanocrystalline diamond films for photonic crystal microcavities*, Hasselt Diamond Workshop 2009, SBDD XIV, Hasselt, Belgium, March 2-4, 2009

- J. Riedrich-Möller, E. Neu, C. Hepp, and C. Becher, *Design of microcavities in diamond-based photonic crystals*, CLEO/Europe - EQEC 2009 - European Conference on Lasers and Electro-Optics and the European Quantum Electronics Conference, art. no. 5191458, 2009

- D. Steinmetz, R. Albrecht, E. Neu, S. Ghodbane, D. Steinmuller-Nethl, S. Deutsch, J. Reichel und C. Becher, *Towards optimized single photon sources based on color centers in diamond*, CLEO/Europe - EQEC 2009 - European Conference on Lasers and Electro-Optics and the European Quantum Electronics Conference, art. no. 5191456, 2009

- J. Riedrich-Möller, C. Kreuzer, R. Albrecht, E. Neu, and C. Becher, *Design of Photonic Crystal Microcavities in Diamond Films for Quantum Information*, Quantum Electronics and Laser Science Conference 2008, San Jose, USA, May 4-9, 2008; in CLEO/QELS and PhAST 2008 Technical Digest (Optical Society of America, Washington, DC, 2008), JThA103, 2008

- C. Kreuzer, E. Neu, and C. Becher, *Design of Photonic Crystal Microcavities in Diamond for Quantum Information*, International Conference on Quantum Information Processing and Communication, QIPC 2007, Barcelona, Spain, October 15-19, 2007

- C. Kreuzer, E. Neu, and C. Becher, *Design of Photonic Crystal Microcavities in Diamond for Quantum Information*, Conference on Lasers and Electro-Optics Europe - Technical Digest, art. no. 4386753, 2007

Danke!

Trotz der Länge der Arbeit soll noch etwas Platz bleiben um jenen zu danken, die diese Arbeit möglich gemacht haben.
Allen voran danke ich natürlich meinem Betreuer Christoph Becher für die Möglichkeit zur Promotion auf einem hochaktuellen und interessanten Forschungsgebiet. Er hatte insbesondere in der anstrengenden Zeit des Neuaufbaus von Labors, Kooperationen usw. immer ein offenes Ohr für unsere Probleme und meist auch einen passenden Spruch dazu ‚try again, try harder' ;-). Ich bedanke mich für das in mich gesetzte Vertrauen und die Möglichkeit, viele eigene Ideen einzubringen und selbstständig umzusetzen. Du hast mich immer dazu gebracht 120% zu geben, auch wenn man manchmal in Versuchung war bei 101% schon Schluss zu machen, und das hat sich denke ich am Ende ausgezahlt.
Gregor Jung danke ich ganz herzlich für die Bereitschaft diese Arbeit als Zweigutachter zu lesen.
Diese ganze Arbeit wäre natürlich ohne die diversen Diamantproben, die mir zur Verfügung gestellt wurden, nicht möglich gewesen. Zuerst sind hier Matthias Schreck, Stefan Gsell und Martin Fischer (Universität Augsburg) zu nennen, mit deren Diamanten auf Ir die meisten der hier vorgestellten Ergebnisse erzielt wurden. Insbesondere Matthias und Stefan hatten nicht nur immer tolle neue Proben und Ideen für mich, sondern auch eine Engelsgeduld darin mir die Geheimnisse der Festkörperphysik/ des Diamantwachstums näher zu bringen, wenn ich mal wieder rätselnd vor Kristallformen, Netzebenen oder ähnlichem stand.
Anke Krüger und ihrem Mitarbeiter Yuejiang Liang (Universität Würzburg) möchte ich für die Herstellung der BASD Nanodiamanten danken und darüber hinaus für viele nützliche Informationen und sehr kurzweilige Diskussionen zum Thema Nanodiamanten.
Diese Arbeit hat mit einer Kooperation mit Doris Steinmüller-Nethl und Hadwig Sternschulte von rho-BeSt Innsbruck begonnen, später kam Slimane Ghodbane in Innsbruck hinzu. In jeder Menge Probenserien haben wir die richtigen Parameter und geeigneten Substrate heraus gefischt. Danke für das know-how und danke fürs Verzeihen der Versuche bei denen ein CVD-Reaktor Putz nötig wurde. Und natürlich ein besonderer Dank an Hadwig für unterhaltsame, ausführliche Diskussionen zur SiV Spektroskopie.
In addition, I'd like to thank Marco Loncar's group at Harvard University. I had the pleasure to spend three weeks there working especially with Birgit Hausmann, Jennifer Choy and Tom Babinec. Thanks for the awesome time and the insights into

diamond nanowire fabrication which was (together with the experience of working in a cleanroom) fully new to me.

Auch innerhalb der Uni durfte ich mich über einigen wissenschaftlichen Support freuen. Insbesondere von Herrn Jörg Schmauch, der die in allen meinen Vorträgen und Publikationen bewunderten REM Bilder angefertigt hat. Karin Kretsch hat mit sehr viel Einsatz dafür gesorgt, dass ich als Anfänger im Chemielabor weder mir selbst noch dem Equipment geschadet habe. In die Geheimnisse des Spin-Coatings wurde ich von Mitarbeitern der AG von Karin Jakobs, insbesondere Ludovic Marquant, eingeweiht.

Neben der wissenschaftlichen Unterstützung darf ich mich bei der Stiftung der deutschen Wirtschaft (sdw) für die finanzielle Förderung dieser Arbeit mit einem 3jährigen Promotionsstipendium bedanken. Im Rahmen eines Programms für Nachwuchswissenschaftlerinnen an der UdS konnte ich wertvolle persönliche Erfahrungen sammeln, wofür ich insbesondere unseren Ansprechpartnerinnen Nicole Riegger und Michelle Froese-Kuhn danken möchte, sowie Klaas Bergmann, der sich bereiterklärt hat im Rahmen dieses Programms die Rolle meines Mentors zu übernehmen.

Experimentalphysik endet nicht an der Labortür, daher auch einen besonderen Dank an unsere Elektronikwerkstatt und an Herrn Rolf Kiefer für das Beseitigen unzähliger Probleme. Und ein besonderer Dank an unser Metallwerkstatt-Team um Michael Schmitt, die die meist nicht wirklich perfekten Pläne von ‚Madame' doch immer in passende Bauteile umgesetzt haben.

Und wenn man mal keine technische Hilfe braucht hat man meist Papierkran zu erledigen. Dafür geht ein besonderer Dank an unser Sekretariat insbesondere an Elke Huschens die immer das richtige Formular parat hatte oder wusste wen man anrufen muss. Ich glaube ohne dich hätte ich bei der Suche nach dem Passierschein A38 wahrscheinlich mehr als einmal die Nerven verloren!

Und als Experimentalphysiker möchte ich natürlich ganz besonders Herrn K. Labauter danken für verrückt spielende Spektrometer, überlaufende Kompressoren, ausfallende Klimaanlagen und Proben mit Fingerabdrücken, ohne die eine Promotion natürlich vollständig langweilig wäre.

Natürlich wäre die ganze Arbeit furchtbar einsam gewesen ohne die Kollegen aus der AG. Denn am besten lassen sich physikalische Themen doch noch immer bei einer Tasse Nespresso diskutieren und ohne ein tolles Team wäre das Photonenfangen bei unseren ‚wahnwitzigen' Experimenten ja auch meist unmöglich. Natürlich auch ein großer Dank an all jene die mir durch das Korrekturlesen dieser Arbeit geholfen haben. Und natürlich auch besonderer Dank an die Diplomanden und Bachelors die an dem 'Projekt SiV' mitgearbeitet haben und die ich auch mal als 'Messsklaven' einsetzen durfte.

Auch wenn man es manchmal zu vergessen droht gibt es ja zum Glück noch ein Leben neben der Uni. In diesem Leben neben der Uni danke ich ganz besonders meinen Eltern für die fortwährende Unterstüzung während Studium und Promotion. Meiner besseren Hälfte Andy allen möglichen Dank für die Unterstützung, das Verständnis für meine Arbeit und das Ertragen meines Temperaments, du machst mein Leben komplett. Und nicht zuletzt bedanke ich mich bei all jenen die mich gelegentlich von der Physik ablenken, insbesondere meinen Freunden aus Schulzeit und Studium.